UNIVERSITY
OF TRENTO - Italy
DEPARTMENT OF INDUSTRIAL ENGINEERING

XXVII cycle

Doctoral School in Materials Science and Engineering

NMR CHARACTERIZATION OF SOL-GEL DERIVED HYBRID NANOMATERIALS: INSIGHT ON ORGANIC-INORGANIC INTERFACES

Evgeny Borovin

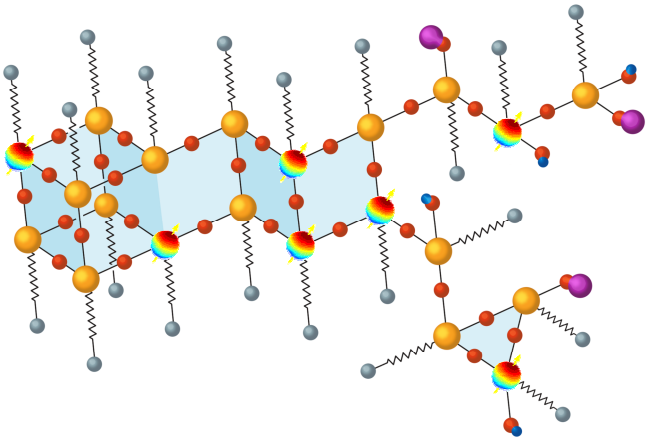

Trento, June 2015

NMR CHARACTERIZATION OF SOL-GEL DERIVED HYBRID NANOMATERIALS: INSIGHT ON ORGANIC-INORGANIC INTERFACES

Evgeny Borovin

E-mail:borovinwin@gmail.com

Approved by:

Prof. Sandra Dirè, Advisor
Department of Industrial Engineering
University of Trento*, Italy.*

Ph.D. Commission:

Prof. Flavio Deflorian,
Department of Industrial Engineering
University of Trento*, Italy.*

Prof. Roberta Maria Bongiovanni,
Department of Applied Science and Technology
Politecnico di Torino, Italy.

Prof. Roberta Bertani,
Department of Industrial Engineering
University of Padova*, Italy.*

University of Trento,

Department of Industrial Engineering

University of Trento - Department of Industrial Engineering

Doctoral Thesis

Evgeny Borovin - 2015
Published in Trento (Italy) – by University of Trento

ISBN:

Trento, June – 2015

It is always possible to explain your idea.

If you cannot – it is not yours.

To beloved Mom and Dad,

who always know how

to explain.

Contents

PREFACE and OBJECTIVES

Nowadays, the impetuous technological development is continuously demanding for new functional materials. Traditional materials as metals, polymers and ceramics are not able to saturate the technological hunger in its vast pool of new applications any more. It has been known for a long while that combination of several materials may demonstrate enhanced properties and new features in comparison with the pure ones. Many materials produced by nature consist of inorganic and organic parts distributed on the molecular- or nano- scale. The inorganic part generally gives particular features like mechanical strength to natural materials, while the organic counterpart provides bonding between the inorganic bricks and/or the soft matter, as in the case of animal bone. The nature of bonding and architectural design in such materials is more and more analyzed by the scientific community, to understand the fundamentals of their formation and to apply this knowledge to artificial materials. The structural bricks in the first organic/inorganic hybrid materials synthesized to mimic the natural ones ranged from the micrometer to the millimeter [1]. The decrease in the size of the inorganic units to the same dimensions as the organic blocks allowed better tuning of properties at the nano-scale..

One advantage ,which makes hybrid materials attractive for many applications, is their processing. Inorganic materials usually require a high temperature treatment for crosslinking and densification; on the contrary, hybrid materials are processed at mild temperatures, because they possess a large amount of organic functions and are usually cross-linked by means of polymerization reactions The hybrids can be easily shaped with low energy consuming processing. From the economical point of view, the bulk hybrids

still hardly compete with classical organic or inorganic materials. However, as thin films they are able to grant their interesting properties to cheaper materials, or renewable biological ones. Instant examples are scratch resistant or hydrophilic/hydrophobic hybrid coatings for organic polymers, glasses or wood [2]. The most attractive feature of Organic-Inorganic hybrids is the possibility to combine the components in the final material from simpler building blocks [3,4] with several benefits as the fine tuning of the material properties. Moreover, due to the nano-sizes of building blocks, the interfaces become so important that are mainly responsible for the final material properties. Indeed, if the nano-objects are small enough (< 5-10 nm), the most of the atoms of the building blocks becomes surface atoms that can interact with those of the other phase

The Sol-Gel process is a well-known synthesis route that offers several opportunities in the preparation of hybrid organic/inorganic nanomaterials. Different sol-gel approaches, from non-hydrolytic to controlled hydrolytic syntheses, have been applied in order to control the structure development in sol-gel hybrids, which allow fine tuning of structure-related properties. Nevertheless, this perspective requires to deepening the knowledge of structural features and finding new tools for the study of the Organic-Inorganic interfaces. In this perspective, the Nuclear Magnetic Resonance spectroscopy, with its ability to probe the local environment of atoms, is an extraordinarily investigation tool and will be extensively employed in the frame of this work for studying hybrid materials obtained by two routes, the first exploiting the traditional hydrolytic sol-gel synthesis and the second one taking advantage of the Nano-Building Blocks approach.

The basic concepts of Sol-Gel process, describing the chemistry beneath the preparation of hybrid materials are presented in the first chapter. **Chapter 1** is an overview of the synthesis strategies and parameters of Sol-Gel derived materials, prepared from molecular precursors ranging from metal alkoxides to organically functionalized silicon alkoxides. General hybrids classification and their design strategies are given in

order to locate the materials, here produced, in the wide sea of hybrids. A brief introduction to characterization techniques applied in the frame of this work finishes the chapter, with particular accent on Nuclear Magnetic Resonance.

Chapter 2 is devoted to the preparation of hybrid Organic - Inorganic silicon-based networks. From an introduction on the versatility in applications and relative facility in preparation of such materials, the chapter is discussing the synthesis and characterization of binary hybrid systems obtained from Tetraethoxysilane and various organofunctional trialkoxysilanes by traditional sol-gel processing. The exploitation of the sensitivity towards selected Volatile Organic Compounds of the synthesized hybrids coatings finishes the chapter.

Chapter 3 is focused on the Nano Building Blocks (NBBs) approach for the preparation of thiol-substituted oligosilsesquioxanes. NBBs examples and advantages are discussed along with their applications, giving insight on the silicon-based systems. The synthesis of thiol-functionalized NBBs and their thorough characterization by different techniques, in particular FTIR and NMR spectroscopy, builds the main body of the chapter. The study by multinuclear NMR of the NBBs growth kinetics, performed in collaboration with the Laboratoire de Chimie dela Matière Condensée at the College de France in Paris, finalizes the characterization to the selection of the best parameters for tuning the silsesquioxane structures.

An introductory study on the application of thiol-functionalized NBBS as active fillers for the preparation of elastomer-based nanocomposites has been made in collaboration with the University of Milan-Bicocca. The preliminary results on the synthesis and characterization of NBBs-rubber nanocomposites are exposed in **Chapter 4**

Chapter 1 Sol-Gel Derived Materials

1.1 Sol-Gel Process

The Sol-Gel process belongs to 'wet chemistry' methods representing a solution synthesis route for oxides preparation in mild conditions. Reactive monomers are used as starting materials and can form inorganic networks (Figure 1).

By creating reactive M-OH groups, which are able to form M-O-M bonds, the molecular precursor in solution transforms into a colloidal suspension (Sol), which by gelation leads to a solid three-dimensional network saturated with liquid phase (Gel). For many applications the residual liquid is removed by drying, resulting in bulk or powder materials. The sols may be produced from various organic or inorganic precursors in non-aqueous or aqueous solutions, but the most widely used precursors are metal alkoxides $M(OR)_n$, where M = Al, Sn, Ce, Ti, Hf, Zr, Si, etc., and R is an alkyl group. Silicon alkoxydes demonstrate low reactivity, thus requiring basic or acidic catalysts, which allow tuning the final structure of the network. Figure 2 summarizes the hydrolysis-condensation reactions of a tetraalkoxysilane precursor, highlighting the different condensation products, which will contribute to the formation of the final network.

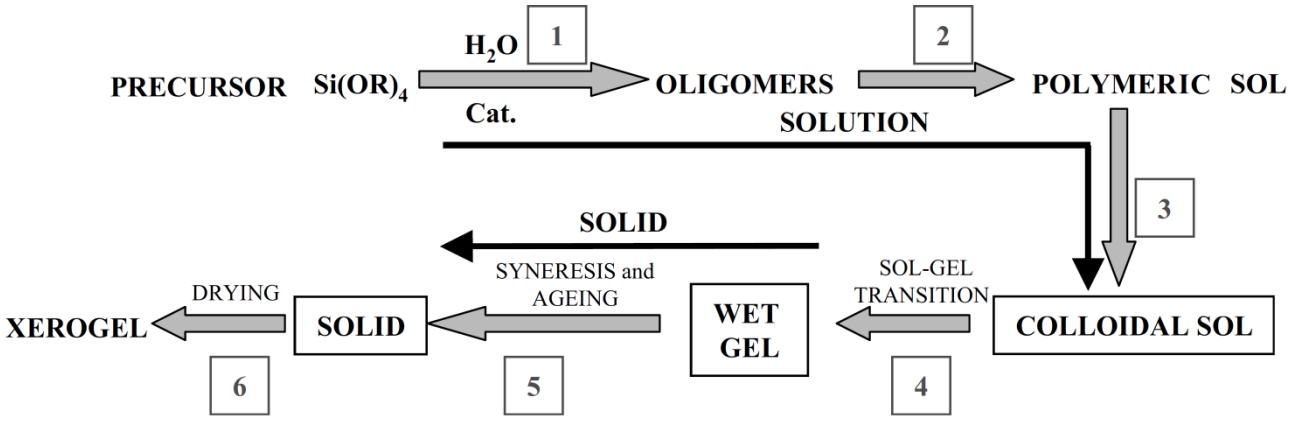

Figure 1. Schematic diagram of the different Sol-Gel process steps with a Si alkoxide [2].

The molecular precursor in the presence of water (Figure 1, (1)) undergoes the hydrolysis reaction; the R group, such as methyl, ethyl, isopropyl, etc., influences the rate of hydrolysis reaction depending on its nature. The smaller the R groups are, the faster the reaction, so that in the same reaction conditions TMOS (tetramethoxysilane) undergoes hydrolysis faster than TEOS (tetraethoxysilane).

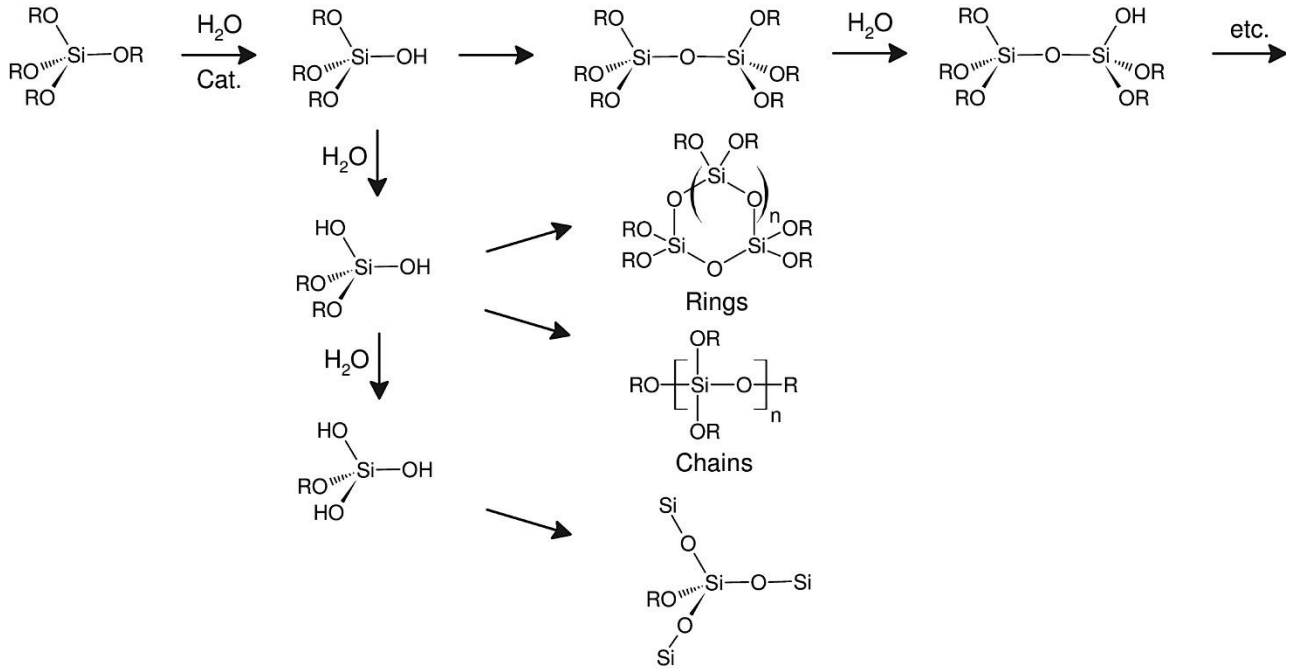

Figure 2. Polycondensation in the Sol-Gel process: an example of tetraalkoxysilanes [3].

With the appearance of the hydrolyzed monomers, the polycondensation reaction starts, leading to oxo-bridges formation. The rate of hydrolysis and condensation reactions

depends on various parameters of the reacting solution: acid or base catalysts, precursor concentration, water and solvent ratios, temperature, etc. Hydrolysis-condensation reactions can be run at mild temperatures and lead to the formation of different linear chains and cyclic oligomers, which bear some residual alkoxide groups (Figure 2). Both reactions occur simultaneously and compete with each other during all steps of Sol-Gel process, resulting in a large variety of different species.

Further hydrolysis of oligomers allows their crosslinking into bigger oligomers and colloids, and turns the solution to transform into the Sol (Figure 1, (3)). At this step, the material can be shaped, if needed, deposited as a coating, or drawn into fibers.

In the next stage, the Sol transforms into the Gel. The Sol – to Gel transition relays on the reactions occurring among colloids, linking them into a rigid network capable to retain the solvent between the net nodes. The material becomes a 'wet solid' occupying all the reaction volume (Figure 1, (4)).

The solid phase development is reached by the increase of inter-colloidal bonds and is shortly followed by the syneresis process, when the solvent discharges from the pores. Further ageing allows fine-tuning important materials characteristics as specific area, density, porosity, hydrophilicity, etc., and usually is followed by drying in order to yield a xerogel (Figure 1, (5-6)).

1.2 Metal Alkoxydes Hydrolysis and Condensation

Polycondensation of metal alkoxides is a process very similar to organic polymerization, and can be studied by following the evolution of both hydrolysis and condensation reactions (Figure 3). The hydrolysis in an organic solvent of the alkoxide group belonging to the molecular precursor introduces a reactive hydroxyl group on the metal (reaction A). Such hydrolyzed precursor is able to react with either similarly hydrolyzed molecule (oxolation – reaction B) or with pristine precursor (olation – reaction C) in order to build oxo-bridges. These condensation reactions release water or alcohol and build the inorganic network.

Hydrolysis:

$$M(OR)_n + H_2O \longrightarrow M(OR)_{n-1}(OH) + ROH \qquad A$$

Condensation:

$$M(OR)_{n-1}(OH) + (HO)M(OR)_{n-1} \longrightarrow M(OR)_{n-1}M\text{-}O\text{-}M(OR)_{n-1} + H_2O \qquad B$$

or

$$M(OR)_{n-1}(OH) + M(OR)_n \longrightarrow M(OR)_{n-1}M\text{-}O\text{-}M(OR)_{n-1} + ROH \qquad C$$

Figure 3. Polycondensation of Metal Alkoxydes: Hydrolysis and Condensation steps [4].

The catalysts have a major impact on the final structure of the derived network. Different structural development is based on the complex interaction between the relative rates of hydrolysis and condensation, variously influenced by the catalysts. In addition, there are also reactivity differences between the variety of non-condensed and partially condensed intermediate species, which lead to the formation of different oxo-bridged structures. The network-forming steps are random in nature, however the morphology and structure of the final framework can be influenced by changing the nature of precursor and solvent, varying reaction temperature, hydrolysis ratio, and the choice of catalyst [4].

1.3 Sol-Gel parameters in Silicon Alkoxydes processing

There are many synthesis parameters influencing the textural and structural properties of Sol-Gel derived materials. The most pertinent ones will be considered below and in 1.3.1 - 1.3.5. As a general rule of thumb for metal alkoxides, electronegativity and reactivity are inversely related, i.e., as the electronegativity of metal atoms increases, the chemical reactivity of the corresponding metal alkoxide decreases. Since silicon has a high electronegativity and a low degree of unsaturation,, the Sol-Gel reactions involving silicon alkoxides are slow and generally require a catalyst to increase the reaction rate [5]. The catalyst can be either a base or an acid, influencing the Sol-Gel reaction in a different manner. The point of zero charge (PZC) of Si–OH-containing species lies between pH 1.5 and 4.5, depending on the degree of condensation (the higher the degree of condensation, the lower the PZC) [1].

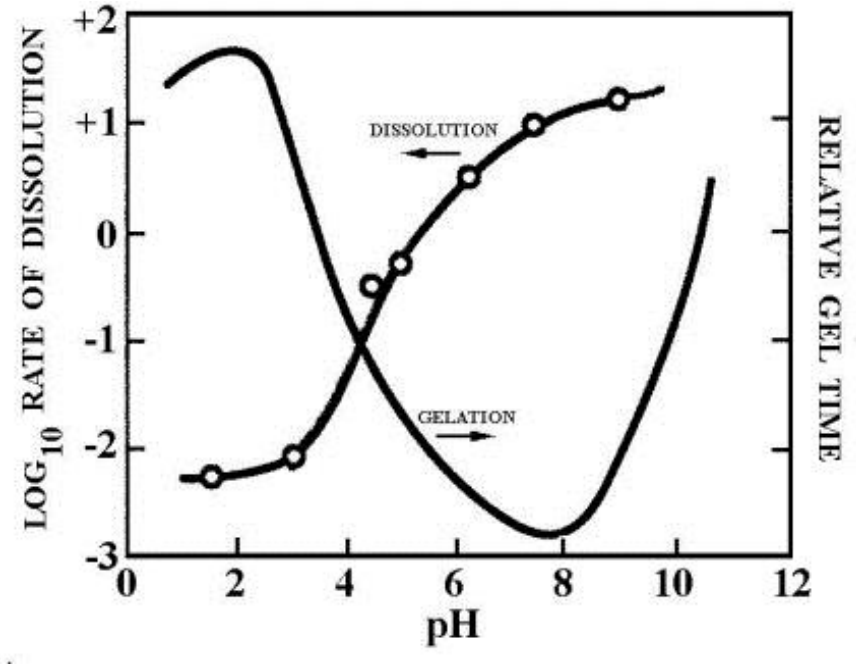

Figure 4. Dissolution rate and relative gelation time as a function of pH for TEOS.

For pH values below the PZC, Si-based species are positively charged, whereas increasing the pH above the PZC (more basic) leads to negatively charged species. Since all

the reactions involved into the Sol-Gel process are equilibria, the reverse reactions induce the dissolution of formed network depending on the system pH (Figure 4). This reverting process and related reactions will be discussed later in section 1.3.5 in details.

1.3.1 Acid-Catalyzed Silicon Alkoxydes Hydrolysis - Condensation

Under acidic conditions the oxygen atom of the Si–OH or Si–OR group is protonated in a rapid first step, and a good leaving group (water or alcohol) is created [1]. In addition, electron density is withdrawn from the central silicon atom, making it more electrophilic and thus more susceptible to be attacked by water (hydrolysis - A) or silanol groups (condensation - B) as shown in the Figure 5.

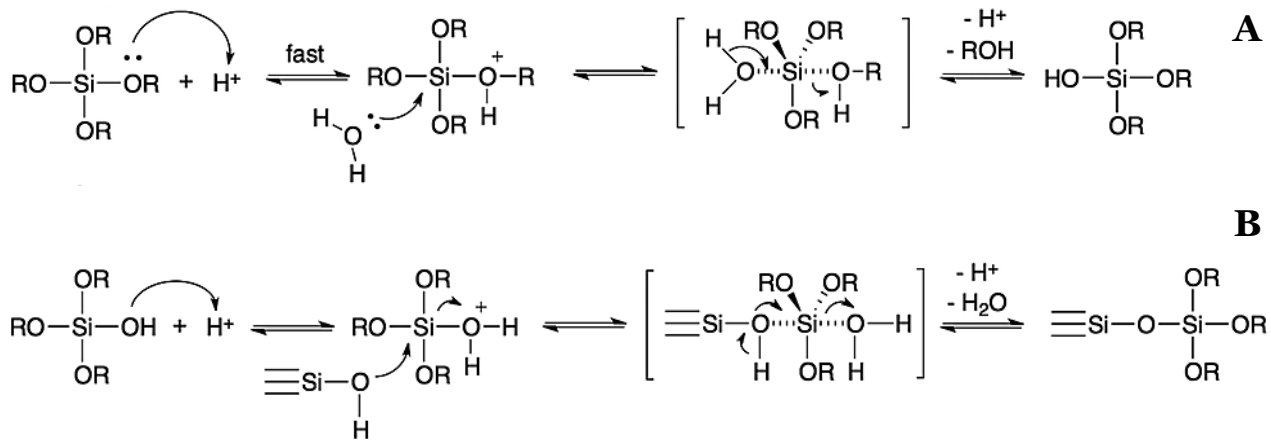

Figure 5. Hydrolysis (A) and condensation (B) in acidic catalysis with five – fold coordinated Si intermediate formation [6]

The pH not only plays a major role in the mechanism but also rules out the micro-structure of the final material. By acid-catalyzed reactions, an open network structure is formed in the first steps of the reaction leading to condensation of small clusters afterwards, since the hydrolysis occurs relatively faster than the condensation. The substitution of only one –OR group by an –OH group has a relatively weak influence on the hydrolysis of the residual –OR groups, so the water molecules are able to attack preferentially other $Si(OR)_4$ molecules than the $Si(OR)_3OH$. Hence, the pristine molecules

are hydrolyzed according to the water availability and tend to form linear oligomers that are occasionally cross-linked and randomly branched. These chains entangle and form additional branches resulting in gelation, as schematically presented in Figure 6.

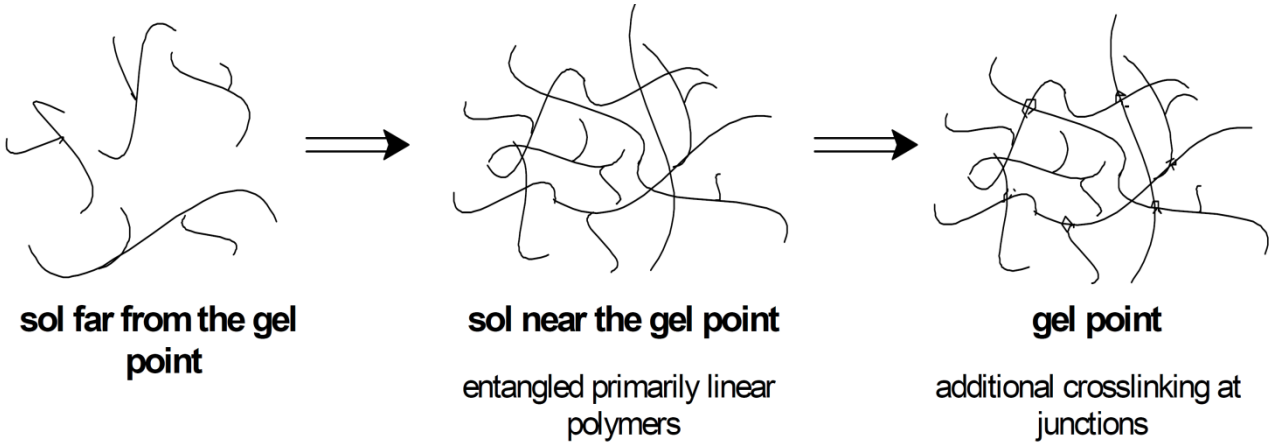

Figure 6. Hydrolysis-condensation structural arrangement in acidic catalysis [7].

Thus, the growth of low-density condensed clusters is obtained with formation of cross-linked 3-D gel with high concentration of silanol groups. Such a Gel Network is mobile and elastic; however, during the drying it can rapidly shrink rearranging to a highly microporous structured solid.

1.3.2 Base-Catalyzed Silicon Alkoxydes Hydrolysis - Condensation

Under basic conditions, i.e. for reactions occurring at a pH > 3, as generally reported, the reaction proceeds via a nucleophilic attack of the OH-group on the Si atom with $-OR^-$ release (Figure 7). The silanol thus obtained is then deprotonated producing a silanolate, which in turn can attack either an alkoxysilane or a silanol to give the Si-O-Si bond [2].

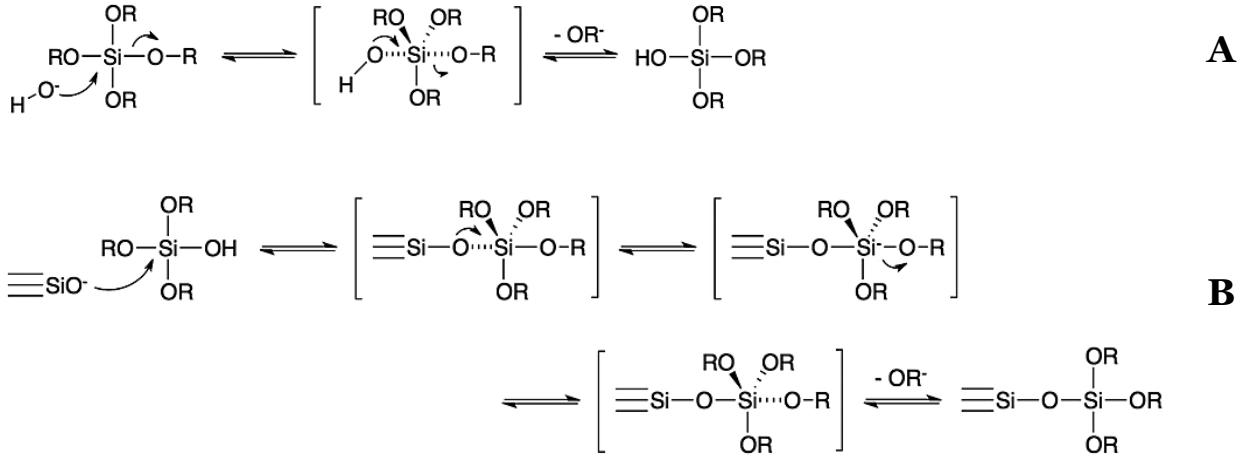

Figure 7. Hydrolysis (A) and condensation (B) in basic catalysis with five – fold coordinated Si intermediate formation [6]

Base-catalyzed conditions improve more the condensation reaction rate than the hydrolysis one, driving the formation of Sols with highly dense colloid particles with narrow distribution in particle size, building highly cross-linked sol particles already in the first steps. Gel point can be addressed to the linkage of such condensed particles, as presented on the Figure 8.

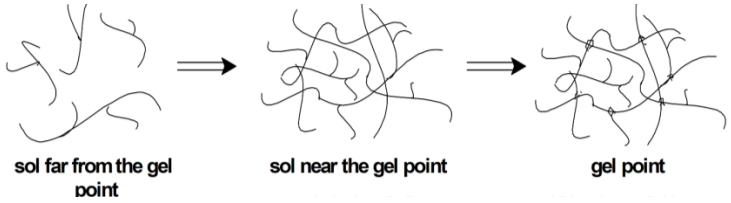

Figure 8. Hydrolysis-condensation structural arrangement in basic catalysis [7].

During the drying step such clusters undergo self-rearrangement; due to their rigidity, the materials shrink only on the early drying steps, resulting in porous solids with larger pores and lower homogeneity than in acid catalysis.

1.3.3 Silicon Alkoxydes Hydrolysis - Condensation: Si/H_2O Ratio

As expected from reactions described in 1.3.1-1.3.2, the water content in the reaction mixture may strongly influence the kinetics of hydrolysis and condensation. Indeed, the effect of the water-to-alkoxide ratio (r) for the Sol-Gel process is such that as the ratio increases, so does the rate of hydrolysis-condensation and transformation to the Gel. Theoretically, for complete hydrolysis, there must be at least one mole of water for every alkoxide group. Depending on the desired properties of the material (either to possess active surface silanol groups or yield in highly cross-linked network) low $r<2$ or high $r>2$ ratios should be used. The drawbacks of using low r value include the increase in gelation time, the decrease of material homogeneity, and the presence of partially hydrolyzed precursor molecules, as discussed by Schmidt [8] and Butler [9]. The higher the r values the higher the extent of hydrolysis that will be achieved prior to condensation between oligomers. Since the condensation reaction can produce either water or alcohol depending on the availability of hydrolyzed reacting species (Figure 3), for the low r values (understochiometric amounts), the alcohol molecules will be preferentially released by the condensation.

It is also possible to control the hydrolysis-condensation extent by providing water to the reaction mixture slowly, synthesizing it directly in the reaction mixture (i.e. In-Situ). The advantages and drawbacks of such route will be discussed in the Chapter 3, which is devoted to the Nano Building Blocks synthesis.

1.3.4 Silicon Alkoxydes Hydrolysis - Condensation: Precursor

Successful synthesis of alkoxysilanes – derived Gels implies meeting at least two requirements for participating precursors: miscibility with water, which is required for hydrolysis, and good reactivity in order to succeed in the Gel formation [8]. Reactivity can be enhanced by catalysis, as discussed previously, and solubility is generally reached by the use of specific solvents. However the nature of precursor plays also an important role in the synthesis evolution. The Steric hindrance in the alkoxysilane affects the hydrolysis rate in such a way that, with increasing in size and branching of the Si alkoxide groups, the hydrolysis rate decreases.

It was shown that with the same reaction conditions and initial molar ratios in hydrolyzing mixtures of TMOS/Methanol/Water, the amount of residual alkoxide groups was smaller than in TEOS/Ethanol/Water mixtures, proving TMOS to be more effective in hydrolysis step than TEOS. Nevertheless, condensation occurs vice versa more effectively for TEOS, meaning that the reactivity of Silanol groups was enhanced for TEOS [10-11]. This behavior, apart from the steric effect can be addressed to the inductive effect, caused by the decrease of electron density on Si atom with replacement of alkoxide by hydroxyl (hydrolysis) or Si-O-Si bridge formation (condensation). Such effect increases the stability of positively (hydrolysis) and negatively (condensation) charged transition states and should be considered in precursor choice (Figure 9).

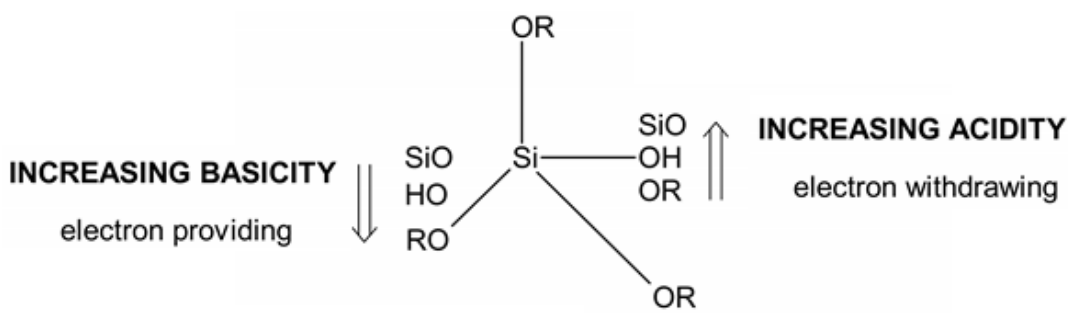

Figure 9. Inductive Effects on Si in dependence on substituents [7].

1.3.5 Silicon Alkoxydes Hydrolysis - Condensation: Solvent

The solvent choice relays generally on its ability to induce solvation of alkoxydes in aqueous media, preventing the phase segregation on the first steps of reaction and allowing better morphological control during the drying. The solvent enhances the reacting system homogenization and allows controlling the concentration of reacting components, influencing the kinetics of Gelation.

Solvents may be either protic or aprotic and are graded in their polarity, hence they may differently influence the solvation extent of polar or nonpolar species. As mentioned in 1.3.1-1.3.2, either deprotonated or protonated silanols drive the condensation reaction depending on the system pH. Aprotic solvents may interact by hydrogen-bond to electrophilic protonated silanols, thus promoting basic catalyzed Sol-Gel condensation and retarding the acid catalyzed. Vice versa, protic solvents establish hydrogen bonding with nucleophilic deprotonated silanols promoting the condensation in acid catalyzed systems and slowing down the base catalyzed oxo-bridging [12].

Another important effect of the solvent is its ability to promote depolymerisation, since all the Sol-Gel reactions are reversible. The solvent acts in reactions such as reesterification (a), alcoholysis (b), and transalcoholysis (c), in the case the alkoxy groups of precursor and alcoholic solvent differ (Figure 10).

$Si(OR)_{4-x}(OH)_x + zR'\text{-}OH \leftrightarrows Si(OR)_{4-x}(OR')_z(OH)_{x-z} + zH_2O$, z<=x (**a**)

$(OR)_{3-x}(OH)_xSi\text{-}O\text{-}Si(OR)_{3-z}(OH)_z + R'\text{-}OH \leftrightarrows (OR)_{3-x}(OH)_{x+1}Si + (OR)_{3-z}(OH)_z Si(OR')$ (**b**)

$Si(OR)_x(OH)_{4-x} + zR'\text{-}OH \leftrightarrows Si(OR)_{x-z}(OR')_z(OH)_{4-x} + zROH$, z<=x (**c**)

Figure 10. Reverse reactions(a-c) and transalcoholysis(d).

Such reactions compete with forward alkoxysilanes hydrolysis-condensation only when protic solvents are used. Deprotonation and formation of sufficiently strong –OH and –OR nucleophiles is an unbearable task for aprotic solvents, since they do not possess enough electrophilic protons. On the other hand, aprotic solvents may interfere in Sol-Gel reaction kinetics by decreasing the strength of electrophiles and increasing that of nucleophiles. Transalcoholysis (or transesterification) reaction is a parasite process, which, however can be used in order to control the hydrolysis rate of reacting alkoxysilane, as discussed before in 1.3.4.

1.3.6 Organically Modified Silicon Alkoxydes

Simple incorporation of organic groups for production of organic-modified inorganic networks is possible, thanks to the presence of hydrolytically stable C-Si bonds in organoalkoxysilanes. There is an enormous variety of commercially available organically modified alkoxysilanes, thus there is an open field for satisfaction of functional hybrid materials demand. The 'magic' of organosilanes, however is limited by the extent to which the nature of organic group dictates the Sol-Gel reaction course. For creating a pure hybrid network, the threefold coordination of $RSi(OR')_3$ precursor is required. General considerations for reacting solution properties discussed in 1.3.1-1.3.2 for tetraalkoxysilanes can be forwarded to organotrialkoxysilanes. Nevertheless, the nature of organic group strongly increases inductive effect on the hydrolysis-condensation chemistry of alkoxysilanes, deeply influencing the properties of Sol-Gel derived hybrids. Under the basic synthesis conditions, the electron-withdrawing organic groups such as cyanoethyl or chloromethyl increase the hydrolysis-condensation rate, but same groups retard the hydrolysis under acidic conditions. Oppositely, electron-donor alkyl groups speed up the hydrolysis-condensation in acid-catalyzed synthesis.

Complementary to inductive, the steric effect plays a role on hydrolysis and condensation rates of the alkyltrialkoxysilanes. Rates enhancements over tetraalkoxysilanes, given by the inductive effect, are rolled back for long alkyl chains as butyl and propyl. Bulky branched organic groups as iso-propyl, sec- and tert-butyl slow down the hydrolysis-condensation reactions to a higher extent [3]. On the other hand, such a behavior can be used as an advantage with an example of phenyl-substituted trialkoxysilanes: the silane triols formed by hydrolysis at ambient temperatures are enough stable not to undergo condensation. These triols can be isolated as crystalline solids and then activated on the demand to react with target silanols, as used for instance in non-

wetting glass applications [3]. The relationship between hydrolysis and condensation reactions rates is quite complex, considering all the factors discussed. Additionally, since the alkoxides being hydrolyzed to silanols become less sterically bulky, the further hydrolysis is expected to speed up proportionally to the number of substituted alkoxide groups. Vice versa, siloxane bonds built by silanols condensation, make the pristine molecule significantly more bulky and hinder the approach to silicon centers, making hydrolysis-condensation kinetics more complex. As a result, described steric effects can decrease the degree of condensation and network density of materials prepared from organoalkoxysilanes, which is usually disadvantageous.

The co-condensation with tetraalkoxysilanes can help to overcome such negative aspects, assuring both functionality and network density of the hybrid. However, as already discussed, numerous parameters influence the equilibrium and the reaction complexity increases even more for multicomponent sol–gel reactions. It is possible in such case that undesired large phase separation of organic and inorganic species in the materials occurs, weakening the hybrid properties. The acquisition of a homogeneous functional material is therefore the result of the control and optimization of all synthesis parameters. In this frame, the Chapter 2 of this thesis is devoted to the synthesis and characterization of hybrid Organic – Inorganic networks prepared by co-condensation of tetra and trifunctional alkoxysilanes.

1.4 Hybrid Materials and Nanocomposites

1.4.1 Classification of Hybrid Materials

In order to define the materials to which this work is devoted, and to locate them in the large family of hybrid nanocomposites on the basis of structural units and nature of interactions, the following classification is given, even though it appears that there is no unique and precise classification of Sol-Gel composite materials.

First of all, following J. D. Mackenzie [13], the applied processing routes can be divided into 2 groups: 1st generation, which results in oxide composites and the 2nd one, which results into hybrid Organic-Inorganic nanocomposites. The Organic-Inorganic nanocomposites depending on the chemical interactions occurring, were classified by C. Sanchez, F. Ribot [14] and U. Schubert [15] into 2 groups. 1st class materials link organic and inorganic parts only by weak physical interactions. Examples are the materials, where the organic molecules are entrapped in the gelling inorganic matrix, or vice versa the inorganic molecules are captured in-between structural zones, formed by the organic molecules chains. 2nd class consists of materials, where the organic counterpart is linked to the inorganic phase by strong covalent, or iono-covalent chemical bonds (Figure 10).

The highly cross-linked Organic-Inorganic hybrid networks (Chapter 2) and the hybrid Nano Building Blocks (Chapter 3), prepared and characterized in the frame of this work both belong to the 2nd class and are composed of an inorganic backbone modified by organic moieties.

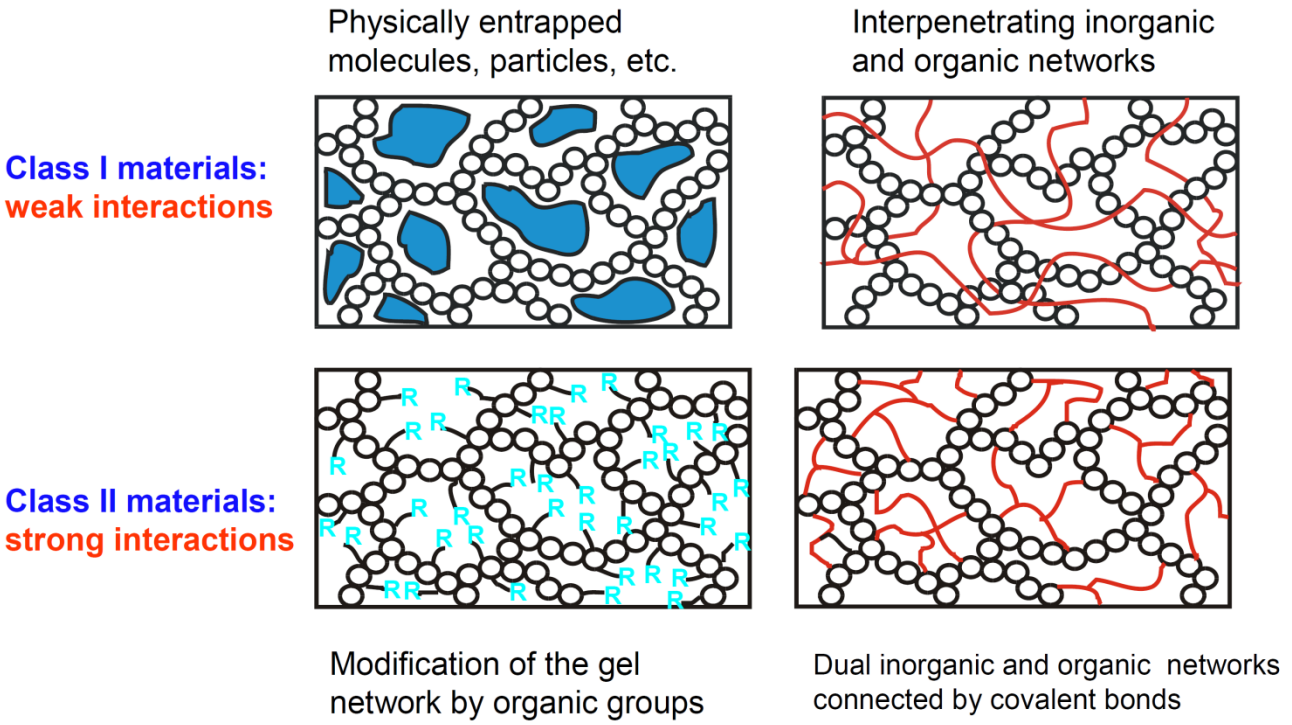

Figure 10. Classes of Organic-Inorganic Sol-Gel derived hybrid materials .

From another point of view, depending on the structural units composing the hybrids, they can be divided into 4 types, as was proposed by Haas [16]. The precursors exploited for synthesis can build and modify the materials' network in different ways (Figure 11), according to following types:

Type 1: The inorganic network formers, such as metal alkoxydes: Al (Al-tri-sec-butylate), Ti (Ti-isopropylate), Zr (Zr-butylate), and previously discussed Si (TEOS - tetraethoxysilane, TMOS - tetramethoxysilane, etc...)

Type 2: The inorganic network formers with organic non-reactive functions. Good representatives are organically modified Si alkoxydes due to the high stability of Si-C bond towards hydrolysis and wide variety of available organic groups for network modification.

Type 3: The inorganic network formers with reactive functions ready for self-polymerization or cross-linking, still able to co-condense via hydrolysis – condensation

reaction. The good examples are MPTMS – methacryloxypropyltrimethoxysilane, GPTMS – glycidoxypropyltrymethoxysilane, etc.. [17].

Type 4: The organic network formers - monomers, which can react via either chemical crosslinking or polymerization reaction with the organically modified metal alkoxydes.

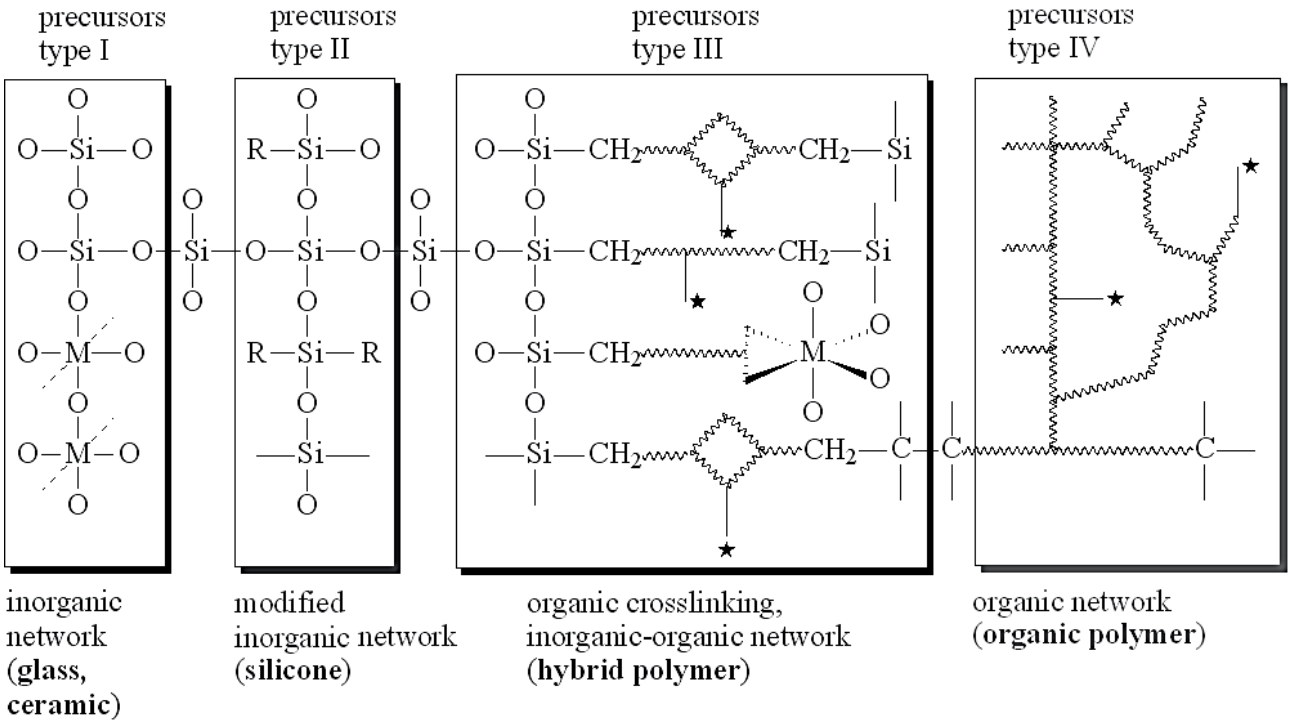

Figure 11. Types of hybrid materials precursors and structures they form [16].

Needless to say that the properties of hybrid materials are not only related to the chemical nature of their precursors, but strongly depend on the synergy of organic and inorganic components as will be discussed in Chapter 2, dealing with Organic-Inorganic hybrid networks obtained from the mixtures of precursors **type 1** and **type 2**; and in Chapter 3 reporting on the hybrid Nano Building Blocks synthesized from only **type 2** precursor.

1.4.2 Design and Synthesis Strategies of Hybrid Materials

The Sol-Gel reactions can be exploited in many different ways in order to yield in various types of hybrid materials, depending on the demand. The main chemical routes leading to nanostructured hybrids were suggested by C. Sanchez, F. Ribot [18] and graphically represented on the Figure 12.

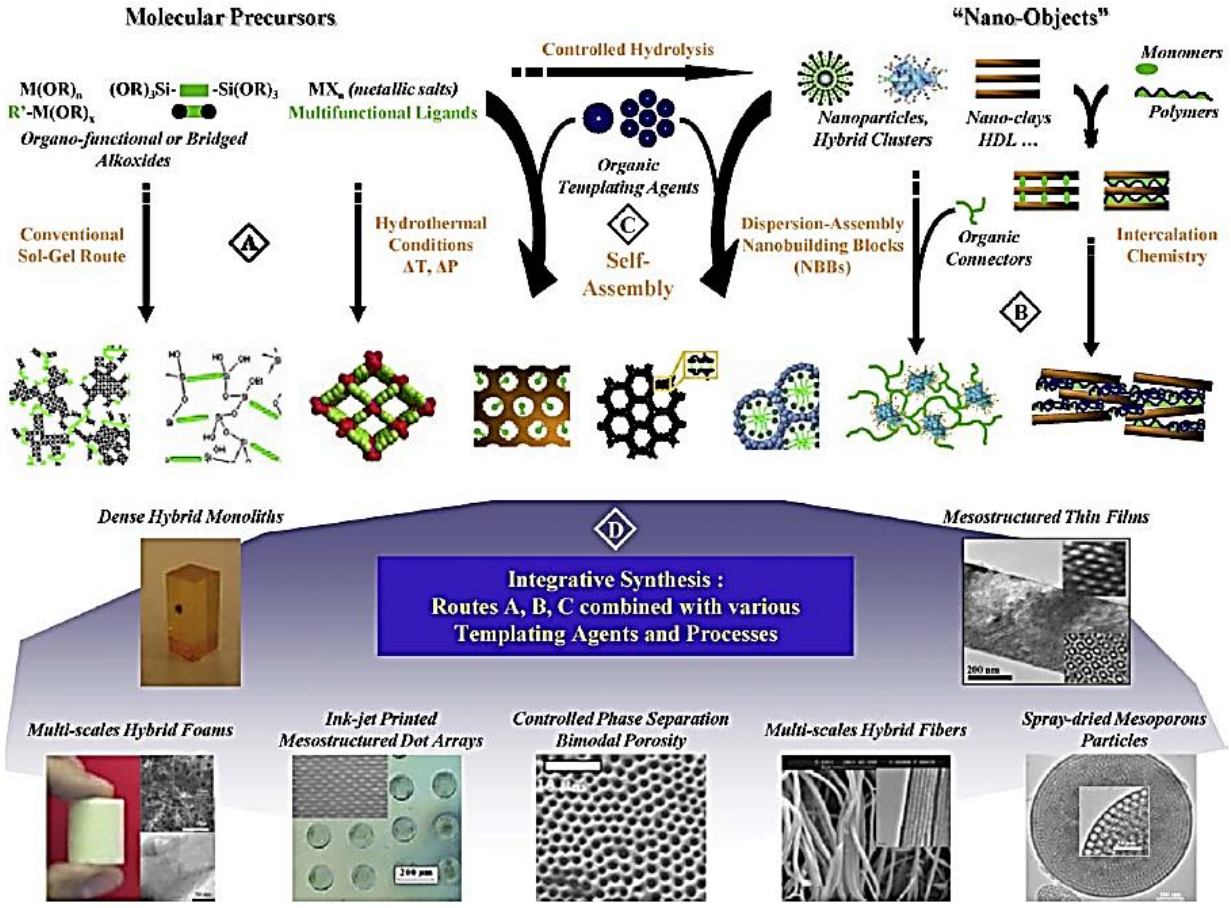

Figure 12. Main chemical pathways leading to nanostructured inorganic and hybrid Organic-Inorganic materials [14].

Path A reflects a versatile soft chemistry pathway, including conventional sol–gel chemistry or exploiting specific bridged and poly-functional precursors, or hydrothermal synthesis. The conventional sol–gel route results in amorphous hybrid networks through hydrolysis–condensation reactions. In the frame of this work, tetra-functional silicon

alkoxides TEOS was paired with other organically modified silicon alkoxides for the preparation of gas-sensitive coatings (Chapter 2). In general, the Sol could also contain an organic- or bio-component that could interact more or less strongly with the inorganic components leading to class 1 or class 2 hybrids.

Path B corresponds to the synthesis, assembling/dispersion of well-defined objects, which keep their integrity in the final material - Nano Building Blocks (NBBs) [19,20]. These NBBs can be either clusters or organically functionalized nanoparticles (NP), or even layered compounds able to be dispersed into the suitable matrix. In this work, the thiol-functionalized NBBs were synthesized and studied in their growth kinetics, as well as in their interaction with polymers matrices (Chapter 3).

Path C is a self-assembling procedure, where organization or shaping of the growing networks is templated by organic surfactants [21]. This strategy allows tuning of the hybrid interfaces and leads to nanocomposites, presented as dispersions of inorganic bricks in a hybrid matrix or segregation of organic polymers within inorganic matrices.

Path D is a controlled design and assembling of hybrid materials in the 1 to 500 Å range. The phase separation phenomena can be exploited to control the shapes of complex objects at the micron scale [21].

1.4.3 Nanocomposites

It is quite problematic to describe the difference between Organic - Inorganic hybrids and Organic - Inorganic nanocomposites. In fact there is no clear borderline between these materials. The term “nanocomposite” can be applied, when one of the structural units, either the organic or the inorganic, is in size range from 1 to 100 nm. There is a smooth transition from hybrid materials to nanocomposites: large molecular building blocks of hybrid materials, such as inorganic clusters, can easily lay in nano-metric scale. It is commonly accepted to use the term “nanocomposite” if discrete structural units are in the respective size scales, and the term hybrid materials is more often used if the inorganic units are formed in situ by molecular precursors, as by exploiting sol–gel reactions [1, 3, 8, 14, 19]. Usually a nanocomposite is formed from the Building Blocks by their incorporation in organic polymers. Emerging techniques in this context rely on polyhedral oligomeric silsesquioxanes (POSS) incorporation. POSS-polymer nanocomposites prepared from both monofunctional and multifunctional POSS monomers are discussed in [22], incorporation of POSS into polymer matrices via chemical cross-linking or physical blending is reported in [23], the importance of filler morphology in final functional properties was well-exploited in [24].

Recent years have seen a growing interest in nanocomposites, their preparation, processing, and application. Among the reports there are many devoted to nanocomposite coatings preparation techniques: fabrication of UV-curable nanocomposite coatings with effectively enhanced thermal and mechanical properties [25], aerosol-prepared nanocomposite coatings for biomaterials, multifunctional therapeutic carriers , ….

The Sol-Gel synthesis is certainly very attractive in nanocomposites preparation because it is very versatile, allowing to chemically adjust the matrix and filler interface for optimizing the materials’ structure and properties. Such nanocomposites are extensively

discussed in the literature, and several books have already been published: they mainly address polymer nanocomposites preparation [29]; or electronic sensors, biomedical and optical devices applications [1]; or use in catalysis [30].

The strategies for nanocomposites preparation can be divided into in-situ and ex-situ techniques [4]. Sol-Gel nanocomposites obtained by in-situ methods may consist of a Sol-Gel matrix (inorganic or hybrid organic–inorganic) with nanoparticles formed In-Situ by chemical reaction or thermal-induced phase separation; or a polymer network with nanoparticles grown inside via Sol-Gel reactions. In ex-situ approach the nanocomposites are obtained by reacting of the two pre-formed components.

1.5 Characterization Methods for Hybrid Materials

The characterization of a functional material is generally performed by structural analysis and property evaluation. Structure analysis can be performed by a variety of microscopic and spectroscopic techniques, while property evaluation depends on the material application. In the case of hybrid Organic - Inorganic materials, one of the main challenges is to determine the degree of components condensation and the level of the interaction between the organic and inorganic components. Both factors are very important for the properties that the hybrids devoted to exhibit [3, 4]. Over the years, different techniques were used for the investigation of the structure and the properties of the nano – hybrids, nevertheless there is continuous demand on technical improvement of existing methods and development of novel approaches in order to characterize the organic – inorganic interfaces. Among the others, the NMR spectroscopy technique is attracting a lot of attention for investigation of the O/I interfaces, being able to provide the information about the local environment of atoms. This unique feature of NMR spectroscopy is the principal reason for its superiority over any other technique for structure elucidation. NMR basics and particular aspects of its application in the hybrid materials structural investigation will be discussed in the following sections.

1.5.1 Nuclear Magnetic Resonance (NMR)

1.5.1.1 Introduction

Nuclear magnetic resonance spectroscopy has been used as a quantitative analytical tool since the early 1950s, shortly after its discovery. However, it has not achieved the same degree of user confidence and widespread routine application as, for instance, optical spectroscopy.

NMR spectroscopy excels in the measurement of relative amounts of the components of a mixture. The absorption coefficient for the absorption of electromagnetic energy is essentially identical for all nuclei of the same species in a molecule or mixture of molecules. In contrast, the absorption coefficient in optical spectroscopy must be calibrated for each spectroscopic transition assigned to the various components of the mixture, because the coefficient is a complex function of transition probability, energy differences, and perturbations of the energy level system. Thus, while an analysis of the relative amounts of the components in a mixture can be carried out by NMR without ever separating the mixture into its components or having authentic samples of them, the absorption coefficients must either be known or measured before such an analysis can be performed in the optical region.

A second advantage for NMR spectroscopy in mixtures arises from the effective isolation of the nuclei from forces acting on the molecules, leading to line widths many orders of magnitude less than those in the optical range. The effective resolution of NMR spectrometers, particularly since the widespread incorporation of high-field superconducting magnets, is far better than their optical counterparts, often resulting in little or no interference or overlap of the analytical peaks [38-44].

1.5.1.2 Basic Principles

The principle behind NMR is that a spinning nucleus, such as a proton, is charged and therefore has a magnetic moment. When it enters an external magnetic field it may either align itself with the field or oppose the field (Figure 13). If the nuclei were in random orientations it would be impossible to observe any net effect. However, it takes energy to oppose the field so slightly fewer nuclei choose to oppose rather than align with the field.

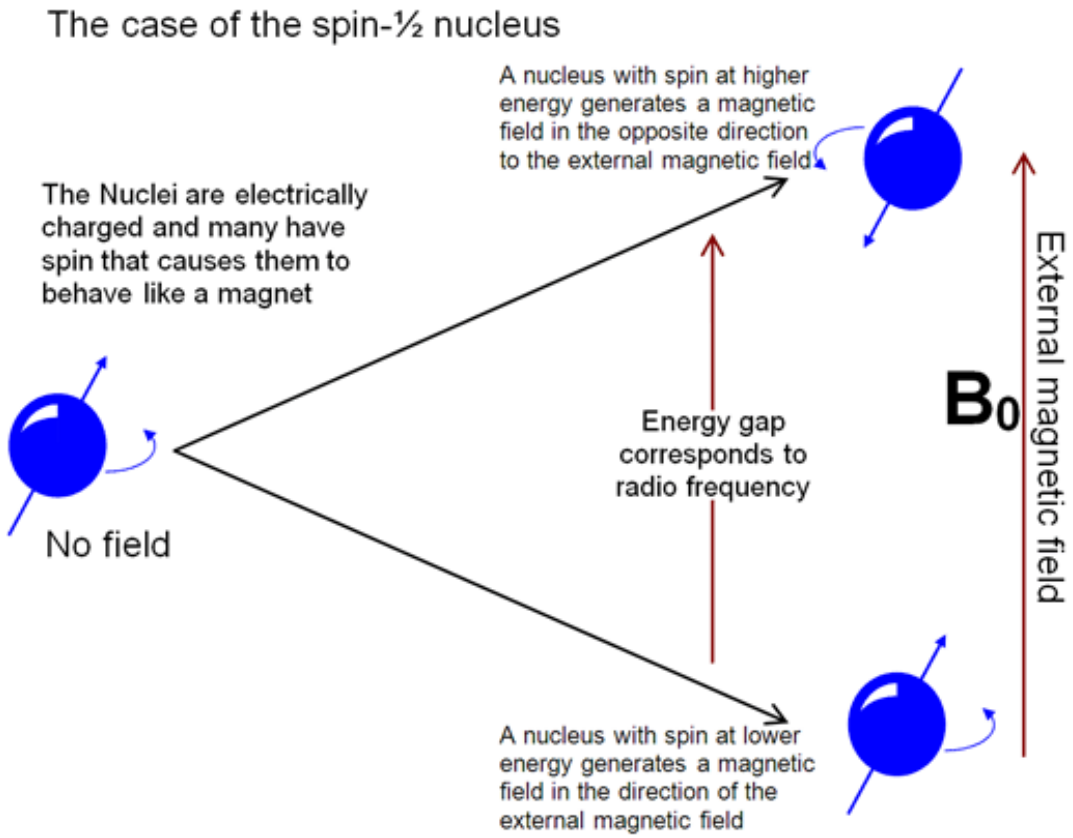

Figure. 13. The spin-1/2 nucleus in an external magnetic field.

This sets up a bulk magnetic moment vector that is the sum of the individual magnetic moments [39]. The overall magnetic moment is called the bulk magnetization of the sample. It is possible to represent the magnetization by a vector in the direction of the

magnetic field. The magnetization vector can be shown against coordinates x, y, z with it on the z-axis of a fixed or laboratory frame (Figure 14).

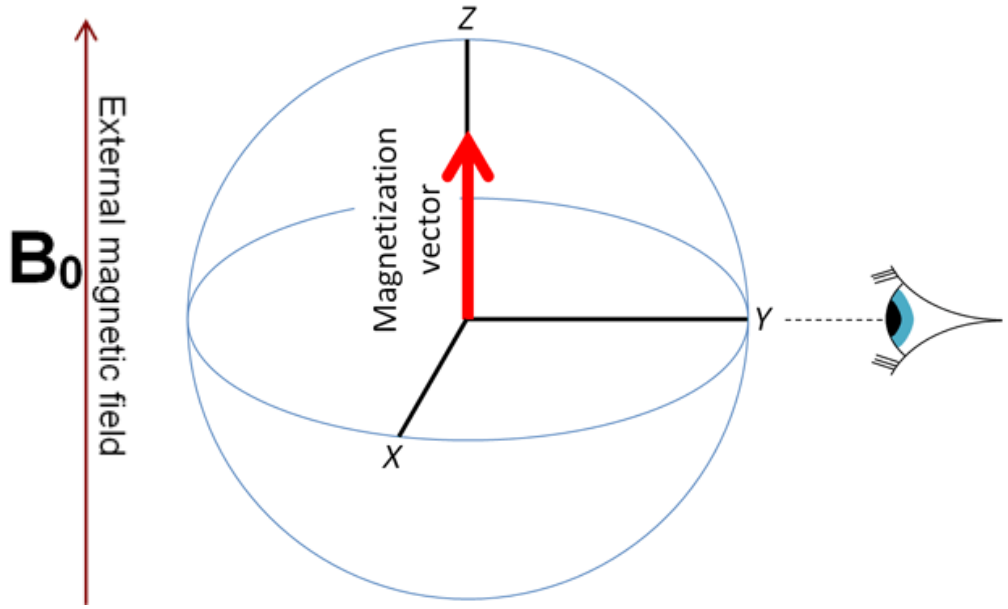

Figure. 14. The laboratory or stationary frame showing the bulk magnetization vector at equilibrium along the z-axis

When the magnetization vector is moved by an angle β from the z-axis, it moves around the z-axis describing a cone with the z-axis at its center. The vector's motion has a specific frequency that is representative of it and is known as Larmor precession [43].

If the magnetic field is $\mathbf{B_o}$ then the Larmor precession frequency will be according to equation: $\nu_o = -\frac{-\gamma B_o}{2\pi}$.

The frequency, ν_o is the same frequency that will be observed in the NMR spectrum. The measurement is carried out with a detector in the x, y-plane and when the magnetic vector crosses it during precession it induces a measurable electric current in the coil. The process is similar to the way electric current is generated by a rotating magnet in a coil.

The magnetization vector can be moved in direction by transmitting a signal (a radiofrequency signal – rf) from a coil in the detector in the x, y-plane. However, the induced magnetic field is much stronger than any electrical signal that can be transmitted through the probe coil of the spectrometer [38]. Instead of using a fixed frame of reference, it is convenient to use a coordinate framework where the x, y-plane rotates about the z-axis at the observation frequency close to the Larmor precession rate of the material under study (Figure. 15).

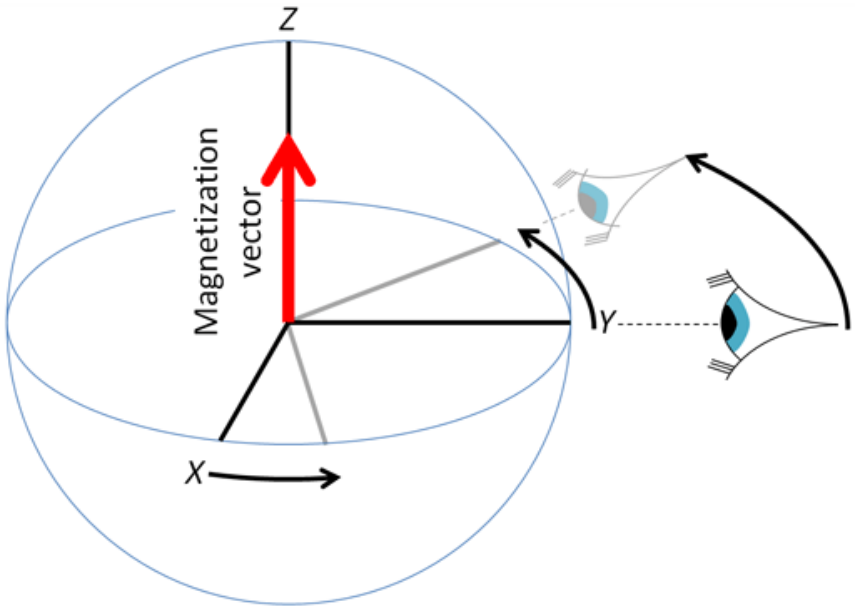

Figure 15. The rotating frame, rotating at or near the Larmor frequency, showing the bulk magnetization vector at equilibrium along the z-axis

The induced field on the z-axis becomes proportionate to the rf signal that becomes a fixed electric field vector (**E**) in the x, y-plane relative on the rotating frame. The correct choice of the rf signal frequency allows the movement of the magnetization vector from the z-axis to the x, y-plane [40].

1.5.1.3 Single Pulse Experiment

The magnetization vector is moved by an angle proportional to the length and intensity of the rf pulse. If the vector is moved by 90° then the process is called a 90° single pulse (Figure 16)

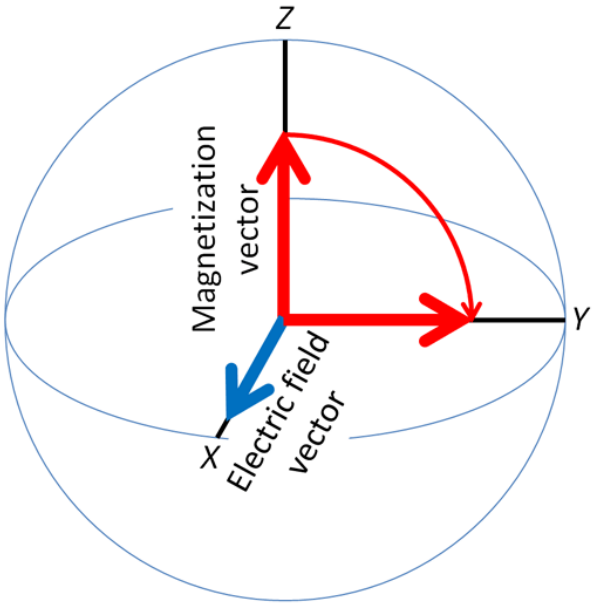

Figure 16. Effect of a 90°x pulse. The magnetization vector is rotated to the y-axis.

The Single Pulse (SP) experiment begins with the system at equilibrium and thus **M** is oriented along the z axis. The first step is a 90° pulse, which means that an excitation field $\mathbf{B_{ex}}$ is applied along the x axis by one of the RF coils. The bulk magnetization precesses about the x axis in response to $\mathbf{B_{ex}}$. Instead of characterizing this precession by a frequency, the time required for **M** to rotate through a particular angle is used. Thus the effect of the 90° pulse is to rotate **M** from the z axis to the y axis. After the pulse has been applied, since the magnetization is not at equilibrium, it returns slowly (typically over a period of seconds) to the equilibrium magnetization along the z-axis (Figure 17). In the process, radiofrequency radiation is emitted. This is acquired at the end of the pulse

sequence and is called the Free Induction Decay (FID). After Fourier transformation of acquired FID, the spectrum can be derived and analyzed.

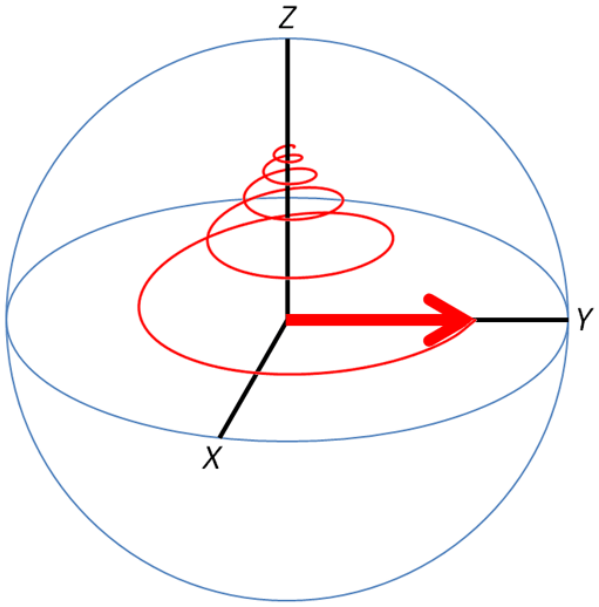

Figure 17. Free induction decay of an excited magnetization vector towards equilibrium in the rotating frame. The magnetization precesses around the z-axis while approaching it.

The chemical shift (resonant frequency relative to a standard)of a particular nucleus can be correlated with its chemical environment, the scalar coupling (or J-coupling) indicates an indirect interaction between individual nuclei, mediated by electrons in a chemical bond, and, under suitable conditions, the area of a resonance is related to the number of nuclei giving rise to it.

1.5.1.4 Nuclei Observed in This Work

Most NMR investigations start with the analysis of the proton spectrum of the sample of interest, with the usual analysis of the chemical shifts and relative signal intensities. Hydrogen atoms are important constituents of hybrid materials, so the ^{1}H NMR provides insight into a wide range of such systems. As compared to applications to organic molecules, an advantage is that there is a lower density of coupled protons in such systems. As a consequence, good ^{1}H spectral resolution can often be achieved, allowing investigating the local structure of hybrid materials and following the occurring Sol-Gel reactions in time [46]. A vast number of studies was devoted to following the hydrolysis and condensation of silicon alkoxides after the first attempts by Vega in the end of 80-s [47-48].

Observation of ^{13}C nucleus is also beneficial for characterization of hybrid materials, since the ^{13}C spectrum offers further characterization of the organic counterpart as it relates directly to the carbon skeleton. Unfortunately, ^{13}C has a lower intrinsic sensitivity than the proton and has only 1.1 % natural abundance, thus specific rf pulse sequences should be applied for enhancing the signal-to-noise ratio in acquired spectra.

In the field of Silicon based hybrids, the observations of Si atom environment is certainly more productive in giving the structural information of materials, since the Si atoms are main building knots of the network structure. Of the naturally occurring isotopes ^{28}Si (92.21%), ^{29}Si (4.70%) and ^{30}Si (3.09%), ^{29}Si only is active in NMR. The low natural abundance and long-lasting Si atoms relaxation elongates the acquisition times and complicates the analysis of fast reacting systems. However, during the last decades, many researchers contributed to the developments of new methods and acquisition techniques. Some of the most complete studies were reported for TEOS, TMOS kinetics behavior of the hydrolysis–polycondensation processes [49-52], and the study on the early

stages of the polymerization of hybrid TEOS-RSi(OR')$_3$ sols with the use of specific pulse sequences and addition of paramagnetic relaxation agent Cr(acac)$_3$ [49]. The application of ^{29}Si NMR spectroscopy provides a way to follow the hydrolysis and the condensation reaction of silicon alkoxides, and is of great interest for acquiring information about the structure of the oligomeric species. The chemical shift of silicon is determined by the chemical nature of its neighbors, namely, the number of siloxane bridges attached to a silicon atom, and T and Q structures are the commonly used notation corresponding to three or four Si–O–Si bridges, respectively.

1.5.1.5 NMR Pulse Sequences

The rf pulse sequence starts with a period of time to allow magnetic equilibration known as the relaxation time. Then a hard radiofrequency pulse excites the nucleus, transferring the magnetization into the x, y-plane. As the nuclei relax towards equilibrium they emit a radiofrequency signal (FID). This sequence relates to the nucleus (such as ^{1}H) which is detected in the observed channel in the experiment (Figure 18).

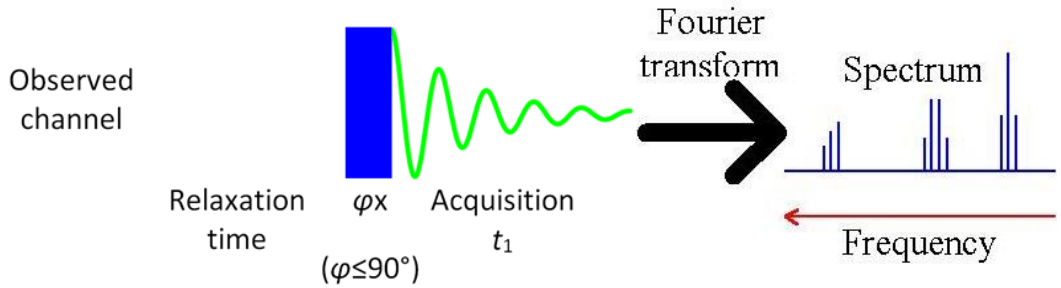

Figure 18. Schematic representation of basic Single Pulse sequence**.** Radiofrequency pulse is a blue rectangle, (FID) is a green decaying sinusoid, φ is pulse duration.

For the less naturally abundant nuclei as ^{13}C and ^{29}Si, it is possible to enhance the acquired signal, or emphasize certain interactions between the nuclei of material with the

use of specific pulse sequences. The experiments exploited in this work are short-listed with description as follows.

1.5.1.6 ^{1}H decoupling sequences

Many experiments involve more than one nucleus and therefore require the use of more than one radiofrequency channel. Each of the rf channels are tuned at different frequencies, matched to different nuclei. In some cases heteronuclear coupling from another nucleus with magnetic spin causes the signal to split and its sensitivity to fall. This effect is especially important for low sensitivity nuclei, as for ^{13}C,.. The required action is to apply decoupling to the neighboring nucleus. There are a number of decoupling methods but the underlying theme is that all of them transmit an rf signal with a bandwidth of a few kilohertz of more at the Larmor frequency of the neighboring nucleus (that differs from the Larmor frequency of the observed nucleus). There result transitions in nuclear spin energy that annul the spin coupling and the signal appears stronger (Figure 19) [39-40].

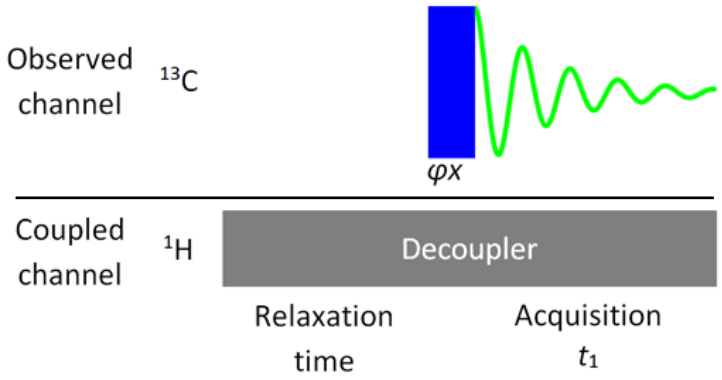

Figure 19. Decoupling pulse sequence, when ^{1}H are decoupled from ^{13}C

1.5.1.7 ^{1}H-^{29}Si Distortionless Enhancement by Polarization Transfer (DEPT)

Distortionless Enhancement by Polarization Transfer (DEPT) is an experiment that utilizes a polarization transfer from one nucleus to another to increase the signal strength of the second nucleus. The polarization transfer occurs from a nucleus with a relatively larger gyromagnetic ratio γ (^{1}H) than the one of the analyzed nucleus (^{13}C or ^{29}Si). DEPT is much more sensitive than a regular pulse experiment. Furthermore, the repetition rate is governed by the relaxation times of the protons and not by those of the second nuclei. Since proton relaxation times are the shortest, the period of time to allow magnetic equilibration (recycle delay) is much shorter than in Single Pulse sequence. This translates to an improved signal-to-noise (S/N) per unit time for DEPT over a regular Single Pulse NMR experiment.

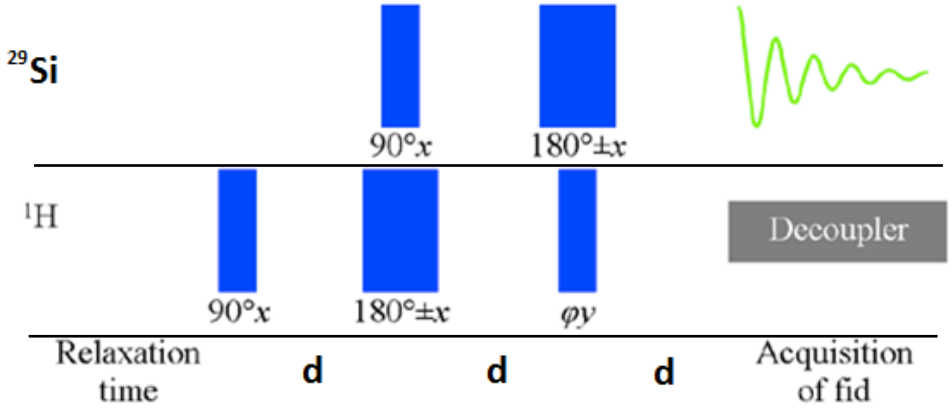

Figure 20. DEPT pulse sequence, when polarization is transferred from ^{1}H to ^{29}Si.

The DEPT sequence on the Figure 20 begins with a 90°(^{1}H) pulse after which proton magnetization evolves under the influence of proton–silicon coupling such that after a period **d** (transfer time) the two vectors of the proton satellites are anti-phase. The simultaneous application of a 90°(Si) and 180°(^{1}H)pulse, at this point produces a new state of affairs, in which both transverse proton and silicon magnetization evolve coherently.

This new state is termed heteronuclear multiple-quantum coherence. During the second delay **d**, the heteronuclear coupling is not evolving, whereas during the following simultaneous 180°(Si) and φ°(^{1}H), the silicon pulse refocus ^{29}Si shift evolution, while the φ° proton pulse creates a different functional dependence as a function of silicon multiplicity. The final evolution delay of **d** allows phasing of ^{29}Si magnetization, and the ^{29}Si channel acquisition is performed under the proton decoupling. Correct choice of the experimental parameters in the DEPT sequence (transfer time **d**, related to 1/2J; and variable ^{1}H pulse angle φ) can lead to optimization of sensitivity and quantitative results in the complex spin systems [53].

In the Si-based Sol-Gel derived hybrid Organic-Inorganic systems, the efficiency of the polarization transfer function depends on the mutual coupling of the silicon nuclei with the protons of the organic backbone and also the coupling of alkoxy groups protons (when starting from organically modified alkoxysilanes).

For an I_nS spins system (n being the number of protons I coupled to the S nucleus, i.e. ^{29}Si in this case), the theoretical signal enhancement E_d of ^{29}Si decoupled spectra in a DEPT sequence depends upon three variables: **d** (transfer time), φ (variable pulse angle) and n the number of protons coupled to ^{29}Si nucleus [54]:

$$E_d = n\,\gamma(^{1}H) / \gamma(^{29}Si)\,\sin\varphi\,\cos^{n-1}\varphi\,\sin(\pi\,\mathbf{d})$$

Optimal enhancement is achieved when the transfer time **d** is set to 1/2 J of ^{1}H- ^{29}Si coupling constant and φ to the following value: $\varphi_{opt} = \arcsin^{-1}(1/n^{-1/2})$ [54]. However, the correct choice of experimental parameters used in the DEPT sequence (**d** and φ) is not obvious in more complex spin system, where there are at least two different kinds of protons coupled to the ^{29}Si nucleus, via two- (^{2}J) and three-bond (^{3}J) ^{29}Si-^{1}H coupling, which is the usual case for organically modified alkoxysilanes

Brunet demonstrated, both theoretically and experimentally, that the polarization transfer efficiency in the ^{1}H-^{29}Si DEPT pulse is specifically sensitive to the extent of hydrolysis, when detecting alkoxysilane monomers in acid-catalyzed MTES Sol-Gel system [54]. On the contrary, different partially condensed species almost do not vary in acceptance of polarization from ^{1}H, once the transfer time D and variable pulse angle φ are properly adjusted.

In the frame of this work, in order to optimize **d** and φ parameters in the studied hybrid Organic-Inorganic systems and increase the different species sensitivity, rough theoretical assumptions and precise experimental surveys were held. The use and advantages of the ^{1}H-^{29}Si DEPT pulse sequence will be discussed in the Chapter 3 of this work, devoted to the Nano Building Blocks.

1.5.1.8 2D Experiments: Heteronuclear Multiple Bond Correlation

The two-dimensional techniques refer to two frequency dimensions, whereas 1D methods have only one. The 2D experiment result is a two-dimensional contour map; one dimension represents the proton chemical shifts, the second one represents the second nucleus chemical shifts, and the contours represent the signal intensity.

Heteronuclear Multiple Bond Correlation (HMBC) pulse sequence is suitable for determining long-range ^{1}H-^{13}C connectivities, providing the information about the chemical shifts of the carbon atoms that are about 2-3 bonds away from the proton to which they correlate. Such experiments contain a mass of data on the molecular skeleton and can be extremely powerful tools in hybrid Organic-Inorganic materials structure elucidation.

HMBC pulse sequence is shown on the Figure 21. The first ^{13}C 90° pulse, which occurs 1/2 J_{CH} after the first ^{1}H 90° pulse, serves as a low-pass J-filter to suppress one-bond correlations in the 2D spectrum. This is achieved by creating heteronuclear multiple quantum coherence for ^{1}H's directly coupled to a ^{13}C nucleus. This unwanted coherence is removed from the 2D spectrum by phase cycling the first ^{13}C 90° pulse with respect to the receiver. After the interval $\mathbf{d}_2$ (which is about 60msec), the second ^{13}C 90° pulse creates the desired heteronuclear multiple quantum coherence for ^{1}H's J-coupled to a ^{13}C nucleus, which is two or three bonds away. This step is followed by the evolution time t_1. The ^{1}H 180° pulse placed halfway through t_1 removes the effect of ^{1}H chemical shift from the t_1 modulation frequency.

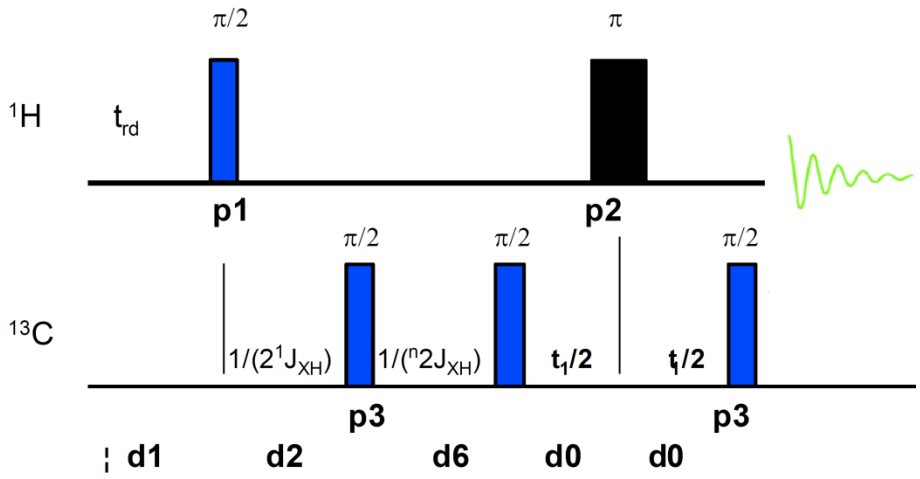

Figure 21. ^{1}H-^{13}C HMBC pulse sequence schematic representation.

The final ^{13}C 90° pulse occurs directly after the evolution period, and is followed immediately by the detection period t_2. After the final ^{13}C 90° pulse, the ^{1}H signals originating from ^{1}H -^{13}C multiple quantum coherence are modulated by ^{13}C chemical shifts and homonuclear ^{1}H J-couplings. Phase cycling of the second ^{13}C 90° pulse removes signal from ^{1}H's that do not have a long-range coupling to ^{13}C. The signal detected during t_2 is phase modulated by the homonuclear ^{1}H J-couplings. The 2D spectrum is generated by a Fourier transform with respect to t_1 and t_2.

1.5.1.9 2D Experiments: Heteronuclear Single Quantum Correlation

The HSQC (**H**eteronuclear **S**ingle **Q**uantum **C**orrelation) correlates the proton signals to a directly bonded heteroatom. The technique relies on magnetization transfer from the proton to its directly bonded carbon atom, and back onto the proton (for higher sensitivity) and thus no responses are to be expected for non-protonated carbons. The ^{1}H-^{13}C GRASP-HSQC pulse sequence is shown on the Figure 22, and is very complex for thorough description, which is reported in [58].

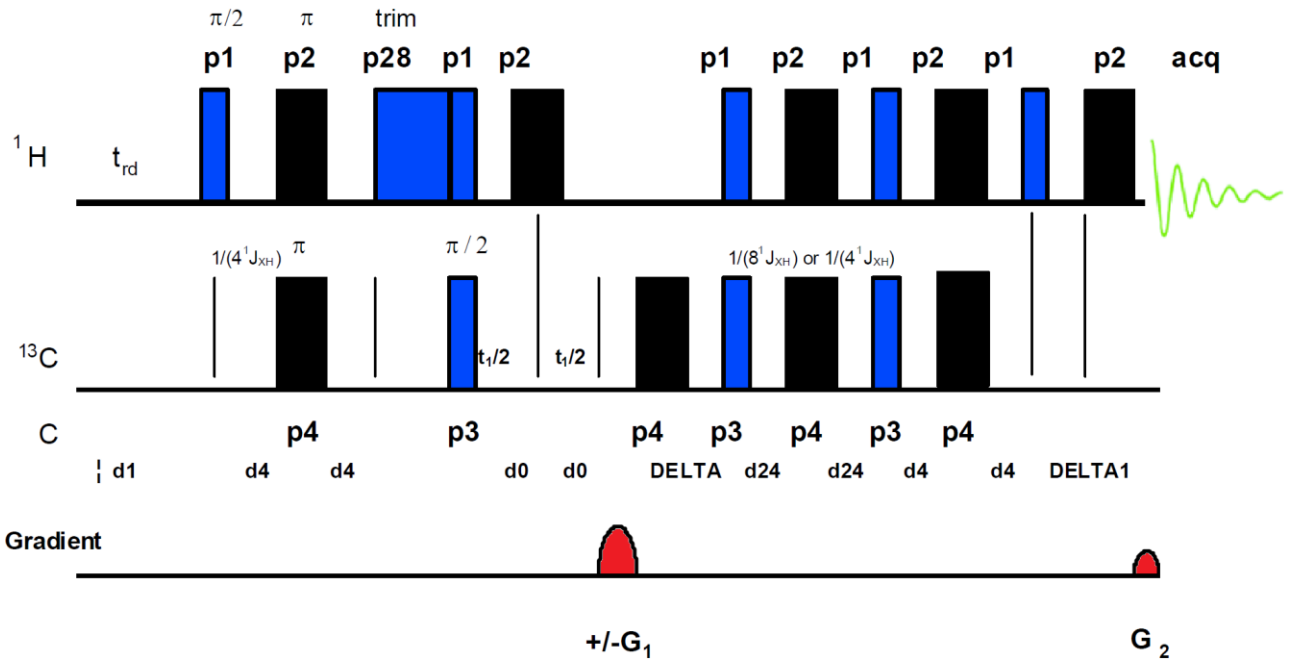

Figure 22. ^{1}H-^{13}C GRASP-HSQC pulse sequence schematic representation.

Nevertheless, the particular feature of represented pulse sequence is the use of gradients in order to improve spectral quality and run spectra in a shorter time. The introduction of pulsed field gradients in high-resolution NMR may greatly improve the problem of suppressing signals from ^{1}H bonded to ^{12}C. While the magnetic field gradient is applied, the resonant frequency (which is proportional to the magnetic field) is different in different parts of the NMR tube. If the magnetic field gradient is applied for a short period of time, the phase (direction) of the magnetization will change differently in different parts

of the tube, such that the overall sum of the magnetization will be zero, making the NMR signal disappear. The application of a gradient in the opposite direction allows the signal to be seen again (Figure 23). In combination with rf pulses that act as quantum filters it is possible to observe correlations between nuclei [59].

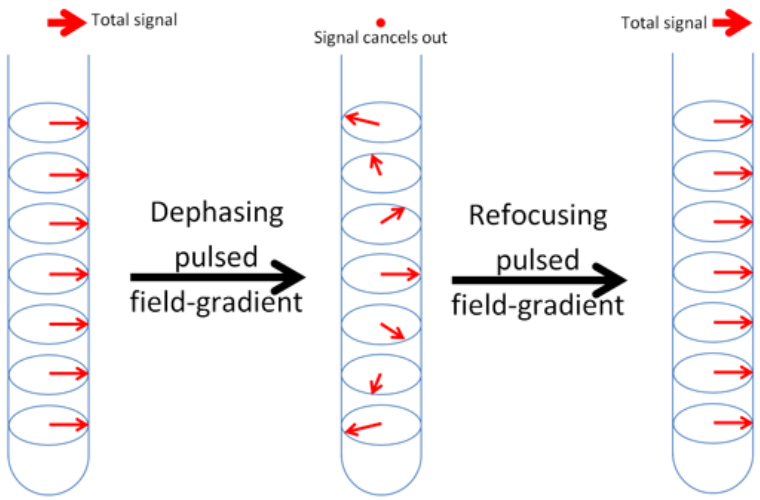

Figure 23. Effect of a magnetic field gradient pulse. The magnetization vector rotates differently at different positions in the tube cancelling out the total signal. A refocusing gradient pulse can make the total signal reappear.

On the Figure 22, G1 gradient dephases all the transverse magnetization. This gradient is located in a spin echo in order to refocus chemical shift evolution during the gradient. Then, a second pulse segment transfers the magnetization to ^{1}H, where it is detected after it has been rephased by a second gradient G2.

HMBC and HSQC sequences are very powerful combination for structural elucidation. Since the properties of the hybrid materials are ruled also by the organic counterpart, it is important to control the organic functions integrity, or highlight their modifications throughout material preparation, unraveling the Organic-Inorganic interfaces development. These sequences were exploited for reaction products identification and control of functionality of Nano Building Blocks, discussed in Chapter 3.

1.5.1.10 ^{1}H DOSY: Diffusion Ordered Spectroscopy

Pulsed Field Gradient (PFG) technique with its effect schematically represented on the Figure 23, can also be used to measure translational diffusion of molecules inside the NMR tube. Refocusing of the signal with PFG can be only achieved for those nuclei that have not moved significantly up or down the tube. However, the molecules in liquid or solution state are in motion and this translational motion is known as Brownian molecular motion or self- diffusion. It depends on a lot of physical parameters like size and shape of the molecule, temperature, and viscosity. Assuming a spherical size of the molecule the diffusion coefficient **D** is described by the Stokes-Einstein equation:

$$\mathbf{D} = kT / 6\pi\eta\mathbf{R_h}$$

where k is the Boltzmann constant, T the temperature, η the viscosity of the liquid and $\mathbf{R_h}$ the (hydrodynamic) radius of the molecule. Diffusion causes some of the nuclei to move away from where their signals can be refocused thereby reducing the intensity of the resulting signal, as shown on the Figure 24.

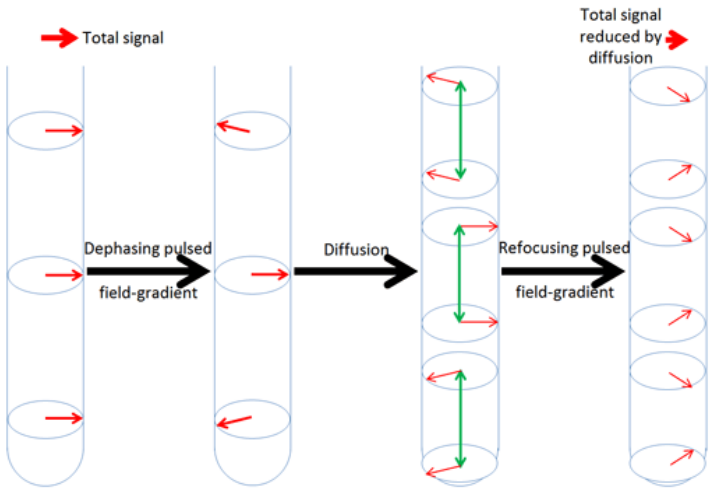

Figure 24. Effect of diffusion combined with magnetic field gradient pulses. The physical movement of nuclei reduces the effectiveness of the refocusing pulse decreasing the resulting signal intensity.

NMR signal intensity is attenuated depending on the diffusion time Δ and the gradient parameters (g, δ). This intensity change is described by:

$$I=I_0 \exp(-\mathbf{D}\gamma^2 g^2 \delta^2(\Delta-\delta/3)),$$

where I is the observed intensity, I_0 the reference intensity (unperturbed signal intensity), **D** the diffusion coefficient, γ the gyromagnetic ratio of the observed nucleus, g the gradient strength, δ the length of the gradient, and Δ the diffusion time.

The easiest pulse sequence to measure diffusion has already been described by Stejskal and Tanner in 1965,who developed the gradient spin echo sequence shown on the Figure 25.

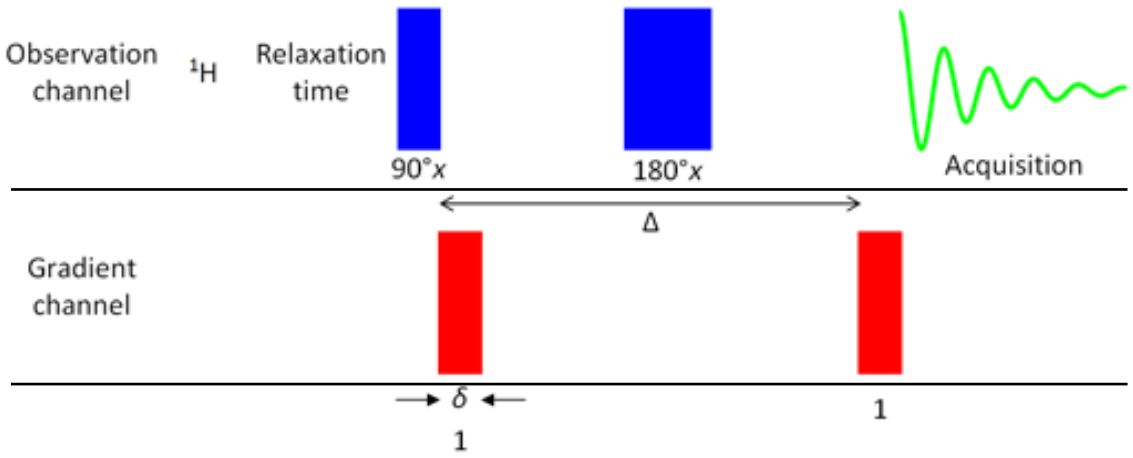

Figure 25. Pulsed Field Gradient Echo (PGSE) sequence : the magnetization is excited with a 90° radiofrequency pulse then dispersed using a magnetic field gradient pulse. After a period of Δ/2 a 180° rf pulse inverts the dispersed magnetization. At this point, a second gradient pulse is applied to refocus the signal.

Nowadays, several pulse sequences have been developed for the diffusion experiments in order to minimize the impact of such factors as non-uniformity of the gradient field, signal distortions, sample movements and thermal convection [44, 60]. Figure 26 represents the pulse sequence for suppression of convection, which is commonly

observed at room temperature for low-viscosity solvents and causes molecules to move in a different way than the diffusion, thus distorting the measurements.

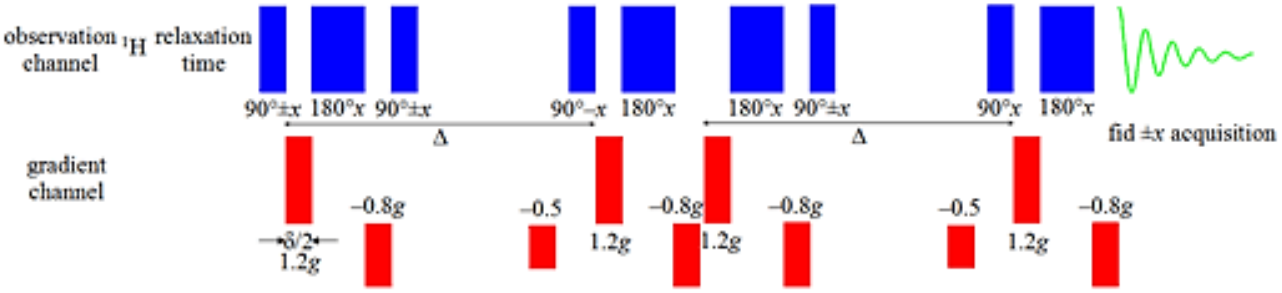

Figure 26. Pulsed Field Gradient Stimulated Double Spin Echo sequence, leading to the suppression of convection.

The DOSY experiment consists of such pulse sequence repeated many times incrementing the gradient strength from the smallest to the biggest available and keeping the delays constant. The Stejskal – Tanner equation, adopted for the sequence from the Figure 25 allows the calculation of the diffusion coefficient of observed nuclei by fitting the experimental curves, plotted for signal intensities as a function of gradient strength:

$$I = I_0 \exp\left[-D\left(\frac{4\delta g \gamma}{\pi} \right)^2 \left(\Delta - \frac{\delta + \tau}{2} - \frac{\delta}{6} - p_\pi \right) \right]$$

where τ is delay after the first gradient pulse and p_π the last 180° pulse duration.

The diffusion coefficient can be used then to separate different component of the subjected mixture, or for the calculations of hydrodynamic radii of detected species. However, analysis of the diffusion dimension involves an inversion of the Laplace transform (ILT). While this is quite accurate at up to 2% for a single decay, it has very low resolution when separating two or more overlapping signals.

To run a diffusion measurement it is necessary to optimize the parameters that determine the decay function, which depend on the length of the gradient pulse δ, diffusion time Δ, viscosity of the subjected solution and its temperature.

This technique was exploited for the characterization of the Nano Building Blocks, discussed in Chapter 3, and elucidated the structural features of these hybrid materials.

1.5.1.11 Solid State NMR

The main difference from liquid measurements is that a series of strong interactions within a solid sample broaden the linewidth to such an effect that a too broad signal appears. The interactions already existing in solution are the Zeeman interaction with the external magnetic field and the spin-spin coupling to other nuclei., but in addition, in solids we must consider:

- direct dipole-dipole interactions with other nuclei, which depend on the magnitude of the nuclear magnetic moments and are most important for spin-½ nuclei with large magnetic moments such as ^{1}H. They are independent of the external field, and dependent on the internuclear distance
- the magnetic shielding by the electrons in dependence on the orientation of the molecule (giving the chemical shift anisotropy)
- and finally, for quadrupolar nuclei there is the field-independent quadrupolar interaction, which is normally the dominant effect in the spectra.

Fast motions of the molecules in the liquid state average all these interactions. Chemical shifts and J values are measured as discrete averages, and the dipolar and

quadrupolar interactions are averaged to zero. Averaging does not occur in the solid state so that spectra are normally more complex, but are also source of information. In order to obtain good quality spectra (reasonable signal-to-noise ratio) a special technique should be applied. The sample spinning at high speed at specific angle to external magnetic field can remove or decrease these interactions to such an extent that high resolution NMR spectroscopy of solid samples becomes possible .

This technique is called the Magic Angle Spinning (MAS), and is dealing with the mathematical expressions for the inter-nuclear interactions, which depends on the factor $(3\cos^2\theta-1)$. This reduces to zero when the θ angle is $54^o44'$. This angle is called the "magic angle", and refers to the axis around which the sample is spun (rotated) relative to the (vertical) axis of the NMR spectrometer. Spinning at few Hz is however not enough in order to remove (at least partially) the chemical shift anisotropy; in order to get the isotropic chemical shift values the sample needs to be spun at rates between 1 and 100 kHz, depending on the nuclei.

1.5.1.12 Solid State NMR: ^{1}H decoupling

As discussed for liquids, the proton decoupling can usually be carried out most readily by simple continuous wave irradiation at the decoupling frequency. Likewise, for solids dipolar decoupling is obtained by high power irradiation at a single frequency, because irradiation at any frequency within a homogeneously broadened line affects the entire line. However, suitable pulse methods are now available to carry out decoupling more effectively and with the use of low rf power reducing the concomitant heating of the sample [60].

1.5.1.13 Solid State NMR: Cross-Polarization

A fundamental RF pulse sequence for solid-state NMR experiments is cross-polarization (CP). It can be used to enhance the signal of nuclei with a low gyromagnetic ratio (e.g.^{13}C,^{29}Si) by magnetization transfer from nuclei with a high gyromagnetic ratio (e.g.^{1}H) if they are present in abundance in material.

To establish the magnetization transfer, the RF pulses applied on the two frequency channels must fulfill the Hartmann–Hahn condition:

$$\omega_X - \omega^1_H = n\omega_r,$$

where n = 0,±1,±2, … and ω_r is the (angular) spinning frequency, ω_X -the X-channel rf field strength, ω^1_H –the ^{1}H channel rf field strength [61].

This condition defines a relationship between the voltage through the RF coil and the rate of sample rotation. Experimental optimization of such conditions is one of the main tasks in performing a Solid State CP MAS NMR experiment.

The main advantage is that in a CP experiment, the recycle time depends on $T_1(^1H)$ relaxation and not on $T_1(X)$, and the former is usually much shorter than the latter. There is also a signal gain associated with CP. The theoretical maximum gain is γ (H) /γ (X), meaning that for low-γ nuclei this enhancement can equate to a substantial improvement in signal-to-noise ratios.

The main disadvantage with CP is that relative signal intensities usually cease to be quantitative. However, that is a price worth paying for the majority of low-abundance nuclei. CP experiment may be desirable for its ability to edit a spectrum in a particular way or to establish relationships between nuclei .

The standard CP pulse sequence is shown in Figure 27. There are four "pulse" elements, each, potentially, with its own B_1 field. First, we apply a ^1H 90° pulse (with field B_1 H (90)). This rotates magnetization from z to -y. Once it is along this axis the pulse is applied on y to keep it there ("spinlock"). With the spinlock in place the pulse is applied on the X-channel (with field B_1 X (contact)). The time for which these two pulses are on together is the contact time. After the contact time the H-irradiation is extended for the time of acquisition.

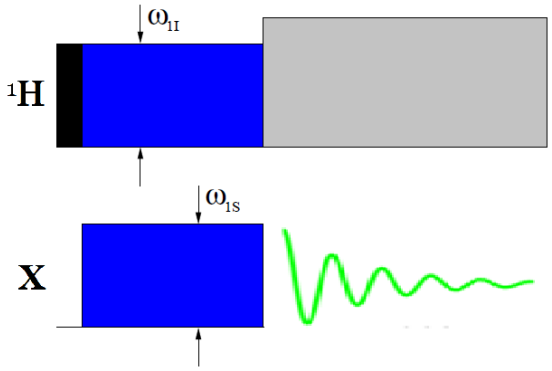

Figure 27. Basic Cross Polarization (CP) pulse sequence.

Duration of the contact time depends on the distance through space between the X nad 1H nuclei, and it can also be varied for some specific experiments (Variable Contact Time VCT) devoted to the analysis of mobility and homogeneity of composite or hybrid materials

Due to its versatility and extraordinarily effective polarization transfer, the CP technique was applied for the characterization of Hybrid Networks (for both ^{13}C,^{29}Si nuclei) in Chapter 2 and for the Nanocomposites characterization in Chapter 4.

Chapter 2 Hybrid Networks

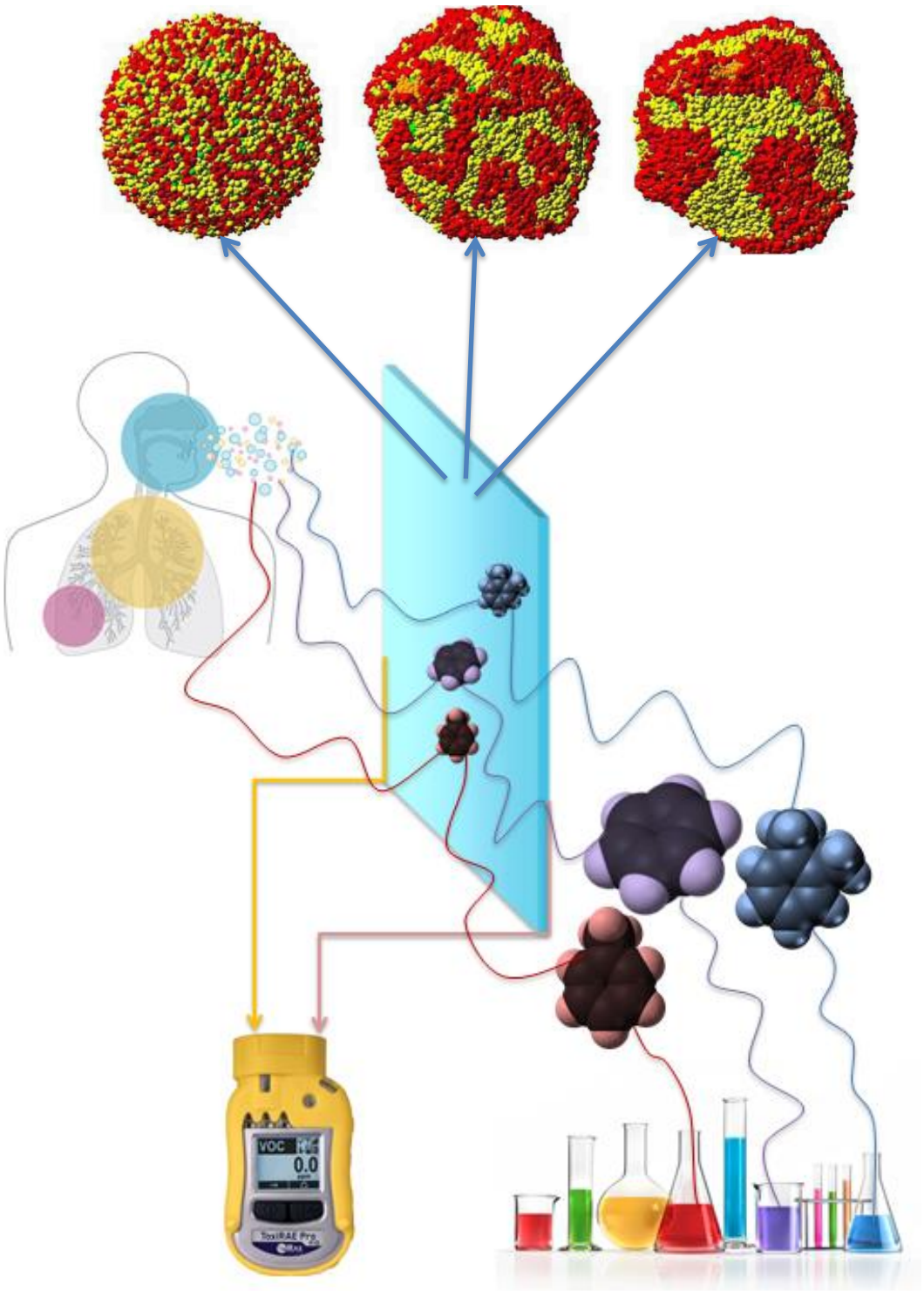

In this thesis two different approaches were used for the formation of hybrid materials: Current Chapter 2 discusses hybrid network structures, which were formed from binary compositions of Si tetraalkoxides and organically modified trialkoxysilanes.

The Chapter 3 is devoted to the synthesis and characterization of well-defined preformed building blocks that can either react with each other to form the final hybrid material, or can be used in formation of nano-composites, however partially keeping their original functional integrity.

Contrary to the building block approach, the traditional Sol-Gel approach exploited for hybrid networks formation transforms discrete precursors molecules to randomly organized multidimensional structures. The distribution of phases and the interfaces between Organic and Inorganic components can be, however, controlled by playing with the chemical composition. It will be demonstrated in this Chapter, that the nano- and micro-structure of the final material are determined by the chemical features of the organic functions linked to the silicon atoms in the precursors and by the load of organically modified precursor in binary system with tetraalkoxysilane. Hence, the properties and the final performance of the derived hybrid networks will depend on their processing and will be evaluated based on the structural information available from the multi-technique approach here implemented. In particular, the synergic use of solid state NMR and XRD for hybrid network characterization allows to study in deep the phase interaction in hybrids, giving information that in their turn will make possible the improvement of materials performance. This result is particularly valuable since it is achieved for amorphous materials for which diffraction analyses usually cannot give a satisfactory structural picture.

2.1 Applications

The combinations of inorganic and organic components in the formation of hybrid materials are almost unlimited, so the materials with novel composition–property relationships can be generated for almost any imaginable application.

This chapter is devoted to the sol-gel preparation of different hybrid Organic – Inorganic coatings made of mixtures of tetraalkoxy-trialkoxysilanes, changing ratio and nature of the trifunctional precursor. The Organic – Inorganic thin layers, prepared from tetraalkoxy-trialkoxysilanes mixtures have been used as reversible adsorbent materials for a set of aromatic compounds and the sorption process, studied by optical spectroscopy, has been related to the structural properties of the adsorbents. The hybrids were characterized by FTIR, solid state NMR, XRD and other techniques.

The historical description and recent advances of most feasible applications for Organic – Inorganic hybrid materials will be short-listed in the following sections to the most relevant to hybrid networks discussed in this work.

2.1.1 Coatings

Coatings represent the main field where most commercial sol-gel products are occupying their niche. The first historical applications of Organic - Inorganic hybrids succeeded in the field of coatings, particularly in scratch or abrasion resistant coatings for transparent polymer substrates [62]. Coatings, based on thermal- or UV- cured Ormosils (organic modified silicates), were deposited on various substrates (ceramics, metals, polymers). Hardness and elastic modulus were measured and confirmed the effectiveness

of the abrasion resistance, however these coatings demonstrated unpleasant optical transparency reduction [63, 64]. Nowadays, novel coatings do not only protect but also provide longevity to coated parts, avoiding their degradation. The sol-gel process provides an excellent synthesis route for such transparent, non-toxic, crack-free, coatings [7], and it shows high potential for the production of multilayer coating systems, which are promising environmentally friendly candidates for replacement of commonly used approaches, such as the chromate-based pretreatments, due to a synergistic effect of good barrier properties and effective "self-healing" action [65].

2.1.1.1 Protective coatings

The first patent related to SiO_2 and TiO_2 protective coatings is dated back to 1939 [66]. Following patent procedure it is possible to synthesize and deposit coatings of various compositions and properties. A wide range of techniques as dipping, spinning, rolling, and electrophoretic deposition can be exploited. The use of a protective film on metals allows the deposition of a "barrier coat" which insulates the metal from the aggressive environment.

Interesting case of particular application is constituted by metal structures used in aerospace industry. The parts are usually made of aluminum and its alloys, and their durability should be ensured for long decades. In this context, hybrid coatings were studied by varying the metal substrate and the precursors in the coating solution [67]. The coated metals' resistance against corrosion was evaluated by the change in the metal gloss in a controlled humidity cabinet. Uncoated aluminized steel demonstrated the color change, indicating oxidation, whereas the coated part maintained the same color, suggesting improved resistance to corrosion. The comparison in performance between inorganic and hybrid coatings through tests of static oxidation, XRD analysis, electrochemical measurements and salt spray corrosion test were conducted by Menning [68]. The result

showed that inorganic thick silica coatings provided the highest protection factor against oxidation at 800°C, but the hybrid coatings reduced O_2 penetration to a greater extent and presented better electrochemical behavior. Galliano and Gallardo performed similar tests on AISI 316L steel and TEOS/MTES hybrid coating produced in acidic medium [69, 70]. Gallardo also demonstrated that the improvement of the O/I hybrid coatings performance in resistance of the metal corrosion depends on the final amount of organic phase present in the coating, showing that high sintering temperature leads to a worsening in the protective properties [71]. The effect of different organic groups (methyl or phenyl) in similarly prepared hybrid coatings deposited on SS 316 steel was demonstrated recently by Subasri [72]. Such coatings derived from a methyl substituted organosilane exhibited superior mechanical and barrier properties when compared to those obtained from phenyl substituted trialkoxysilane. Indeed, the higher rate of hydrolysis and condensation reactions allowed formation of a denser silica network and improved desired properties of coatings derived from methyltriethoxysilane.

The Sol-Gel precursors can be also pre-modified to increase the adhesion towards the substrate. Coatings corrosion resistance performance in acidic environments was demonstrated by Chawada [73]with using an epoxy bis-silane precursor prepared by reaction of liquid epoxy resin and aminopropyl triethoxysilane. The anticorrosion properties of the coatings were studied using electrochemical impedance spectroscopy, DC polarization techniques, neutral salt spray test and showed that very dense and protective hybrid coatings on mild steel can be obtained by controlling the resin/silane ratio during synthesis of the precursor.

Nowadays Organic – Inorganic hybrid anticorrosion coatings are focused on eco-friendly “barrier coats”, which also i) protect local areas of exposed substrate and stop the spread of damage; ii) slow down or inhibit the oxygen and other oxidants mobility toward the metal surface; iii) minimize water and electrolyte penetration and iv) release embedded

inhibitor species that contribute to substrate passivation or block corrosion reactions [65]. Such innovative coatings, deposited on aluminum-based substrates were developed by Zheludkevich [74]. These coatings possessed self-healing properties, thanks to doping with nano-fillers able to release entrapped corrosion inhibitors.

Hybrid materials are also used as additives in composite materials, exploiting the UV curing technique to cure the final coating. This method is efficient, environmental friendly and needs just a suitable UV photoinitiator to crosslink the coating in a very short time [75]. Attaching of organic species to the surfaces of inorganic nanoparticles is generally employed to improve the compatibility and even to render the reactivity of nanoparticles with organic matrix. Methacryloxypropyltrimethoxysilane (MPS) is one of the commonly employed surface modifiers for oxide nanoparticles, since its trimethoxysilyl group can bind to the free –OH groups at the surface of the nanoparticles while its methacrylate group makes the nanoparticles polymerizable in radical polymerization. The MPS-functionalized nanoparticles were used in the fabrication of UV-curable nanocomposites by Bauer [76, 77], who incorporated MPS-functionalized silica or alumina nanoparticles into a radiation curable formulation, comprising with aliphatic urethane hexaacrylate and 1,6-hexandiol diacrylate (HDDA), for preparation of abrasion and scratch resistant nanocomposite coatings. More recently other MPS-functionalised silica nanocomposites were produced by both bottom-up and top-down approaches leading to 80 mm film thickness [78]. Physical and electrochemical performances of the coatings were tested, resulting in stiffness improvement and in better barrier properties for both approaches. The works related to MPS-based hybrid coatings published in 2014-2015 discuss mainly the pathways of hybrids preparation and coatings deposition procedures on different substrates. For instance, the innovative hybrid coating product was applied on a calcareous stone substrate, typical of Apulia Region and as result, evidenced an extraordinary hydrophobicity, able to guarantee a very high preservation of the stone from

water actions [79]. Same UV-curable hybrids were deeply characterized and proposed as coatings for other materials from metal and concrete to wood [80]. Hybrid protective coatings based on different binary and ternary blends of sol–gel precursors were studied in [81]. It was concluded that adding vinyl- or methacrylate- functionalized silica domains caused the formation of a restrained layer in the vicinity of the inorganic phase, and subsequently rate of polymerization and final degree of conversion increased. The combination of classic corrosion protection by hot-dip galvanization (HDGS) of steel and hybrid coatings deposition was tested in alkaline medium by Figueira [82]. These hybrid coatings based on siloxanes, obtained by sol–gel process, were assessed as possible eco-friendly alternatives to replace the use of Cr^{6+} based pre-treatments. Developed coatings mitigated the reactions that occur in the first instants of contact of HDGS with fresh concrete.

2.1.1.2 ART protection and conservation

The sol-gel process has been used in the last years as elective technique to preserve and conserve artistic handwork, from wood to stone consolidation or glass and metal surfaces protection [83]. The first patent in stone preservation is dated by 1926 [84]. A very delicate point in art conservation is that each conservation situation requires a peculiar analysis and a deep knowledge of degradation process and interactions between material and coating [85, 86]. Since 1998, sol-gel derived materials were proposed by Sym [87] as suitable materials for artists, and allowed hybrids successful applications to stone [88, 89], wood [90], and glass [91]. Methyltrialkoxisilanes are probably the most used reagents in conservation as they render stones water repellent and are able to consolidate marbles [92, 93]. The conservation and restoration of metals remains one of

the most complex conservation issues; however, recently, the methyl–modified silica coatings obtained using trimethylchlorosilane (TMCS) and hexamethyldisilozane (HMDS) as tetraethylorthosilicate (TEOS) modifying agents were applied to protect the copper-made parts [94]. The surface of the coated copper substrates was not affected by corrosion at ambient conditions, suggesting the use of such coatings for conservation of copper-made heritage. Aimed to improve coating-copper interaction and adhesion, Jin Han exploited 3-mercaptopropyltrimethoxysilane (MPMS) as network modifier of TEOS and succeeded in preparation of coatings possessing excellent thermal stability below 300 °C, high resistance to scratch and good protection performance for copper [95].

2.1.1.3 Automotive functional coatings

Another interesting application of coatings is for functional purposes. In the field of automotive functional coating, the main products are sun-reflective windows, antireflective glasses and optical filters and blue-reflecting car rear view mirrors. Usually reflective applications exploit a layered system in which the layers are stacked and have alternating refractive index; moreover the layer thickness is in the range of light wavelength. The reflected light is reduced by destructive interference and does not exceed 0,2%. When nanoparticles (NP) were used in the coatings, it was also possible to decrease the reflective loss at 550 nm to 1% [96]. Compared to traditional vapor deposition technologies, the sol-gel process has several advantages especially for the treatment of plastics and glass large area parts [97]. These advantages are mainly due to the ability to coat both sides of the substrate at the same time and the low cost for coating area. An example of O/I hybrid material that leads to low refractive index layer was studied by Takahashi and co-workers in 1997 and has found an application in the automotive field as antireflective coating for windows [98].

Interesting application of sol-gel in the automotive field is the HUD (head up device) system, originally developed for aircraft use, and commercialized in 1988 by Nissan Motor after a joint study with Central Glass. A HUD is a transparent display presenting data without requiring the user to look away from the usual point of view. It consists of an ultra-bright vacuum fluorescent tube used as display light source, optical lenses for focusing the images, a reflective mirror, a transparent curved aperture cover, and a combiner. The coating is prepared from a mixed silicon e titanium alkoxides solution and deposited by dip coating. This technique permits to fulfill all the standard requirements demanded by ANSI and the Japan Industrial Standards.

Another application is the design of water repellent automotive glasses for securing sight of the drivers. Various coatings have been prepared starting from solutions containing polyfluorinated alkylsilanes [99]. The superhydrophobic properties that allow the water sliding are very attractive. Furukawa studied the relationship between sliding angle and contact angle hysteresis of a series of fluorinated polysiloxanes with perfluorooctyl groups and trichlorosylilethyl groups, plus three different fluorinated silane coupling agents. The sliding angle decreases as the mobility of the polymer surface increases and the easiness of alkyl chain reorientation in polysiloxanes is an important factor that affects slipperiness of water droplets. The produced coating exhibited a high durability [100]. The advanced coatings possessing superhydrophobicity were recently (2014-2015) designed on the idea of imitation of botanic or animal wax/fat [101]. By casting the Sol-Gel derived reactive solution under ambient condition, a hierarchically structured surface was obtained. The crystallization of the surface building blocks resulted in the formation of the rough microstructure, while its low surface tension granted the resultant surface with superhydrophobicity.

Alternatively to the largely employed solution deposition methods, the deposition from vapor phase can create better-functionalized films, and could be identified as a

possible replacement to the classical reaction in highly anhydrous and apolar conditions [102]. Soliveri confronted the two techniques, suggesting the use of vapor deposition to obtain a good quality of the hydrophobic layer without the use of environmentally unfriendly solvents. This most recent hybrid coatings preparation is based on a combination of TEOS–Glymo matrix with functionalized silica filler particles and a hydrophobic additive. The coatings with 15 wt.% loading of 10–20 nm silica fillers were found to have good mechanical properties and resistance to weathering and were able to maintain the required hydrophobicity even after the removal of the top surface by accelerated abrasion, showing up to 96% self-cleaning efficiency [103]. The developed coating method appears to be simple, low cost, and can be easily scaled-up for large outdoor structures that require mechanically robust and durable self-cleaning functions.

2.1.2 Catalysts

Heterogeneous catalysis provide the opportunity for recovering and recycling catalysts from the reaction medium with the possibility to improve processing steps, and to achieve better process economics and environmentally friendly industrial manufacturing. The sol-gel technology has the ability to increase the catalytic activity of dopant molecules thanks to the superior thermal stability, inertness, porosity and high surface area of the supports towards the entrapped molecules [3, 7]. Depending on the application, sol-gel materials can be microporous (pore diameter < 20 Å), mesoporous (pore diameter in the range 20 Å – 50 Å) or macroporous (pores larger than 50 Å), and offer several advantages over the classical immobilization procedure employed in the preparation of heterogeneous catalysts [104]. If the reagents in solution have smaller size respect to the average pore diameter, these materials afford superior catalytic performances respect to similar heterogeneous catalysts prepared by impregnation methods. The grafting procedure on amorphous silica is one efficient method for obtaining efficient catalysts. For example, aminopropyl- functionalized silicas have been the most widely studied organic- inorganic hybrid solids. Angeletti and co-workers showed that these hybrid organic/inorganic solids could be effective base catalysts for the Knoevenagel condensation reaction at room temperature in continuous flow reactors [105]. Macquarrie and co-workers examined guanidines tethered to silica as base catalysts for epoxidation reactions [106]. Harmer et al. [107] reported the use of perfluorosulfonic acid-silane in the co-condensation of silica, using traditional sol-gel techniques. In this case the activities of both grafted and co-condensed silica hybrids were reported as similar. The grafted acid catalyst was tested in several acid-catalyzed reactions, such as aromatic alkylation, alkenes isomerization, and Friedel-Crafts acylation and the respective conversions were 99, 95 and 89%. Recently, Suzuki proposed new type of sulfonic acid-functionalized monodispersed mesoporous silica spheres [108]. The catalytic activity of such spheres in condensation reactions

between 2-methylfuran and acetone appeared highly dependent on the particles' diameters, but always was much higher than that of other forms of mesoporous silica due to particles' radially-aligned mesopores. Same group reported on catalytic activity of amino-functionalized monodispersed mesoporous silica spheres with ordered hexagonal regularity [109]. Variations in synthesis procedures allowed decreasing the particles size, meanwhile keeping the desired porosity for catalytic activity.

Other catalysts are obtained from the family of mesoporous materials (M41S, SBA-15, MCM-41). These materials have relatively uniform pore sizes and void volumes [110]. The pore sizes can be tailored on the basis of the synthesis method and can range from about 15 to 100 Å. Rather than amorphous solids, ordered mesoporous materials can serve as well defined supports, and can be modified by grafting organic groups, in order to obtain a catalyst. Sartori and co-workers used aminopropyl-functionalized MCM-41 as a catalyst for the nitroaldol condensation of aldehydes and nitroalkanes [111].

2.1.3 Biomedical applications

Bioactive hybrids find many applications in the field of biotechnology. Enzymes are the biological catalysts responsible for the chemical reactions in living organisms. Their high specificity and huge catalytic power are due to the fact that the geometry of the active site can fit exactly that of the substrate. Many biocatalysts such as enzymes or catalytic antibodies are available for performing a variety of synthetically important transformations or for bio-sensing applications [14]. The highly active enzymes, antibodies or microorganisms, which perform such specific reactions, could be immobilized on or embedded in solid substrates in order to be reusable and protected from denaturation. Historically, polymers are used for bio-immobilization via covalent binding or entrapment,

however materials with inorganic network such as Sol–Gel processed hybrids offer significant advantages over organic polymer hosts. They exhibit better mechanical strength together with improved chemical and thermal stability, and do not swell in most solvents preventing the leaching of entrapped bio-molecules [18].

Mesoporous silicas possess pore systems, which are large enough to accommodate small biological entities as proteins or enzymes. The immobilization can involve both physisorption and chemical bonding, although with the latter there is the risk of denaturation of the biological entity and the loss of the activity [7, 14, 18]. Various enzymes (trypsin, lysozyme, lipase,) were immobilized in either MCM-41/48 or SBA-15 phases with good results in [112-115].

Immobilization of cells is also an important challenge for biotechnology. Cells' metabolic activity can be used in a large variety of processes for food industry, waste treatment, production of chemicals or drugs and even cell transplantation [19]. In particular the biocompatibility of silica gels and their high porosity favoring water retention and nutrient diffusion make them interesting hosts for the bio culture [116].

Drug delivery and a "curing magic bullet" design are emerging topics in biology, since compared with conventional dosage forms, controlled drug release systems (DRS) offer numerous advantages, such as reduced toxicity, enhanced drug efficiency and improved patient compliance [7]. To be effective drug carriers need therefore low toxicity, biodegradability, encapsulation and release ability and finally specific surface functionalities. As discussed, biocompatible polymers can be employed as carriers, however in these matrices the major problem is the drug distribution homogeneity into the polymer, which can affect the drug release rates and consequently reproducibility. Silica nanoparticles (NP) have been proven to be non-toxic and to have an easily functionalizable surface that improves the drug delivery capability and efficiency [117]. The surface of silica

NP is generally modified with specific functional groups typical of bio-macromolecules by chemical binding or physical adsorption [118, 119]. Many researchers focused on bio-application of mesoporous materials, studying the different surface properties, pore textures and other properties as very well reviewed in [120]. In this frame, the functionalized ordered mesoporous materials containing various types of organic groups via organosilane co-condensation and post-grafting onto mesoporous silica were synthesized by Asefa [121]. Comparative studies of their adsorption and release properties for various model drug molecules showed that the release of the adsorbed molecules is dependent on the synthetic strategy, the type of functional groups in the materials and selective for the drug type.

Another interesting field of hybrids applications is dealing with in vivo imaging via fluorescent functionalized nanoparticles. This alternative optical imaging technique by using persistent luminescent nanoparticles is increasingly used for in vivo investigations. The nanoparticles can be excited before injection, and their in vivo distribution can be followed in real-time without the need for any external illumination source. The most intriguing is that the chemical modification of the nanoparticles surface led to lung or liver targeting or to long-lasting blood circulation, thus making the functionalization of both the interior and exterior of particles very important. Silica particles can be used as core particles because they are easy to prepare and separate, their surfaces may be modified or labeled, they are highly hydrophilic, and most importantly are biocompatible. Nakamura demonstrated the size-controlled, fluorescent-tuned thiol-organosilica particles, which were detected as distinct peaks by flow cytometry, and observed with cells clearly on microscopy [122]. Consequently, the same group demonstrated that ring-shaped hybrid silicon-based nanoparticles with a high tetrakis(4-carboxyphenyl)porphyrin (TCPP) content, with the PEG-modification of such nano-rings provided clear imaging and sensitive detection of tumor by NIR fluorescence imaging [123]. The groups' further work

concentrated on fluorescent thiol-organosilica nanoparticles with 100 nm diameter, which were exploited for time-lapse fluorescence imaging with quantitative analysis of endosomal uptake and movements in single cells. Such fluorescent hybrid particles showed high potential as new markers for time-lapse fluorescence imaging and quantitative single cell functional analysis for nano-medicine development [124].

Metal nanoparticles are being extensively used in various biomedical applications due to their small size to volume ratio and good thermal stability. Gold nanoparticles are an obvious choice due to their amenability of synthesis and functionalization, less toxicity and ease of detection. Functionalization facilitates targeted delivery of these nanoparticles to various cell types, bioimaging, gene delivery and other therapeutic and diagnostic applications. Silicon-based hybrid materials with desired organic functions can be successfully used for the metal nanoparticles functionalization or encapsulation in a core-shell type structures [125, 126]. Recent review about multifunctional nanotheragnostics discussed the imaging techniques development for disease diagnosis, targeted gene delivery, and monitored gene expression (or silencing). Many concepts for functionalization of metal nanoparticles and design of integrated imaging probes carrying both gold nanoparticles and nucleic acids are presented in [127]. However, unfortunately despite the significant advances in nonviral vectors and nanotheragnostics, their potential toxicity and systemic clearance have not been fully elucidated. This fact slows down the research activity towards such systems, even if this field is very attractive.

2.1.4 Membranes and Sensors

Since asymmetric cellulose membranes were developed in the 1960s for water desalting, various breakthroughs in membrane applications have been achieved with the use of synthetic polymers and advanced ceramics. At the present time the design of new materials for membrane application is constantly in progress and has to match severe selectivity criteria. Industrial membrane processes under development as gas separation, nano-filtration or sensing deal with small gas, vapor or liquid concentrations [3, 4, 7]. Examples of satisfactory separation that are possible only thanks to the membranes produced in recent years are nitrogen/oxygen gas separation, or the selective extraction of biological molecules of interest from their natural environment media, as the discussed separation of one specific amino acid from a mixture of several amino acids [128, 129].

Firstly – employed inorganic membranes were based, mainly, on silica-derived materials. Silica membranes are still widely used and usually they are synthesized by the acid catalyzed hydrolysis and condensation of tetraalkoxysilanes. The structure of the networks resulting from the sol-gel process depends on the nature of catalyst used in the reaction (acid or basic), temperature and sol concentration [130].

Mesoporous Organic - Inorganic hybrid materials offer all the attributes for efficient electrochemical reactions and their employment in the field of sensors. They exhibit a network of nanoscopic oxides that can serve as an uninterrupted three-dimensional pathway for ions and electrons conduction, and an interpenetrated through-connected mesoporous network, which serves as “host material” for electro-active species. In this way, fast ionic or electronic carriers transport in the internal surface area of the mesoporous network may occur. Furthermore, the organic entities, present at the surface of these mesoporous hybrid structures, exhibit a pseudo-diffusive electron hopping between the redox species and the inorganic network [14]. The transport of molecules in

these mesoporous hybrid architectures can, however, be tuned and depends on the nature of the functional groups attached to the pore surface (the length of organic chains, the functionality size or polarity) and on the geometrical constraints including the pore size, the pore orientation and their interconnection [131, 132].

2.1.4.1 Liquid Phase Sensors

Starting from various trifunctional precursors (methyl-, vinyl-, propyl-, isobutyl- and phenyltrimethoxysilane) co-polymerized with tetramethoxysilane, different matrices were prepared by Avnir [133]. From solvatochromic studies it was found that the polarities of the hybrids depend on the precursor, the precursor proportion and the solvent at the interface. The ratio between trimethoxy substituted silane (R-TMS) and TMOS has a great influence on polarity, which decreases with increasing the R-TMS : TMOS ratio. These results allowed to prepare sensing materials for polar and apolar solvents by changing TMOS/ R-TMS ratio.

Recently, Ou discussed the development of hybrid monolithic capillary columns, which are becoming an attractive and popular alternative to pure silica-based monoliths in application for CEC and capillary liquid chromatography separation, as well as for sample pretreatment of solid-phase microextraction and immobilized enzyme reactors [134]. “One-pot” process can be applied for preparation of hybrid monolithic stationary phases, in which various organo-functional siloxane monomers can be directly used in the preparation of hybrid monoliths with desired functionalities allowing miniaturization of separation devices and microfluidic chips.

The group of Sanchez developed the synthesis technique for mesoporous silica thin films functionalized with silylated β-diketone compounds and applied them as fast uranyl species sensors with high selectivity and sensitivity [135]. These hybrid optical sensors

showed very good preparation reproducibility with as-made triethoxydibenzoylmethane (SDBM) probe located inside the pores.

The highly sensitive hybrid organic–inorganic sensor for continuous monitoring of hemoglobin was demonstrated by Naaman [136]. The surface of GaAs-based Molecular Controlled Semiconductor Resistor (MOCSER) was modified by the 3-mercaptopropyl trimethoxysilane (McPTMS) molecules by binding to the substrate through thiol ends and exposing silane groups, which were co-condensed then with a 3-aminopropyl trimethoxysilane (APTMS) for the further binding of required sensing biological molecules. The selectivity and sensitivity of demonstrated sensor made the technique relevant for sensing in vivo for medical applications, demanding little costs for the sensor preparation.

2.1.4.2 pH Sensors

First big improvement in this field was made when hybrid materials were used instead of inorganic silica, as in the case of networks prepared from phenyltrimethoxysilane (Ph-$SiOMe_3$), and other trialkoxysilanes. The resulting hybrid displays distinctly improved properties in terms of long-term stability, and gas permeability [7]. Carbon dioxide and other acid gases are usually tested via acid-base reactions occurring inside sensor membrane. For weak acids, as CO_2, a bicarbonate buffer (pH 8-9) is contained in a gas-permeable polymer. The following acid-base reaction occurs in the buffer:

$$CO_2 + H_2O + HCO_3 \leftrightarrows 2HCO^-_3 + H^+$$

The change in pH is detected by a pH indicator dye contained in the sensor layer. The reaction is fully reversible. Generally the pH indicator is suspended in an aqueous buffer solution in form of small droplets, into a hydrophobic polymer. This device presents several drawbacks, like the difficulty in controlling the osmolarity and ionic strength of the water-buffer system and the droplets size, which are not stable. To overcome these problems, a new approach was used based on a common dye, pyranine, which is immobilized in a hydrophobic sol-gel derived glass. The glass matrix offers a highly stable microporous environment that can easily be deposited on a suitable substrate by the dip-coating technique [137]. This material offers high sensitivity and rapid response of the polymer films. With the same dye, Von Bülzingslöwen et al. [138] developed a CO_2-sensor for modified atmosphere packaging applications. The internal buffer system was a solution of cetyltrimethylammonium hydroxide. The obtained system (Ruthenium complex/pyranine) is compatible with lifetime based fluorimetric sensors and with established optical oxygen sensor technology. The sensor is stable for over seven months.

Very recently, Hu et al. [139] reported on the novel pH sensing devices based on Si nanowire field effect transistors (Si NWFETs) modified by 3-aminopropyltriethoxysilane (APTES). The highly repeatable pH sensing results reflected the stability of superficial APTES monolayers in such systems. Both the Molecular Layer Deposition (MLD) and solution methods were applied in production for comparison and showed an improved pH response of the sensor prepared by MLD compared to the one prepared by the solution treatment, which indicated higher surface coverage of APTES in the case of MLD use.

2.1.4.3 Volatile Organic Compounds Sensors

The detection of volatile organic compounds (VOCs) represents an important objective in the field of air quality monitoring. VOCs are air pollutants, not only released by chemical, petrochemical and related industries, but also involved as key reactants in

photochemical reactions occurring in the atmosphere, and which lead to serious environmental hazards [140]. Monocyclic aromatic hydrocarbons such as benzene, toluene, xylenes and other aryl compounds are responsible for relevant health risk, particularly in the case of exposure to benzene, which is carcinogenic [141]. Moreover, the removal by an adsorption process of these organic compounds from gas streams is a practice that has been receiving increasing attention during the last years [142, 143]. Mesoporous and microporous inorganic materials are widely investigated as adsorbents potentially useful for VOCs removal, but they do not represent the only solution for performing this task. As a matter of fact, the organic modification of sol-gel-derived silica networks allows tuning the microstructure and the polarity of the hybrid O/I materials, thus adjusting the network features in order to trap the desired molecules. In fact, depending on the nature of substituents, benzene and its derivatives differ in steric hindrance and electron density over the ring, leading to preferential interactions with the solid adsorbent. The ability of decreasing the network polarity both on external surface and pore walls, on one side, decreases the water sorption phenomenon and on the other, by fine tuning, allows to discriminate between similar compounds. The preparation of hybrid O/I adsorption layers, due to the low mass of adsorbent, offers the possibility of operating at low temperature both for adsorption and desorption steps [144].

Up to now, different types of optical chemical sensors for organic vapors have been investigated, which employed different experimental set-ups based on bulk optics, integrated optics or fiber optics [145]. The detection of aromatic compounds with sol-gel based sensitive layers was studied by collecting the UV spectra of immobilized hydrocarbons [146-149], but the process appeared irreversible for the examined compounds.

2.2 Synthesis and Characterization of Hybrid O/I coatings for VOC sorption

My work has been devoted to the synthesis of hybrid coatings to be employed as adsorbent materials towards volatile aromatic compounds, with the aim of relating the observed properties to the chemical and structural features of the hybrid organic/inorganic networks.

The hybrid xerogels and coatings were prepared by co-condensation of tetraalkoxysilane and different organofunctional Si-alkoxides under acidic conditions, varying the compositional ratios. The final xerogels and coatings were characterized by multi-technique approach. The coatings sorption ability was evaluated and related to the structural features and the nature of the organic groups linked to the network.

2.3 Experimental

2.3.1 Precursors

Tetraethoxysilane (TEOS) was purchased from ABCR and used without further purification (Figure 28). The choice of TEOS as the main phase is related to the fact that this precursor was historically studied in detail and its properties and reactivity are well known. Furthermore, it is less toxic and it is available with a higher purity grade than TMOS and has a reasonably controllable rate of reaction. The main reason for employing Tetraethoxysilane stays in the ability of tetrafunctional alkoxysilanes of behaving as network formers, as highlighted in chapter 1, thus allowing to increase the crosslinking degree of hybrid networks obtained from trifunctional organosilanes. This is beneficial both for the functional properties, since playing with composition leads to modulation of

structure-related properties, and for increasing the robustness and chemical resistance of the prepared materials.

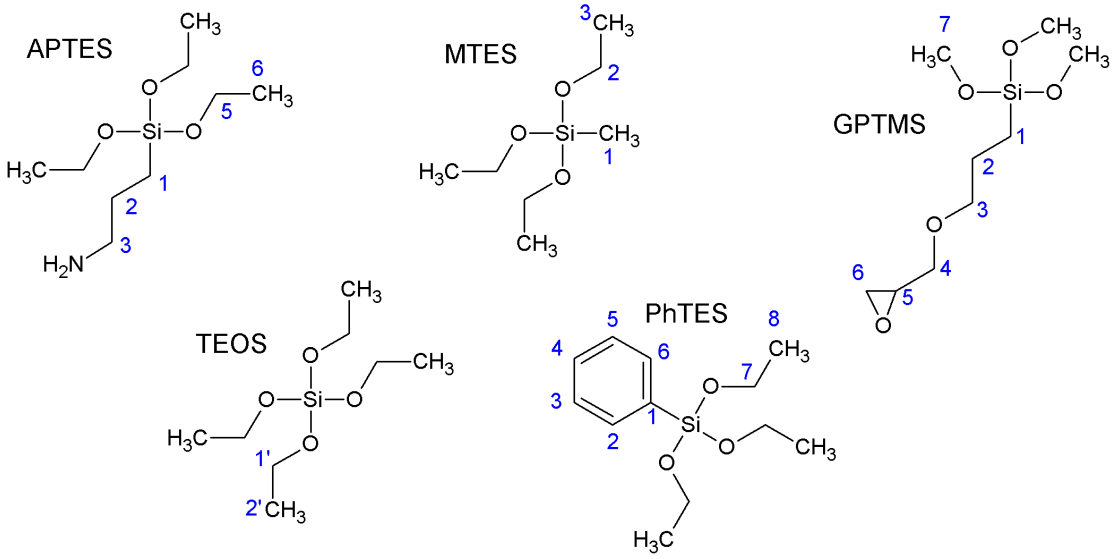

Figure 28. Structure and NMR carbon labeling of TEOS, APTES, MTES, PhTES ,GPTMS.

Methyltriethoxysilane (MTES), 3-aminopropyltriethoxysilane (APTES), 3-glycidoxypropyl trimethoxysilane (GPTMS) and phenyltriethoxysilane (PhTES) are commercially available trifunctional Si-alkoxides bearing organic reactive functions (Figure 28), which allow to organically modify the obtained networks. These reagents were purchased from ABCR and used without further purification. The condensation between TEOS and a trifunctional precursor leads to products with the presence of reactive methyl, 3-aminopropyl, 3-glycidoxypropyl and phenyl groups respectively. The choice of the different trialkoxysilanes was done on the basis of the chemical and structural features of the organic groups linked to silicon, in order to vary steric hindrance, electron donor or acceptor behavior, and consequent influence on the sol-gel reactions in terms of condensation ability of molecular precursors.

2.3.2 Synthesis Procedure

All the Sol-Gel reactions were conducted under a nitrogen atmosphere at room temperature conditions. Hybrid Organic - Inorganic Gels were prepared from binary solutions of TEOS and a selected trifunctional alkoxide in 9/1 and 7/3 M ratio respectively. The amounts of Ethanol (purchased from Sigma-Aldrich and used as-received) and distilled water were adjusted in order to maintain the following molar ratios: **ethanol/silicon = 1/4**, **water/alkoxide groups = 1/1**. Sol compositions and sample labels are reported in Figure 29.

Sample label	Precursors	Molar ratio
TM 7/3	TEOS/MTES	7/3
TM 9/1	TEOS/MTES	9/1
TA 7/3	TEOS/APTES	7/3
TA 9/1	TEOS/APTES	9/1
TP 7/3	TEOS/PhTES	7/3
TP 9/1	TEOS/PhTES	9/1
TG 7/3	TEOS/GPTMS	7/3
TG 9/1	TEOS/GPTMS	9/1

Figure 29. Compositions and sample labels of hybrid sols. Abbreviations stand for Tetraethoxysilane (TEOS), Methyltriethoxysilane (MTES), 3-aminopropyltriethoxysilane (APTES), Phenyltriethoxysilane (PhTES) , 3-glycidoxypropyl trimethoxysilane (GPTMS).

All samples were prepared with a pre-hydrolysis step of TEOS with distilled water ("A" Figure 30), except for the samples derived from TEOS/ APTES, which were prepared

under acidic conditions (HCl 0.1 M) in order to avoid a fast gelation of the solution. After 1 h of pre-hydrolysis, the trifunctional alkoxide was added to the solution ("B", Figure 30).

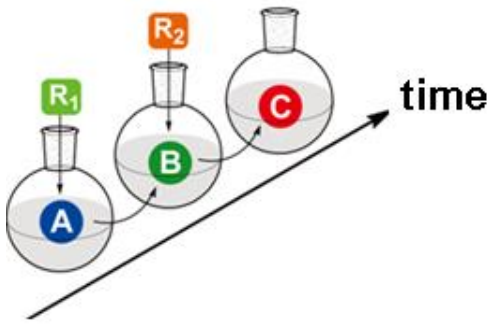

Figure 30. Schematic representation of Hybrid Sol production. "A" – TEOS (R_1) prehydrolysis, "B" – addition of trifunctional alkoxide (R_2), "C" – Hybrid Sol.

Within 30 minutes after the trifunctional alkoxide addition, the Sol ("C",Figure 30) was used for the monolayer films preparation on soda-lime glass sheets (2 x 4 cm) by the dip-coating technique (Figure 24). The substrates, previously cleaned with distilled water and acetone, and dried at 80 °C, were dipped into the sols at 6 cm min^{-1} drawing rate. The dipping process was controlled in order to obtain the same-coated area for all the samples (4 cm^2 for each side of the substrate). The coated sheets were stored in a desiccator at ambient temperature before their use as sorbent layers. The residual sols were allowed to gel and resulted in xerogels after drying for 24 hours at 80°C .

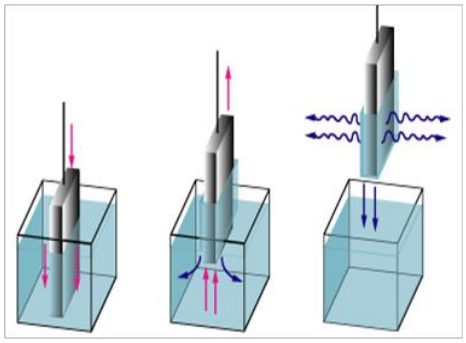

Figure 24. Schematic representation of the dip-coating process.

2.3.3 Characterization Techniques

2.3.3.1 Fourier Transformed Infrared Spectroscopy (FT-IR)

FT-IR was used to control the reaction precursors and products. FT-IR spectra of the xerogels were recorded with a Thermo Optics Avatar 550 instrument in transmission mode, using KBr as carrying medium, in the 4000–400 cm^{-1} range (256 scans, 4 cm^{-1} resolution). For liquid samples, the KRS-5 windows were used with the same acquisition set-up.

2.3.3.2 X-Ray Diffraction (XRD)

X-ray diffractograms were collected on films with a Rigaku D-Max III diffractometer in glancing-incidence configuration, using CuK α radiation and a graphite monochromator in the diffracted beam. Asymmetric scan geometry was adopted in order to enhance the film microstructure; typical measurements were performed in 1 – 40° (2θ) range with an incidence angle of 1°; a sampling interval value of 0.1° and a counting time of 60 s were also adopted. The XRD diffractograms of xerogels were collected in θ - 2θ configuration in the 1.2 - 30 ° (2θ) range with 0.1° sampling interval and 20 s counting time.

2.3.3.3 Nuclear Magnetic Resonance (NMR)

Multinuclear solid state NMR analyses were carried out on a Bruker 300 WB instrument operating at 300 MHz proton frequency. The powdered xerogel samples were packed in 4 mm zirconia rotors and spun at 6.5 kHz. NMR spectra were acquired with cross-polarization (CP) and single pulse (SP) MAS experiments according to the following conditions.

^{1}H spectra were run at 300.13 MHz, with $\pi/2$ pulse width of 4.5 ms and 5 s recycle delay. Q_8M_8 and EtOH were used as external secondary references.

^{13}C CP MAS spectra were recorded at frequency 100.07 MHz with $\pi/2$ pulse width of 3.5 ms, and 5 s recycle delay; 2 ms contact time was used for CP.

^{29}Si SP MAS spectra were obtained at 59.62 MHz, and $\pi/2$ pulse (5 ms) and recycle delay (300 s) were chosen to account the long T_1 relaxation times.

^{29}Si CP MAS exploited 5 s contact time and 10 s recycle delay. The spectra were analyzed using the TOPSPIN 1.3 program provided by Bruker. Best fits were obtained at 95% of confidence level.

2.3.3.4 N_2 - physisorption

N_2-physisorption measurements on films were performed with a Micromeritics ASAP 2010 instrument. The samples were degassed below 1.3 Pa prior to the analysis. In order to reach a good accuracy of the sorption measurements, the adsorption isotherms were recorded with a fixed equilibration time of 300 s for each measured point. The N_2 sorption measurements were performed two times on each film composition. Moreover, a further analysis was performed using Ar with the aim of comparison. The Specific Surface Area (SSA) of the samples was evaluated from the N_2 sorption isotherms with the BET equation within the relative pressure range: $0.05 \leq P/P_0 \leq 0.33$. Typical measurements were carried out on a large number of films, at least 10, deposited on thin cover glass sheets, which were broken and put into the sample-holder; the results were compared with those obtained on the clean substrates and the final values were expressed as surface area/mass of the films.

2.3.3.5 Complementary techniques

The density of the xerogels was measured by He picnometry with a Micromeritics 1035 instrument. The film thickness was evaluated with a Hommelwerke T8000 stylus prophylograph; at least three scans were collected for each sample, both up- and downwards the onset of the film. Scanning Electron Microscopy (SEM) was run on films using a JEOL JSM-5500 instrument, operating at 10 kV.

2.3.4 Optical Characterization of the Films Sorption Ability

The capability of hybrid films to adsorb VOCs molecules was analyzed by optical methods. Reagent grade benzene, toluene, chlorobenzene and o-xylene were purchased by Sigma Aldrich and were used as-received. The samples were put into a 1 dm^3 chamber through which a constant flux of VOC vapors was carried with pure nitrogen from a glass flask and the optical absorbance of the analyte fluxing in the chamber was monitored as a function of the time (Figure 31). The measure chamber was a stainless steel cell with four silica windows (Figure 32), placed inside a Jasco 570-V UV-Vis-NIR spectrophotometer and connected to two mass flow controllers, suited to assure an accurate real-time control of the vapor concentrations into the chamber during the spectra collections.

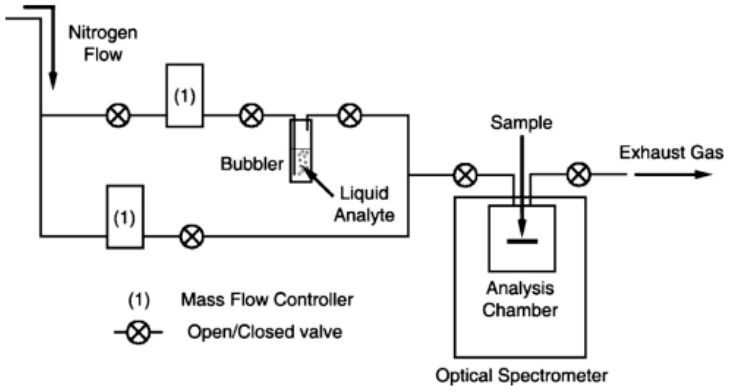

Figure 31. Schematic representation of experimental apparatus used for the UV tests of sorption capability of hybrid thin films.

Two different mass flow controllers were employed in this apparatus. The former (AERA FC-7800CD) allowed controlling the flow rate of carrier gas bubbling through a glass balloon flask containing 100 ml of analyte between 1 and 1000 standard cubic centimeters per minute (sccm). The latter (AERA FC-7700CD) controlled the flow rate of pure nitrogen from 1 to 5000 sccm and it was used to suitably dilute the vapor stream coming from the other gas line. The sccm units are given in standard conditions for all the examined VOCs.

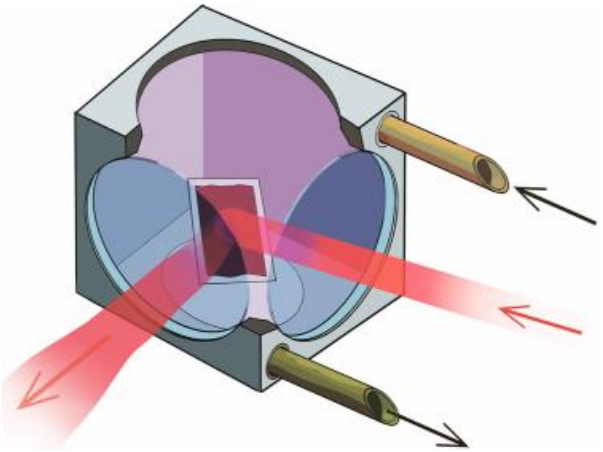

Figure 32. Measure chamber in stainless steel cell with four silica windows.

2.4 Results and Discussion

2.4.1 FTIR Characterization of the Precursors

Infrared spectroscopy has been one of the most extensively applied analytical tools to investigate the different stages of the reactions in the various steps of the sol–gel process. Analysis of the IR-spectra can give important indications on the materials structural evolution and on the influence of processing parameters. One of the main advantages of this technique is the fast acquisition time and sample preparation, which makes it very convenient in rapid samples characterization. Control of the organic functions availability in the final hybrid materials is quickly achievable with FTIR by pointing out the specific vibrational "fingerprints".

For the sake of clarity and convenience, the spectra of silicon precursors and ethanol are presented below (Figures 33- 38) with the assignments of the main peaks with the acronyms used:

st: strong

m: medium

w: weak

br: broad

ν: stretching vibration

δ: deformation vibration

ρ: rocking vibration

ω: wagging vibration

ip: in plane

oop: out of plane

as: antisymmetric

s: symmetric

Assignment	Wavenumber (cm^{-1})
ν as (CH_3)	2976
ν as (CH_2)	2929
ν s (CH_3)	2890
δ as (HCH)	1365
δ (CH_3)	1168
ν as (Si-OC)	1082
δ (H_3CO)	965

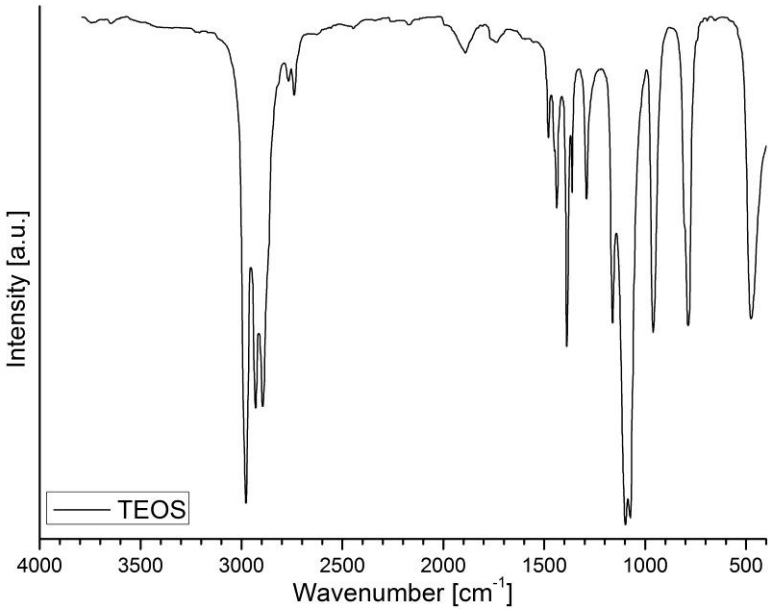

Figure 33. FTIR transmission mode spectrum and peaks assignment of TEOS.

Assignment	Wavenumber (cm^{-1})
ν as (CH_3)	2976 (st)
ν (CH_2)	2926 (w)
ν s (CH_3)	2880 (w)
δ as (HCH)	1444 (w)
δ (Si-CH_3)	1268 (st)
ν as (Si-OC)	1107, 1082 (st)
δ (H_3CO)	957 (m)

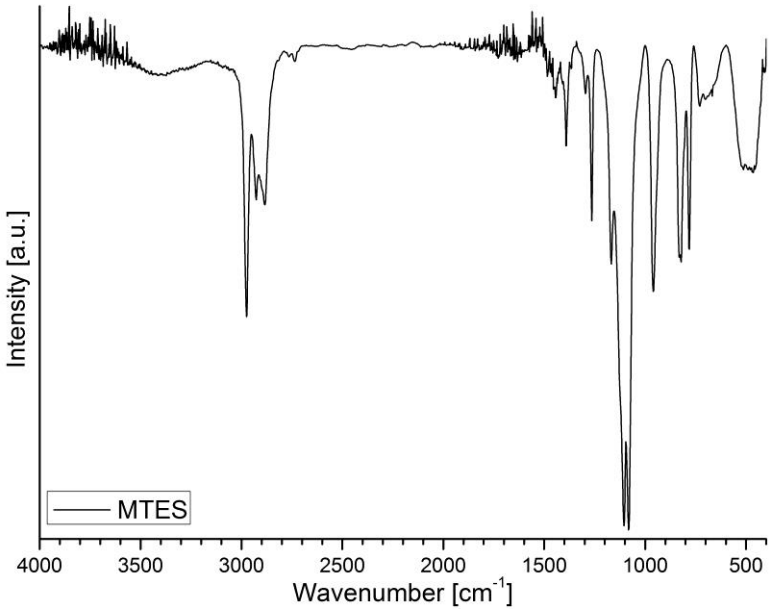

Figure 34. FTIR transmission mode spectrum and peaks assignment of MTES.

Assignment	Wavenumber (cm^{-1})
ν s (N-H)	3470(br, m)
ν as (CH_3)	2979 (st)
ν (CH_2)	2928 (w)
ν s (CH_3)	2880 (w)
ν s (N-H)	1643 (w)
δ (N-H)	1578 (st)
ν as (Si-OC)	1083 (st)

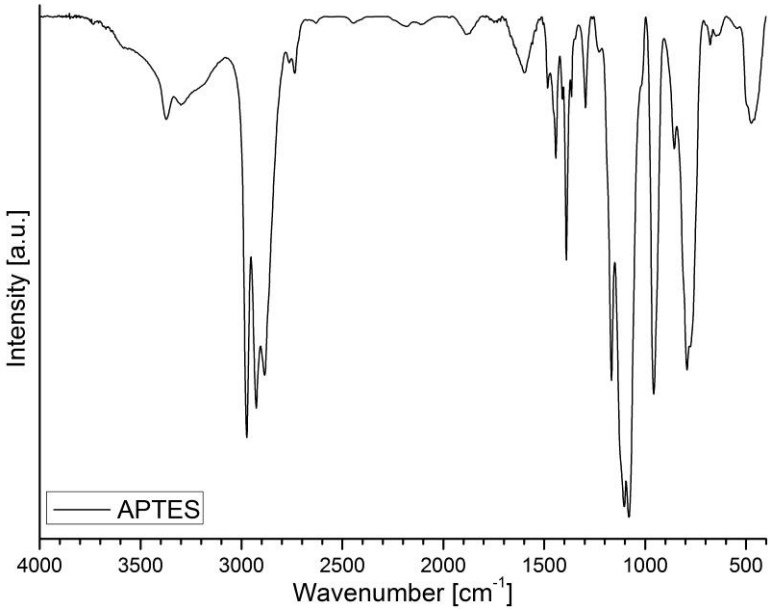

Figure 35. FTIR transmission mode spectrum and peaks assignment of APTES.

Assignment	Wavenumber (cm^{-1})
ν CH [ring]	3067, 3047 (m-w)
ν CH_3	2980 (st)
ν CH [CH_2]	2930 (w)
ν CH [$OCH_2\underline{CH_3}$]	2880 (w)
ν C=C	1594 (m)
δCH_2+ ring vibr	1427 (m)
ω -OCH_2	1390 (m)
Si-OCH_2-	1165 (m),
X sensitive band ν[Si-Ph]	1128 (st)
ν_{as}Si-OC [-OEt]	1103, 1074 (st)
ν_sSi-OC	965 (m)
δ_{oop}CH [ring]	741 (s), 699 (s)
δ_{oop}Si-C-C [ring]	507 (m)

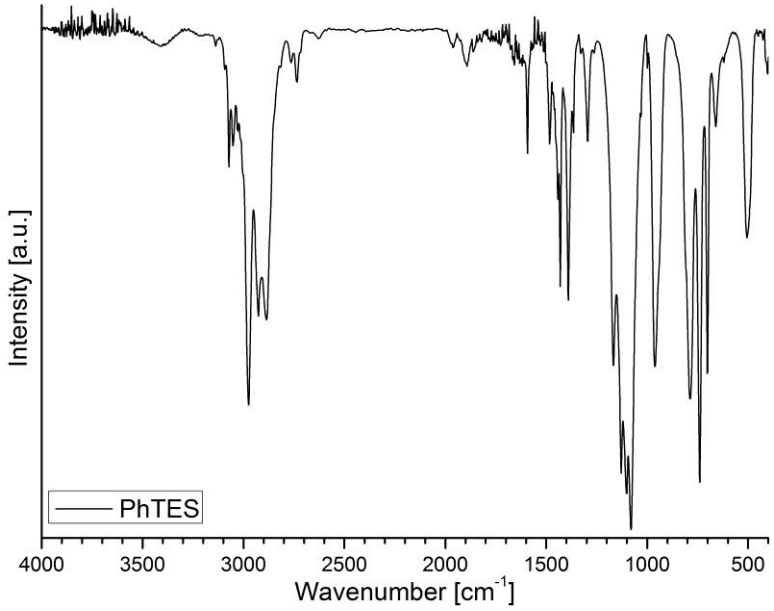

Figure 36. FTIR transmission mode spectrum and peaks assignment of PhTES.

Assignment	Wavenumber (cm^{-1})
ν CH (epoxy ring)	3047 (w)
ν_{as} CH [CH_3]	2943 (st)
ν_s CH [CH_3]	2841 (w)
ν -OCH_3	2838 (st)
δ_{ip} CH_2	1467 (w)
ν_s epoxy ring	1256 (w)
ν_{as} epoxy ring	912 (m)
δ epoxy ring	855 (w)
Si-OMe	1193 (m), 1085 (st)

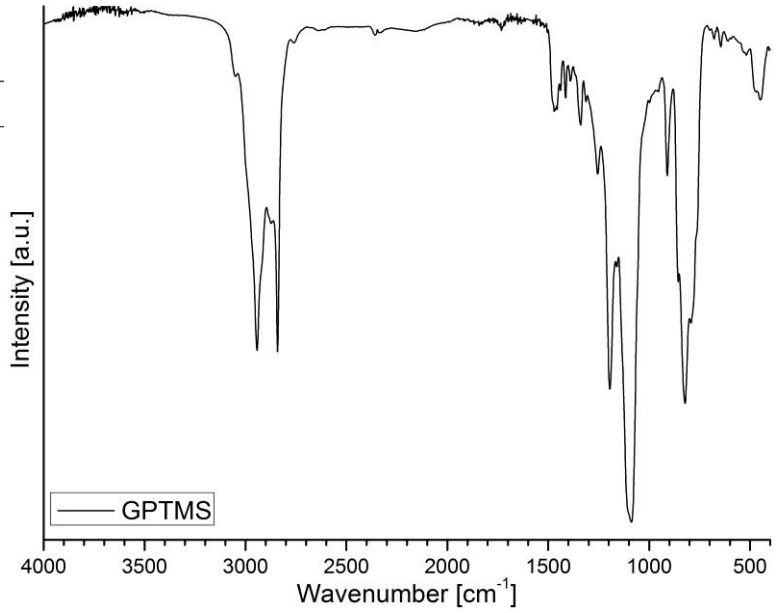

Figure 37. FTIR transmission mode spectrum and peaks assignment of GPTMS.

Assignment	Wavenumber (cm^{-1})
ν OH	3350 (br)
ν_{as} CH_3	2974 (m)
ν_s CH_3	2922 (w)
ν_{as} CH_2	2891 (w)
δ CH_2	1450 (m)
ν CO	1093, 1049 (st)

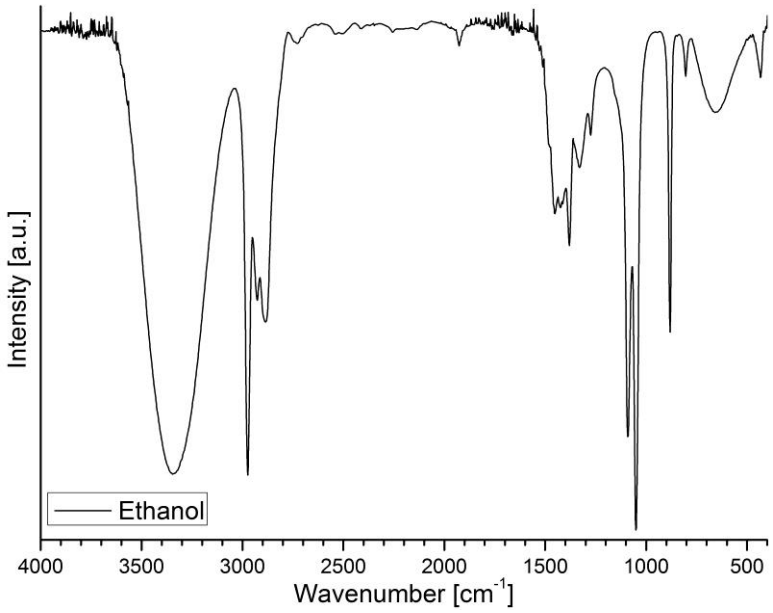

Figure 38. FTIR transmission mode spectrum and peaks assignment of Ethanol.

2.4.2 FTIR Characterization of the Hybrid Xerogels

The xerogels of all prepared hybrid systems were studied by FTIR and acquired vibrational spectra are presented on the Figures 39-43. Despite the different organically-modified trialkoxysilanes used, all the spectra recorded on the xerogels demonstrate typical broad Si-O-Si asymmetric stretching bands in the 1300-800 cm^{-1} range with the main transverse optical (TO_3) signal around 1080 cm^{-1} attributed to transversal ν as (Si-O) of silicon – apical oxygen units and a shoulder at about 1130 cm^{-1}, corresponding to longitudal ν as (Si-O) within structural units [150]. The broadness of the siloxane band suggest that a large number of randomly oriented different species is forming the hybrid network. In the low frequency range, the band at around 460 cm^{-1} is assigned to δ (SiO) [151].

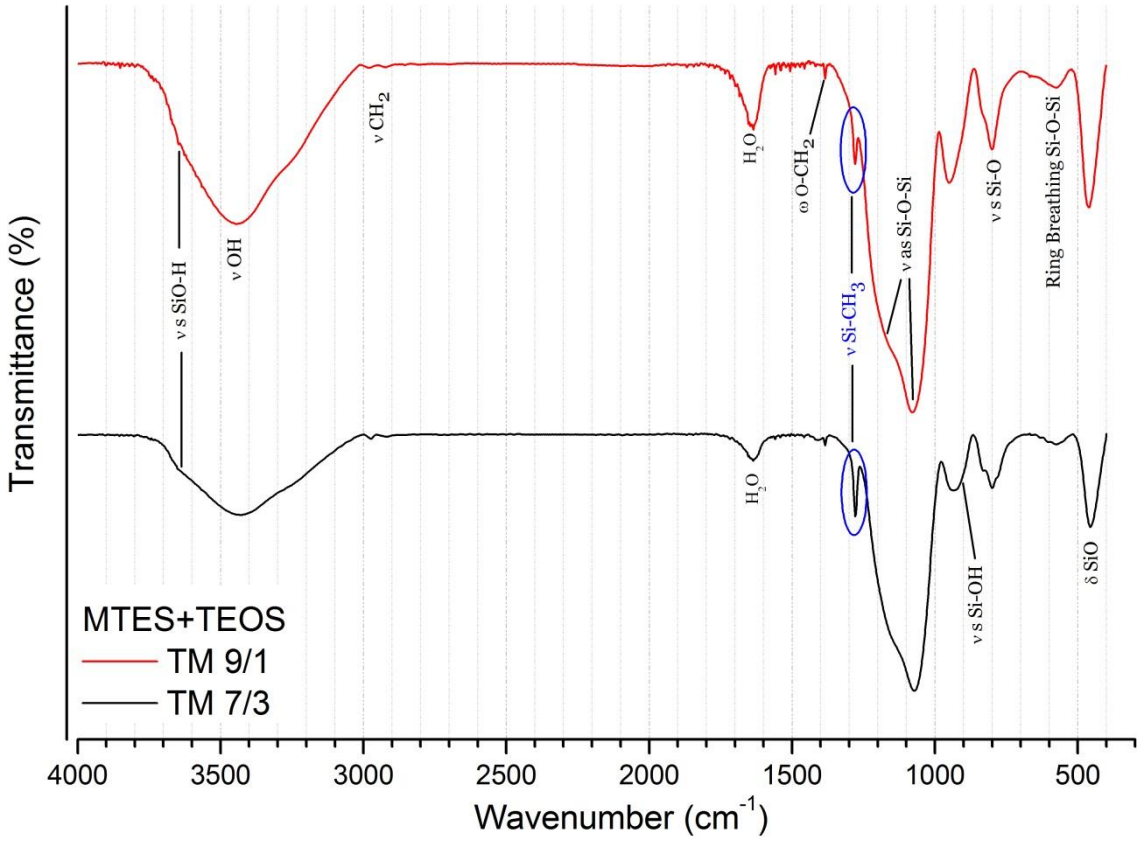

Figure 39. FTIR transmission mode spectra of TM7/3 and TM9/1 xerogels.

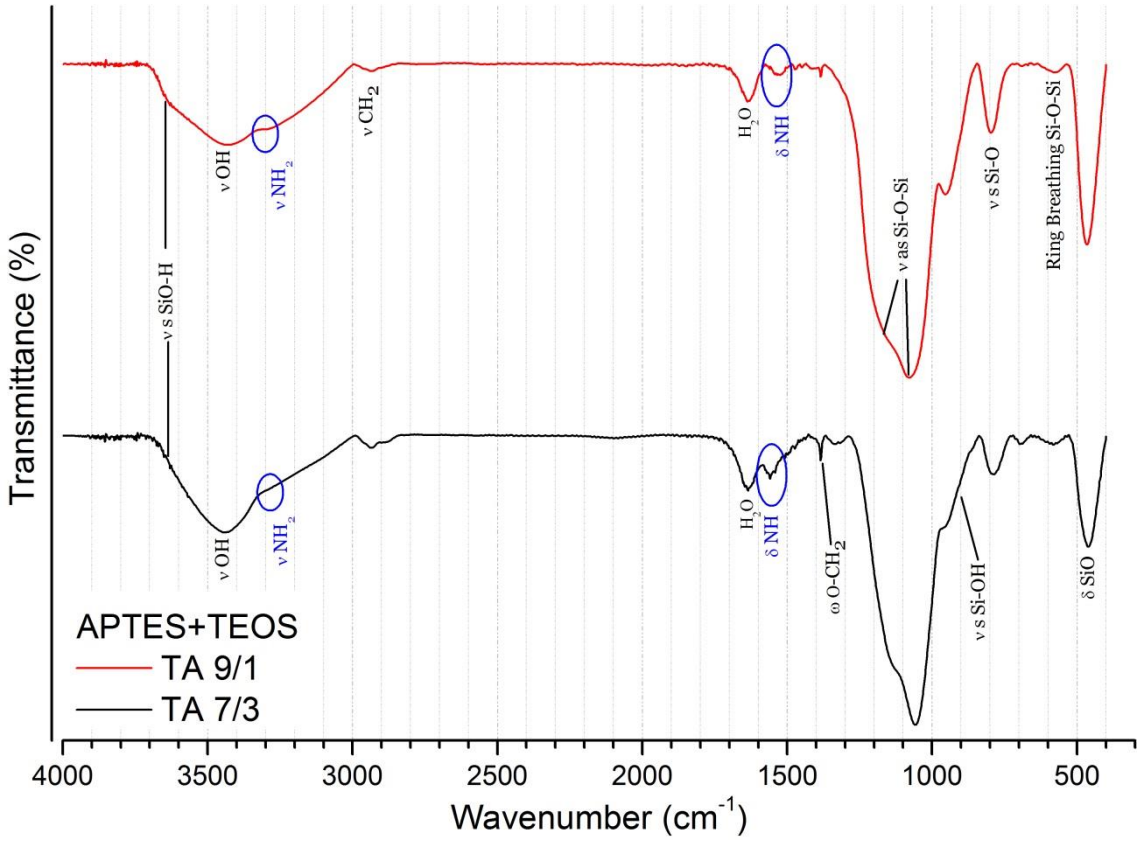

Figure 40. FTIR transmission mode spectra of TA7/3 and TA9/1 xerogels.

Figures 39 and 40 show the spectra acquired on TM and TA samples respectively; the low intensity of the signals related to C-H stretching vibrations reveals an extended hydrolysis, as expected in the case of MTES and APTES due to the inductive effects of the functional groups. The O-H stretching vibration band is the result of overlapping of water, alcohol and silanol contributions; from spectra of Figures 39 and 40 the SiO-H presence is highlighted by the shoulder at 3635 cm^{-1} [152].Importantly, the IR spectroscopy evidences the maintenance of organic groups in the final hybrids. For both TM7/3 and TM9/1 (Figure 39), the stretching vibration of methyl group linked to silicon ν(Si-CH_3) causes a strong and sharp characteristic peak at 1276 cm^{-1} (as observed in MTES spectrum- see Figure 34).

For TA7/3 and TA9/1 xerogels spectra, presented on the Figure 40, the characteristic ν(N-H) stretching vibrations at 3470 cm^{-1} are overlapped with the broad –O-

H band for both samples, thus it cannot be accounted as the evidence of amino-propyl function presence in hybrid xerogels. However, the bending mode of free -NH_2 group, detected as a weak broad band at 1560 cm^{-1}, confirms that both TA7/3 and TA9/1 hybrids keep the amino-propyl function in their network.

The IR spectra of TP7/3, TP9/1, TG7/3 and TG9/1 are shown on the Figures 41 and 42. The hydrolysis extent of the ethoxy groups can be followed by the fade of the typical signals at 2935 (νCH_2), 2880 (νCH_3) [153]. In comparison to TM and TA samples spectra, the TP9/1, TG7/3 and TG9/1 samples spectra suggest lower extent of hydrolysis due to the presence of medium-intensity bands in the 2980-2880 cm^{-1} region.

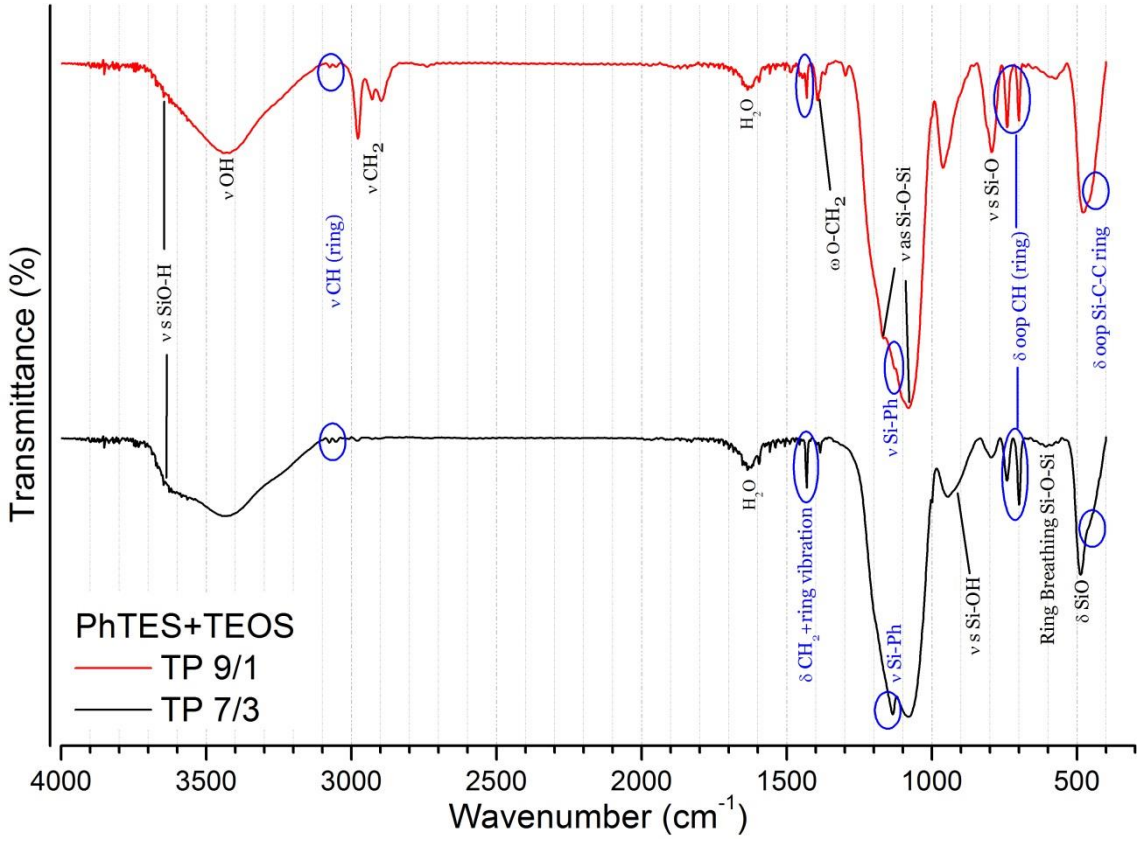

Figure 41. FTIR transmission mode spectra of TP7/3 and TP9/1 xerogels.

The presence of the phenyl group in both TP7/3 and TP9/1 xerogels (Figure 41) is confirmed by the bands at 3073 and 3048 cm^{-1} (νCH_{aryl}), and the characteristic signals due to the in phase out of plane vibrations of the 5 H in the monosubstitued aromatic ring by

intensive peaks at 741 cm^{-1} and 699 cm^{-1} ; and series of the sharp weak bands in the region of 1440-1590 cm^{-1}, attributed to the ring stretching vibrations [154]. Due to the high amount in the TP7/3 sample, phenyl groups contribute to the siloxane band with the sharp shoulder at 1130 cm^{-1}, attributed to the cumulative impact of ring stretching, ring bending and ν(Si-Ph) stretching.

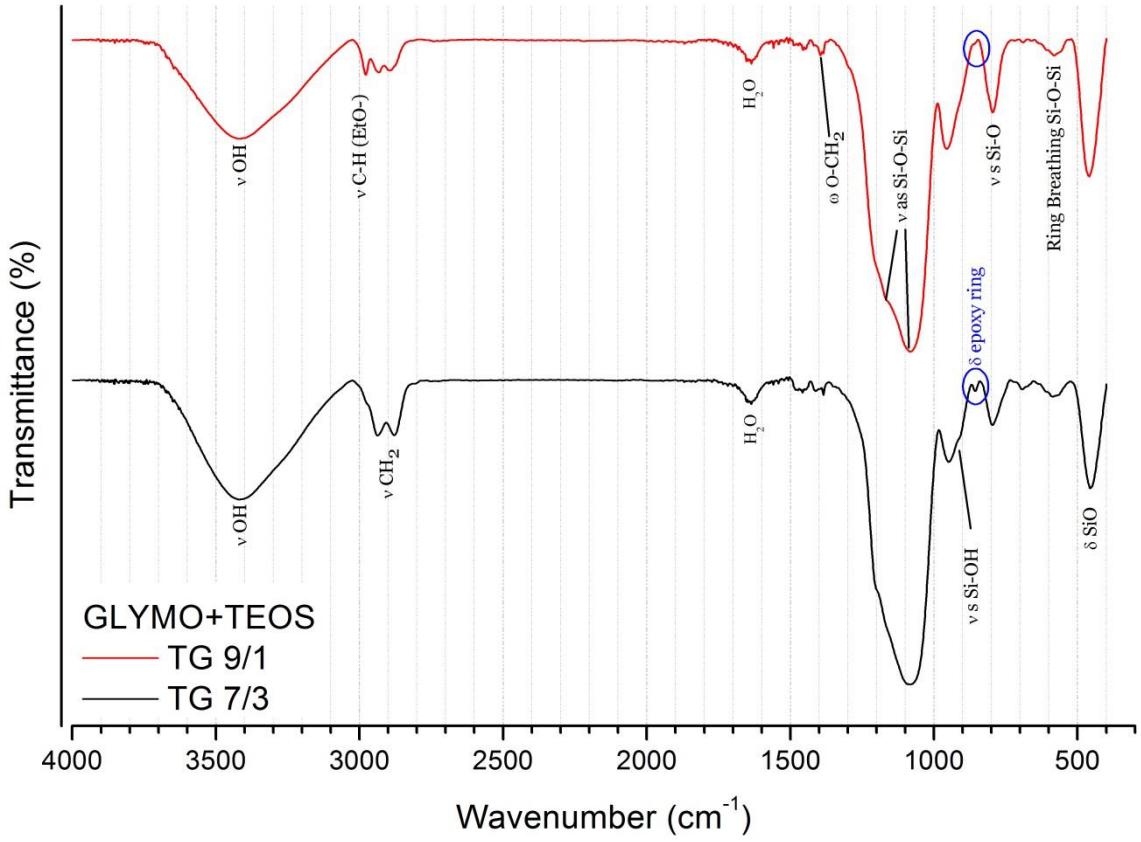

Figure 42. FTIR transmission mode spectra of TG7/3 and TG9/1 xerogels.

The analysis of the "fingerprints" of ν(CH) stretching of epoxy ring at 3047 cm^{-1} is complicated due to the –OH and ethoxy groups vibrations contributions to that region (Figure 42). Nevertheless, the very weak bands at 913 cm^{-1} and 855-860 cm^{-1} can be attributed to ν as (of epoxy ring) and ρ (of the ring) respectively, thus confirming the maintenance of functional groups in both TG7/3 and TG9/1 hybrids.

The attempt of recording the infrared spectra on thin films using the ATR technique failed, due to the thickness of the deposited layers on glass substrates. The thickness was

measured by using a stylus prophylograph, and the results are reported in Table 1. In general, the thickness appears almost constant in all cases with the exception of TA samples, which are much thicker than the other layers in agreement with the different catalytic conditions used for the Sol preparation.

Sample label	Thickness, µm
TM 7/3	0.14 ± 0.01
TM 9/1	0.16 ± 0.01
TG 7/3	0.08 ± 0.01
TG 9/1	0.12 ± 0.01
TA 7/3	0.35 ± 0.01
TA 9/1	0.67 ± 0.01
TP 7/3	0.08 ± 0.01

Table 1. Coatings thickness, measured by a stylus prophylograph.

2.4.3 ^{29}Si MAS NMR Characterization of the hybrid xerogels

Multinuclear solid state NMR was used in order to study the extent of hydrolysis – condensation of the hybrid siloxane networks as a function of the composition. ^{29}Si MAS spectra were recorded on xerogel samples both in CP and SP experiments. Spectra were labeled using the common NMR notation, according to which, Q^n and T^n are tetrafunctional SiO_4 and trifunctional $SiCO_3$ units, respectively and n is the number of siloxane bridges, as presented on the Figure 43.

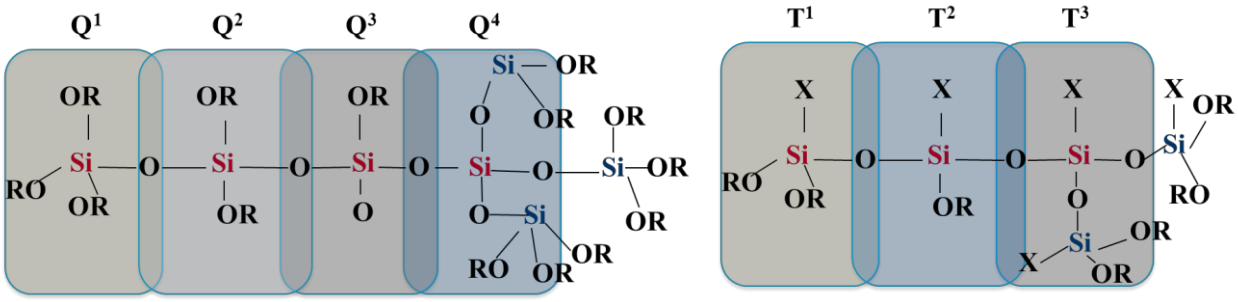

Figure 43. ^{29}Si NMR classical T^n and Q^n structural units notation.

The ^{29}Si CP MAS spectra were recorded on 9/1 and 7/3 samples series and show the typical signals of T units (-50 ÷ -70 ppm) and Q units (-90 ÷ -120 ppm). The spectra of 7/3 xerogels are presented on the Figure 44. In the T units range, the signals of T^2 and T^3 species are present in different ratio depending on the organic function linked to Si. The cross-polarized spectrum of TP 7/3 shows the most intense T^2 peak, as a consequence of the limited condensation ability of PhTES due to the steric and inductive effects displayed by the phenyl groups, which limit the access to Si condensation centers and do not stabilize the intermediate silicon species during the sol-gel reactions.

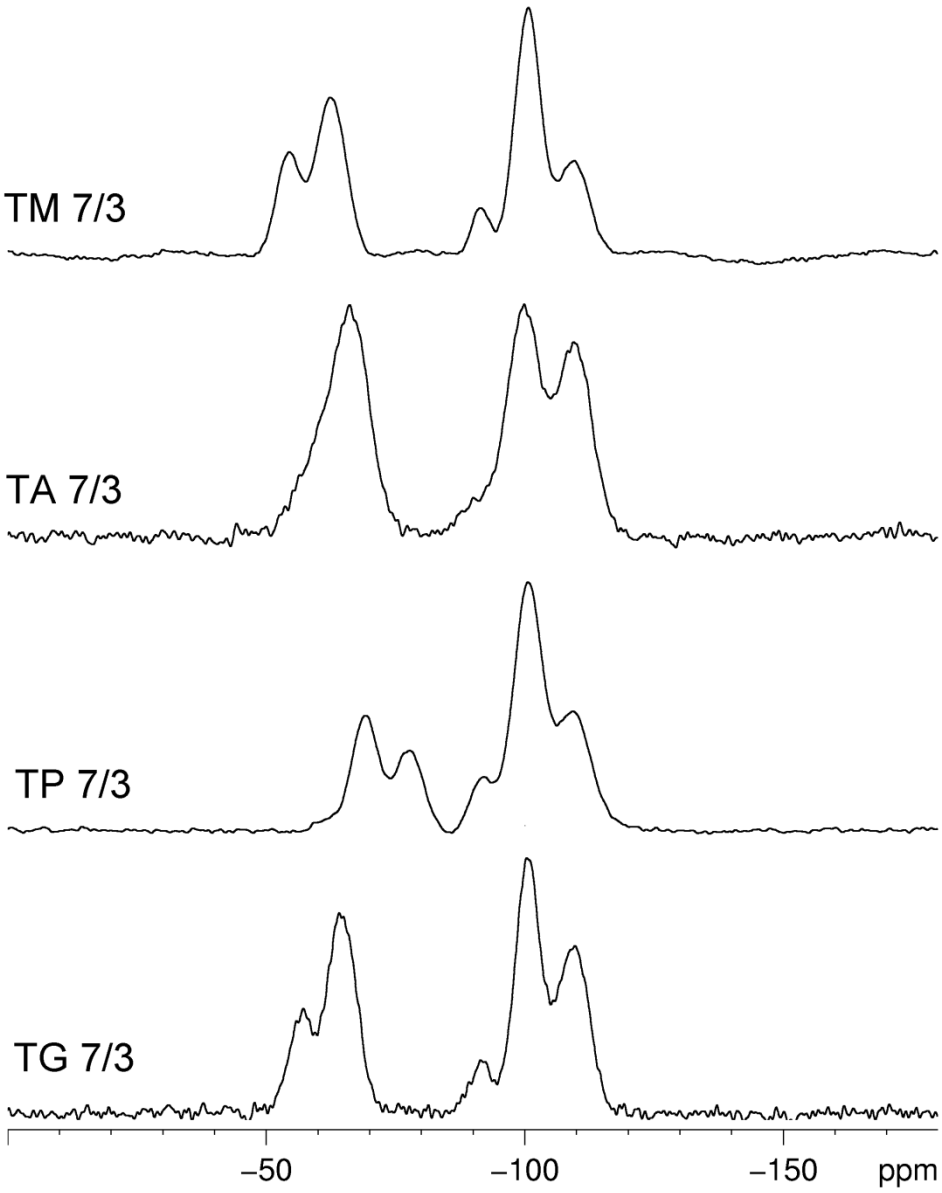

Figure 44. ^{29}Si CP MAS NMR spectra of TM7/3, TA7/3, TG7/3, TP7/3 xerogels.

On the contrary, aminopropyl and glycidoxypropyl groups promote the T network condensation as suggested by the increase of T^3 peak in TA and TG spectra of 7/3 samples. In the Q signal range, the peaks due to Q^2, Q^3 and Q^4 units are almost similar in all samples with the exception of TA7/3.

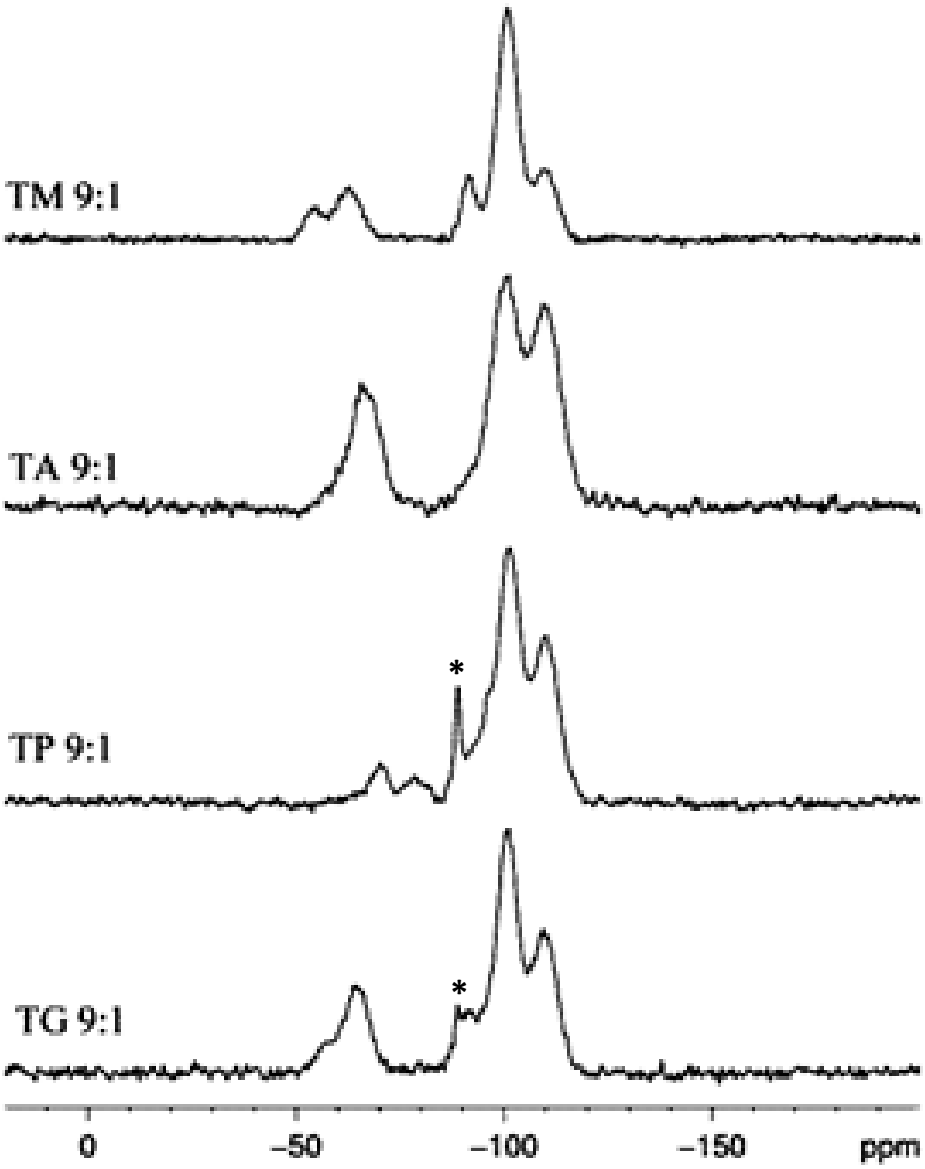

Figure 45. ^{29}Si CP MAS NMR spectra of TM9/1, TA9/1, TG9/1, TP9/1 xerogels, * attributed to impurities.

The spectra of 9/1 xerogels are shown on the Figure 45. In comparison to 7/3 samples, the T units range is decreased in intensity as expected from the composition, however the T^2 and T^3 species ratio is kept unchanged. TP 9/1 demonstrate very low intensity of T-units, and its Q^2 region is polluted by impurities.

Since CP MAS spectra cannot give quantitative results, the SP MAS experiments were run on the samples and the obtained spectra were analyzed by means of fitting deconvolution. The Voigt approximation with Gaussian-Lorentzian sum function was used to fit and separate spectral peaks. Variable parameters were: chemical shift, peak intensity, line broadening and Gaussian-Lorentzian ratio. The fittings are presented for the TA samples on the Figure 46, where the blue line corresponds to experimental spectrum, the red line is the calculated curve and the green lines are the peak components used for the profile fitting analysis.

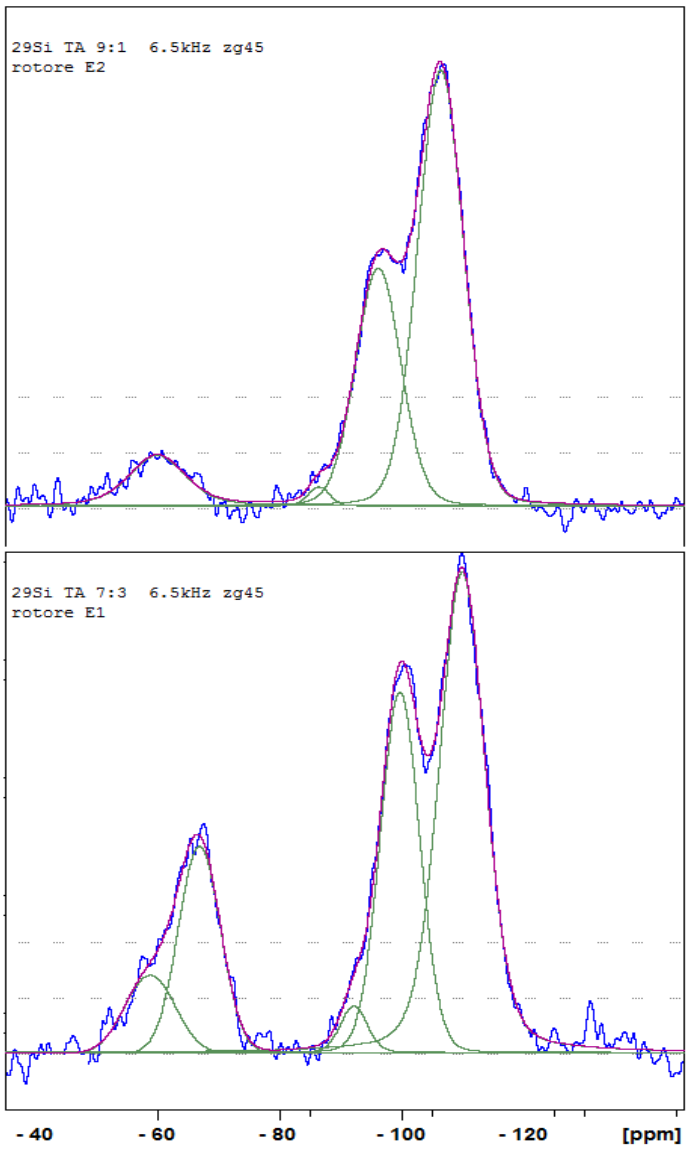

Figure 46. ^{29}Si SP NMR spectra fitting of TA9/1 (top) and TA7/3 (bottom) samples.

All the acquired SP MAS spectra were subjected to the deconvolution, and the acquired values are summarized in Tables 2 and 3 for 9/1 and 7/3 samples respectively, indicating that the nominal ratio between T and Q units is almost respected in the final hybrid networks, with the exception of TA 7/3, which presents a lower T units content (24.7 %), and TP 9/1 that is composed by less than 5% of the silsesquioxane component and the related quantitative analysis is meaningless.

TM 9/1		TA 9/1		TG 9/1		Assignment
δ ppm	A %	δ ppm	A %	δ ppm	A %	
-57	1.0	-56	0.8	-57	1.0	T_2
-63	7.2	-66	8.2	-64	9.0	T_3
-92	6.2	-91	2.1	-92	4.3	Q_2
-101	32.4	-100	30.8	-100	27.1	Q_3
-110	53.2	-110	58.1	-109	58.6	Q_4

Table 2. Peak assignments and areas calculated from ^{29}Si SP-MAS spectra of 9/1 samples.

TM 7/3		TP 7/3		TA 7/3		TG 7/3		Assignment
δ ppm	A %	δ ppm	A %	δ ppm	A %	δ ppm	A %	
-54	10.9	-69	16.1	-57	4.4	-57	4.5	T_2
-62	17.7	-78	15.7	-66	20.3	-65	25.1	T_3
-91	3.4	-92	3.6	-92	0.1	-92	1.0	Q_2
-100	27.9	-101	33.1	-100	33.8	-101	21.3	Q_3
-110	40.1	-111	31.5	-110	41.4	-110	48.1	Q_4

Table 3. Peak assignments and areas calculated from ^{29}Si SP-MAS spectra of 7/3 samples.

The degree of condensation (DOC) was calculated from spectra deconvolution according to the literature [155], and using the following equation:

$$DOC = \frac{2T^2 + 3T^3 + 2Q^2 + 3Q^3 + 4Q^4}{3(T^2 + T^3) + 4(Q^2 + Q^3 + Q^4)}$$

As presented in the Table 4, the DOC generally decreases by increasing the T units content, from 9/1 to 7/3 samples. Moreover, it depends on the organic function linked to Si.

The DOC values confirm the higher condensation ability of APTES and GPTMS compared to the behavior of MTES and particularly PhTES, which is in agreement with FTIR. According to inductive effects, discussed in Chapter 1, the presence of amino and epoxy functions improves silanol condensation by stabilizing the positive partial charge on silicon.

Sample	DOC	T^3/T^2	$Q^4/(Q^3+Q^2)$
TP 7/3	84.7	0.97	0.86
TM 7/3	87.7	1.62	1.28
TM 9/1	88.3	7.2	1.38
TA 7/3	89.8	4.61	1.22
TA 9/1	90.9	10.25	1.76
TG 7/3	92.5	5.57	2.16
TG 9/1	90.6	9.0	1.87

Table 4. DOC (degree of condensation) and ratio between units calculated from data reported in Tables 2 and 3.

The DOC value decrease for 7/3 samples is mainly related to the decrease in T^3/T^2 ratio, rather than to the $Q^4/(Q^3+Q^2)$ ratio (Table 4). The lower condensation ability of the T units in the 7/3 series could be the consequence of the increased stiffness of the gel related to the formation of silica domains leading to a more constrained network, which inhibits the chains mobility necessary to the cross-linking of the silsesquioxane network.

Taking into account the decrease of DOC from 9/1 to 7/3 samples, the ^{29}Si NMR results indirectly suggest that the extent of interaction between Q and T units changes according to the composition. The separation between T and Q domains is expected to increase by increasing the silsesquioxane phase content.

2.4.4 ^{13}C MAS NMR Characterization of the hybrid xerogels

The ^{13}C CP MAS study gives information on the extent of hydrolysis reached during the sol-gel process and suggests if the polimerizable functionalities undergo to self-condensation or other chemical transformations. The carbon spectra of 7/3 and 9/1 samples are shown on the Figure 47 and 48 respectfully.

TM and TA show an extended hydrolysis of alkoxide groups both for 7/3 and 9/1 samples, displaying almost negligible signals attributed to the residual ethoxyde functions at 18 ppm (O-CH_2-$\underline{C}H_3$) and 60 ppm (O-$\underline{C}H_2$-CH_3). On the contrary, the hydrolysis is not completed for TG 7/3 sample, whose spectra display appreciable amounts of residual ethoxyde groups, which is also in agreement with FTIR observations.

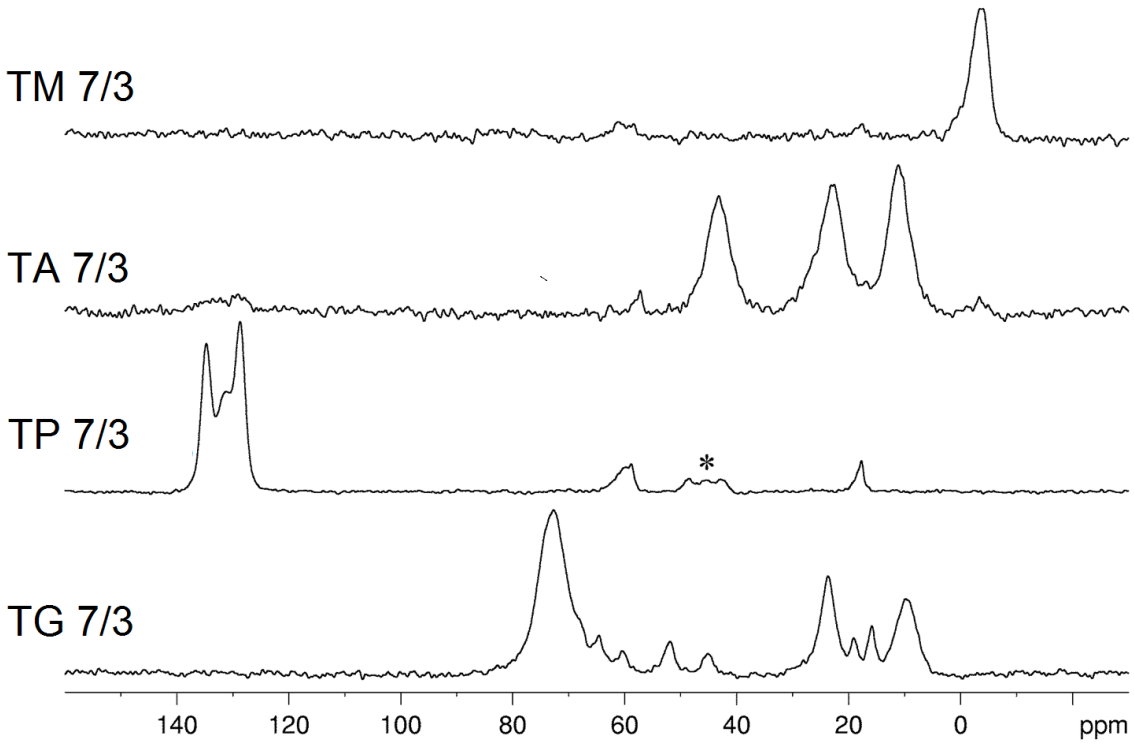

Figure 47. ^{13}C CP-MAS spectra of 7/3 samples (* indicates spinning side bands).

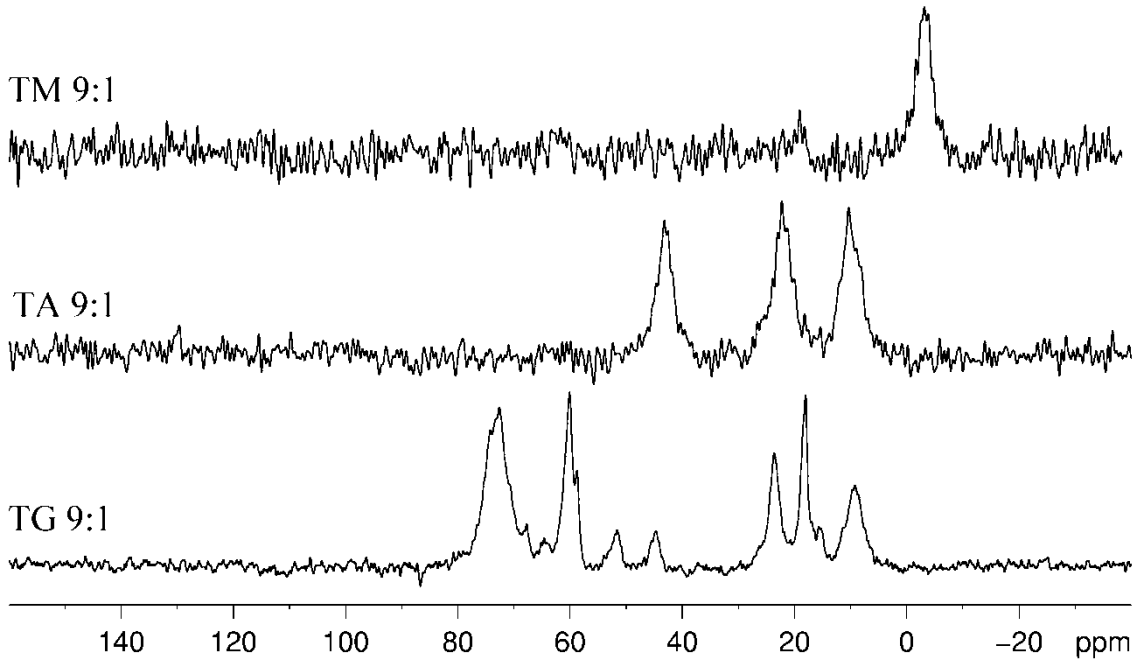

Figure 48. ^{13}C CP-MAS spectra of 7/3 samples (TP 9/1 is excluded due to low organically modified counterpart content).

In agreement with the decrease of DOC value compared to the one of TG7/3, (see Table 4), TG 9/1 sample presents strong signals attributable to ethoxy groups. These groups are supposed to derive from the trans-esterification reaction of the pristine methoxy functions of GPTMS in ethanol solution.

The maintenance of the organic function bonded to the trifunctional silicon in the final hybrids is also proved by the carbon spectra. TM spectra are dominated by the intense signal due to the methyl groups directly bonded to silicon at -3.5 ppm. TA spectra display the signals of C1, C2 and C3 carbon atoms of the aminopropyl chain at 10.4, 22.2 and 43.2 ppm, respectively.

The phenyl groups in TP sample give a complex group of aromatic signals in the range 140 ÷ 120 ppm. TG samples show the characteristic peaks of the backbone organic chain C1, C2 and C3 carbon atoms at 10.3, 23.1 and 44.2 ppm, respectively. The other peaks are suggesting a partial epoxy ring opening, which is proved by the comparatively

low intensity of peaks at 52.1 and 45.3 ppm due to C5 and C6, respectively. together with the presence of new peaks, which can be attributed to diol-β-C at 67.8 and α-C at 64.7 ppm.

2.4.5 ^{1}H MAS NMR Characterization of the hybrid xerogels

^{1}H NMR analysis also confirms the presence of residual unreacted alkoxide groups in TP and TG samples and the maintenance of the organic functions linked to silicon, in agreement with the carbon results and FTIR analysis. Sharp signals are visible in the ^{1}H spectra of TM9/1 (3.9 ppm), which can be attributed to free silanols (Figure 49).

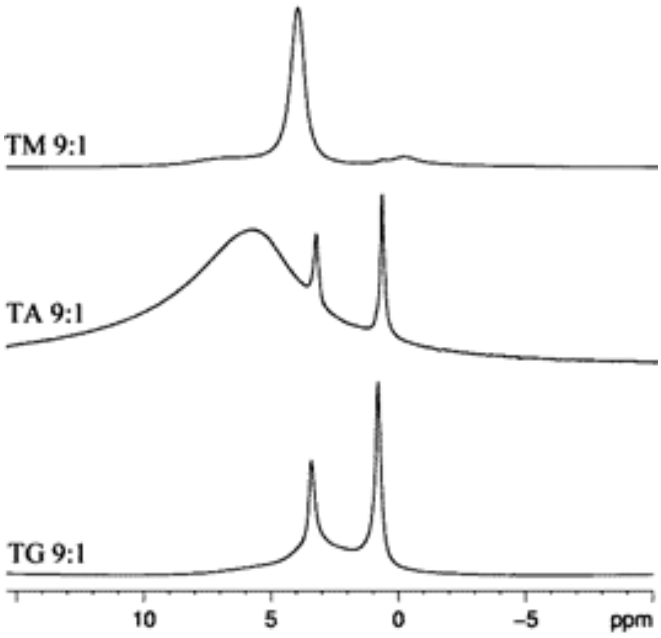

Figure 49. ^{1}H MAS spectra of 9/1 samples

This conclusion is in agreement with the almost full hydrolysis of alkoxide groups shown by ^{13}C NMR and the low DOC (table 4) exhibited by the samples obtained from MTES. Proton spectra of TA and TG samples show extensive peak broadening and intense peaks due to adsorbed water, attributable to interactions with their polar organic functions. In the case of TG9/1 the signals of ethoxide protons are probably overlapped by

the water protons. TA 7/3 and 9/1 proton spectra also show a silanol signal at 5.7 ppm, in agreement with the results of carbon spectra suggesting an almost complete hydrolysis step.

2.4.6 XRD Characterization of the hybrid xerogels

Scattering methods have been extensively used to study the morphology and the structure of nanomaterials. X-Ray Diffraction is a fundamental tool for the phase analysis in materials. Rapid and simple method for structural characterization that does not require a special preparation of the samples, it was used for xerogels (grinded into powders) and thin films characterization in order to get more information on the medium-long order arrangement in the networks. Powder XRD diffractograms of 9/1 and 7/3 hybrid xerogels are presented on the Figures 50 and 51.

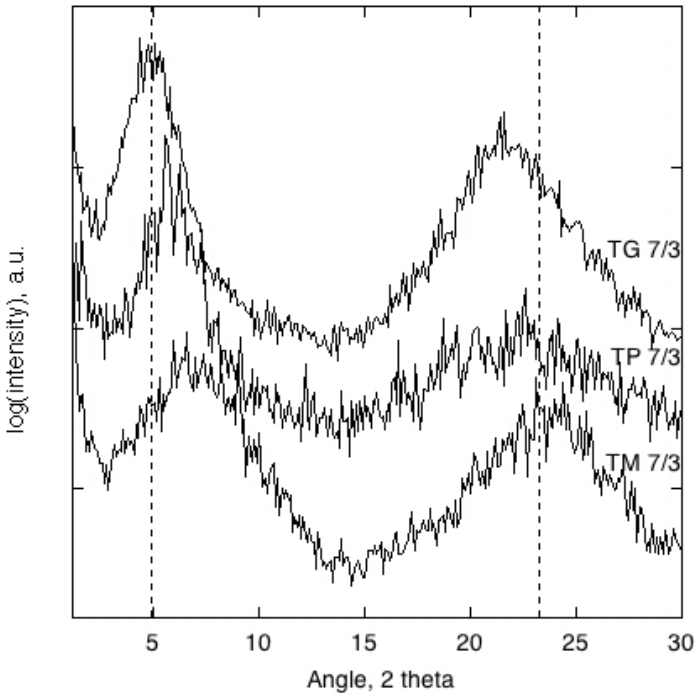

Figure 50. XRD diffractograms of 7/3 samples (reference lines are at 5 and 23°).

The diffraction diagrams are characterized by two different signals, which can be attributed to silsesquioxane-based domains (T units) in the range $2\theta = 2 \div 16°$ and amorphous silica (Q units) at $2\theta \approx 23°$. The silica halo is well visible in 7/3 samples (Figure 50), with the exception of TA that shows an extremely low intensity signal (therefore not reported in the Figure 43).

The signal related to Q domains does not present appreciable changes in position with the exception of TG 7/3, which shows a shift of the silica halo towards lower angles. In TM 7/3 the peak due to T domains is present at 8.4° whereas TP 7/3 and TG 7/3 show the same signals at 5.9° and 5° respectively, according to a progressive d spacing increase of T domains, shifting from 1.052 nm (TM), to 1.497 nm (TP) and 1.766 nm (TG).

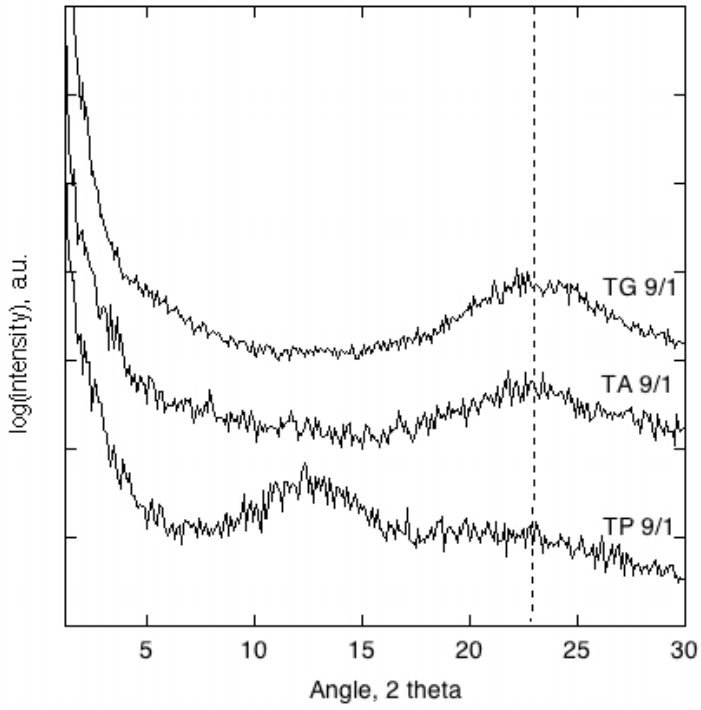

Figure 51. XRD diffractograms of 9/1 samples reference line is drawn at 23°.

As a general behavior, the signal attributed to the silsesquioxane phase disappears in 9/1 samples (Figure 51) and, despite the high silica concentration, the silica halo shows a relevant decrease in intensity leading to a flat XRD trace for TM 9/1 (not reported). In the

case of TP 9/1, the amorphous silica signal is not visible and a single broad halo is present at 12.6°. The XRD diagrams of TA samples appear quite similar and seem to be almost unaffected by the increase of T units load.

These results suggest that the extent of phase interaction changes according to the nature of the trifunctional precursor. Higher interactions between T and Q units could explain the lack of a well-defined signal of silica and silsesquioxane phases in XRD diffractograms. This allows to describe the case of 9/1 samples, according to the formation of a highly co-condensed network made of T and Q units. The XRD signals of silica and silsesquioxane phases appear well defined in the XRD spectra as the phase separation increases, as a consequence of the formation of larger T and Q regions.

2.4.7 XRD Characterization of the hybrid coatings

The above considerations on the hybrid network arrangement at short and medium-range order can be applied also to the XRD results collected on hybrid films deposited on glass substrates. From an experimental point of view, asymmetric scans do not completely remove the reflexes of the glass substrate and the interpretation of the XRD diffractograms of the films cannot neglect this aspect. In Figure 52 the diffractogram of TG 7/3 film is compared with that recorded on the clean glass substrate.

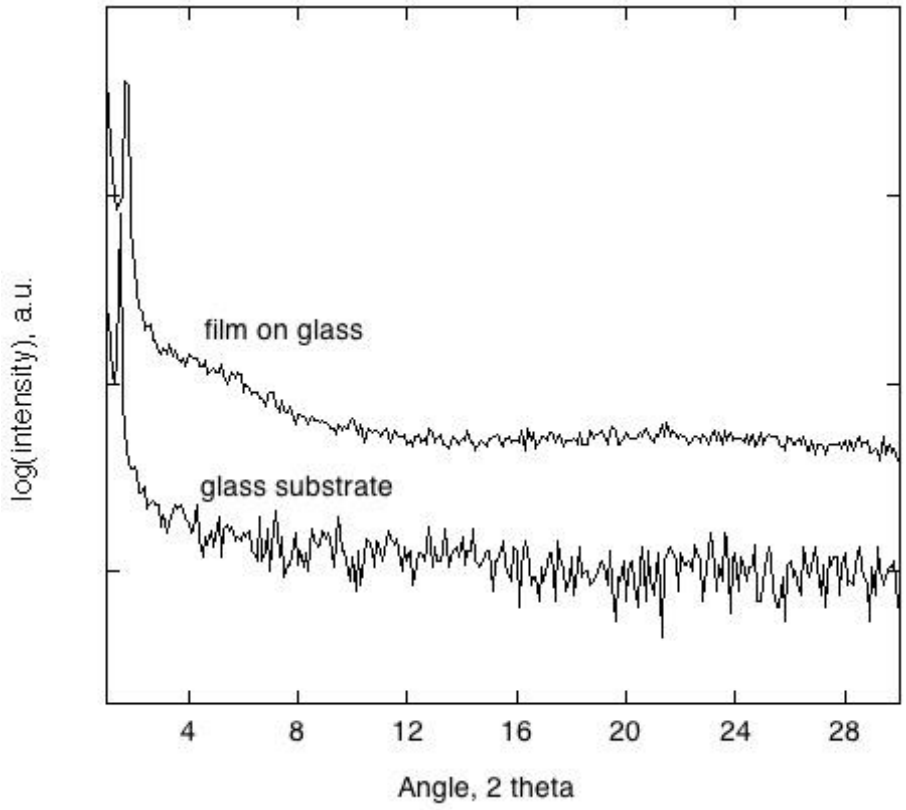

Figure 52. XRD diffractograms of TG 7/3 xerogel and reference glass substrate

Besides the silica basal peak at about 2°, which is slightly shifted and enlarged in comparison with the same signal of the substrate as a consequence of interaction with coating, the TG 7/3 spectrum presents two weak and broad signals: the halo at 2θ =23°, due to Q domains, and the T domains signal centered at 5°, i.e. at the same position found in the XRD trace of TG 7/3 xerogel (Figure 50). The same behavior is found for all the other layers, which present structural features similar to those of the corresponding bulk samples. Accordingly, the conclusions of the xerogel characterization have been extended to coatings, besides the different experimental conditions leading to films and bulk samples.

2.4.8 Surface Characterization of the hybrid coatings

The coatings demonstrated to the SEM analysis typical amorphous dense and featureless surfaces, as can be seen on the Figure 53 for TM 7/3 sample.

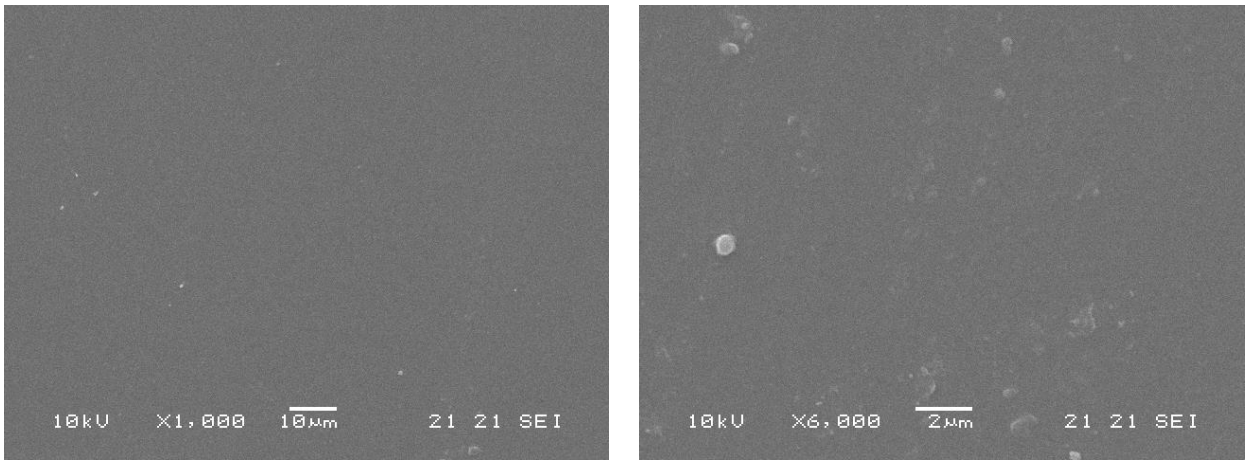

Figure 53. SEM micrographs of TM 7/3 coating with different magnifications.

The coatings porosity was characterized using N_2 adsorption measurements. The glass substrate was subjected for reference and presented a specific surface area of 0.030 ± 0.003 $m^2\ g^{-1}$. The samples were analyzed and type II adsorption isotherms, typical of non-porous materials, were recorded in all cases, as presented on the Figures 54-57.

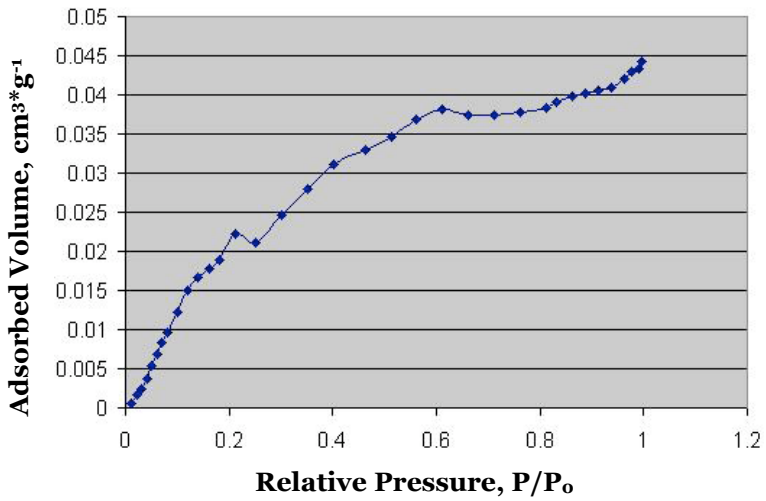

Figure 54. N2 sorption isotherm of TM 7/3 coating.

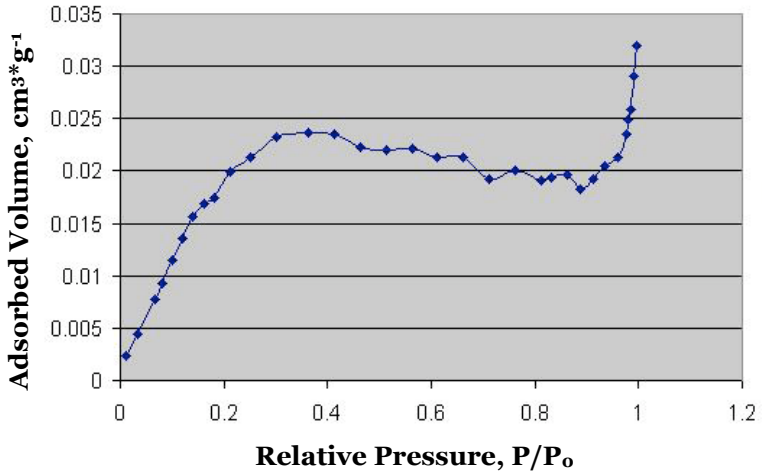

Figure 55. N2 sorption isotherm of TA 7/3 coating.

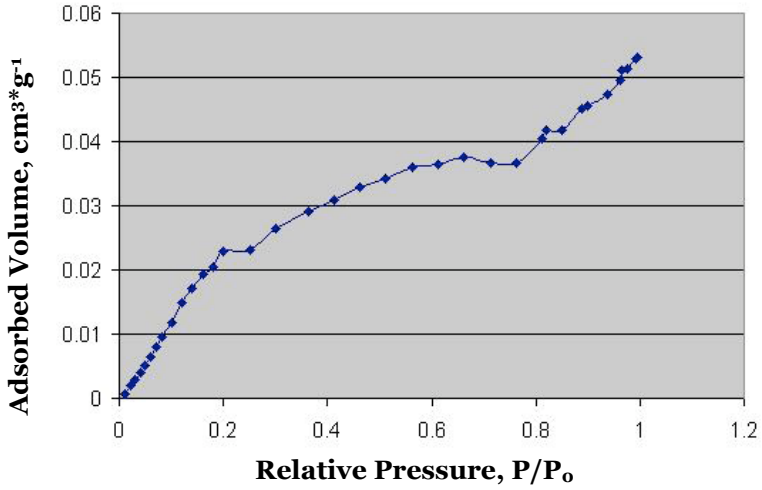

Figure 56. N2 sorption isotherm of TP 7/3 coating.

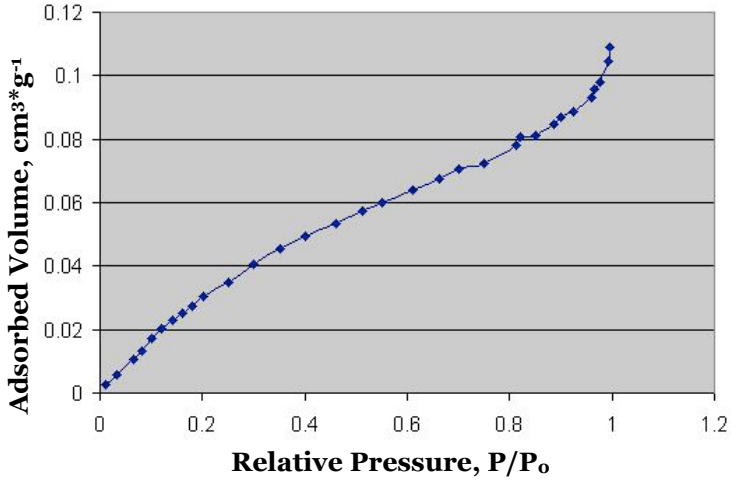

Figure 57. N2 sorption isotherm of TG 7/3 coating.

Accordingly, the layers are almost dense and present low specific surface area (SSA) values, as reported in Table 5. Similar results were obtained from the N_2 sorption isotherms recorded with the xerogels samples, which display SSA values below 1 $m^2\ g^{-1}$. The total mass of the deposited layers can be calculated from coated area, layer thickness and density values. Taking into account the great similarity between xerogels and films, the density values measured by the He picnometry on xerogels can be employed for the calculation. The values calculated for TM and TG samples are in the range 1.42 - 1.84 g cm^{-3}, in agreement with the degree of crosslinking calculated from NMR results and the low porosity.

Sample label	SSA, $m^2\ g^{-1}$	Thickness, µm
TM 7/3	0.82 ± 0.04	0.14 ± 0.01
TM 9/1	1.0 ± 0.2	0.16 ± 0.01
TG 7/3	0.44 ± 0.04	0.08 ± 0.01
TG 9/1	0.32 ± 0.03	0.12 ± 0.01
TA 7/3	0. 31 ± 0.02	0.35 ± 0.01
TA 9/1	0. 08 ± 0.02	0.67 ± 0.01
TP 7/3	0. 31 ± 0.02	0.08 ± 0.01

Table 5. Coatings total specific surface area (SSA) and thickness of different samples.

2.4.9 Optical Characterization of the Films Sorption Ability

The hybrid films were subjected to the evaluation of their capability to adsorb VOCs molecules. The samples response to the benzene, toluene, orto-xylene and chlorobenzene was analyzed by optical methods by positioning the hybrid films into the analytical chamber (see Figures 31, 32), through which a constant flux of VOC vapors was carried with pure nitrogen. In order to test the retaining capability of the films, absorption spectra were acquired through thin films deposited on pure silica substrates, so that the UV absorbance spectra of the analytic molecules entrapped in the film cage could be analyzed.

The absorption spectra of benzene (B), toluene (T), chlorobenzene (Cl-B) and o-xylene (oX) in the vapor phase have been recorded in the range 190 - 400 nm. Each aromatic molecule can be easily recognized from the characteristic absorption feature, given by the combination of the electronic transition, as the well-known $S_0 \rightarrow S_1$ transition for benzene at 254 nm, with the related vibrational peaks.

For the coatings test measurements, 20% vol. of VOC vapor in nitrogen (200 sccm of pure nitrogen mixed with 50 sccm of saturated vapor in pure nitrogen) was fluxed into the chamber with the hybrid samples The corresponding concentrations of the VOC in the chamber were calculated from the empirical expression of the vapor pressure [156], resulting in 2064 ppm for benzene, 6170 ppm for toluene, 1390 ppm for orto-xylene and 2620 ppm for chlorobenzene..

The first tests were performed introducing the hybrid samples of different composition into the cell and measuring after fixed time intervals of fluxing, the organic vapor absorption spectra, which were compared to those recorded at the same intervals in the empty cell. The sorption ability of the clean glass substrate was also evaluated in

comparison with results obtained with the empty cell, showing a negligible influence of the substrate.

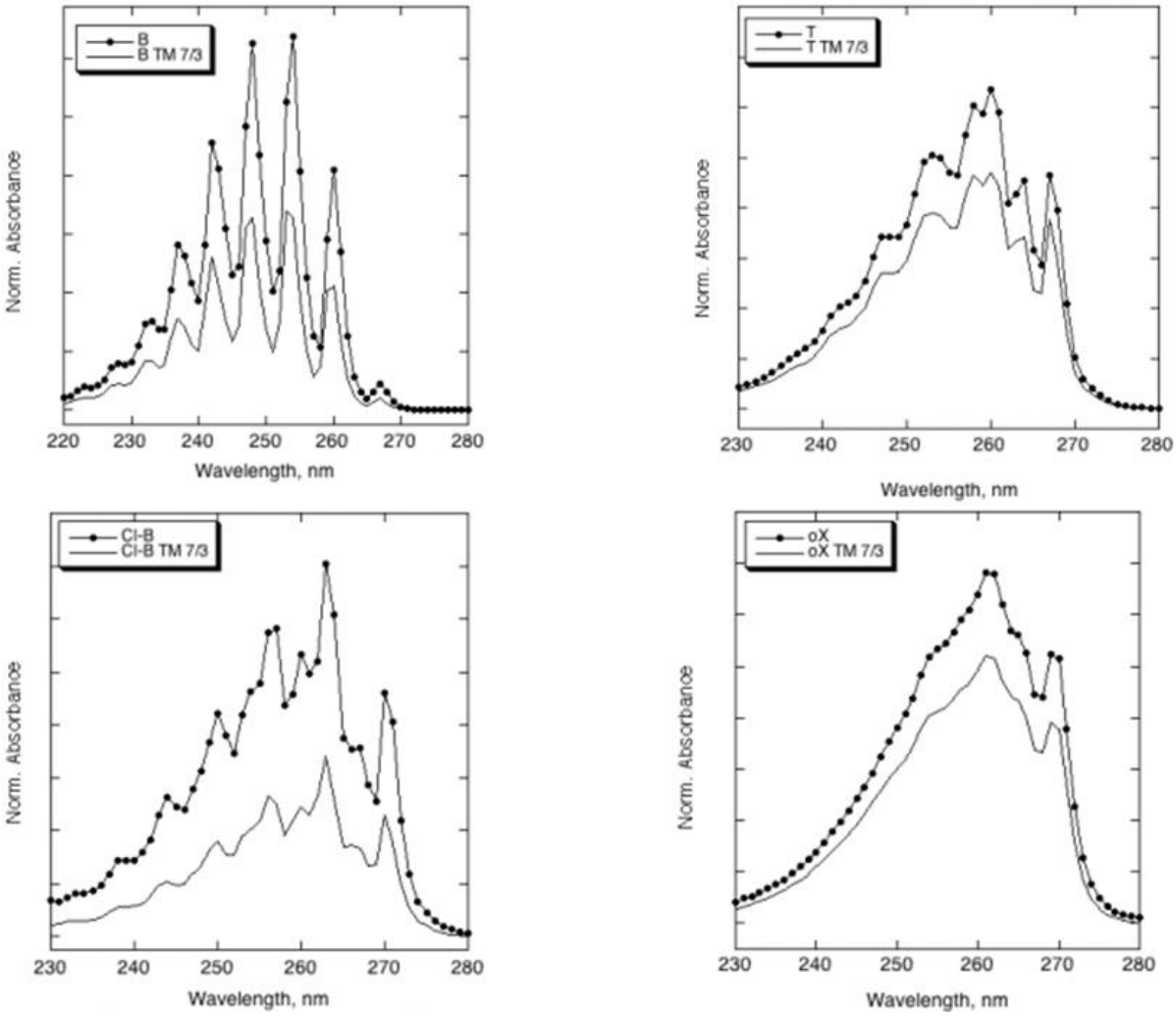

Figure 58. Absorption spectra, collected after 3 minutes of vapor fluxing, of benzene (B), toluene (T), chlorobenzene (Cl-B) and o-xylene (oX) both with the empty chamber and with TM 7/3 layer

Figure 58 presents the spectra recorded in the case of TM 7/3 sample after filling the measure cell for 3 min with 200 sccm of pure nitrogen mixed to 50 sccm of saturated vapor carried by pure nitrogen, in comparison with the results obtained without the sample (lines with dots on the Figure 58). The absorbance reduction observed in the presence of the sample accounts for the interaction of the aromatic compounds with the layer surface.

The difference (in percentage) between the residual VOC concentrations without and with the samples can be obtained from the difference between the amplitudes of the absorbance spectra. In particular, for benzene and chloro-benzene a difference of 48% and 51% was calculated respectively, while for toluene and o-xylene a variation of 26% and 24%, respectively, took place.

Since the UV-observed sorption process in the chamber is a dynamical process, at this stage the evaluation of the amount of adsorbed molecules appears quite difficult. However, it can be stated that TM7/3 films exhibit a better affinity to benzene and chloro-benzene than to toluene and o-xylene. This result could be related to the presence on toluene and xylene of the methyl groups, which can affect the sorption process of the adsorbate molecules both by inductive effects and steric hindrance.

The extent of the sorption process changes for the same aromatic molecule changing the film composition from the 7/3 to the 9/1 series samples (Figure 59) and appears also dependent on the nature of the organic functions present on the surface layer. In particular, the sorption ability seems to be improved by well-interconnected and condensed networks with a low content of silanols, as in the case of the 9/1 series. In the case of spectra presented in Figure 59, a concentration difference of 51% is calculated for the 9/1 film, with respect to the 7/3 film that produces a variation of 25% on the vapor concentration. The indirect information of the film desorption ability has been achieved by fluxing the cell with N_2 after the adsorption step: the organic molecules are completely released from the cell within 30 min.

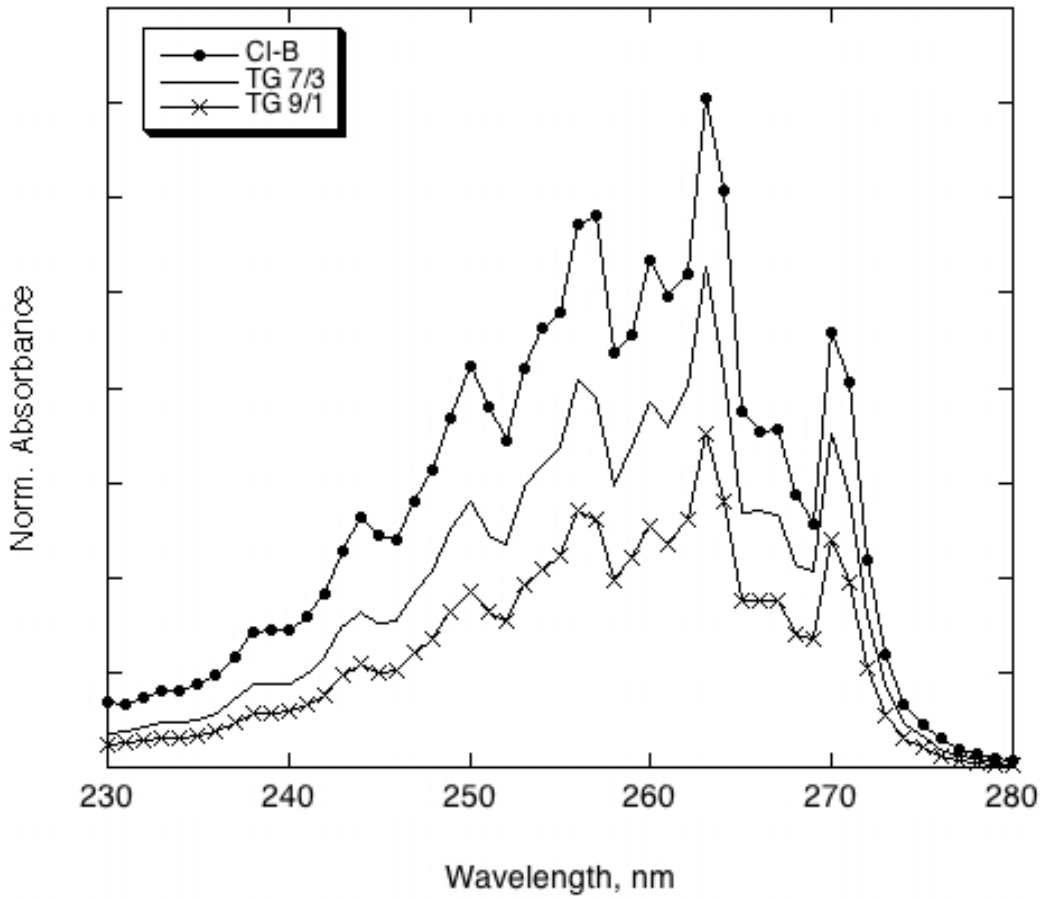

Figure 59. Absorption spectra, collected after 3 minutes of vapor fluxing, of chlorobenzene with the empty chamber and with TG 7/3 e TG 9/1 layers

A different approach was used in order to study in more detail the sorption ability of selected films. In particular, the benzene absorption value at 254 nm was recorded during the filling of the chamber containing samples TM and TG. These films were chosen as representative of different cross-linking degree, surface polarity and steric hindrance, depending on the organic functional groups (methyl and glycidoxypropyl).

Figure 60 shows the absorbance value at 254 nm as a function of the time collected by fluxing 20% of benzene saturated vapour in the chamber, without samples and with samples TM9/1, TM7/3, TG9/1 and TG7/3. The absorbance was normalized on the

saturation value, since it can change at every measurement run depending on the laboratory temperature.

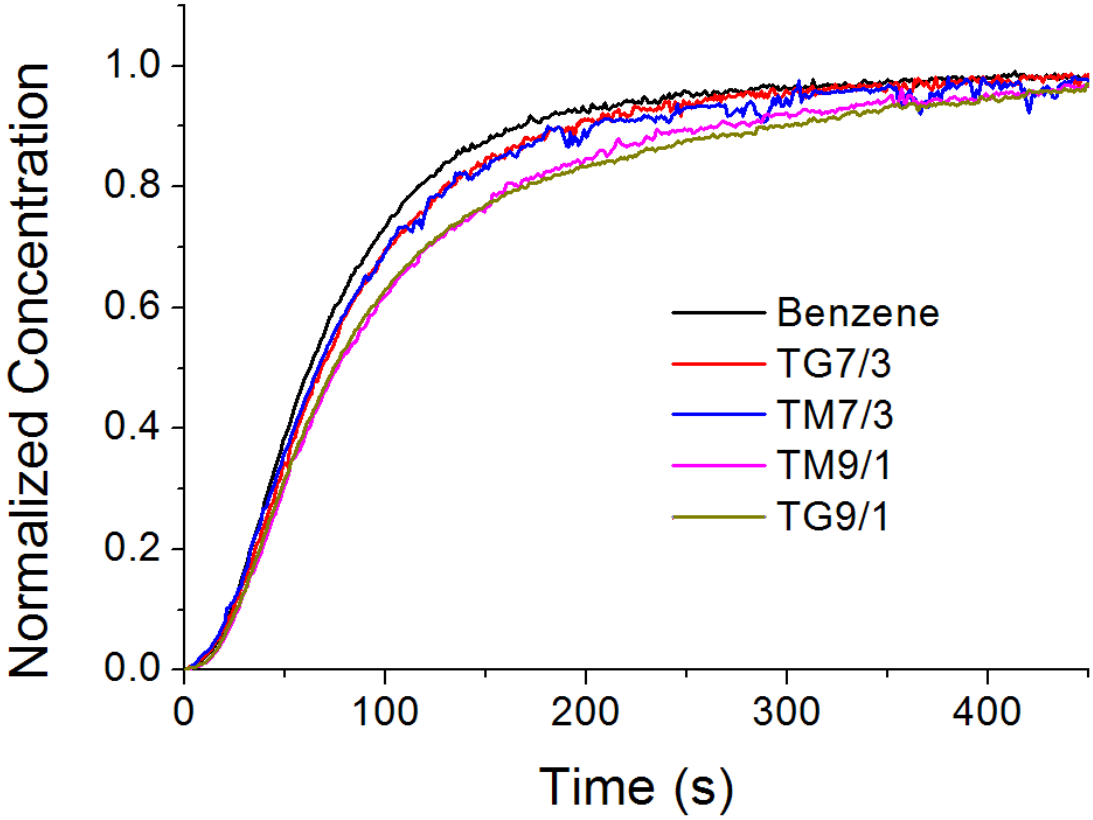

Figure 60 Normalized absorbance values collected at 254 nm observed during the filling of the chamber with 20% vol. of benzene saturated vapor. The curves report the measurements performed without any samples (labeled: Benzene) and with samples TG 7/3, TM 7/3, TM 9/1 and TG 9/1.

As it can be observed, the filling rate of the chamber with the samples is lower with respect to the chamber without the samples. In particular, it is lower for samples 9/1 with respect to samples 7/3. A detailed analysis of the mechanism is beyond the scope of this work. Nevertheless, it can be argued that in different points of the curve the absorbance difference between the empty chamber and the chamber with the sample can give an estimation of the amount of molecules collected by the film. In particular, the molecule

amount from the absorbance difference at 140 s was evaluated. This time has been chosen empirically, since it corresponds to the shoulder of the curve and it is a time long enough to take into account the molecule diffusion into the film. By considering the values of the total mass available to sorption for the different films, which are reported in table 6, it is possible to estimate the coatings sorption ability. Besides the low sorption values due to the dense and non-porous layers, the obtained values are in agreement with the general behavior pointed out above in discussion of the spectra on the Figures 58 and 59.

As a further step a simple kinetic model was used for comparing the adsorption capability of the different films based on the assumption that the time dependence of vapor molecules concentration c(t) into the chamber increases with the time following the relationship:

$$c(t) = c_0 [1- \exp(- t/\tau)],$$

where c_0 is the saturation value (normalized to 1) of benzene concentration and the time constant depends both on the incoming vapor flux and on the number of molecules per second absorbed both by the chamber walls and by the thin film surface.

It is expected that when the film is placed in the chamber, the time constant is higher, with respect to the empty chamber, due to the vapor adsorption at the film surface which delays the filling of the system. In the Table 6, the different time constants calculated by the fitting of the rising curves are reported. The fitting was performed with the use of c(t) equation as the function of the time (reported above); the error bars were evaluated by Origin fitting code.

Sample	Mass of film (g)	Sorption ability (mg_B/g_{film})	τ (s)	τ_{sample}(s)
Empty	-	-	81.23 ± 0.65	-
TM9/1	$2.33 \cdot 10^{-4}$	0.70	107.74 ± 0.64	26.51± 0.91
TM7/3	$1.61 \cdot 10^{-4}$	0.37	86.91 ± 0.63	5.68 ± 0.91
TG9/1	$1.36 \cdot 10^{-4}$	1.19	110.23 ± 0.67	29.00 ± 0.93
TG7/3	$9.09 \cdot 10^{-5}$	0.66	90.77 ± 0.66	9.54 ± 0.93

Table 6. Sorption ability values (calculated at 140 s from the filling curves of Figure 9) for the hybrid films as a function of their total mass. The time constants have been evaluated by fitting the curves with Eq. (1). The values of τ_{sample} are obtained by subtracting the time constant with the sample from the time constant without the sample.

The time related to the sorption capability of the film can be extracted by subtracting the time constant calculated without the sample from the time constant with the sample. The corresponding values are reported in the third column of Table 6.

As it can be observed, the time constant is higher for sample TM 9/1 and TG 9/1 with respect to TM 7/3 and TG 7/3, respectively. Moreover, it is higher for samples TG with respect to samples TM. The results of the kinetic model appear in agreement with the sorption estimation calculated from the data of absorbance difference at 140 s.

Taking into account the structural features evidenced by multinuclear MAS NMR and XRD, it is possible to conclude that favored sorption process takes place on more cross-linked hybrid layers characterized by high extent of interaction between Q and T domains, such as in the case of 9/1 samples. Moreover, the comparison between TG and TM samples also indicates that the sorption process does not take advantage of the small increase in specific surface area found in the case of TM samples, suggesting a mechanism different from the adsorption onto porous materials. Considering the lipophilic behavior of

benzene, the higher interaction with TG samples could be due to the better availability of the interacting sites; indeed the longer glycidoxypropyl chain can probably reduce the steric hindrance effect that can affect the surface of TM samples. Moreover, according to the NMR results, TM samples display a higher content of free silanols that can act as hurdles in the sorption mechanism on the surface.

2.5 Conclusions

Hybrid Sol-Gel layers were prepared by dip-coating technique from hydrolyzed tetrafunctional and trifunctional alkoxysilanes mixtures, changing the organic functional group linked to silicon and the ratio between the precursors. The xerogels derived from the residual Sols were characterized by various techniques in order to highlight structural properties and interactions on the interfaces between organic and inorganic parts. The films were subjected to similar analyses when possible and the results suggested the similarity of the bulk xerogels structural features and the films.

FTIR spectra evidence that structurally different condensed species are forming the hybrid network. The broadness of the siloxane band in all bulk samples suggests the absence of highly ordered architectures in the inorganic matrix, but hints at the randomly organized network. Most importantly, the IR spectroscopy confirms the maintenance of organic group in the final hybrids, which is also confirmed by ^{1}H and ^{13}C MAS NMR analyses.

^{13}C MAS NMR particularly detected the partial epoxy ring opening in TG samples, but, as most valuable, highlighted the extent of hydrolysis for all hybrids, suggesting that both organic function type and the precursor compositional ratio strongly affect the hydroxylation.

^{29}Si MAS NMR was used in order to study the extent of condensation of the hybrid siloxane networks as a function of the composition. Quantitative analysis showed the decrease of degree of condensation from 9/1 to 7/3 samples, but also indirectly suggested that the extent of interaction between Q and T units changes according to the composition.

Synergic use of XRD with NMR fulfilled the characterization and allowed to study in deep the phase interaction in hybrids. It shows that the degree of cross-linking and the

interaction between T and Q domains is influenced by the organic function linked to Si in the trifunctional silane and by the ratio between silica and silsesquioxane phases. The 9/1 samples are more cross-linked and present higher T-Q co-condensation than 7/3 samples.

Two different approaches were combined in order to study in details the sorption ability of selected films, chosen as representative of different cross-linking degree, surface polarity and steric hindrance, depending on the organic functional groups (methyl and glycidoxypropyl).

Despite the different chemical composition, the hybrid samples studied in the frame of this work present specific surface area lower than 1 m^2/g. Consequently, the kinetics of benzene sorption process onto dense hybrid O/I films, studied by optical measurements, appears to be more dependent on the cross-linking degree rather than on the exposed surface of the films. The 9/1 samples are more efficient in the sorption process, which seems also to take advantage of more accessible organic functions as deduced by the comparison between films substituted by glycidoxypropyl and methyl functions. The sorption process is reversible under the used experimental conditions.

As final highlight, prepared hybrid coatings appeared promising in the field of detection and removal of VOCs at low temperatures, possessing the ability to quickly desorb entrapped volatiles. Contrary to meso- and micro-porous inorganic materials they allow tuning not only the microstructure, but also the polarity of the effective coatings surface. Fine adjustments of such hybrids could allow to discriminate between similar compounds and decrease the water sorption phenomenon.

Chapter 3 Nano Building Blocks

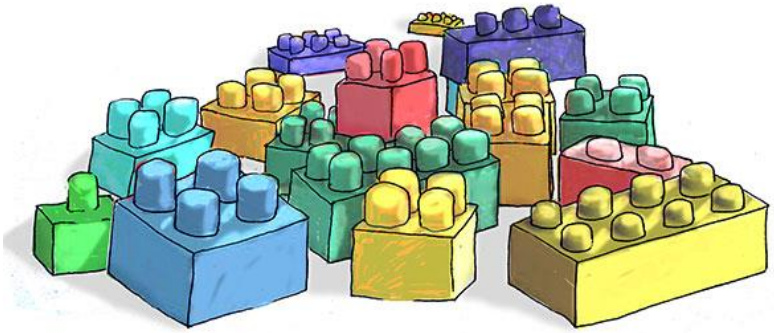

Nano Building Blocks, discussed in this chapter, are pre-condensed nanometric sized species, containing reactive polimerizable ligands and non-reactive functionalities. They can assemble trough their reactive organic groups to obtain Organic - Inorganic hybrid materials with controlled extent of phase interaction, thus allowing the possibility to tune the structure properties relationship [7, 19].

As mentioned in introduction to Chapter 2, Building Blocks are expected to keep their molecular integrity throughout the material formation. This is indeed, the main advantage of the nano building block (NBB) approach, because well-defined structural units usually do not undergo significant structural changes during the material preparation, and consequently the typical properties of these building blocks mainly survive in the final network. Hence, NBB approach allows better structure–property

predictions if compared with the conventional Sol-Gel method where the material precursors are transformed into randomly organized networks (discussed in Chapter 2).

Generally speaking, the NBBs can be either inorganic or organic in nature, but their compatibility with counterparts can be achieved by their surface functionalization.

Prime examples of inorganic building blocks that can keep their molecular integrity are cluster compounds of various compositions. Usually clusters are defined as agglomerates of elements that either exclusively contain pure metals or metals in mixture with other elements. The organic modification of these systems can tailor the clusters interface, making the inorganic core compatible for interactions with the matrix. Furthermore, such building blocks can be designed to give the best performance in the materials' formation, for example enhancing the solubility of inorganic compounds in organic monomers by surface groups showing a similar polarity [3, 4].

Two methods can be used for the synthesis of such surface-functionalized hybrid building blocks: either the surface groups are grafted to a pre-formed cluster ("post-synthesis modification" method) or they are introduced during the cluster synthesis ("in-situ" method) [5]. In the post-synthesis modification, functionalized building blocks are formed in two steps, which are distinctly separate from each other: the inorganic core is formed first, and the functional organic groups are introduced later in a different reaction [3]. An alternative method ("in-situ"), exploited in the frame of this work, is the formation of the hybrid building blocks by the use of poly-functional organically modified metal alkoxydes, that participate in NBBs formation and contain the desired functionality. One limitation is that the organic groups have to withstand the reaction conditions of the cluster core formation. Sol-Gel reactions can occur at mild temperatures, thus they usually do not bring restriction for the majority of potential surface functionalizations [3, 14, 19].

The nature of the interface between organic and inorganic moieties, the connectivity and the functionality of the hybrid Organic – Inorganic NBB are of paramount importance in determining the final structure of the material [7, 14, 19]. If only one reactive function is present, organic polymers with inorganic pendants are obtained, whereas if the functionality is equal to two, linear chains are obtained. In the case it is higher than two, polymerization leads to cross-linked systems as depicted in the following Figure 61.

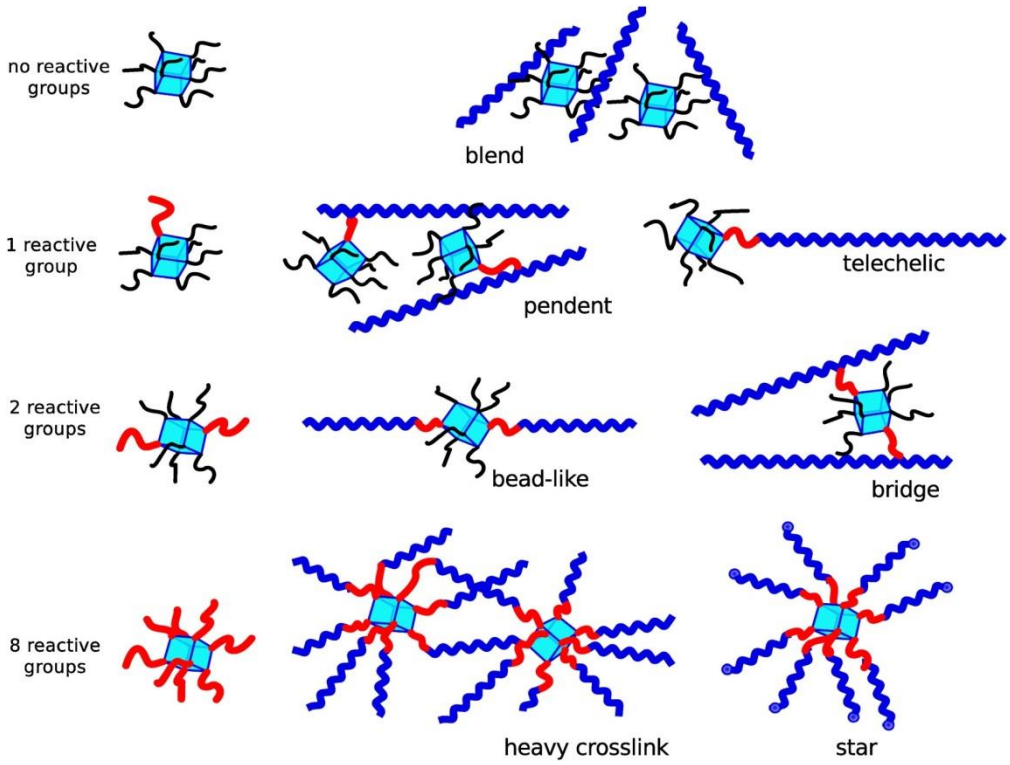

Figure 61. Polymerization pathways for NBBs with various amounts of active functions [7].

In recent years many Nano Building Blocks were synthesized and used for the preparation of hybrid materials. Many future applications, in particular in nanotechnology, focus on a bottom-up approach in which complex hybrid Organic – Inorganic structures are hierarchically formed by these small building blocks [3, 14, 19]. The use of NBBs as starting molecular bricks developed with various systems, which will be briefly discussed in their features and applications in the following section.

3.1 Variety of Nano Building Blocks and their Applications

3.1.1 Polyoxometalates (POMs)

Polyoxometalates discovery dates back to the end of 19th century, when early transition elements of groups 5 and 6, such as V, Ta, Mo, W and Nb were found to form, in their higher oxidation states, polynuclear oxo-anions in aqueous solution under acidic conditions. In the most cases, they are small compact oxide networks based on the sharing of MO_6 structural units (M = Mo, W, or V) and form a peculiar class of clusters with very interesting structure, electronic properties and final use in different fields from medicine to catalysis and magnetic materials [157].

The large number of synthesized POMs can be split in three classes:
a) heteropolyanions, including hetero anions such as SO_4^{2-}, PO_4^{3-} . These represent by far the most explored subset of POM clusters. The most studied are Keggin and Wells-Dawson anions, which are the archetypal systems (Figure 62). In particular W-based POMs are robust and this has been exploited to develop Keggin's derived ions with vacancies that can be systematically linked to larger aggregates using electrophiles [157].

b) isopolyanions, composed of a metal oxide framework, but without the internal heteroatom/heteroanion. These clusters are very unstable with respect to the ones with the "heteropolyanion core". They can be easily functionalized with organic functions through M—O—Si—C bonds, by grafting on lacunar polyoxometalates [7].

c) Mo-blue and Mo-brown, related to the molybdenum blue type species reported by Scheele in 1783. Their composition was unknown until Muller et al. in 1995 reported their synthesis and structural characterization. A long work on the crystallization conditions allowed to obtain the molecule {Mo132}, which has the shape of a giant wheel and is

responsible of the intense blue colour obtained by the reduction of acidified solutions of molybdate (Mo(VI) [7]. This molecule is composed of 132 molybdenum atoms with an inner cluster shell of 60 Mo(V) atoms with icosahedral symmetry arranged like the C60 bucky ball [158] and has 20 nanoscale pores and 20 channels providing access to the inside of the capsule. Incorporating POMs into suitable polymer matrices may increase material processability and long-term stability, as well as thermomechanical properties. Furthermore, and more importantly, the possibility to chemically tailor the composition, structure and functionalities of the inorganic building block and of the polymer matrix pave the way to the obtainment of multifunctional materials [157].

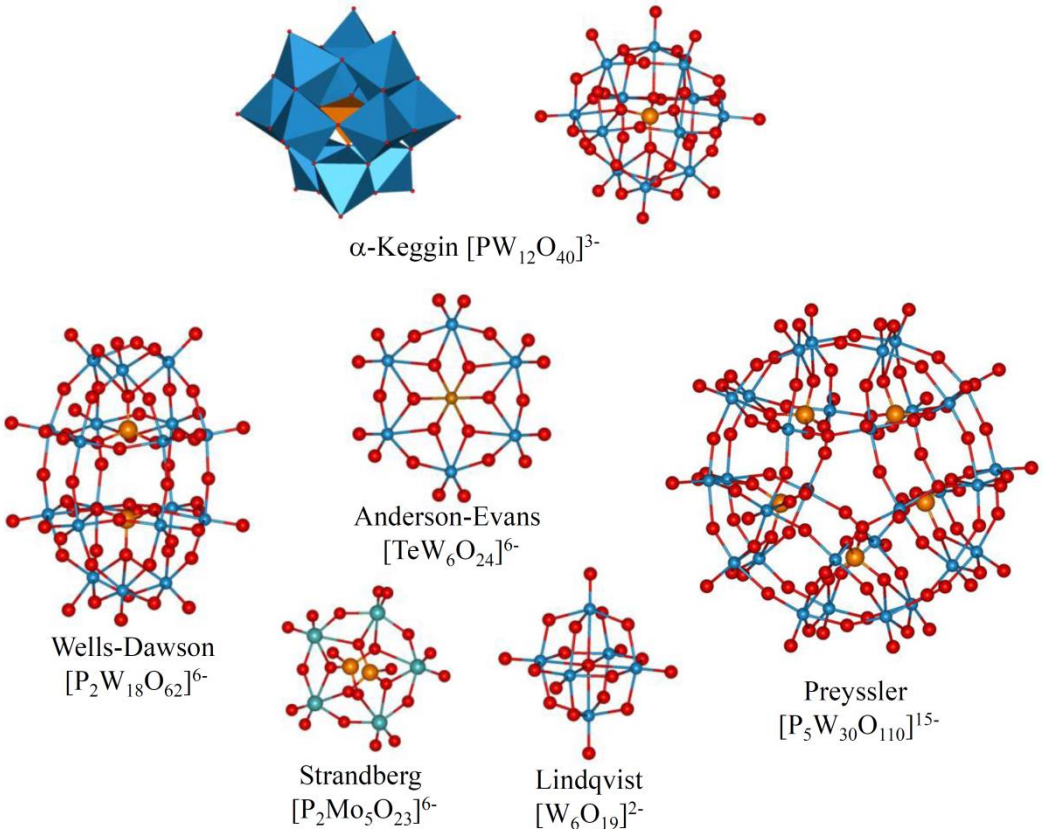

Figure 62. Top: polyhedra (left) and ball & stick (right) representations of α-Keggin polyoxotungstate $[PW_{12}O_{40}]_{3-}$; bottom: ball & stick structures of other representative polyoxometalates. [157].

3.1.2 Metal Oxoclusters

Oxoclusters of early transition metals are a class of polynuclear compounds, typically based on 3–5 groups metal atoms in their highest oxidation state, such as Ti(IV), Zr(IV), Hf(IV), or Nb(V) linked by oxygen bridges and coordinated by organic ligands. They display different nuclearities, coordination number of the metal atoms and connectivity fashions of the metal-oxygen coordination polyhedral [157]. Unlike POMs, these compounds are globally neutral and discrete species, having the general formula $M_xO_y(OR)_z$.

The chemical properties, the tailored synthesis and modification, the structural issues of these oxoclusters, as well as their use as Building Blocks for the preparation of hybrid materials were thoroughly described in some reviews [157, 158, 159]. Because of the presence of several alkoxy groups on the surface, these NBBs exhibit a poor stability in presence of water or nucleophiles (except for titanium ones) [7]. The structure of titanium and zirconium oxo clusters are the most reported in literature and can be used as model systems to understand the construction of hybrid materials, particularly at the organic-inorganic interface. Selected examples of these oxoclusters are depicted in Figures 63, 64.

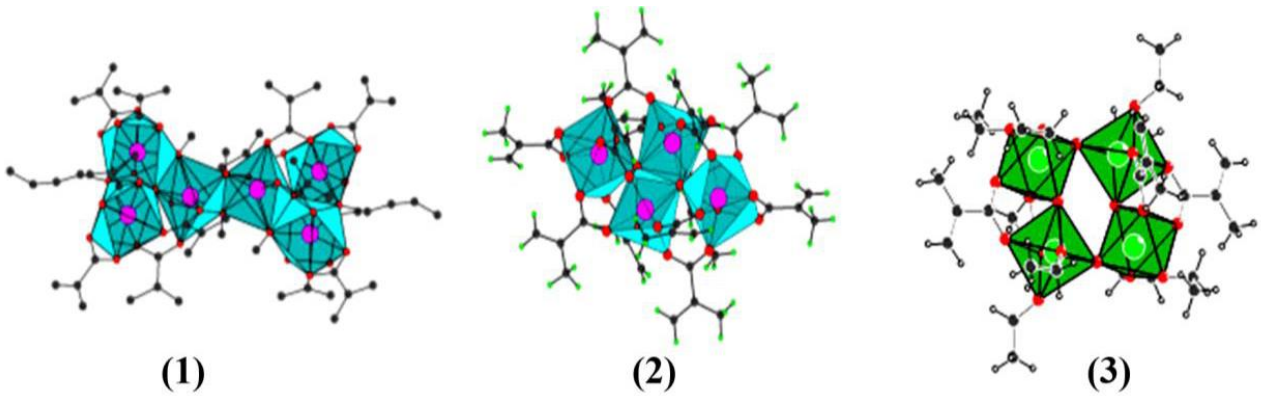

Figure 63. Polymerizable methacrylate (OMc))-functionalized transition metal oxoclusters: (**1**) $Zr_6O_2(OBu)_{10}(OMc)_{10}$; (**2**) $Zr_4O_2(OMc)_{12}$; (**3**) $Ta_4O_4(OEt)_8(OMc)_4$ [157].

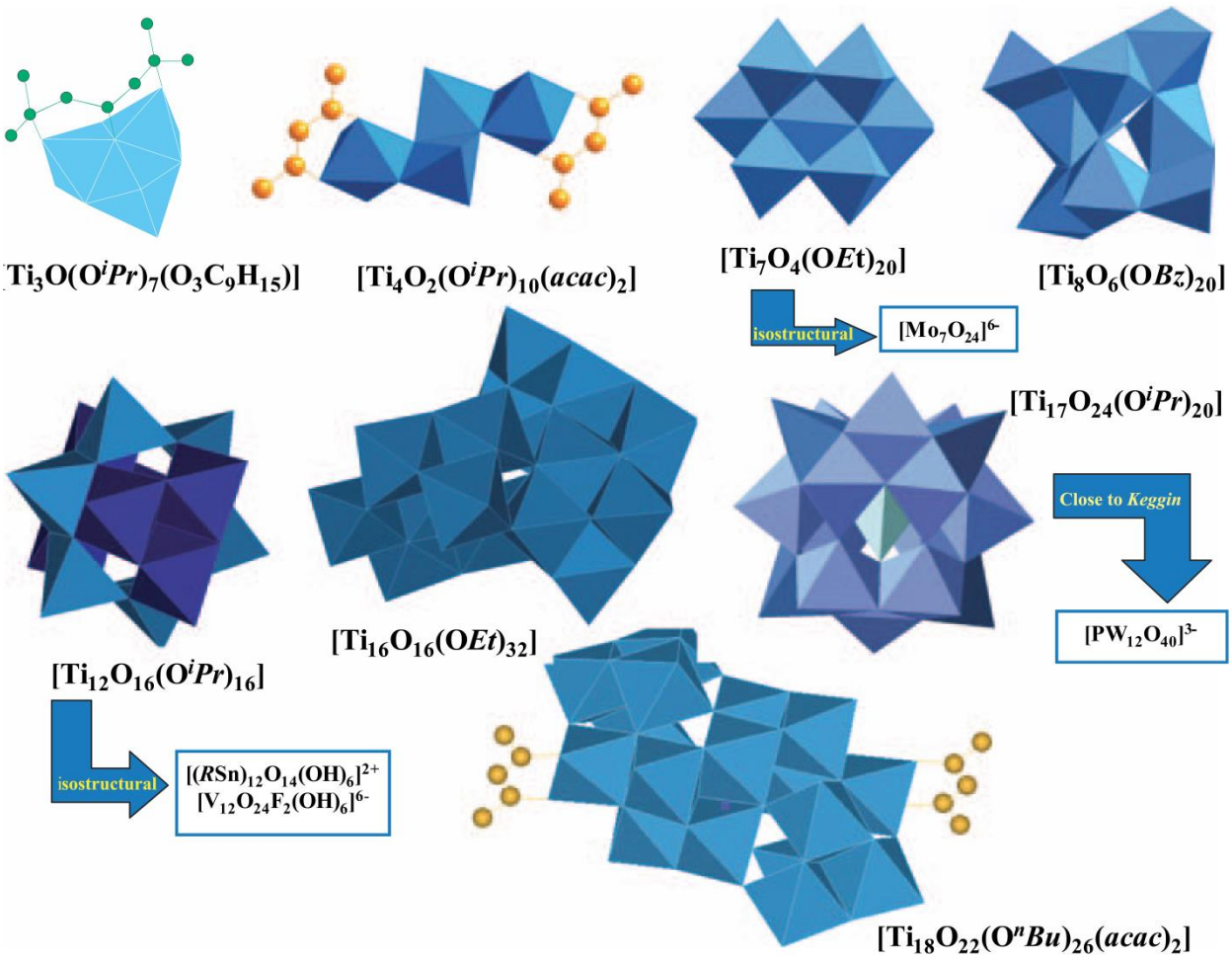

Figure 64. Polyhedral Ti oxo-alkoxy clusters [160].

Literature demonstrates that the chemistry of titanium-oxo clusters is rich, varied, and versatile [157-160]. Indeed these zirconium- and titanium-oxo based NBBs are good models to allow the designed construction of new hybrid organic–inorganic nanocomposites. Better understanding of the stability/lability of the hybrid, and better control of hybrid interfaces can be transferred then to the construction of more complex hybrid materials, which exhibit many interesting properties and applications [20, 160].

3.1.1 Tin-Based NBBs

Tin as silicon is characterized by the high stability of M-C(sp^3) bond, particularly towards nucleophilic attacks. This characteristic offers a strong covalent link between tin-oxo polymers and functionalized organic moieties and, on the other hand, reduces the inorganic functionality of tin favoring the formation of oxo clusters that can be used as NBBs [7, 14]. In 2005 Ribot reported seven new hybrid materials, synthesized by combining a new tin(IV) alkoxo-dimer Nano Building Block [Sn(OPri)2(OMc)2]2 with different organic monomers (Figure 65) [161]. The methacrylate ligands bonded to the tin core permit the copolymerization of the dimer with the organic monomers in such a manner that the tin cores act as cross-linkers of the polymeric chains. The nature of the organic monomer influences the Organic - Inorganic interaction since the more similar groups facilitate the interpenetration of the polymer chains in the tin(IV) aggregates, and thus, improves the quality of the resulting hybrid polymers. Characterization of the physical properties showed that the thermal stability of the materials has improved in all the cases, the more stable being those composed of poly(methyl methacrylate) [161].

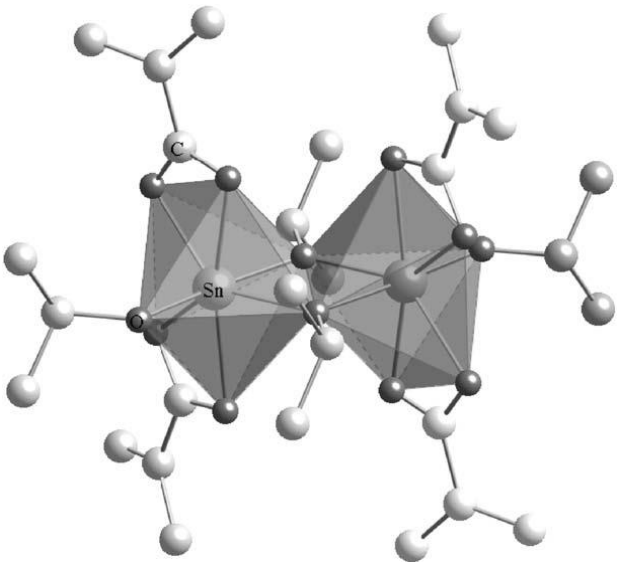

Figure 65. Molecular structure of $[Sn(\mu_2\text{-}OPr^i)(OPr^i)(OMc)_2]_2$ [161]

Consequently, in 2014 [162], the same group reported on the novel tin-based POSS analogue, butylstannoxane dodecamer (Figure 66). It was incorporated as chemically active nanofiller in epoxy resins and demonstrated a considerable anti-oxidative activity already for 0.05 wt% and very high activity for 1 wt% loads. The amino-functionalised nanofiller displayed a high reactivity towards the resin components during the curing step and was very poorly extractable. Interestingly, at elevated temperatures, the stannoxane nanofiller, whose functional substituents are attached by ionic bonds, displayed a considerable short-range mobility in the matrix, and with a nano-phase-separation process, rearranged and polymerized to needle-like nano-domains. This effect leads to additional crosslinking in the nanocomposite. [162]

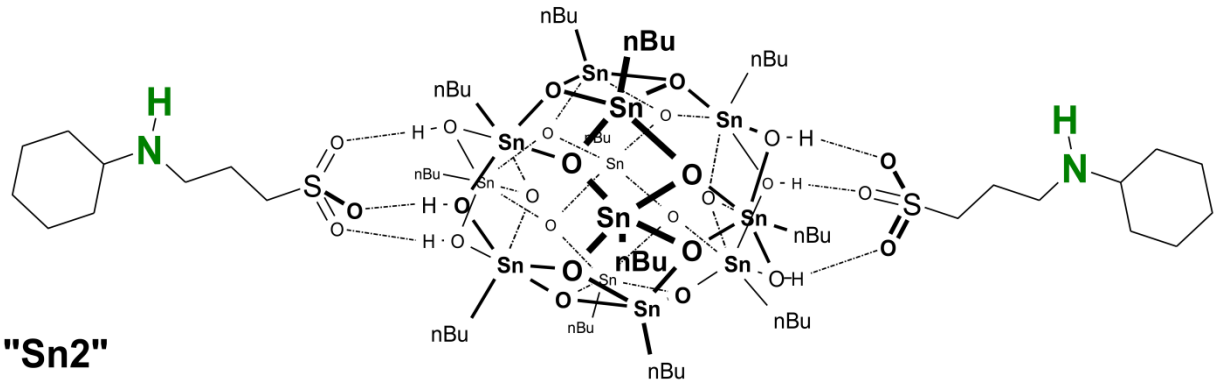

Figure 66. N-butylstannoxane dodecamer with N-cyclohexylamino end groups (Sn2), which was incorporated as a linear unit in epoxy resins [162]

Such a feasible progress did not only offer new building blocks for interesting materials, but induced the development of characterization techniques, which can be applied to other types of NBBs and help analysis of interactions on the Organic – Inorganic interfaces.

3.1.2 Silicon-Based Nano Building Blocks

Silicon-based NBBs are probably the most interesting building blocks for the preparation of hybrid materials, since they offer a large possibility for organic functionalization thanks to the stability of the Si-C bond. Generally, they correspond to cage structures of common formula $(RSiO1.5)_n$, with n ranging from 6 to 18 [7, 163], known as polyhedral oligomeric silsesquioxanes - POSS (Figure 67).

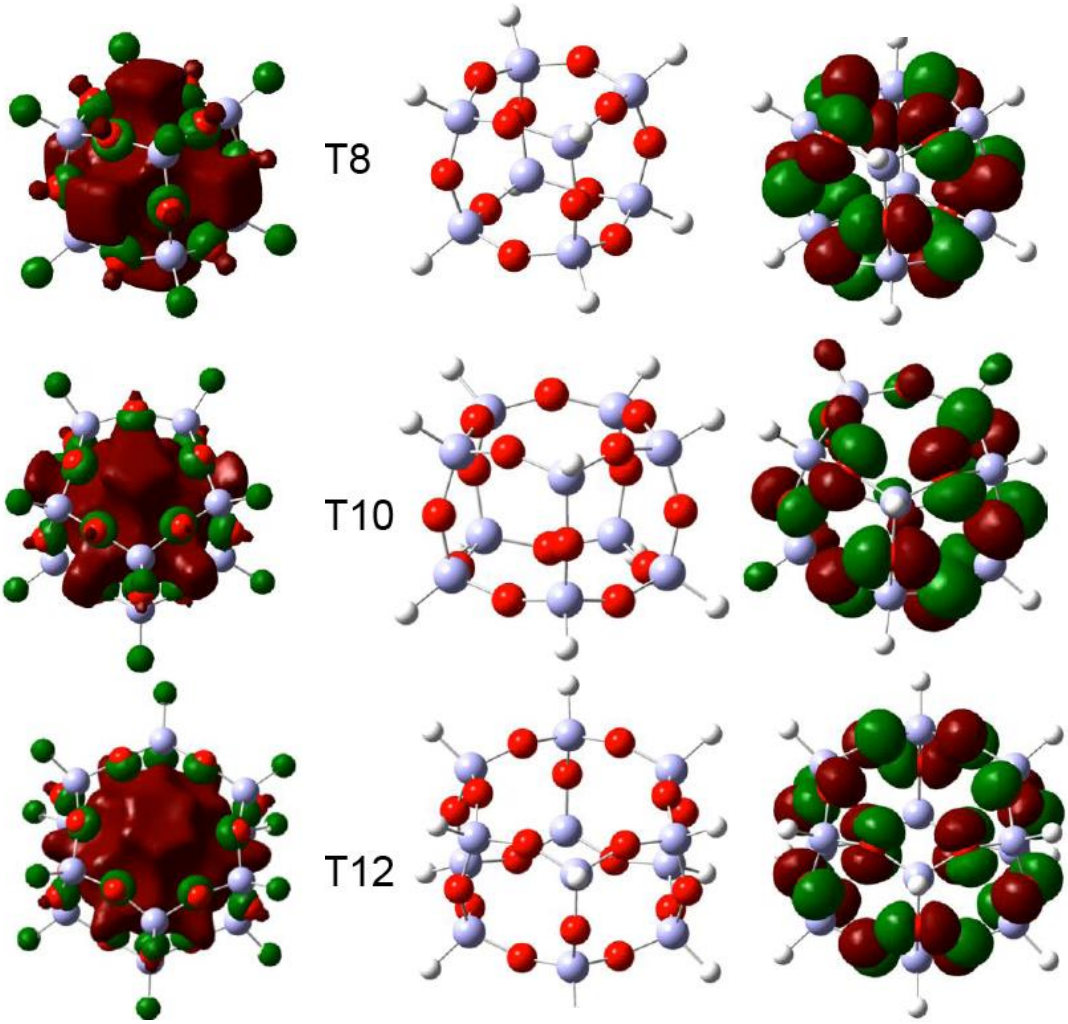

Figure 67. Molecular structures and electron density incontours of some cage-like polysilsesquioxanes (POSS). HOMO – LUMO representations [163]

The term silsesquioxane denotes that each silicon atom is connected to three oxygen atoms. The prefix “oligo” is often used to indicate a small number of silsesquioxane links and the prefixes “octa-, penta-, deca-, etc” are used to indicate a specific number of these links. POSS are also commonly abbreviated as T^m_n (T is the designation for a silicon bearing three oxygen atoms, n is the number of silicon atoms present in the cage, m is the number of oxo-bridges). Figure 68 [164] represents some similar to POSS, but not fully condensed frameworks, which also can be used as nano-bricks precursor for hybrid materials preparation.

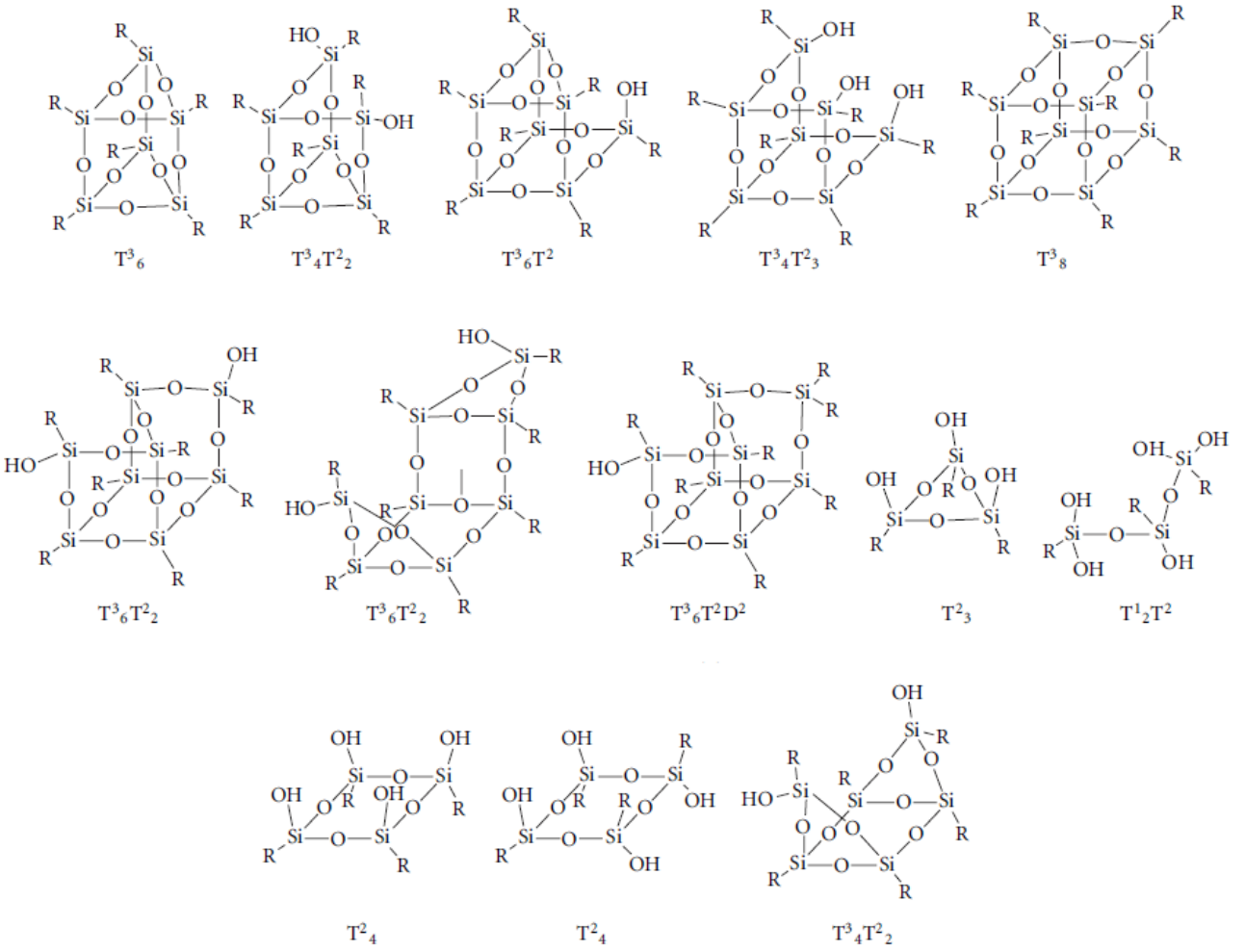

Figure 68. Some possible structures of oligosilsesquioxanes. Silanol groups (Si–OH) offer further condensation possibilities for such Building Blocks to form hybrid materials.

Oligomeric silsesquioxanes were reported for the first time in 1955 by Sprung and Guenther who identified as T_8 and T_6 structures the small amounts of white precipitate that they observed while performing polymerization reactions of alkyltriethoxysilanes [30]. Since then, the knowledge of this family of inorganic-organic hybrid compounds and the range of their applications have grown steadily.

Due to the huge choice of the R-groups, oligomeric silsesquioxanes can be soluble in many organic solvents. This property is important for most of their applications, including those related to catalysis [3, 30]. The applicability of oligomeric silsesquioxanes has been initially hindered by their time-consuming synthesis, which for some structures could require months to achieve moderate product yields [165 a)]. However, the synthesis methods have been much improved through the years and many types of silsesquioxanes can now be synthesized in good yields in a matter of days [165 b)]. This also prompted the commercial production of oligomeric silsesquioxanes, and a variety of structures are available for purchase nowadays.

The range of applications of oligomeric silsesquioxanes is vast, highlighting the versatility of these compounds. Silsesquioxane-containing materials have found uses in catalysis and as model compounds for silica-based materials, as thermoplastics and thermosets, as flame retardants, as electrolytes, in electronic and photonic devices, in cosmetics, as ionic liquids, and as materials for biological and medical applications [3, 4, 5, 14, 30, 165, 166, 167].

The reports concerning synthesis and applications of oligo- and poly-silsesquioxanes are too numerous to mention them all, however some of the most interesting are reported in the following paragraphs.

3.1.2.1 NBBs derived porous materials

With an appropriate tuning of porous properties, NBBs - derived monolithic materials have a wide variety of flow-through applications, excellent integrative features, and are the materials of choice for related engineering applications. Such porous adsorbents that combine the desirable properties of a permanent high surface area and porous structure (as found in inorganic silica-based monoliths), with the tuning of chemical behavior by the presence of the organic functional groups (as for polymer-based scaffolds), were prepared based on a vinylsilsesquioxane cage mixture (vinyl-POSS) and reported in [168]. Similar concept was applied for liquid chromatographic separations [169], where caged silsesquioxanes with long chain alkyl groups have been used to silylate and tailor the surface characteristics of stationary phases and for extraction of components of interest.

3.1.2.2 Adsorptive thiol- rich NBBs

Extremely “hot” topic, where the benefits of polysilsesquioxanes NBBs can be demonstrated concerns their capacity of being pollutants scavengers. Ecological problems including that of heavy metal removal from aqueous solutions are objects of permanent concern for scientist in many countries. Adsorption is one of the good alternatives available for such situations. In this context, a new modified oligosilsesquioxane was prepared and evaluated for its heavy metal adsorption characteristics from aqueous solution in [170]. Batch and column experiments were conducted to investigate Fe (III), Cr (III), Cu (II), Cd (II), Pb (II) and Ni (II) removal from dilute aqueous solution by adsorption onto modified oligosilsesquioxane. The results obtained in the flow experiments, showed a recovery of ca. 100% of the metal ions adsorbed in a column packed with 2.0 g of nanomaterial. The use of NBBs presents great advantages for adsorption of

transition-metal ions, due to the large adsorption capacity, the great stability, reutilization possibility, rapidity in reaching the equilibrium and mechanical resistance.

Thanks to recent advances in ^{13}C and ^{29}Si CP MAS NMR characterization techniques [171, 172], which were applied to various forms of thiol - functionalized mesostructured silica in their examination as candidates for mercury removal, the possibility to analyze the activity of thiolates in pollutants adsorption has increased. Armed with such powerful characterization techniques, the group of Song modified mesoporous ZMS (SBA-15) using POSS with sulfhydryl terminal groups (-SH) post-modified by sulfonic acid terminal groups as adsorption active groups [173]. The POSS-SH - modified ZMS showed higher efficiency in removing NH_3-N in drinking water than the unmodified materials.

In another very recent study, a thiol-rich polyhedral oligomeric silsesquioxane (POSS-SH) has been used for the adsorption and pre-concentration of mercury species [174]. Mercury and its derivatives exist widely in the environment, including atmosphere, water, soil and plants. The high toxicity of mercury has gained extensive attention due to its accumulation effect in many circumstances. It is well known that the toxicity of mercury depends strongly on its speciation [174]. Organic mercury is more toxic than its inorganic counterpart due to its high bioaccumulation factor in the food chain, and it tends to cause serious damage to nervous system of mammals. In this respect, the effective removal of the different mercury species from water bodies is highly necessary. It was shown by W. Wang, that the presence of thiol groups in the POSS-SH framework structure exhibited strong affinity for mercury and provided a favorable adsorption efficiency and capacity for both Hg^{2+} and CH_3Hg^{+}. The adsorbed mercury species were recovered by thiourea in hydrochloric acid and quantified with atomic fluorescence spectrometry.

3.1.2.4 Thiol-functionalized NBBs and thiol-ene “click”

A very different approach to exploit mercapto-functionalized POSS and other poly- and oligosilsesquioxanes is inspired by the magic of thiol-ene “click” reaction. This reaction is well documented in the literature as proceeding at rapid rates while being not inhibited by oxygen, releasing no by-products, and requiring no solvents to attain quantitative conversions [175]. Moreover, the thiol-ene reaction mechanism proceeds through a series of alternating propagation and chain transfer events prior to termination that makes the reaction very attractive.

In the frame of pollutants removal and thiol-ene “click”, He et al. reported on nanomagnetic POSS incorporated with dithiol organic anchors [176]. A functionalizable organosiliceous hybrid magnetic material was constructed by surface polymerization of octavinyl POSS on Fe_3O_4 nanoparticles. The resultant Fe_3O_4@ POSS was identified as a mesoporous architecture with an average particle diameter of 20 nm and high specific surface area. Afterwards, it was tethered with an organic chain containing dithiol via thiol–ene addition reaction. The ultimate material slightly decreased in specific area with almost identical porous morphology. It turned out to be a convenient, efficient single adsorbent for simultaneous elimination of inorganic heavy metal ions and organic dyes in simulated multicomponent wastewater at ambient temperature. Importantly, the Fe_3O_4@POSS-SH nanoparticles could be readily withdrawn from aqueous solutions within a few seconds under moderate magnetic field and exhibit good stability in strong acid and alkaline aqueous matrices. Contaminants-loaded Fe_3O_4@POSS-SH could be easily regenerated with either methanol–acetic acid mixtures (for organic dyes) or hydrochloric acid (for heavy metal ions) under ultrasonication. The renewed one kept appreciable adsorption capability towards both heavy metal ions and organic dyes, and the removal rate for any of the pollutants exceeds 92% , after repeated use for 5 cycles, on simulated

wastewater with several pollutants. This appears to be a highly flexible route concerning POSS, as for well-tailored functionalized magnetic porous materials for various applications in which anticipated multifunctions, as well as high surface areas are required.

One of the brightest examples of exploiting thiol-ene “click” reaction focuses on dental impression material design and synthesis. Enticed by the limited bonding ability of sulfur, which leads to less volumetric shrinkage in the thiol-ene polymerization, the group of Cole synthesized and evaluated rapid set elastomeric dental impression material [177]. Thiol-functionalized Siloxane-based systems prepared utilizing radical-mediated technique demonstrated faster setting times with stronger hydrophilic characteristics in the unset period and hydrophobic characteristics when set than leading polyvinylsiloxane materials. More importantly, NBBs cured by the thiol-ene reaction displayed highly accurate detail reproduction, and in the presence of greater mechanical strength that would be achieved through variable filler loading, would prove a superior impression material in clinical dentistry.

Chen also recently exploited “click” reaction for a one-step approach preparation of organic–inorganic hybrid monoliths [178]. After vinyl-functionalized organic monomers and azobisisobutyronitrile (AIBN) were mixed with hydrolyzed tetramethoxysilane (TMOS) and 3-mercaptopropyltrimethoxysilane (MPTMS), the homogeneous mixture was introduced into a fused-silica capillary for simultaneous polycondensation and “thiol-ene” click reaction to form the organic-silica hybrid monoliths. Compared to previous methods, the approach developed by the group shows simpler, more efficient and time-saving preparation procedure. Two different types of organic-silica hybrid monolithic column were successfully prepared by this approach. Both monoliths exhibited favorable domain size, desirable functionalities, and excellent column efficiency and hydrophilic interaction

chromatographic separation resolution, representing a new option to prepare a variety of organic-silica hybrid monoliths with desirable functional groups.

Many researchers used the thiol-ene reaction in the frame of “graft onto” strategy for preparation of novel NBBs. A new oligosilsesquioxane species functionalized by eight trimethoxysilyl groups bonded through a thioether bridge to the Si-atoms of the silsesquioxane cage, having 24-hydrolysable alkoxy groups was synthesized by Rozga-Wijas [179]. A similar cage oligosilsesquioxane with mixed vinyl and trimethoxysilyl functions and many others were also generated. All these compounds are new NBBs, which can play a role of precursors for silicon-based materials.

Another valuable example demonstrates the use of photochemical induction of thiol-ene reaction [180]. New dendrimers derived from cages silsesquioxanes were acquired, where a large number of external branching sites on the core lead to high concentrations of dendrimer branch ends. The method appears extremely facile and can help in fast and efficient desired organic modification of well-defined POSS.

3.1.2.5 NBBs based Nanocomposites

The idea of Si-based NBBs incorporation to the polymer matrix to acquire nanocomposites intrigued many researchers since long ago. Compared to traditional composites, such as glass fiber reinforced polymers, the extent of the interface between the matrix and the inorganic phase is much larger in such nanocomposites leading to a strong improvement of filler-polymer interactions. Hence, the amount of Nano Building Blocks introduced in the matrix can remain very small to show large effects on the overall materials properties [4]. Recent advances in this field are aimed on the understanding and smart use of interactions on the component interfaces. Since the key points of

nanocomposite's properties were discussed already in the introduction, some highlights only will be reported below.

Among the different fillers, SiO_2 is commonly used in the tire industry to enhance the static and dynamic mechanical properties, to improve the tear strength and the abrasion resistance and to reduce the rolling resistance of the tires [181]. The reinforcement effect of silica in rubber composites strongly depends on the filler-rubber and filler-filler interactions, which determine the formation of a percolative filler network in the rubber matrix, essential for providing effective reinforcement [182, 183]. These interactions depend on the particle size and shape, on the surface characteristics of the filler as well as on the chemical nature of the polymer and on the extent of the Organic - Inorganic interface. Recently, it was also demonstrated that particle anisotropy and alignment could provide, beside an increase of the filler-filler interactions, a relevant percentage of immobilized elastomers leading to a higher reinforcement [184].

In this frame, in the last years it has been reported that even small loading of POSS nano-units [185, 186] with tailored morphology, incorporated into different polymers, strongly improves their mechanical properties. Li et al. studied the effect of inter- chain interaction on the compatibility using POSS as a pendant moiety attached to the polymer main chains. The study was devoted to the comparison of miscibility behavior for two different POSS copolymers and the corresponding homopolymers [187]. The review by Ayandele discusses the influence of the incorporation of POSS into polymer matrices via chemical cross-linking or physical blending on the structure of nanocomposites, as affected by surface functional groups, and the POSS concentration [188]. The group of Matejka continuously studied electrical and thermomechanical properties of epoxy-POSS nanocomposites and demonstrated, that the glassy epoxy-POSS nanocomposites based on DGEBA-Laromin network represent promising insulation material for electrotechnical applications. The electrical properties of those POSS-containing hybrids were closely

related to the morphology [189]. Lately, they elucidated the POSS effect on mechanical properties by using theoretical methods applying the theory of network formation, the theory of rubber elasticity and the model of mechanical properties of the particulate composites [190]. Very recently, Wang reported on UV-curable epoxy acrylate modified with octamercaptopropyl-POSS (OMP-POSS). This material was prepared via thiol-ene photopolymerization approach and provided protective effects on the carbonaceous char [191]. The further study of modified char combustion indicated, that such nanocomposite displayed both the slower heat release rate and lower total heat release. The overall progress in POSS related polymer nanocomposites synthesis and applications are very well revised in [192], [193(2015)] and [194(2015)].

3.1.2.6 Ladder-like polysilsesquioxanes NBBs

Ladder-like polysilsesquioxanes (LPSQ), which are shaped by inorganic double-chained backbone, have attracted considerable interest because they possess excellent thermo-resistant and mechanical properties, as do POSS. As already discussed, in nanocomposites the enhancement of properties depends largely on the shape and distribution of the nanofiller. Hence, tunable aspect ratio in LPSQs backbone, as well as enhanced mechanical properties and thermal stability compared to usual linear polysiloxane make ladder-like polysilsesquioxanes very strong competitors to POSS in nanocomposites applications.

Since the first trials in 2001 by Li et al. [195], in evaluation of both epoxy/POSS composites and epoxy/LPSQ, a lot of synthesis and characterization of such NBBs took place. After synthetic advances of Unno [196] and Handke [197], the functional ladders were successfully incorporated in polyimide by Gao [198].

3.2 Synthesis and Characterization of thiol-functionalized NBBs

In the following section, the results obtained by the controlled hydrolysis-condensation process applied to 3-mercaptopropyltrimethoxysilane, with the aim of growing thiol-functionalized oligosilsesquioxanes, will be presented.

In the conventional sol-gel method, based on hydrolysis-condensation of molecular precursors by water addition, which was exploited for the Hybrid Networks preparation discussed in Chapter 2, the major problem was the poor ability in controlling the reaction rate, resulting in a poor control of the microstructure of the final material. An alternative strategy is the in-situ water production (ISWP) route. The main advantage of this approach is the possibility to control the sol-gel reactions rate and the structure of the final products by controlling the water production, which is generated directly into the reaction medium. The in-situ water production (ISWP) exploits an esterification reaction, where both the amount and the kinetics of water produced can be properly tuned.

3.2.1 Precursors

The choice of 3-mercaptopropyltrimethoxysilane (McPTMS)(Figure 69) as starting precursor was in favor of suitability of -thiol function for the different applications described above[165-200]. Such applications require particular control of availability and reactivity of –SH functions in final hybrids. McPTMS was purchased from ABCR and used without further purification.

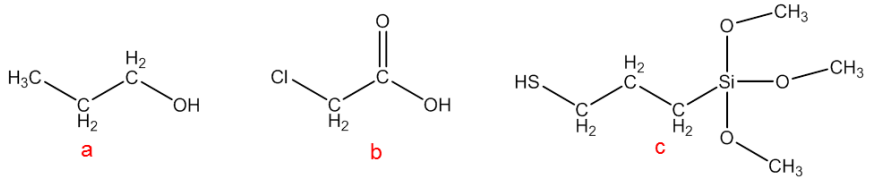

Figure 69.:Reagents from left to right: 1-PrOH (a), ClAA (b), McPTMS (c).

Thiol-functionalized NBBs were synthesized by sol-gel chemistry via the in-situ water production (ISWP) approach, exploiting the esterification reaction of chloro-acetic (ClAA) acid and 1-propanol (1-PrOH) (Figure 69). Both reagents were obtained from Sigma Aldrich and ClAA was used as-received, whether 1-PrOH was dried before use following standard procedures [201]. The choice of ClAA and 1-PrOH for water production relies on comparative study of various acid-alcohol pairs efficiency and influence on the cross-link architecture of silsesquioxanes in ISWP production route, reported by Tagliazucca [202]

Two different catalysts were exploited as alkoxysilanes condensation promoters: trifluoroacetic acid (TFA) and dibutyldilauryltin (DBTL)(Figure 70). DBTL catalytic performance in conventional Sol-Gel systems was discussed in [203, 204] and TFA was used for non-hydrolytic alkoxysilanes condensation in [205]. Both catalysts were purchased from ABCR and used as-received.

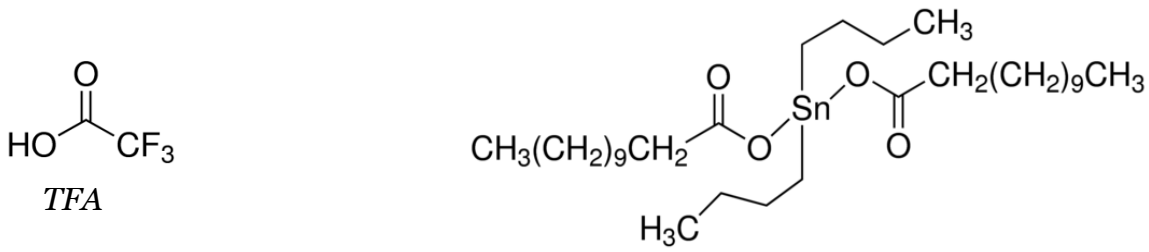

Figure 70.: Catalysts used in Sol-Gel reaction: (left) trifluoroacetic acid (TFA) and (right) dibutyldilauryltin (DBTL).

Deuterated solvents, for Liquid State NMR analyses were tetrahydrofuran (THF-d8), chloroform ($CDCl_3$) and water (D_2O); THF was also employed as mobile phase in Gel Permeation Chromatography. All the reported reagents were obtained from Sigma-Aldrich and used as-received.

3.2.2 Synthesis route and procedures

3.2.2.1 ISWP route

For the preparation of functionalized Si-based nano-building blocks the Sol-Gel process was employed under strictly controlled conditions. As the group of Dire reported recently, the in-situ water production (ISWP) by means of the esterification reaction of a carboxylic acid with an alcohol gives the opportunity, using different acid/alcohol mixtures, to tuning the condensation degree of silsesquioxanes derived from diphenylsilanediol / methacryloxypropyltrimethoxysilane (DPDO/MPTMS) mixtures [202]. The pK of the carboxylic acid used in the esterification reaction has a valuable influence on the silanes cross-linking ability. In general, acids with low pK values and heteroatoms substituents favor the silane hydrolysis and allow the growth of high molecular weight species. On the contrary, using the acetic acid/ethanol mixture leads in the case of DPDO/MPTMS to a narrow distribution of silsesquioxane species [202].

The esterification reaction exploited in this work for NBBs synthesis between a chloroacetic acid and 1-propanol, according to the equation

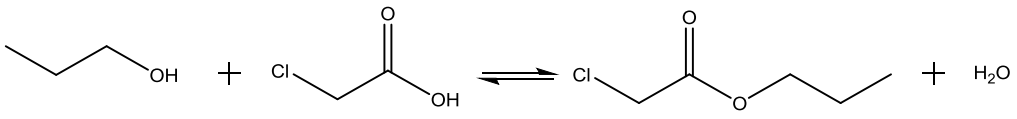

(a)

provides in-situ water, required for the hydrolysis-condensation of the McPTMS. The water availability depends on the kinetics of the reaction (**a**), which is also affected, apart from the other factors, by the reaction temperature conditions. Since the nature of alkoxy groups of 1-propanol and McPTMS is different, the following equation

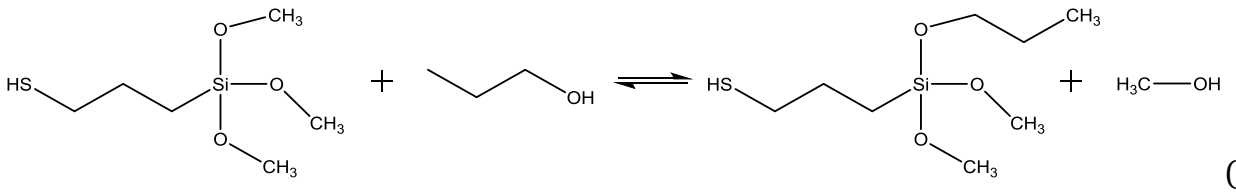

(b)

governs the trans-alcoholysis reaction, where the newly produced methanol participates in following

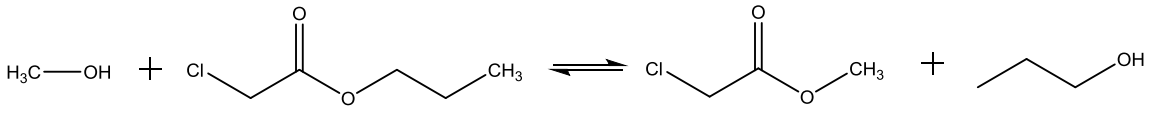

(c)

transesterification reaction (c). All three reactions are simultaneous and related by reagent-products interaction, thus the water production kinetics of such a system is expected to have a quite complex influence on the growth of silsesquioxane NBBs.

Apart from influence of the hydrolytic conditions, the knowledge of role of different catalysts is also a fundamental issue in order to get insight in the growth mechanism of silsesquioxanes. Influence of both factors in the conventional sol-gel polymerization of glycidyloxy-propyl trimethoxysilane by water addition was recently investigated by Matejka et al. [206] using different catalysts and hydrolysis ratio. It has been shown that glycidyloxy-propyl trimethoxysilane polymerization is dominated in the early reaction stage by non-random cyclization and the further growth occurs by combination of partially condensed cages; the increase in cages yield is observed with increasing the hydrolytic ratio. However, since the preparation conditions are different in conventional Sol-Gel process and ISWP approach, a deepening on the effect of synthesis parameters on the silsesquioxane growth is required for the ISWP route.

In order to clarify the relative effect of each of the factors, the silsesquioxane growth was studied in two steps. Firstly, the different catalysts and hydrolysis ratio influences were analyzed applying for all compositions the same synthesis protocol with fixed

temperature and reaction time conditions. Secondly, the chosen catalyst and the esterification reaction parameters were fixed and the NBBs growth kinetics was studied under different temperature conditions as a function of reaction time. Such approach allowed fine tuning of all the conditions to yield in desired oligomeric structures.

3.2.2.2 Synthesis procedures

One-pot synthesis of the thiol-functionalized silsesquioxanes was performed starting from McPTMS by means of the ISWP Sol-Gel process, changing the catalysts and amount of water available from esterification reaction. All procedures were carried out in nitrogen atmosphere.

3-Mercaptopropyltrimethoxysilane was diluted in 1-propanol in a two-neck flask equipped with a condenser; different amounts of chloro-acetic acid and 1.5 mol% (calculated respect to Si) of the condensation promoter (either DBTL or TFA) were added to the solution under vigorous stirring. The molar ratio between 1-propanol and chloro-acetic acid was fixed to 1:3.

Sample label	Catalyst	r=ClAA/McPTMS, (molar ratio)	Sample label	Catalyst	r=ClAA/McPTMS, (molar ratio)
DBTL1	DBTL	1	TFA1	TFA	1
DBTL1.5	DBTL	1.5	TFA1.5	TFA	1.5
DBTL3	DBTL	3	TFA3	TFA	3
DBTL6	DBTL	6	TFA6	TFA	6

Table 7. Samples labeling and synthesis parameters.

Table 7 reports the labeling of the prepared samples, the employed catalyst and the molar ratio r between ClAA and McPTMS. The clear solutions were refluxed at 100°C under stirring for 24 h. Afterwards, the side-products were removed under vacuum at 50°C for 1 h and at 70 °C for 30 min, until a constant pressure of 10^{-2} torr was reached, and transparent yellowish viscous oils were obtained.

3.2.3 Characterization Techniques

3.2.3.1 Fourier Transformed Infrared Spectroscopy (FTIR)

The FT-IR spectra of NBBs were recorded on a Thermo Optics Avatar 330 instrument, in transmission mode in the range 4000 to 400 cm^{-1} using KRS-5 windows (64 scans, 4 cm^{-1} resolution).

3.2.3.2 Gel Permeation Chromatography (GPC)

GPC traces were recorded with a Knauer system equipped with Smartline Pump 1000 and RI detector 2300, using Polymer Laboratories-Varian PLgel 5 mm MIXED-C columns (7.5 x 300 mm). The samples were dissolved in THF at a concentration of 0.5 wt%, injected (20 μl) and pumped through the columns with a flow-rate of 1 $ml*min^{-1}$. The calibration curve was obtained using polystyrene standards (Polymer Laboratories) with M_w in the range 580 – 100,000 Da. The GPC traces of the different samples were compared using as reference the solvent peaks.

3.2.3.3 Nuclear Magnetic Resonance (NMR)

3.2.3.3.1 NMR for tuning the catalysts and hydrolysis ratio

Multinuclear liquid state NMR analyses were carried out on a Bruker 400WB instrument with a carrier frequency of 400.13 MHz (^{1}H), equipped by BBO probe. Samples were diluted in d8-toluene in 5mm quartz tubes The chemical shifts are referenced to tetramethylsilane (TMS).

The ^{1}H NMR spectra were collected using the following parameters: single pulse sequence with π/2 pulse length of 10 μs, recycle delay of 10 s, 16 scans;

^{29}Si power gated single pulse sequence with π/2 pulse length of 5.6 μs, recycle delay of 20 s, proton decoupling for 80 μs with waltz16, 1k scans. $Cr(acac)_3$ (5 mmol) was added in order to shorten the ^{29}Si relaxation time. The silicon units are labeled according to the NMR notation: $T^{m}_{n}[x]$ (T is the designation for a silicon bearing the three oxygens, n is the number of units in the silsesquioxane structure, m is the number of oxo-bridges and x represents the number of linked –OH groups).

3.2.3.3.1 NMR for NBBs growth kinetics

Solution NMR spectra were collected on a Bruker Avance 400WB instrument applying a carrier frequency of 400.13MHz (^{1}H) equipped by BBO- 10 probe. Samples were were analyzed as prepared non-invasively in 10mm pure silica NMR sample tubes with a central 3 mm filled with D_2O capillary inserted for the lock. The chemical shifts are referenced to tetramethylsilane (TMS).

^{1}H NMR spectra sequence were collected using single pulse with π/2 pulse length of 9.8 μs, recycle delay of 7.44 s, acquisition time 2.55 s, 16 scans;

^{1}H DOSY NMR spectra were recorded on a Bruker Avance 250 (250.13 MHz) equipped with a Bruker BGU z-gradient unit providing a maximum gradient strength of 51 G cm^{-1}. Tubes of 5 mm diameter with THF-d8 as solvent were used. Experiments were performed, at 25 ^{o}C, using a pulse sequence with shaped gradient pulses of amplitude. The amplitude of the field gradient was varied from 0.5 to 48 G cm^{-1} over 32 increments, while the eddy current delay was fixed at 5 ms. The diffusion delay and the gradient pulse duration were set to 200 ms and 14 ms, in order to achieve an intensity attenuation range of about 95%.

Spectral deconvolution was performed with the Dimfit software, version dmfit#20111221, available from http://nmr.cemhti.cnrs-orleans.fr/dmfit/. The Voigt approximation with Gaussian-Lorentzian sum function was used to fit and separate spectral peaks. Variable parameters were: wavenumber, peak intensity, line broadening and Gaussian-Lorentzian ratio.

^{29}Si NMR SP spectra were collected with power gated single pulse sequence with π/2 pulse length of 13.9 μs, recycle delay of 10 s, proton decoupling for 100 μs with waltz16, acquisition time 0,7 s.

^{29}Si DEPT (distortionless enhancement by polarization transfer) pulse sequence was used for shortening the acquisition time with delay of 20ms, 3rd ^{1}H pulse of 24°, recycle delay of 5 s, J(Si-H) of 9. Spectra with a good signal-to-noise ratio were obtained in 30 min, allowing to properly monitor the species along the ageing time.

3.2.3.4 MALDI-TOF mass spectrometry

MALDI-TOF measurements were performed on Bruker Daltonics Ultraflex MALDI-TOF-TOF mass spectrometer (Bruker Daltonics, Bremen, Germany) equipped with a reflector unit. The acceleration voltage was set at 20 kV. For desorption of the components, a nitrogen laser beam (λ = 337 nm) was focused on the template. The laser power level was adjusted to obtain high signal-to-noise ratios, while ensuring minimal fragmentation of the parent ions. All measurements were carried out in the delayed extraction mode, allowing the determination of monoisotopic mass values (m/z; mass-to-charge ratio). After crystallization at ambient conditions, positive ion spectra were acquired in the reflectron mode, giving mainly sodiated adducts ([M + Na]+). Samples dissolved in acetonitrile were directly applied onto the stainless-steel plate as 1 μL droplets, followed by the addition of 1 μL of α-Cyano-4-hydroxycinnamic acid (HCCA) matrix solution. Every mass spectrum represents the average of about 100 single laser shoots.

3.3 Tuning the Catalyst and Water ratio: Results and Discussion

The reactivity of 3-mercaptopropyltrimethoxysilane is relatively poor if compared to diphenylsilanediol/methacryloxypropyltrimethoxysilane precursors, applying similar synthesis conditions and exploiting acetic acid/ethanol mixture for ISWP [202]. Thus, the use of a different acid/alcohol mixture (chloroacetic acid/1-propanol) and increase in the reaction temperature were required for promoting the hydrolysis-condensation process. For evaluating the influence of the water provided by the esterification reaction on the degree of cross-linking and architecture of the resulting products, different amounts of ClAA were added to the McPTMS solution in 1PrOH, according to the ratio r reported in Table 1, keeping constant the molar ratio between carboxylic acid and alcohol. Considering the low condensation ability of McPTMS, a catalyst was also added to the reaction mixture. Either trifluoroacetic acid or dibutyldilauryltin were used as condensation promoters. Since the catalytic active species for DBTL is supposed to be a stannasiloxane [207], the structural development of the silsesquioxanes might differ from that achieved with strong acidic catalysts as TFA (pK=0.23).

The molar ratio between ClAA and McPTMS was changed between 1 and 6, in order to study the sol-gel reactions both in under-stoichiometric and over-stoichiometric hydrolytic conditions in the presence of the two different catalysts. The solutions, after reacting for 24 h at 100°C, were dried in vacuum and the obtained oily liquids were investigated by different characterization techniques.

3.3.1 FTIR Characterization of the Precursors

For the sake of clarity, the FTIR spectra of Si precursor, solvent, and acid used for reactions are presented below with vibrational bands assignments (Figures 71-73). The spectra of catalysts can be found in Appendix A.

Assignment	Wavenumber (cm^{-1})
ν as (CH_3)	2963, st
ν s (CH_3)	2875, st
ν (SH)	2559, w
δ as (HCH)	1455, m
ν as (Si-OMe)	1192, st
ν as (Si-OMe)	1089, st
ν s (Si-OC)	812, st

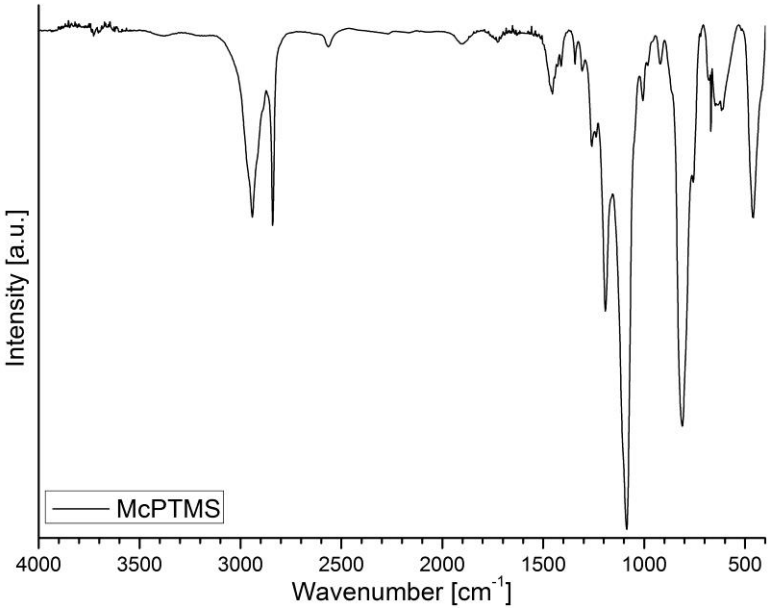

Figure 71. FTIR transmission mode spectrum and typical characteristics of McPTMS

Assignment	Wavenumber (cm^{-1})
ν (OH)	3333, st, br
ν as (CH_3)	2963, st
ν as (CH_2)	2936, st
ν s (CH_3)	2878, st
δ s (CH_2)	1464, m
ν as (CO)	1096, 1053 st
ν as (CC)	1017, st
ν s (CC)	969, st

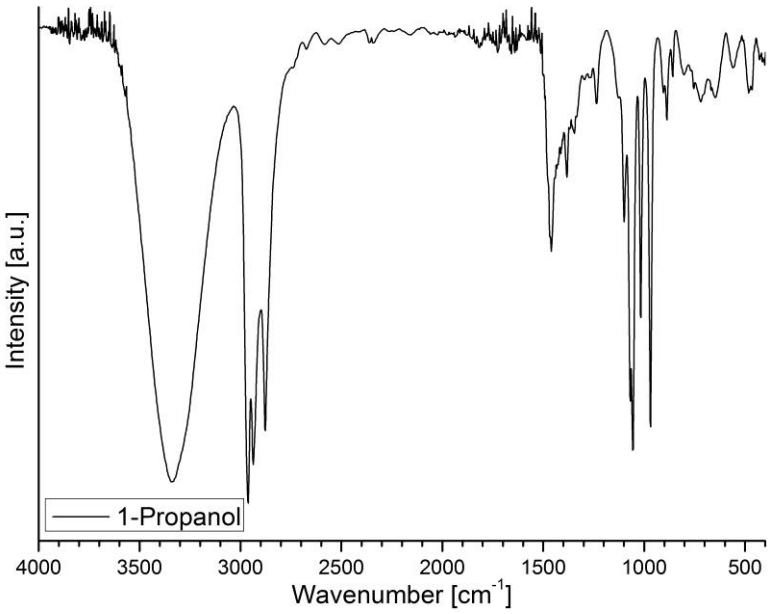

Figure 72. FTIR transmission mode spectrum and typical characteristics of 1-PrOH

Assignment	Wavenumber (cm^{-1})
ν (OH)	3414, st, br
ν s (CH_3)	2967, st
ν (C=O)	1736, st
δ ip (OH)	1411, st
ν (CO)	1216, m
δ oop (OH)	932, st
ρ (CH_2)	794, st

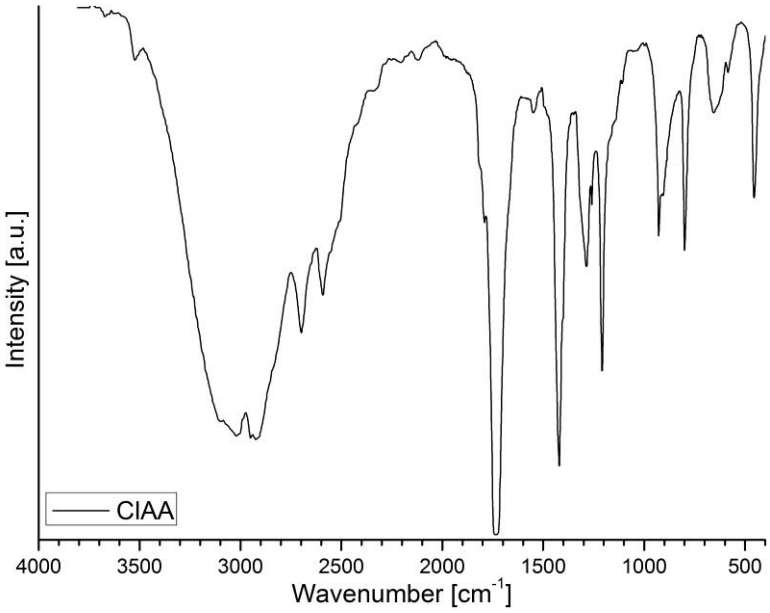

Figure 73. FTIR transmission mode spectrum and typical characteristics of ClAA

3.3.2 FTIR Characterization of the silsesquioxane NBBs

Despite the different experimental conditions, the presence of the thiol function of McPTMS is confirmed in all samples by the detection of the weak S-H stretching vibration at 2559 cm^{-1}, as marked with red line on the Figure 74. Residual solvent and by-products are present in the analyzed samples. The signals in the range 1750-1650 cm^{-1} point out the incomplete removal of carboxylic acid and ester after drying the solutions in vacuum, with the only exception of TFA1 (blue line on the Figure 74).

The C-H stretching vibrations give rise to a complex band in the range 3000 - 2800 cm^{-1}, due to the overlapping of several signals (enlarged on the Figure 75). The signals at 2960 and 2875 cm^{-1} are due to asymmetric and symmetric stretching modes of methyl groups in the organic chains.

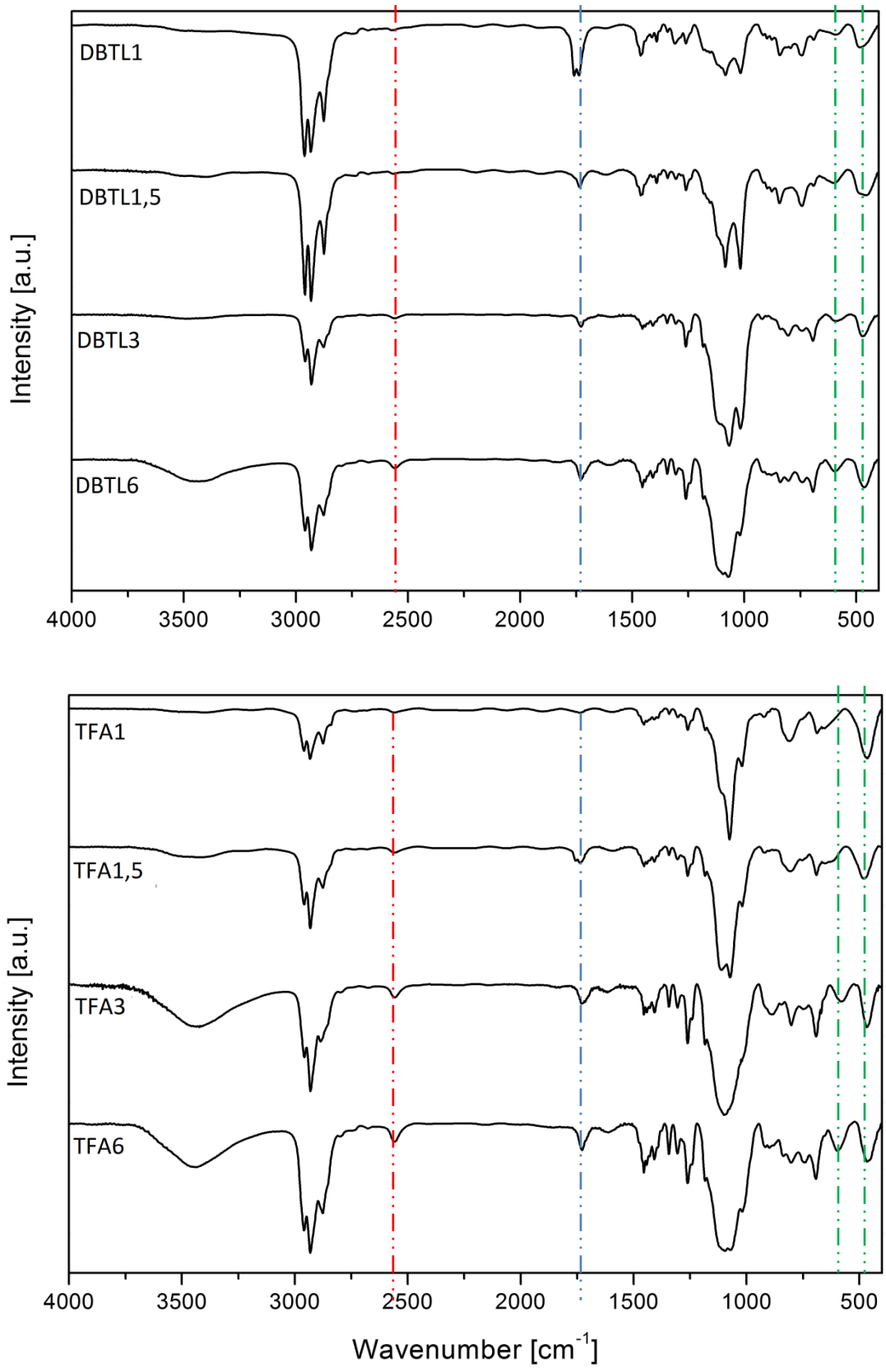

Figure 74. FTIR spectra of DBTL-catalyzed (top) and TFA-catalyzed (bottom) samples.

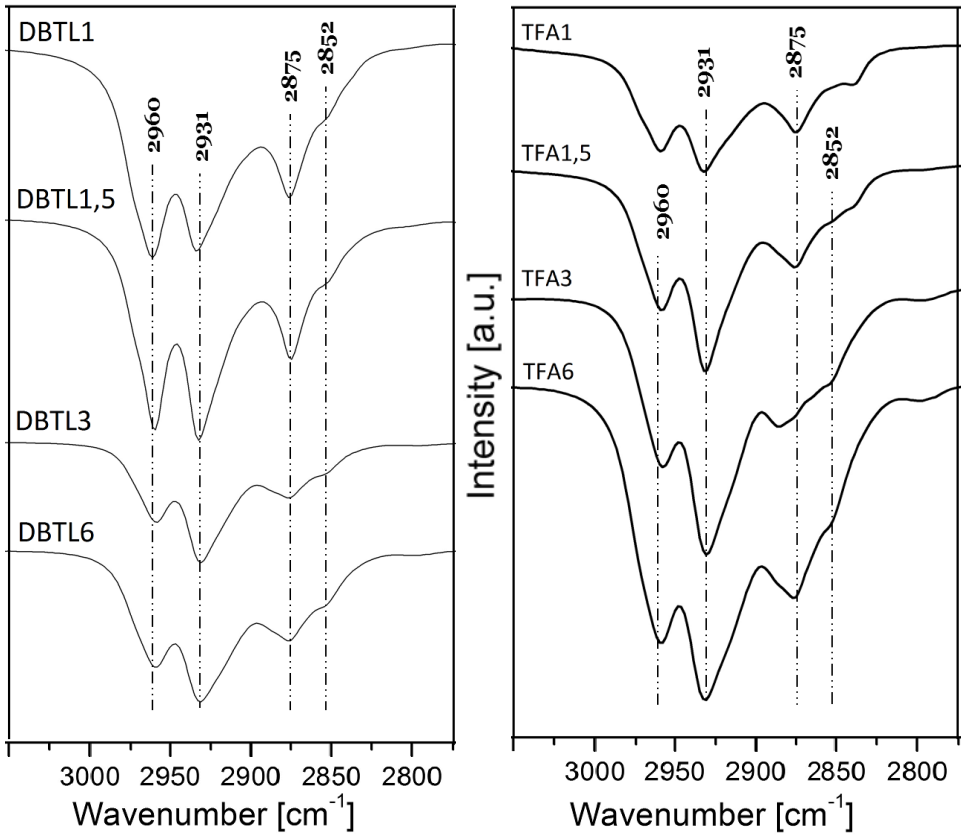

Figure 75. C-H stretching region in FTIR spectra of DBTL (left) and TFA (right) samples.

The vibrations at 2931 cm^{-1} (ν_{as}) and 2852 cm^{-1} (ν_s) can be assigned to the methylene groups of mercaptopropyl chain and 1-propanol. The increase in intensity of the signal at 2931 cm^{-1} from DBTL1 to DBTL6 (Figure 75 - left) and from TFA1 to TFA6 (Figure 75 - right) is probably due to the difficult removal of 1-propanol (used in higher content according to the r value) in agreement with the intensity of the O-H stretching band at 3400 cm^{-1}. However, it could be also the result of the trans-alcoholysis reaction between Si-OCH_3 groups and 1-PrOH leading to the formation of Si-$OCH_2CH_2CH_3$ functions [12]. Indeed, the characteristic signal of the SiO-CH_3 group, which is found at 2838 cm^{-1} in the pristine McPTMS, is extremely weak or absent in all samples. The asymmetric Si-O stretching vibrations are detected in the 1200–900 cm^{-1} range, and the comparison between the siloxane region of DBTL-catalyzed (left) and TFA catalyzed (right) on Figure 76 deserves particular attention.

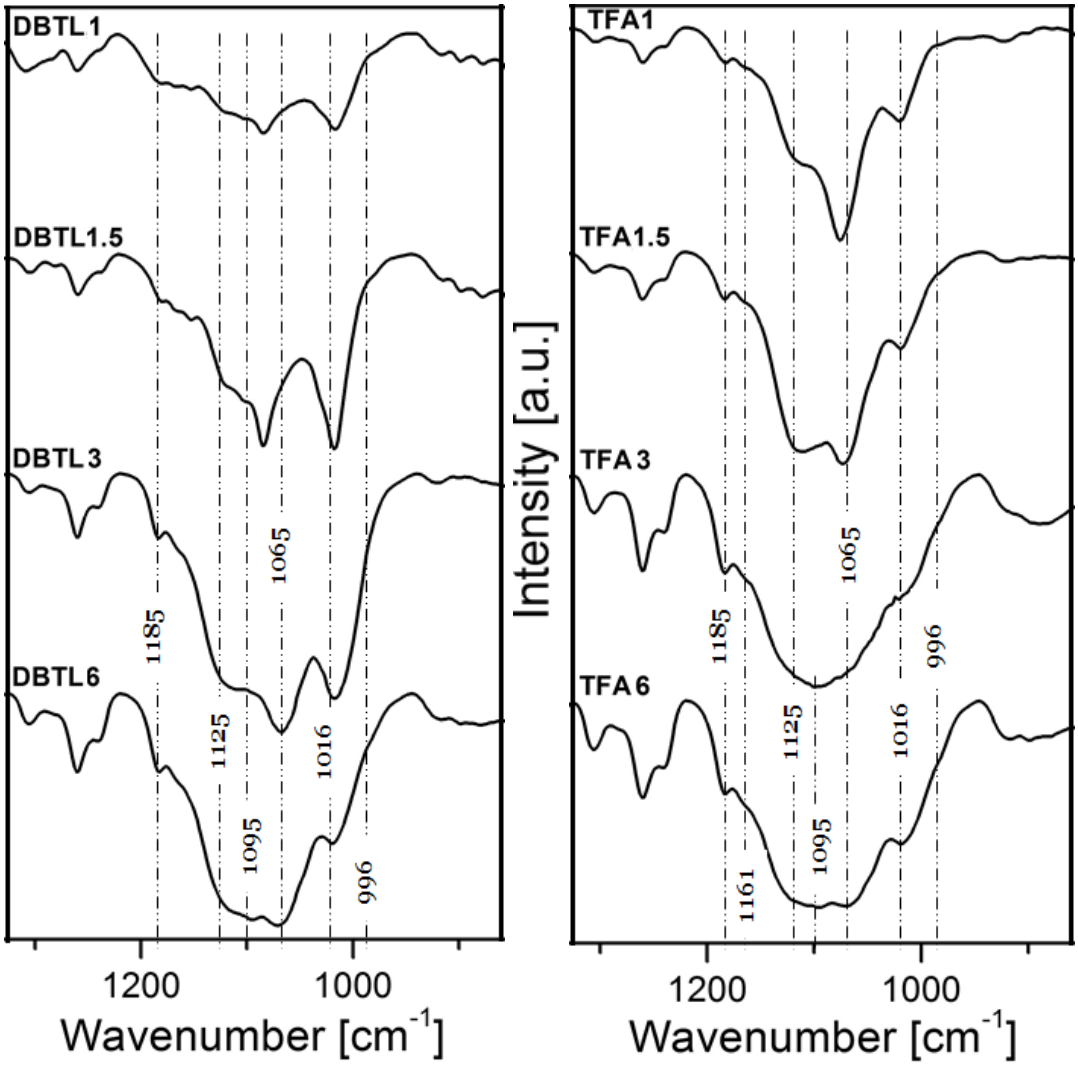

Figure 76. Siloxane region in FTIR spectra of DBTL (left) and TFA (right) samples.

The main components of the siloxane band can be assigned to three members cycles, cyclic tetramers, larger cycles and linear units in ladder-like structures, [205, 208] (in the range from 1016 to 1095 cm^{-1}) and to cage-like structures (1125 cm^{-1}) [165b, 198, 202, 205]. The employ of DBTL and TFA produces different features in the siloxane band, showing a more complex band shape evolution vs. hydrolysis ratio in the case of DBTL catalyzed samples. It is clear from Figure 61 that, in the case of r = 1 and 1.5, the different catalyst strongly affects the development of the siloxane network. In DBTL1 and DBTL1.5 (Figure 76 - left) the main signals appear at 1016 and 1080 cm^{-1}, pointing out low condensation degree and preferential formation of small cycles and di-siloxane units. TFA1 and TFA1.5 (Figure 76 - right) show the main signal at 1070 cm^{-1} with a second component

at 1125 cm^{-1}, in agreement with the presence of larger cycles and cage-like structures. The signal at 1125 cm^{-1} grows in intensity with increasing water availability, according to a higher cross-linking degree than in the corresponding DBTL-catalyzed samples. The large presence of small cycles and ladder-like structures characterizes the DBTL3 spectrum, whereas the increase of cage-like structures can be detected in the corresponding TFA3 spectrum. The siloxane band of the two samples prepared with r = 6 display less remarkable differences, but the shoulder at 1125 cm^{-1} appears more intense in TFA6 than in DBTL6. In the low frequency range (Figure 74, green lines), the band at about 460 cm^{-1} is assigned to the $\nu_s(SiO_2)$ bending [209] and the low intensity band in the range 570 to 585 cm^{-1} can be attributed to Si_2O vibration in cycles [210, 211]. From the FTIR spectra, it can be concluded that employing the ISWP process the increase of ratio r favors the formation of cage-like structures. As it was reported above, playing with different shape and anisotropy features of NBBs is the key-point for the preparation of new polymer-based nanocomposites with effective tuning of the filler-filler and filler-matrix interactions. Thus, for quantifying the yield of different structures (Figure 77) with respect to the employed catalyst, the profile fitting of the siloxane bands was obtained for all the samples, and the fitting is shown on the Figures 78 and 79 (in absorbance mode).

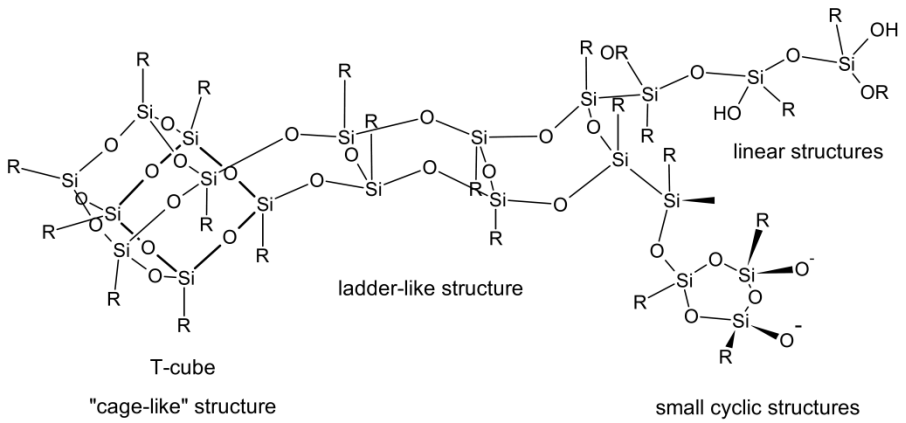

Figure 77. Representation of different structural units of NBBs based on FTIR assignment.

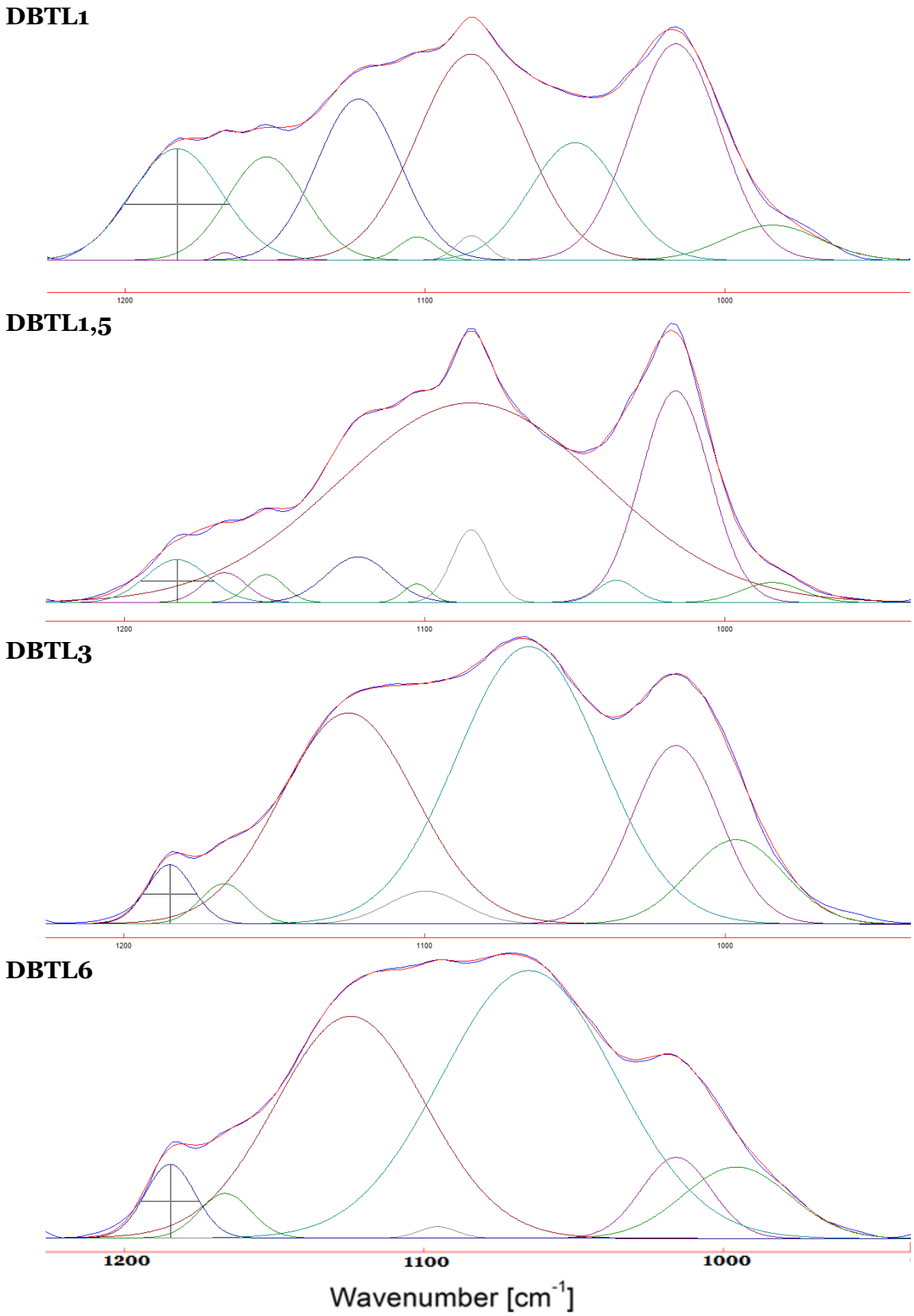

Figure 78 FTIR spectra fitting of DBTL-catalyzed samples.

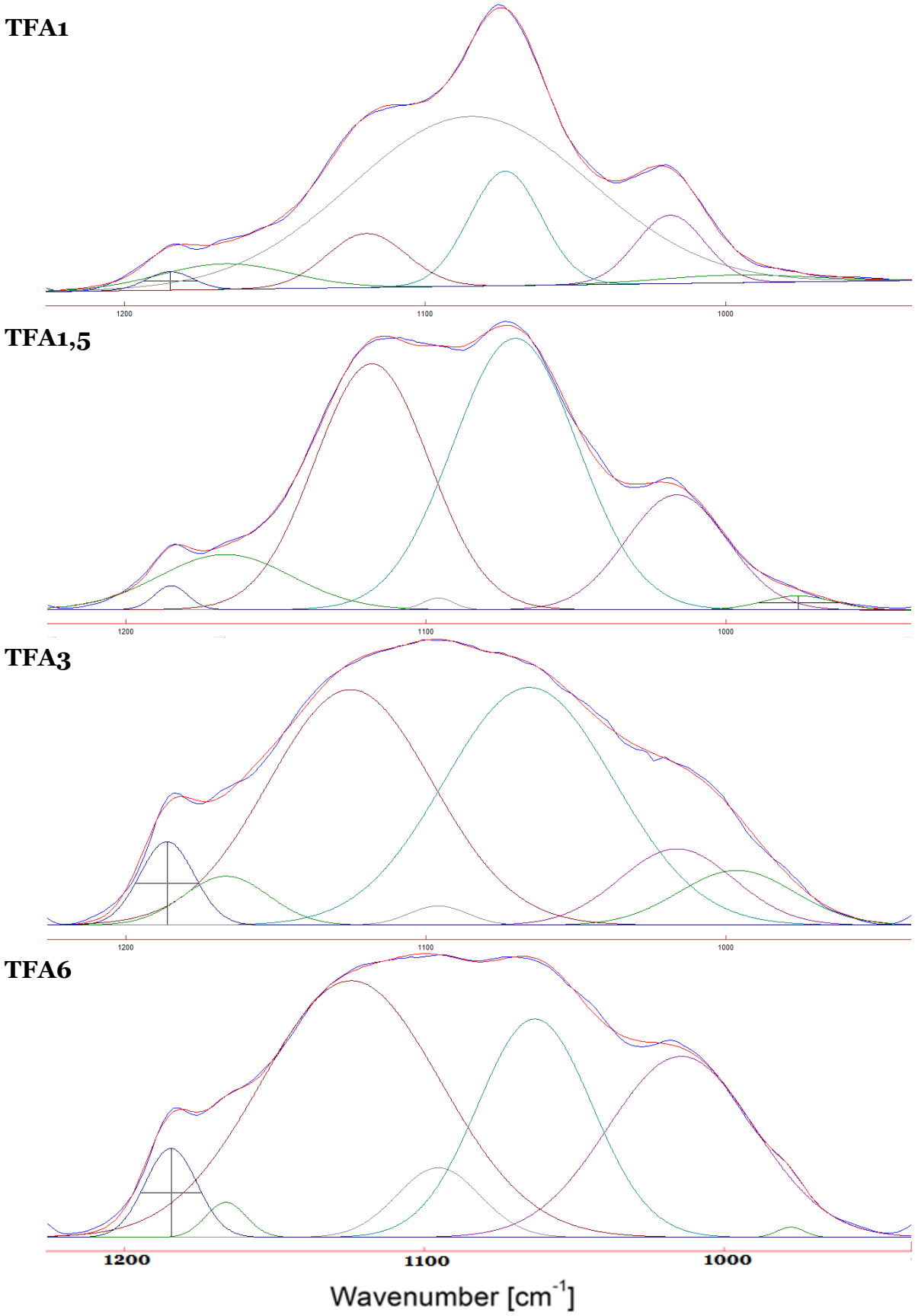

Figure 79 FTIR spectra fitting of TFA-catalyzed samples.

The signals are assigned according to the literature [165b, 197, 205, 212-214], and account for the presence of cage-type silsesquioxanes ($T_6(OH)_2$ at 996 cm^{-1}, T_8 cages at 1125 cm^{-1} and polycages at 1185 cm^{-1}) and ladder-like structures (T_3 cycles at 1016 cm^{-1}, $T_7(OH)_3$ at 1065 cm^{-1}, and linear $T_2(OH)_4$ at 1095 cm^{-1}).

The deconvolution data confirmed that the cage- and ladder-like species formation is preferred for the high r ratios (3 and 6) and the results are reported in Figure 80 for the samples prepared with r = 3 and 6 (DBTL3, DBTL6, TFA3 and TFA6)

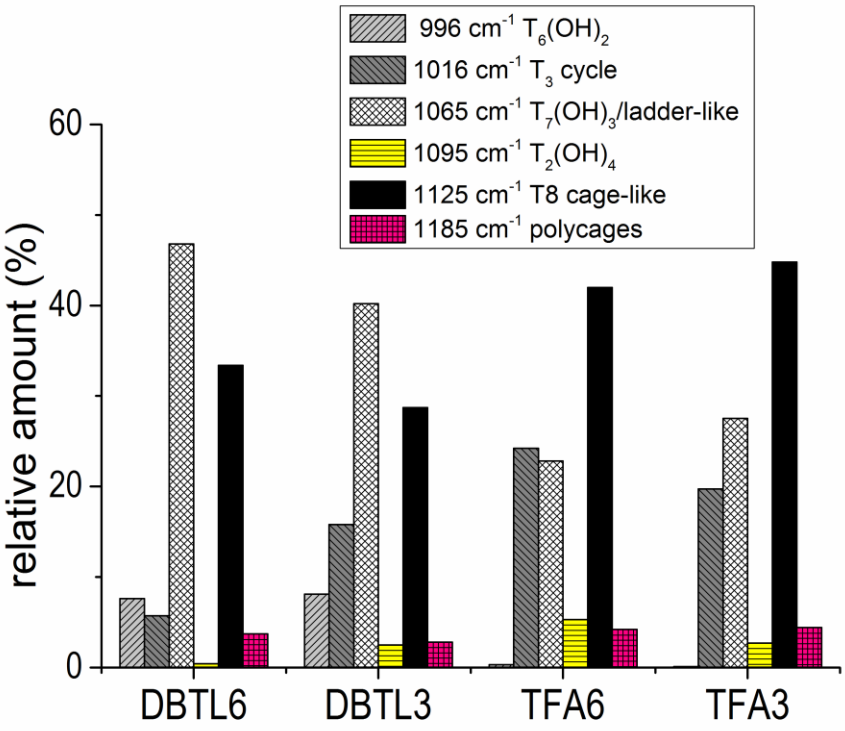

Figure 80. Quantitative results of the profile fitting of the band in range 1200-900 cm^{-1}.

According to the intensity of the signal at 1125 cm^{-1}, the amount of T_8 cages is higher for TFA-catalyzed samples than for DBTL-catalyzed ones. The increase in cage formation is observed for DBTL increasing r from 3 to 6 whereas in the case of TFA the maximum yield is obtained using r = 3.

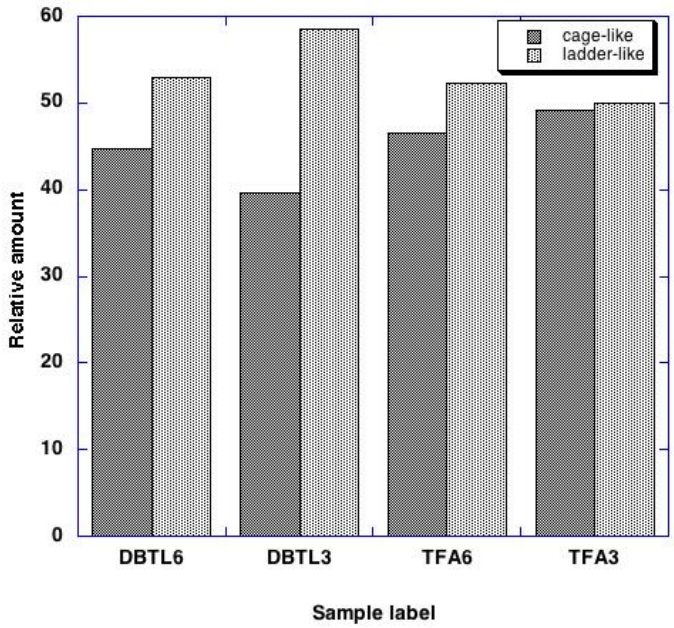

Figure 81. Comparison of the yields in cage- and ladder-like species for different catalysts and r ratios, derived from profile fitting of the band in the range 1200-900 cm^{-1}.

As can be seen from the Figure 81, the signals related to ladder-like structures present higher intensity for DBTL–catalyzed samples, reaching the maximum value for DBTL3 (60%). However when the highest amount of water is provided to the sol-gel reaction by ClAA/1-PrOH esterification (r = 6), the total yield in cages and ladder-like structures, calculated by summing the related peaks contribution, is almost the same and appears independent on the employed catalyst (cages yield 44.7% and 46.5 % for DBTL6 and TFA6, respectively).

It is worth of noting that the performance of trifluoroacetic acid is more complex than that of DBTL, since, according to its pKa (TFA pK=0.23), it has to improve the kinetics of sol-gel reactions and influence the esterification reaction as well. Moreover, in the chemistry of silicones the reactivity of TFA towards siloxane cycles, leading to cleavage of siloxane bonds and structural rearrangement in the ring-opening polymerization process, is well known [215].

3.3.3 ^{1}H NMR Characterization of the silsesquioxane NBBs

^{1}H NMR spectroscopy was used in order to achieve information on the extent of transesterification and hydrolysis-condensation reactions changing the ISWP conditions. Figure 83 presents the ^{1}H NMR spectra recorded on DBTL and TFA catalyzed samples with r = 1 and 6.

The proton NMR spectrum of the pure McPTMS is presented on the Figure 82 with corresponding signals centered at 0.61 ppm (-OC<u>H</u>$_2$CH$_2$CH$_2$-SH, **i**), 1.60 ppm (-OCH$_2$C<u>H</u>$_2$CH$_2$-SH, **h**) 2.39 ppm (-OCH$_2$CH$_2$C<u>H</u>$_2$-SH, **g1**), 1.41 ppm (-OCH$_2$CH$_2$CH$_2$-S<u>H</u>), and 3.42 ppm (-OC<u>H</u>$_3$)

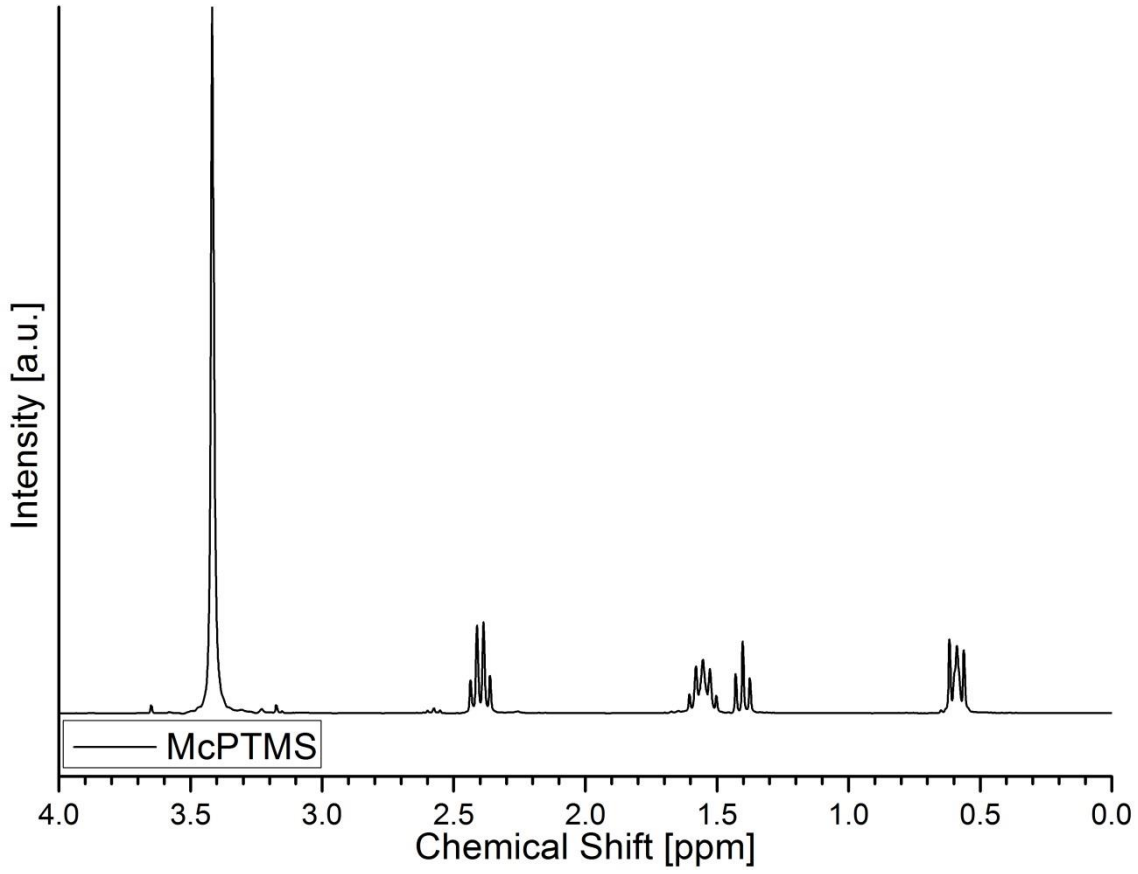

Figure 82. ^{1}H NMR spectra of pure McPTMS.

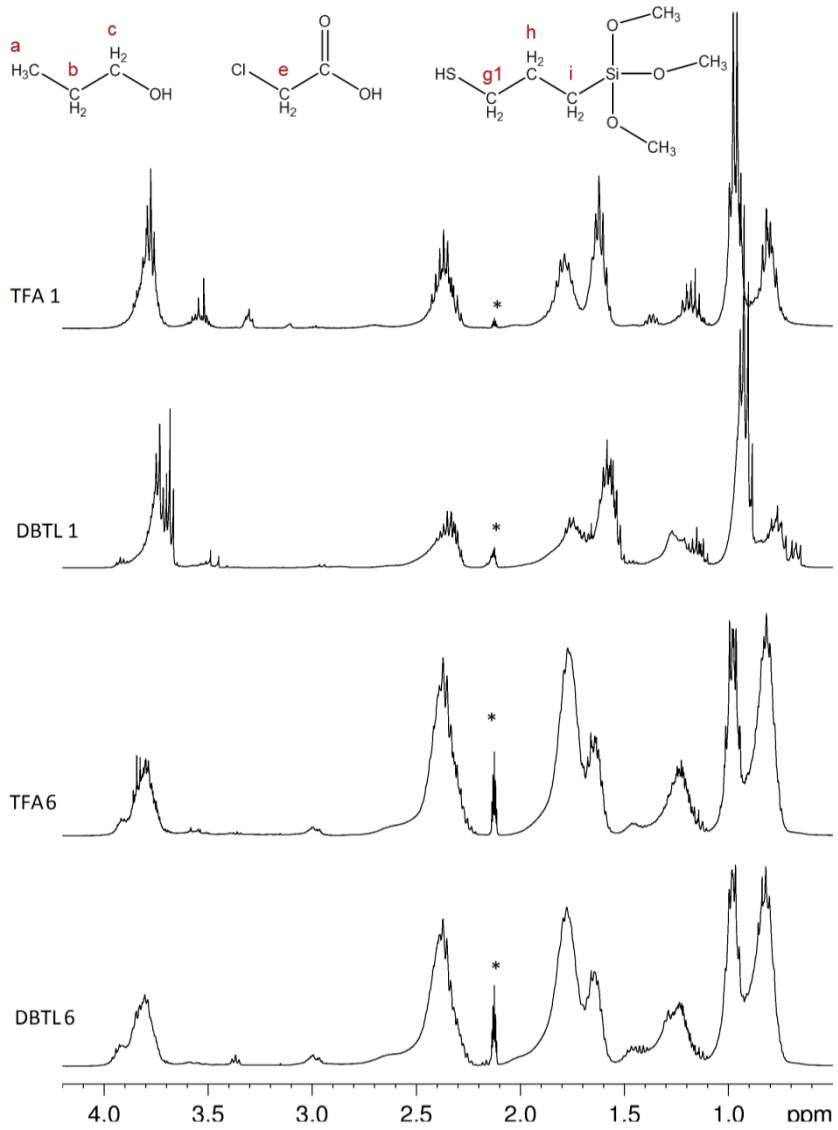

Figure 83. ^{1}H NMR spectra of samples prepared with DBTL and TFA and r = 1 and 6. The peak marked with * is due to d8-toluene.

The signals appear broad and present a down-field shift in comparison with the pristine McPTMS, in relation with the hydrolysis-condensation process experienced by the Si atoms bearing the mercaptopropyl chains. The protons of the mercaptopropyl chain linked to silicon present resonances at 0.82 ppm, 1.77 ppm and 2.37 ppm due to **i**, **h**, and **g1** protons of the Si–CH_2-CH_2-CH_2-SH chain respectively. In the case of DBTL1, the shift of the **i**-protons signal is almost negligible, in agreement with the low extent of condensation pointed out by the FTIR study.

After 24 h reaction at 100°C, the signals of the methoxide groups completely disappear in DBTL6 and TFA6, whereas TFA1 and DBTL1 still present a residual signal at 3.5 ppm due to Si-OCH_3. In return, new broad signals are clearly detected at 0.93 ppm, 1.59 ppm and 3.75 ppm, which can be assigned to the overlapping contribution of **i, h** and **g1** protons of the Si-$OCH_2CH_2CH_3$ groups created by transesterification reaction, and the protons resonances in the propyl chain of 1-PrOH/ClAA esterification product. The low-field resonance at 3.9 ppm that is absent in TFA1 can be probably attributed to the methylene protons of chloroacetate groups, in agreement with the results of the FTIR

According to the literature [216] and the spectrum of pristine McPTMS (Figure 82), in oligomeric structures the -SH proton should present a resonance at 1.4 ppm, which cannot be clearly identified in the spectra of Figure 83 due to the overlapping and broadening of other peaks in the range 1.1 ÷ 1.5 ppm that are due to overlapping of 1-PrOH and esterification reaction by-products resonances.

The relatively large half-width of the proton signals may be related to the sample viscosity and limited mobility of the involved species. It is worth of noting that the peaks are better resolved in the case of DBTL1 and, in a lower extent, of TFA1 and the signal fine structures disappear in samples prepared with r = 6. The contribution of other resonances such as silanol groups in different cage-like and ladder-like structures, whose presence has been detected by FTIR, cannot be clearly identified. According to Feher et al. [217] the chemical shift of silanol groups in partially condensed cages is low-field shifted in comparison to the isolated one and the shift depends on the number of interacting silanol groups [218]. Thus, the ^1H NMR chemical shift of the silanol groups should depend on weak interactions and condensation of the silsesquioxane network leading to different resonances.

3.3.4 ^{29}Si NMR Characterization of the silsesquioxane NBBs

The ^{29}Si-NMR spectra of the samples prepared with different r ratio and catalysts are shown in the Figures 84, 85. The hydrolysis-condensation process can be easily followed since a down-field shift of the ^{29}Si NMR signals is expected with increasing hydrolysis of alkoxyde groups, and condensation leads to an up-field shift of the signals [219]. Furthermore, the substitution of methoxide by propoxide groups by transesterification reaction can be detected by observing the shift of the related signals [220].

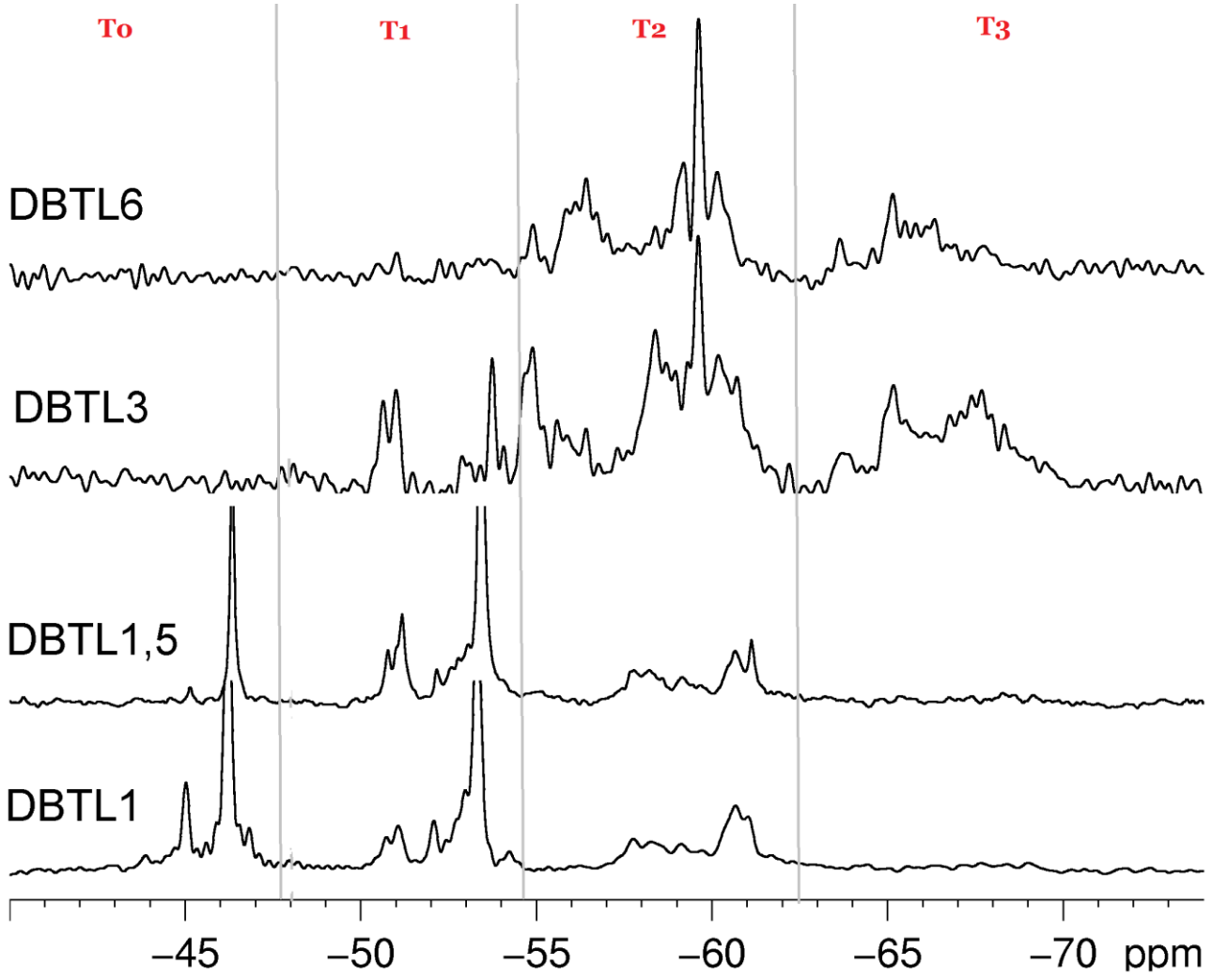

Figure 84. ^{29}Si NMR spectra of all samples prepared with DBTL.

The spectra point out both disappearance of the signal of the pristine McPTMS (-42.8 ppm) and different extent of hydrolysis-condensation as a function of the hydrolysis ratio. In general, the spectra of DBTL and TFA catalyzed samples are quite similar for over-stoichiometric conditions, whereas relevant differences can be observed in the case of samples prepared with low r ratio. The quantitative results obtained from the integration of the ^{29}Si NMR spectra (according to the T^0-T^3 ranges highlighted in the Figures 84, 85) are summarized in Table 8, which reports also the degree of condensation (DOC) calculated according to equation:

$$DOC = \frac{T^1 + 2T^2 + 3T^3}{3\left(T^0 + T^1 + T^2 + T^3\right)} \times 100$$

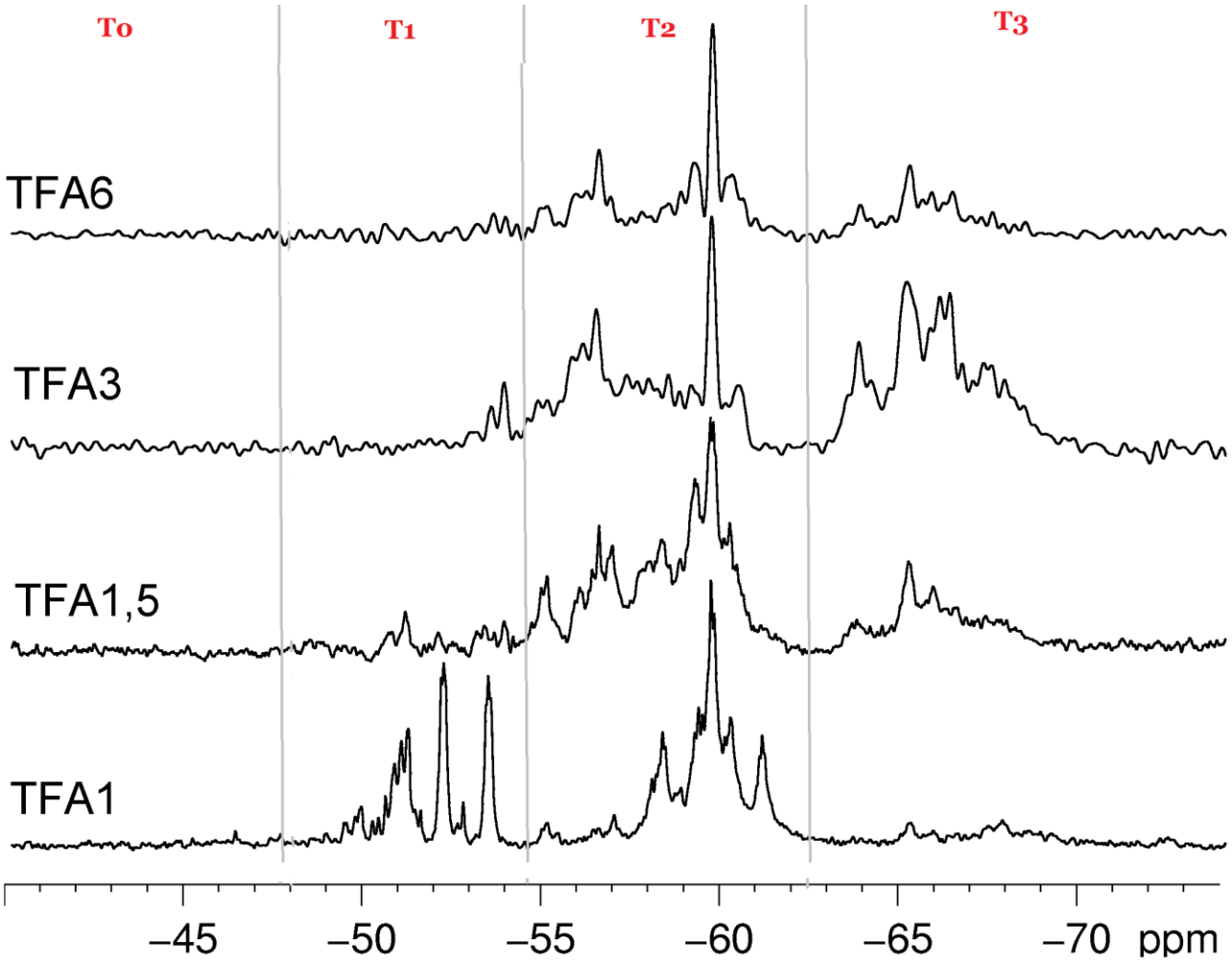

Figure 85. ^{29}Si NMR spectra of all samples prepared with TFA.

Sample	T^0	T^1	T^2	T^3	DOC
TFA6	0,0	2,0	67,2	30,8	76,3
TFA3	0,0	6,0	44,4	49,6	81,2
TFA1,5	0,0	5,3	69,4	25,3	73,3
TFA1	0,1	31,9	57,5	10,5	59,5
DBTL6	0,0	3,6	67,1	29,3	75,2
DBTL3	0,0	11,7	56,6	31,7	73,3
DBTL1,5	16,7	53,5	29,8	0,0	37,7
DBTL1	35,2	40,6	24,2	0,0	29,7

Table 8. ^{29}Si NMR integrated amounts of structural units and Degree Of Condensation

DBTL1 and DBTL1.5 spectra display very low condensation degree, in agreement with residual signals in the T^0 range (-40 ÷ -47ppm) and lack of signals due to T^3 units in the range -62 ÷ -70 ppm. Two resonances up-field shifted with respect to McPTMS (-42.8 ppm) appear at -45.02 and -46.23 ppm, which can be attributed to T^0[1] and T^0[0] Si units bearing propoxide groups. The substitution of methoxide groups with propoxide groups affects the chemical shift of the signals due to hydrolyzed T^1 units (–51.1, –52.1, and –53.3 ppm). The signals of T^2 units appear in the range -54 ÷ -62 ppm.

Increasing r leads to the disappearance of T^0 units and the appearance of signals due to T^3 units in DBTL3 spectrum, which is characterized by a very broad distribution of large signals from -50 to -68 ppm. The half width of the signals increases drastically suggesting the formation of species with high molecular weight and limited mobility, in

agreement with the FTIR results that highlighted the large content of ladder-like structures. In the T^2 range, two groups of resonances appear centered at -55 ppm and -59 ppm. Considering the effect of ≡Si-O-Si≡ bond angle on the ^{29}Si chemical shift [221], these resonances can be assigned to Si units involved in cycles of different size and linear chains [206]. T^3 units show a distribution of unresolved resonances between -63 and -68 pm that are related to the presence of cage-like structures [206, 222, 223]. Better-resolved peaks due to T^2 and T^3 units characterize DBTL6, which displays the highest condensation extent among DBTL-catalyzed samples.

If the sol-gel reaction is catalyzed with TFA, the structural development is fundamentally different. At the lowest ratio r = 1, T^0 signals are negligible and the intense resonances at –51.1, –52.1, and –53.3 ppm can be attributed to progressively hydrolyzed T^1 units. In the T^2 units range, strong resonances appear from -58 to -61 ppm. In agreement with FT-IR the beginning formation of cage-like structures can be confirmed due to the presence of weak signals at chemical shift from –65 to –68 ppm. Increasing r from 1.5 to 6 leads to the increase of the condensation degree in TFA-catalyzed samples. The signals due to cage-like structures, as the resonance at -66.7 ppm attributed to T_8 [224], show higher intensity in TFA3 than in TFA6, in agreement with TFA3 highest DOC value and the cage yield calculated from the FTIR spectra (Figure 80). In agreement with the results of the FTIR study, the ^{29}Si NMR spectra of TFA6 and DBTL6 present almost the same features with similar degree of condensation.

3.3.5 Gel Permeation Chromatography (GPC) Characterization

GPC analyses strengthen the results of the ^{29}Si NMR spectra and the discussion on the observed structural evolution. Figures 86 and 87 presents the GPC traces of samples, obtained after 24 h reaction, as a function of both water availability (r) and employed catalyst (TFA or DBTL). In the case of TFA samples (Figure 86), the increase of the value r produces a continuous increase of the molecular weight. Changing r from 1 to 6 leads the main peak to move from 23 ml to 21 ml retention volume, and the position of the second component changes from 21.5 ml to 20 ml. Moreover, in TFA3 and TFA6 a third weak component centered at a retention volume of 19 ml is visible in the GPC traces. These peaks correspond on average to the formation of species based on four to ten Si units, with calculated molecular weight in the range from 800 to 2000 Da.

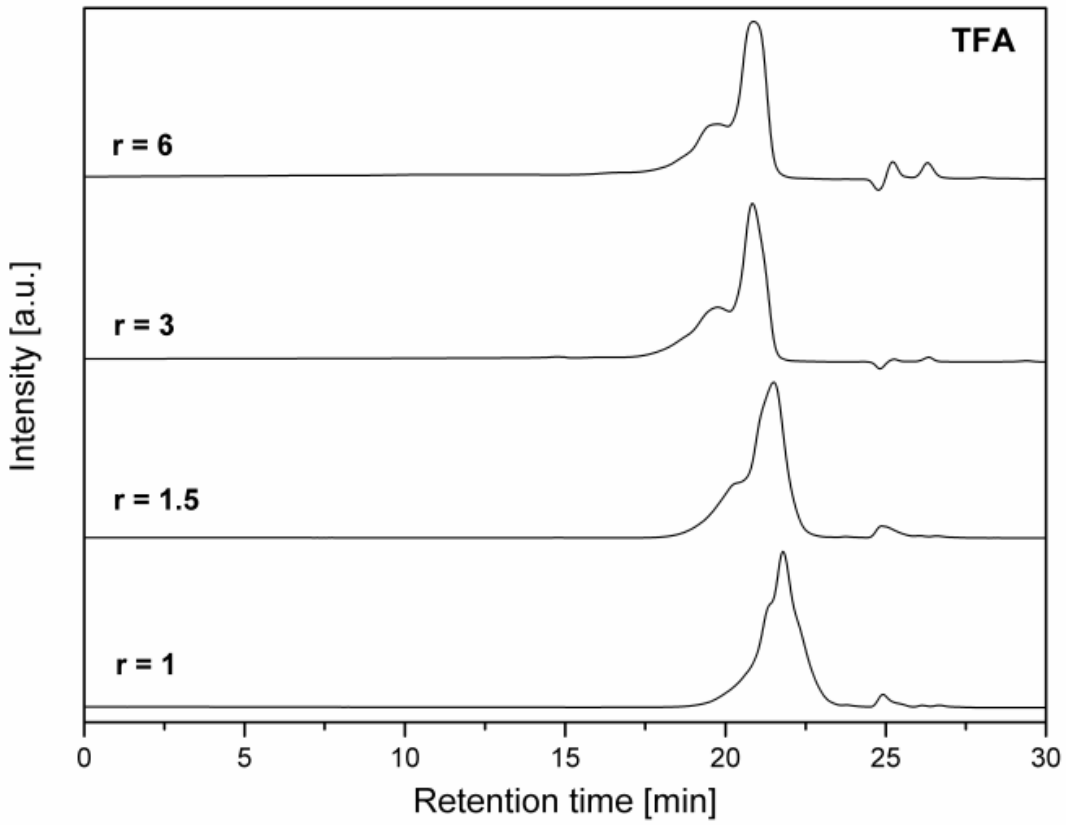

Figure 86. GPC traces of the NBBs , catalyzed by TFA for different r ratios

The samples prepared with DBTL (Figure 87) present a complex behavior. DBTL1 and DBTL1.5 show the presence of peaks in the range of 21-24.6 ml retention volume, in agreement with a very low condensation degree. DBTL3 trace is surprisingly different featuring a broad band generated by the overlapping of peaks in the range 14-22 ml. The GPC trace points out the formation of structures with molecular weight from 20000 to 700 Da, according to the highest amount of ladder-like structures deduced from the FTIR study and the broad distribution of large signals observed in the ^{29}Si NMR spectrum. The DBTL6 trace resembles TFA6 one, and presents the main peak at 21.8 min corresponding to a molecular weight of 830 Da, a second contribution at 21.4 min (1115 Da) and a third weak component at a retention volume of 19 ml (2000 Da).

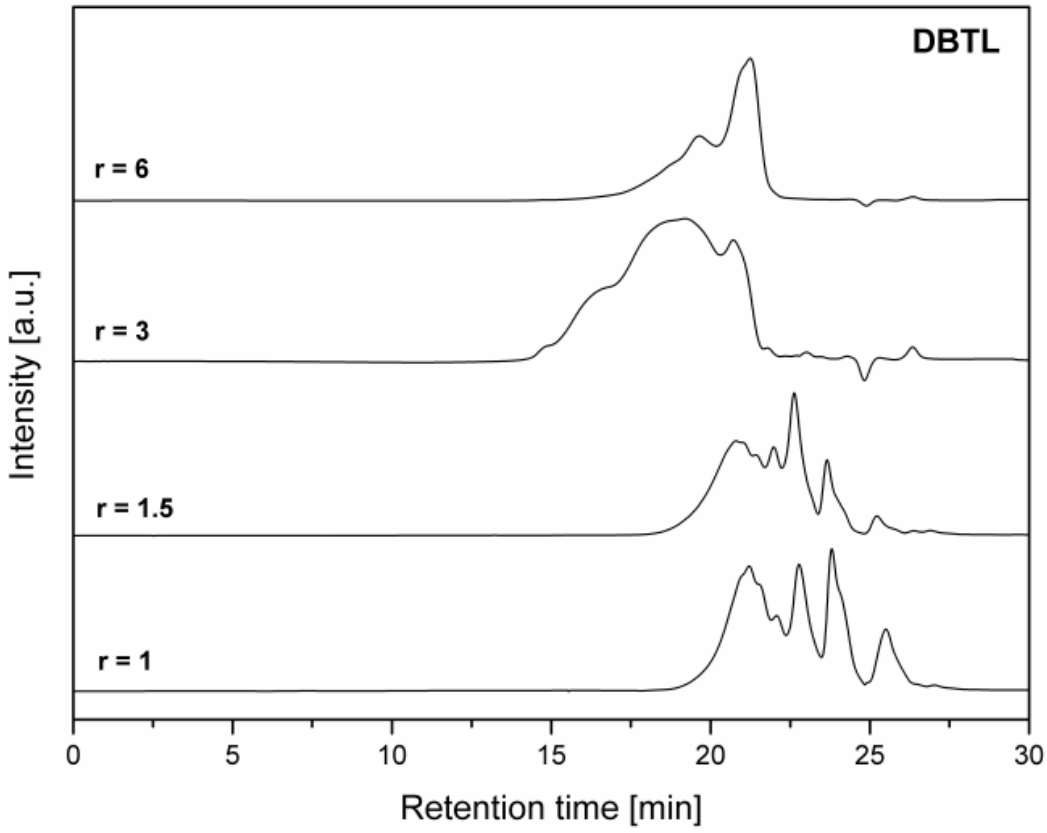

Figure 87. GPC traces of the NBBs, catalyzed by DBTL for different r ratios

The reason for the unusual behavior of DBTL3 is still unclear. Further kinetics experiments (which will be discussed later) have shown that the broadening of the molecular weight distribution occurs between 6 and 24 hours of reaction. However, increasing the reaction time up to 96 hours results in the decrease in size of the silsesquioxane species with the narrowing of the molecular weight distribution in DBTL3.

As a general trend, the GPC traces show a clear shift to lower retention time with increasing the water availability corresponding to the formation of larger structures. However, with under-stoichiometric (r= 1 and 1.5) and stoichiometric (r=3) amounts of water, the use of TFA rather than DBTL leads to a more efficient control on the obtained structures. For r = 6 the development of silsesquioxane structures appears only slightly dependent on the employed catalyst, in agreement with the results of the ^{29}Si NMR and FTIR spectra.

The GPC study confirms the formation of more condensed structures as the water provided by ISWP process increases; however, only relative molecular weights can be calculated on the basis of the calibration curve obtained using PS standards.

3.3.6 MALDI-TOF Characterization

Taken into consideration the poor reliability of molecular weights calculated from the GPC traces, the MALDI-TOF spectra on the samples prepared with under-stoichiometric and over-stoichiometric conditions using DBTL as condensation promoter have been collected, with the help of Prof. Graziano Guella at the Department of Physics at the University of Trento. We have selected DBTL1 and DBTL6 samples, in order to relate the water availability only to the ClAA/1PrOH ratio and remove any interference due to TFA, according to the previously reported considerations. The oligomers were detected from m/z 500 to about 1300, the lower limit being defined by matrix interference and the upper one by the signal to noise ratio. The MALDI-TOF analysis of polysilsesquioxanes was already reported in different publications [225-228]. The matrix-assisted laser desorption ionization is a soft ionization technique in mass spectrometry allowing the analysis of polymers without the occurrence of fragmentation. Thus, the distinct morphologies of the NBBs can be assessed. The interpretation of ion-positive MALDI-TOF spectra of polysilsesquioxanes (M) relies on the finding [227] that they usually appear as single charged (z = +1) sodium-adducts $[M+Na]^+$.

The exact mass of the monoisotopic peak in every species-cluster can be evaluated by the following equation:

$$\mathbf{m = (136.001\ n) + 18.011\ (1-t) + (42.037) + y\ (14.016) + 22.989}$$

The variables in above equation are based on the following definition:

n is the number of (3-mercaptopropyl) hydroxysilanone units,

t is the number of closed rings present in the case of cyclic or cage like units,

x is the number of propyl groups and **y** the number of methyl groups present in a given species.

On the other hand, the numerical values in this equation are the exact (mono-isotopic) masses of the monomeric (3-mercaptopropyl) hydroxysilanone (136.001 Da), water (18.011 Da), propylidene (42.037 Da), methylidene (14.016 Da) and sodium atom (22.989 Da). Since we are dealing with processes involving only partial hydrolysis-condensation steps, free alkoxy or hydroxy-groups can still be retained in the material but their total number (x+y) can never exceed the value assumed by the structural constrain given by $x+y \leq [n+2(1-t)]$ in every considered polysilsesquioxane species. In turn, the maximum number of free hydroxyl groups depends on the parameters t and n.

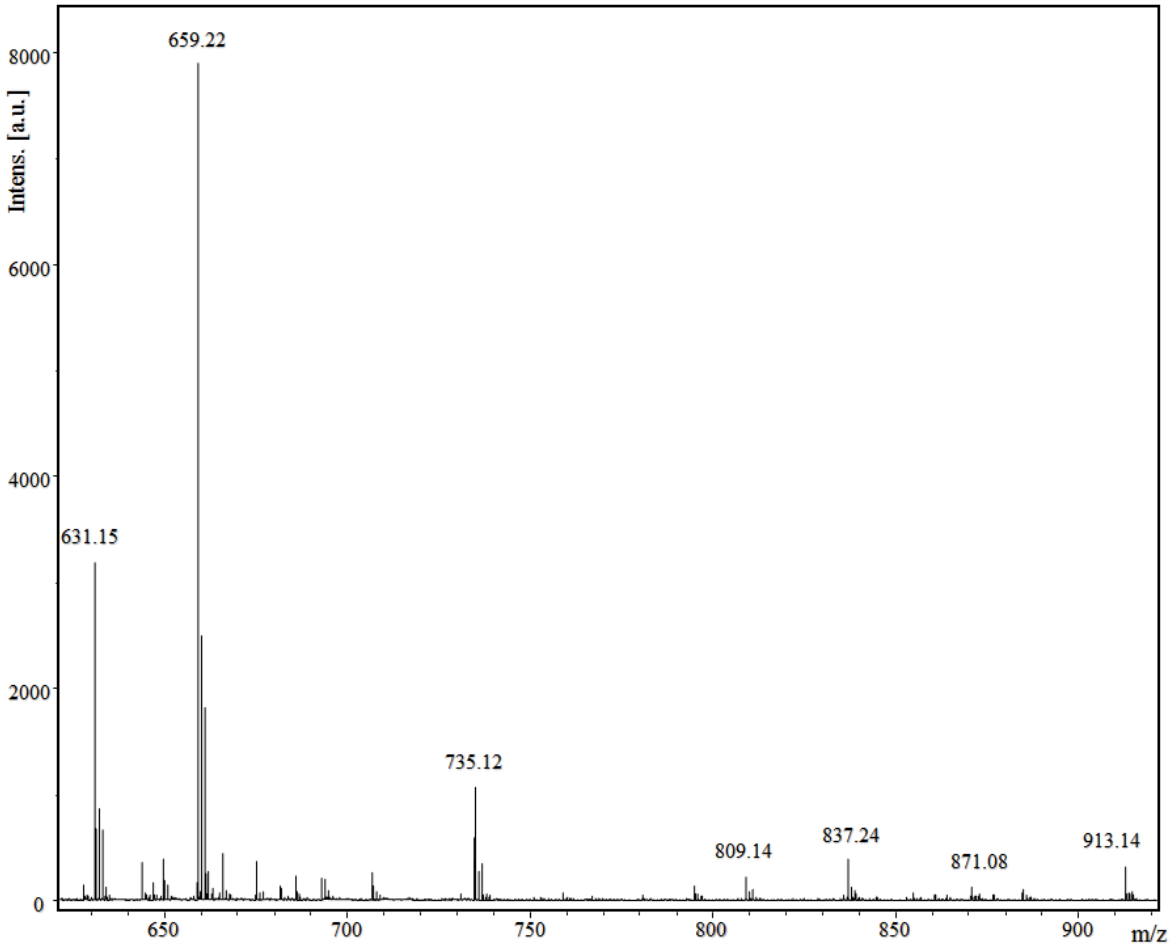

Figure 88. MALDI-TOF spectrum of DBTL1 sample

The main peaks detected in MALDI-TOF spectra for DBTL1 are shown in Figure 88. Their structure assignments, summarized in Table 9 with related structures demonstrated

on the Figure 89, have been obtained by evaluating the exact mass of every species, compatible with the boundary conditions discussed above.

m/z (exp.) $[M+Na]^+$	Species				Structure of the neutral $T_n(OR)_m$ silsesquioxane	Molecular formula of sodium adducts	Theoretical mass of monoisotopic peak (Da)
	n	t	OPr	OMe			
631.15	3	1	4	1	$T_3(OPr)_4(OMe)$	$C_{22}H_{52}NaO_7S_3Si_3$	631.208
659.22	3	0	5	0	$T_3(OPr)_5$	$C_{24}H_{56}NaO_7S_3Si_3$	659.239
735.12	4	1	4	0	$T_4(OPr)_4$	$C_{24}H_{56}NaO_8S_4Si_4$	735.183
809.14	4	0	5	1	$T_4(OPr)_5(OMe)$	$C_{28}H_{66}NaO_9S_4Si_4$	809.256
837.24	4	0	6	0	$T_4(OPr)_6$	$C_{30}H_{70}NaO_9S_4Si_4$	837.287
871.08	5	1	4	0	$T_5(OPr)_4(OH)$	$C_{27}H_{64}NaO_{10}S_5Si_5$	871.184
913.14	5	1	5	0	$T_5(OPr)_5$	$C_{30}H_{70}NaO_{10}S_5Si_5$	913.231

Table 9 . Signals detected in MALDI-TOF spectra of DBTL1 sample

Since 1-propanol (Pr-OH) has been used as a solvent, the -OMe groups have been almost fully replaced by -OPr groups in all the detected ions, in fair agreement with FT-IR and NMR results. The only significant peak containing one residual methoxy- group is the

linear trimeric silsesquioxane $T_3(OPr)_4(OMe)$ at m/z 631.15 whilst its tetrameric analogue $T_4(OPr)_5(OMe)$ at m/z 809.14 is present in very low abundance.

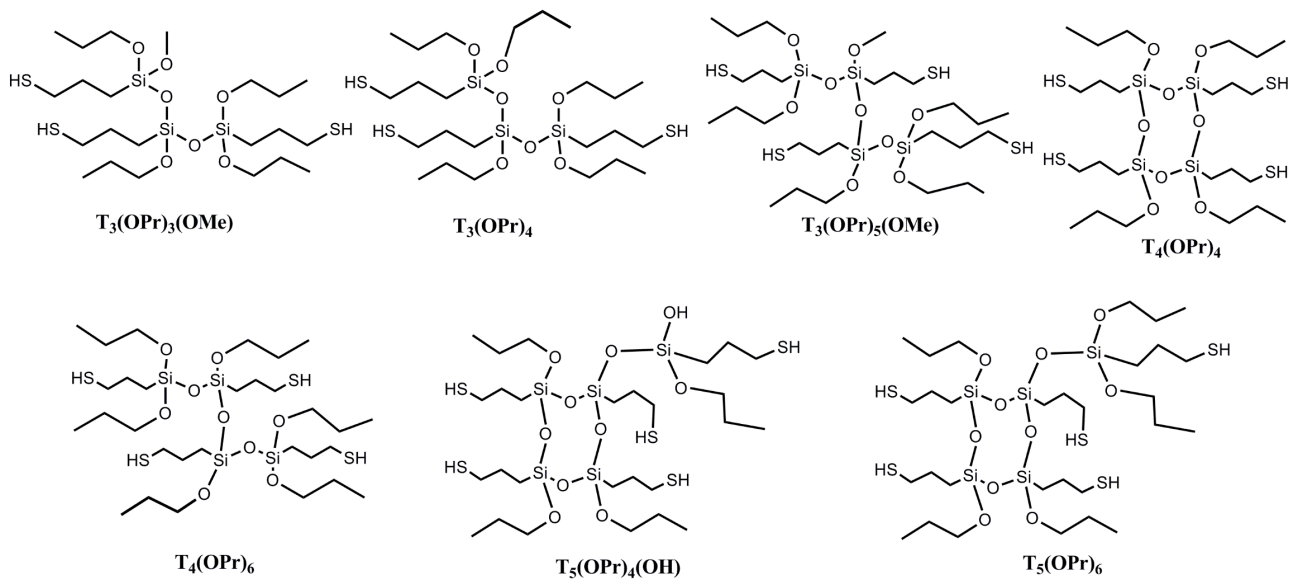

Figure 89 . Structural assignments of the signals detected in MALDI-TOF spectra of DBTL1

It worth of note that MALDI-TOF spectra of samples obtained in water under-stoichiometric conditions (r = 1) confirm the formation of small linear T_3 species followed by minor amount of T_4 and T_5 cyclic species.

The spectra of sample DBTL6 (see Appendix A) obtained in over-stoichiometric conditions (r=6) strongly indicate that major ions were attributable to multimeric cyclic (open cages and ladder-like) species within the range T_3-T_8 in structures although no signal could be attributed to closed T_8 cages. However, the low accuracy in the ion-mass detection due to difficulties to obtain optimal matrix/sample ratio and the presence of different pseudo-molecular ions (M+H, M+Na and M+K) for every species, affords broad spectra of great complexity thus hindering the evaluation of ions exact masses and their structural assignment**.**

3.4 Kinetics of NBBs growth: Results and Discussion

According to FTIR, NMR and GPC results, both the condensation degree and the amount of cage structures increase using TFA and increasing the value r. Only in over-stoichiometric conditions, the structural development appears unaffected by the used catalyst. The products obtained using DBTL and TFA present the same condensation degree, cage-to-ladder ratio and distribution of molecular species, according to the GPC results. The presence of TFA makes difficult to assess the dependence of silsesquioxane growth on the theoretical amount of water provided by ISWP, since TFA also interfere in the esterification process. Consequently, DBTL creates the most favorable conditions for relating the oligomers growth to the parameter r.

The MALDI-TOF spectra acquired on DBTL1 (under-stoichiometric ISWP conditions) clearly demonstrate the limited crosslinking process leading mainly to the formation of small linear T_3 species and minor amount of T_4 and T_5 cyclic species. On the contrary, the sol-gel reactions run in water over-stoichiometry conditions (DBTL6) drive the network to develop T_3-T_8 oligomers organized as multimeric open cages and ladder-like species. Further optimization of the hydrolysis-condensation extent with preferential cage-like and ladder-like small oligomers formation can be reached by time-dependent analysis. The introduction of additional processing variables such as the different reaction's temperature (room temperature (RT) in contrast to 100°C) allows to follow the kinetics of NBBs structural development at the early stages of Sol-Gel reaction and unravels the competition features of hydrolysis vs. transalcoholysis reactions.

According to the above conclusions, the over-stoichiometry conditions (sample DBTL6) were chosen for the reaction kinetics study.

3.4.1 FTIR Characterization of the NBBs growth

In order to follow structural development and growth of NBBs, the FTIR spectra were acquired on solutions reacted at 100°C after different reaction times from 2 to 380 hours, without solvent removal. The stack plot of the DBTL6 sample reacted for 2, 6, 24, 72, 96 and 380 hours is shown on the Figure 90. The pristine solvent, acid and by-products are present in the analyzed samples.

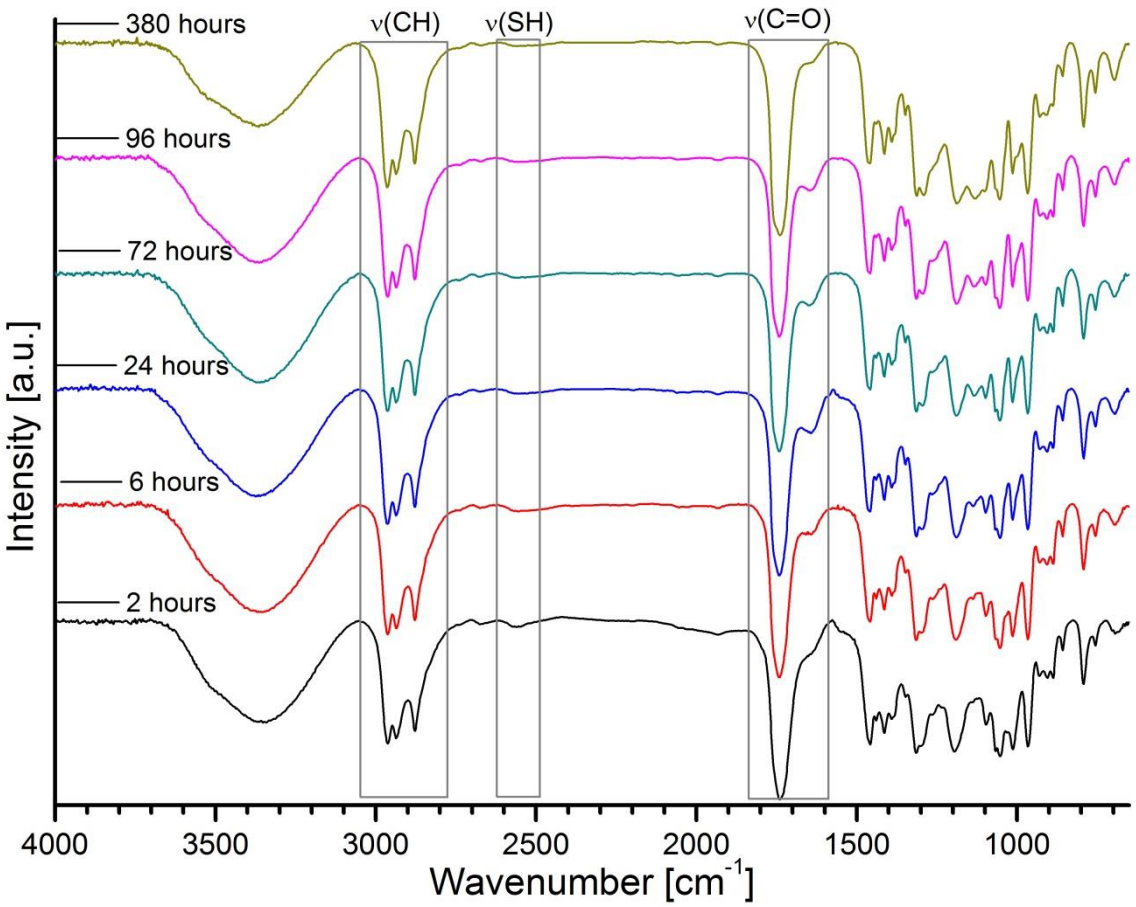

Figure 90 . FTIR transmission mode spectra of DBTL6 sample collected after different reaction times.

The presence of the thiol function of McPTMS is confirmed after all reaction times by the detection of the weak S-H stretching vibration at 2559 cm^{-1}. Minor broadening and decrease in intensity is observed with increasing reaction time. The C-H stretching

vibrations give rise to a strong complex band in the range 3000 - 2800 cm^{-1}, due to the overlapping of several signals, but predominantly originated from 1-PrOH. The signals at 2962 and 2875 cm^{-1} are due to asymmetric and symmetric stretching modes of methyl groups in the organic chains. The vibrations at 2931 cm^{-1} (ν_{as}) and a shoulder at 2855 cm^{-1} (ν_s) can be assigned to the overlapping methylene groups of mercapto-propyl chain and 1-propanol. The intensity of a) the O-H stretching band at 3350 cm^{-1} , as well as b) the C=O stretching vibrations band at 1760 and 1730 cm^{-1} of the pristine carboxylic acid and formed ester, and c) C-H stretching vibrations of 1-PrOH exhibit constant value throughout investigated time range, as expected. The 1200–900 cm^{-1} range, due to ν_{as} Si-O stretching vibrations carries valuable information on the structural development (Figure 91).

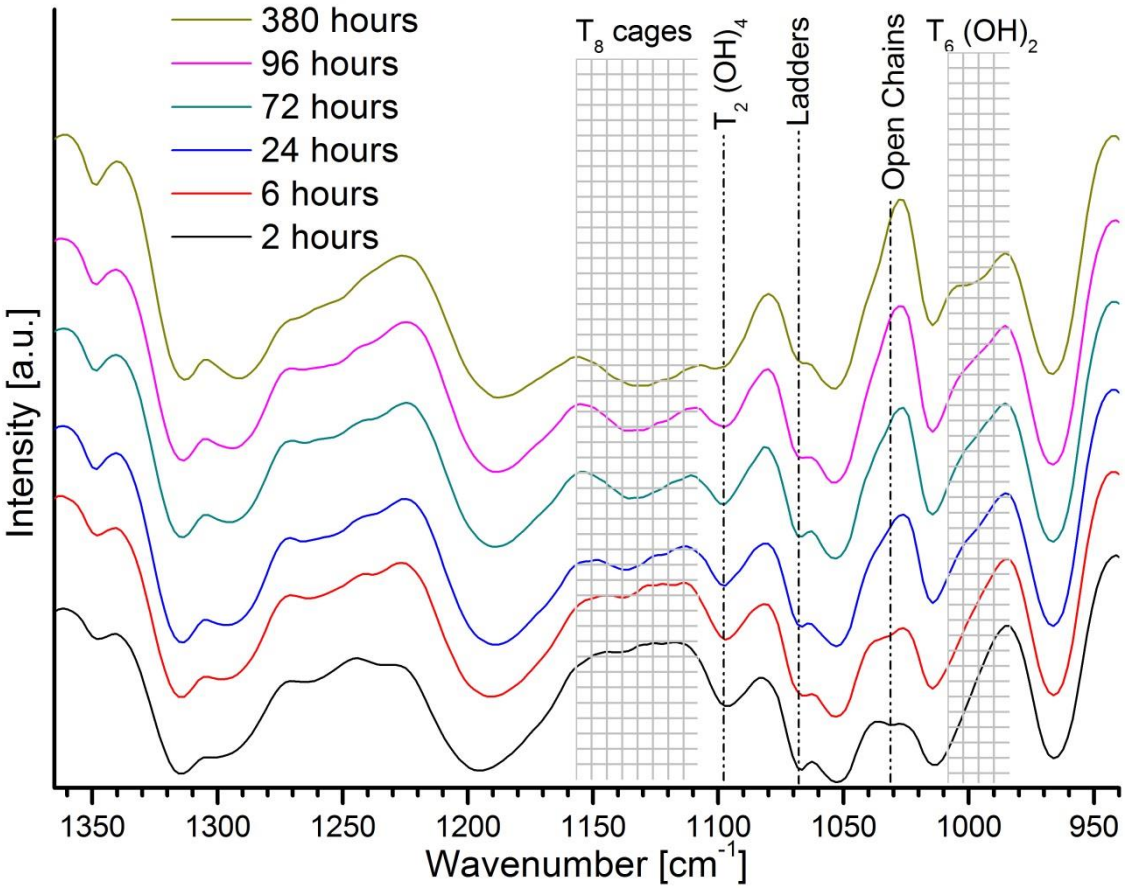

Figure 91 . FTIR spectra of DBTL6 in siloxane region versus reaction time.

The assignment of the species is complicated by the presence of pristine reagents and by-products in analyzed solutions, however the main components of the siloxane band

as open chains, ladder-like structures and cage-like species can be followed in their development in time (see Figure 80 for main species assignment).

The band at 1033 cm^{-1} that can be attributed to the open chains [202], is visible at the early stages of reaction, but begins to fade already after 6 hours of reaction, due to further condensation into more complex systems, and fully disappears after 72 hours. Generally speaking, such behavior is expected also for the $T_2(OH)_4$ species with corresponding band at 1095 cm^{-1}, since they possess four –OH groups for condensation.

However, it appears that strong bands at 1097 cm^{-1} and 1053 cm^{-1} of 1-propanol, highly abundant in sols, contribute to $T_2(OH)_4$ and also to $T_7(OH)_3$ ladder-type species region, turning the trend analysis complicated. Nevertheless, the band at 1067 cm^{-1}, attributed to $T_7(OH)_3$, keeps constant intensity from the first hours of reaction till 72 hours, when it begins to fade in contrast to the one at 1053 cm^{-1} of 1-propanol, suggesting ladders rearrangement after 72 hours of reaction. Indeed, the behavior of the band at 996 cm^{-1}, attributed to $T_6(OH)_2$ open cages, is opposite, showing the gradual intensification of related shoulder after 24 hours of reaction.

The band around 1130 cm^{-1} can be attributed to T_8 cage-like species, and is slightly shifted towards higher frequencies in comparison with the dried sample, which presented the same vibration at 1125 cm^{-1} (Figure 80). The amount of T_8 cage-like species increases starting from 2 hours and reaches its maximum by 72 hours of reaction, when the corresponding peak keeps constant intensity till 380 hours of reaction.

From the FTIR spectra, it can be concluded, that already from the early stages of reaction (6 hours at 100°C) open chains and linear $T_2(OH)_4$ species tend to recombine into cage-like structures, reaching maximum yield of T_8 cage-like species by 72 hours. The analysis of ladder-like species evolution is difficult due to the overlapping of the strong 1-

PrOH signals, however it is possible to envisage also their rearrangement after 72 hours of reaction.

The time–dependent evolution at room temperature is not presented: the low temperature process leads to very small changes in structure that are quite difficult to be analyzed by FTIR.

Multinuclear NMR study of NBBs growth

The multinuclear NMR study of kinetics of the NBBs growth was performed in the frame of the collaboration between the Materials Chemistry Group at the University of Trento (prof. S. Dirè) and the Laboratoire de Chimie de la Matière Condensée de Paris-UPMC, Collège de France (Dr. F. Babonneau). Thanks to both the bilateral agreement between University of Trento and Collège de France and the COST Action MP1202 ("Rational design of hybrid organic/inorganic interfaces: the next step towards advanced functional materials", 2012-2016), during a four months stage it was possible to run in collaboration with Dr. Francois Ribot at UPMC - Collège de France several experiments, which gave strong improvement on the elucidation of NBBs growth pathway .

3.4.1 ^{1}H NMR Characterization of the NBBs growth

In order to follow the development of the Sol-Gel and esterification reactions, the ^{1}H NMR spectra were acquired for solutions reacted either at 100°C or at room temperature (RT) after different reaction times from 0.5 to 96 hours. For the analysis of the RT kinetics, the reaction mixture was introduced into the NMR tube equipped with D_2O capillary under nitrogen atmosphere, sealed and left reacting inside the NMR instrument for continuous measurements of both ^{1}H and ^{29}Si nuclei at 23° C. For monitoring the 100°C reaction, samples were extracted from the reaction solution at fixed time intervals, the extracted volume was rapidly cooled down, inserted into NMR tubes with D_2O capillary under nitrogen atmosphere, and sealed before measurements.

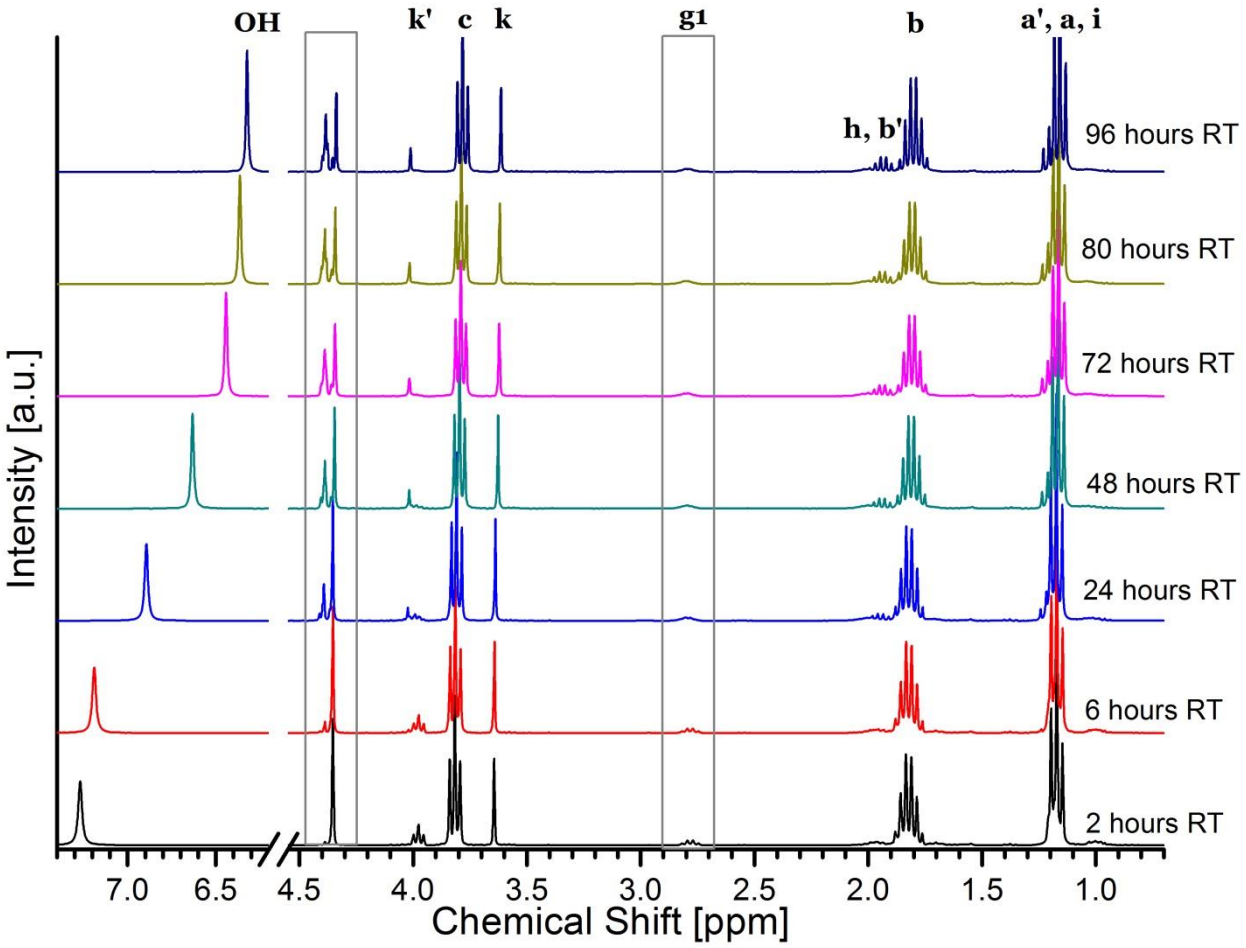

Figure 92 . ^{1}H NMR spectra of DBTL6 sample reacting at RT versus reaction time.

^{1}H NMR spectra evolution during reaction at RT is presented on the Figure 92. The labeling used for assignment of the peaks is shown in the Figure 93. The region from 2.7 ppm to 2.9 ppm is enlarged on the Figure 94 to control throughout the reaction the presence of the quadruplet at 2,73 ppm attributed to Si-$CH_2CH_2\underline{C}H_2$ –SH (g1). The peak broadening at higher reaction times is due to the loss of instrumental shim and does not reflect reaction development. The region from 4.22 ppm to 4.42 ppm is also enlarged to follow the progress of the esterification reaction, since the peaks attributed to pristine Cl-AA (**e**) and produced Methyl-Chloroacetate (**e'**) and Propyl-Chloroacetate (**e"**) are weak in intensity and overlapped with each other (Figure 94 - left).

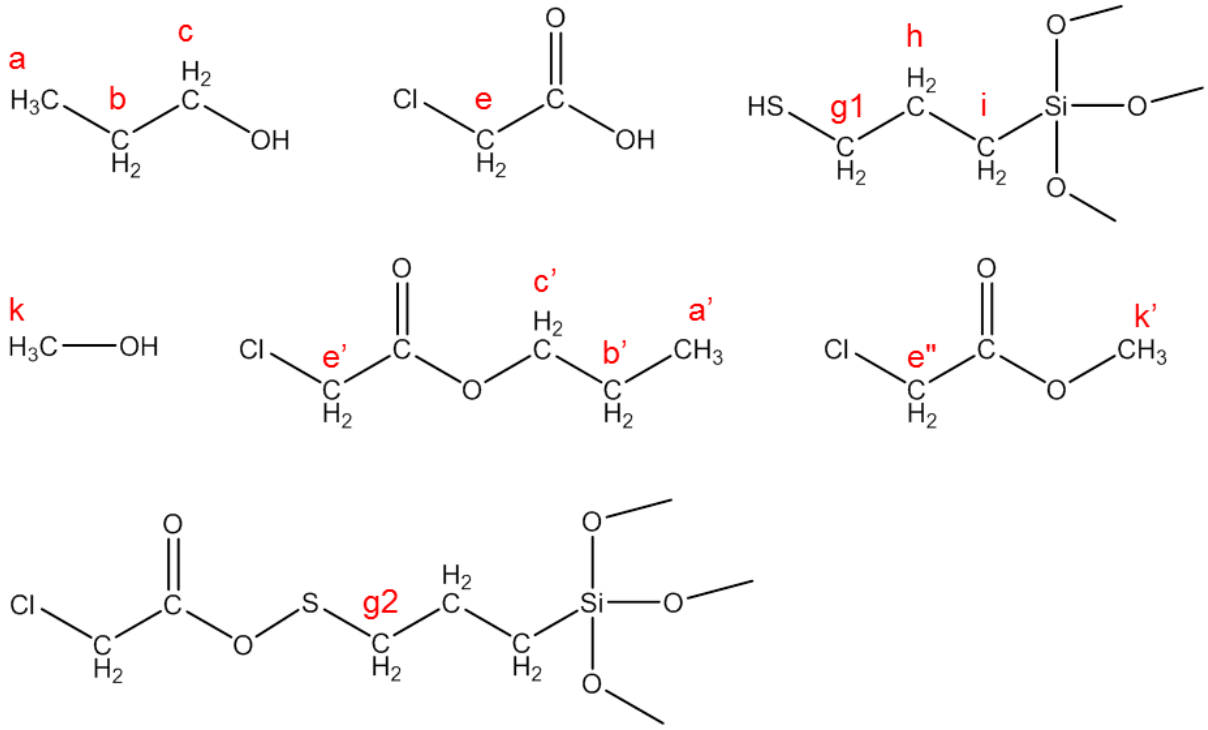

Figure 93. ^{1}H NMR labeling of reagents and products of reaction.

The high field region (around 1 ppm in the Figure 92) is crowded by overlapping signals of –CH_3 protons of propyl chain in both 1-PrOH(**a**) and propyl-chloroacetate (**a'**) as well as Si-$C\underline{H}_2CH_2CH_3$–SH(**i**). However, the development of (**a'**) with increasing reaction time is clearly seen, as conditioned by the production of propyl-chloroacetate. This ester also contributes to the group of peaks around 1.85 ppm, which is composed by (from left to

right) Si-$CH_2\underline{C}H_2CH_2$ –SH(**h**); sextet attributed to (**b'**) of propyl-chloroacetate; and sextet (**b**) of 1-PrOH. The singlet, found at 3,58 ppm, suggests that methanol was released already at the early stages of reaction by either hydrolysis or transalcoholysis reactions. The singlet at 3,97 ppm, attributed to methyl-chloroacetate (**k'**) suggests that released methanol undergoes esterification reaction with ClAA, competing with 1-PrOH, from the early stages of reaction. The position of –OH group is drifting towards high fields with reaction duration, suggesting the change of reaction mixture polarity, which may be explained by ClAA consumption by esterification reaction.

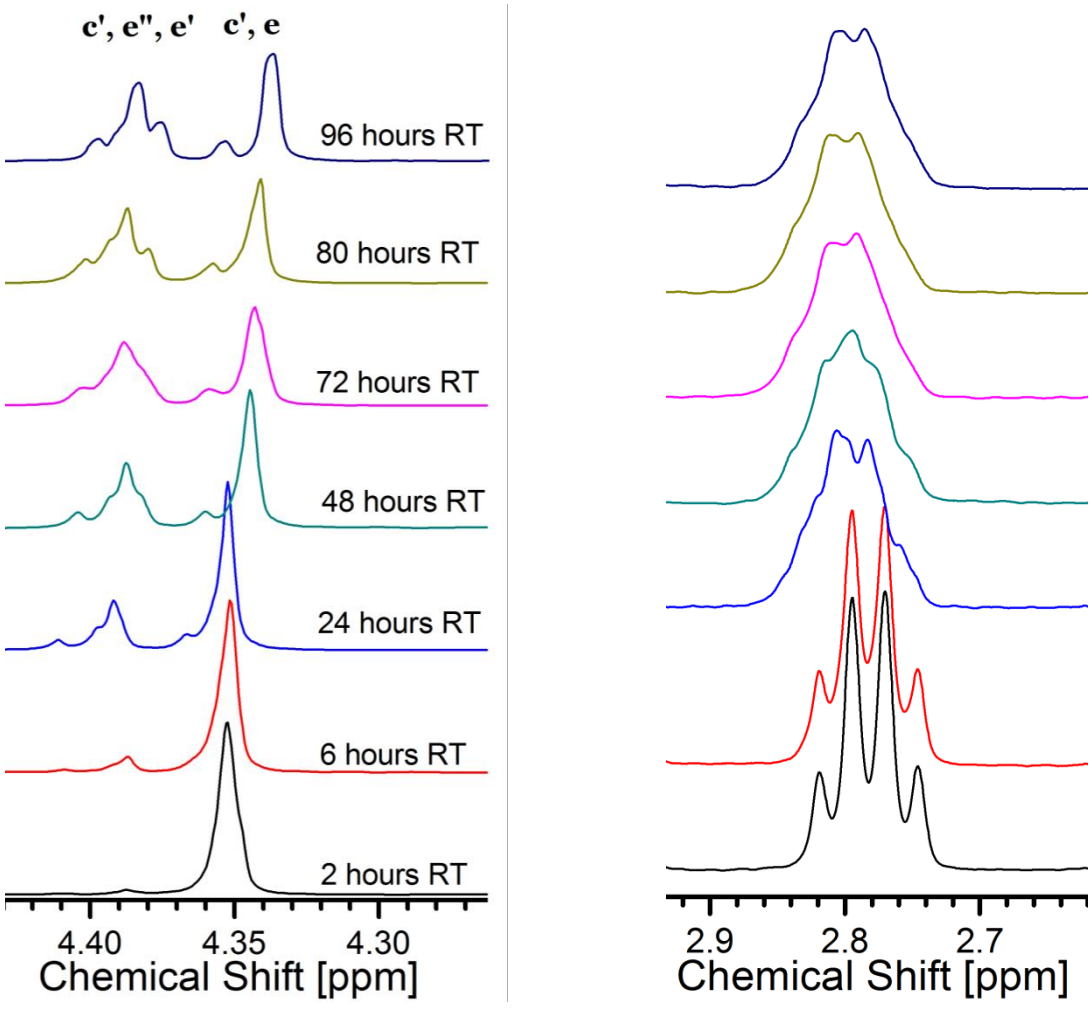

Figure 94. ^{1}H NMR enlarged regions for monitoring the development of esterification reaction (left) and maintenance of –SH function throughout reaction (right).

It can be concluded from above ^{1}H NMR spectra discussion, that even at RT, the esterification reaction occurs already at the early stages of reaction. However, since the amount of available water needed for McPTMS hydrolysis-condensation depends on the kinetics of esterification reaction, the profound analysis of the region of 3.9-4.4 ppm in ^{1}H NMR spectra is demanded to calculate the content of water produced In-Situ. For such calculations, the overlapping components (Figure 94 - left) attributed to Cl-AA (**e**), Methyl-Chloroacetate (**e'**) and Propyl-Chloroacetate (**e"**), were separated by deconvolution and the integral areas of corresponding fitting peaks were used in the following equation, which derived the water molecules amount in respect to the initial ClAA amount:

$$A(H_2O) = \frac{1}{2} * e'/(\frac{e + e' + e''}{12}) + \frac{1}{2} * e''/(\frac{e + e' + e''}{12})$$

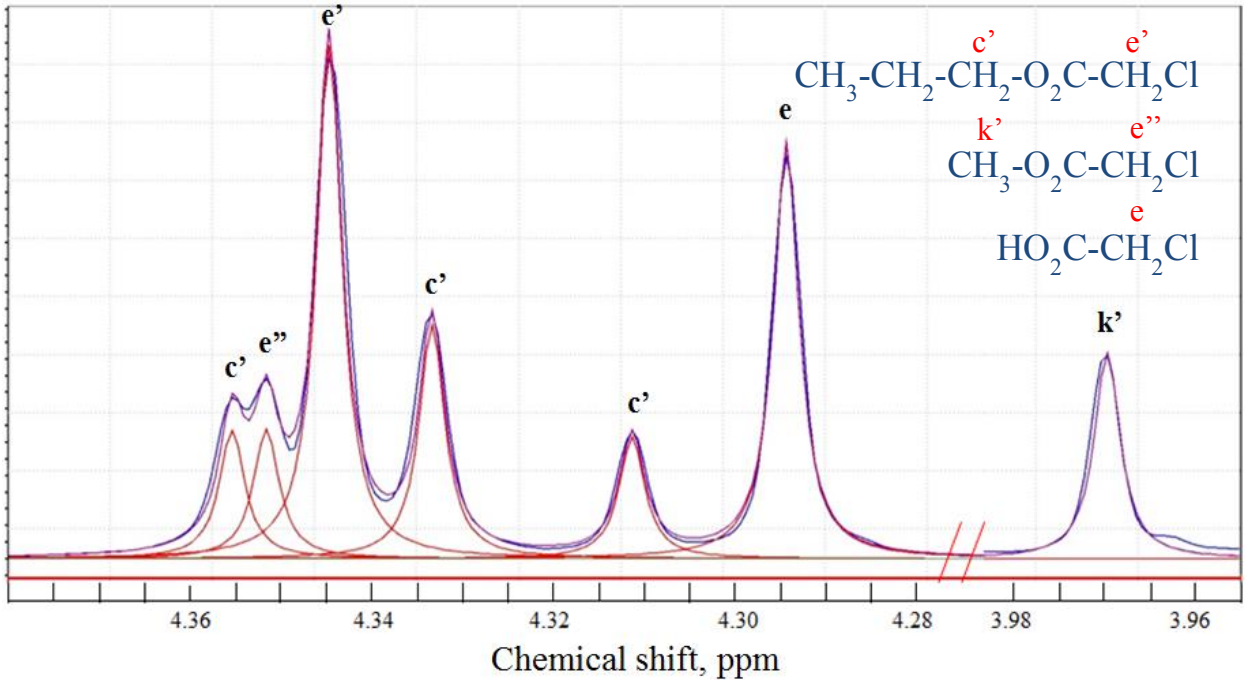

Figure 95. ^{1}H NMR spectrum fitting example for in-situ water amount calculations.

The same procedure was applied to all spectra, recorded at each reaction time step for both RT and 100°C reactions, where the peaks were resolved enough for the deconvolution. Figure 95 represents an example of the fitting procedure applied to the

NMR peaks of the sample reacted for 24 hours at 100°C. Table 10 contains the values of calculated water amounts in percentages referring to the maximum theoretical amount that can be produced by ClAA.

Reaction time at 100°C, h	1	2	3	15	24	48
Water amount, %	46.28	60.56	68.96	84.91	91.20	86.42
Reaction at Room Temp, h	18	26	34	50	74	84
Water amount, %	15.55	24.11	27.89	32.57	39.45	44.92

Table 10. Calculated amount of water produced In-Situ at 100°C and RT.

It is noteworthy to say, that In-Situ water production at room temperature yields only 45% of theoretical amount by 84 hours of reaction, whereas the same amount of water is produced by 1 hour if the temperature is increased to 100°C. The maximal water production at 100°C is reached by 24 hours with the value of 91% of theoretical amount.

3.4.2 ^{29}Si NMR Characterization of the NBBs growth at RT

In order to follow the evolution of the pristine McPTMS and NBBs growth as a consequence of hydrolysis-condensation and transalcoholysis reactions, the ^{29}Si NMR spectra were acquired. As observed with proton NMR, the release of methanol can be due to either hydrolysis or transalcoholysis reactions occurring on the early stages of RT reaction. The number of different Si-based monomer species that theoretically can be formed due to both transalcoholysis and hydrolysis reactions is ten, and all of them may be identified by the high resolution ^{29}Si NMR. The main problems in silicon nucleus observations with NMR are that the natural abundance of ^{29}Si isotope is only 4,67%, and the T_1 relaxation times in liquid are quite long (starting from 5 s); thus the experimental time needed for reasonable S/N ratio spectra acquisition can exceed the time after which the subjected system changes. So, the profound analysis of fast reacting system by means of ^{29}Si NMR is possible only if polarization transfer from abundant nucleus as proton to less receptive silicon is exploited.

DEPT (distortionless enhancement by polarization transfer) pulse sequence was employed to obtain spectra with a good signal-to-noise ratio in 30 min, allowing to properly monitoring the species along the ageing time. Since polarization transfer functions for different Si units can vary depending on the number of vicinal protons, participating in polarization transfer, the quantitative interpretation must be considered very carefully. For instance, the hydrolysis reaction of McPTMS replaces CH3 groups, bearing three protons, with OH groups, having just one proton: since the DEPT sequence is very sensitive to the proton amount, such spectra should not be interpreted quantitatively but just qualitatively analyzed. Nevertheless, the T^0 species identification at the early stages of reaction at RT was only possible by using the DEPT sequence. The stack plot of spectra in the time range of 2,5 -72 hours is presented on the Figure 96.

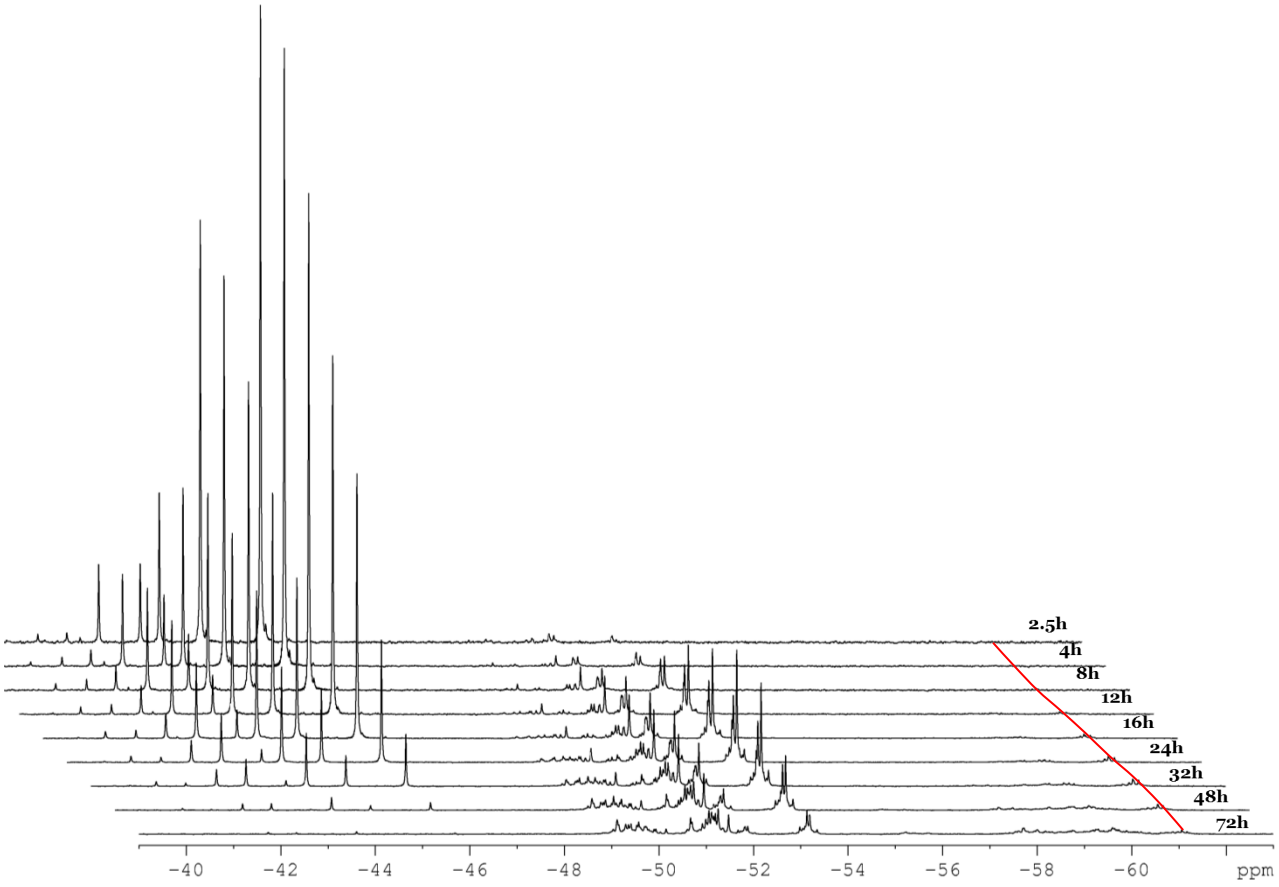

Figure 96. ^{29}Si NMR DEPT spectra versus reaction time at RT (from top to bottom: 2,5; 4; 8; 12; 16; 24; 32; 48; and 72 hours of reaction)

The condensation of the reacting monomers results in the replacement of Si-OR groups by Si-O-Si, and this is indicated in the NMR spectrum by highfield shifts caused by the increase in negative electron density of the oxygen [220]. This leads to three separated groups of peaks corresponding to the number of Si-O-Si bridges: T^0 (39 -43 ppm), T^1 (48-54 ppm), T^2 (56-62 ppm).

T^3 units were not formed yet after 72 hours of reaction at RT, thus the corresponding spectral range (63-70 ppm) is not presented. As can be seen on the Figure 96, T^2 units (red curve) appear only after 10 hours and weakly develop in time, demonstrating low extent of condensation in NBBs in the evaluated time range. The signal of pristine McPTMS can be found till 48 hours of reaction, however from the first hours, vast amount of monomers are formed as the T^0 range clearly shows. The identification of

these monomers is of the most interest, and the T^0 range is presented enlarged on the Figure 97.

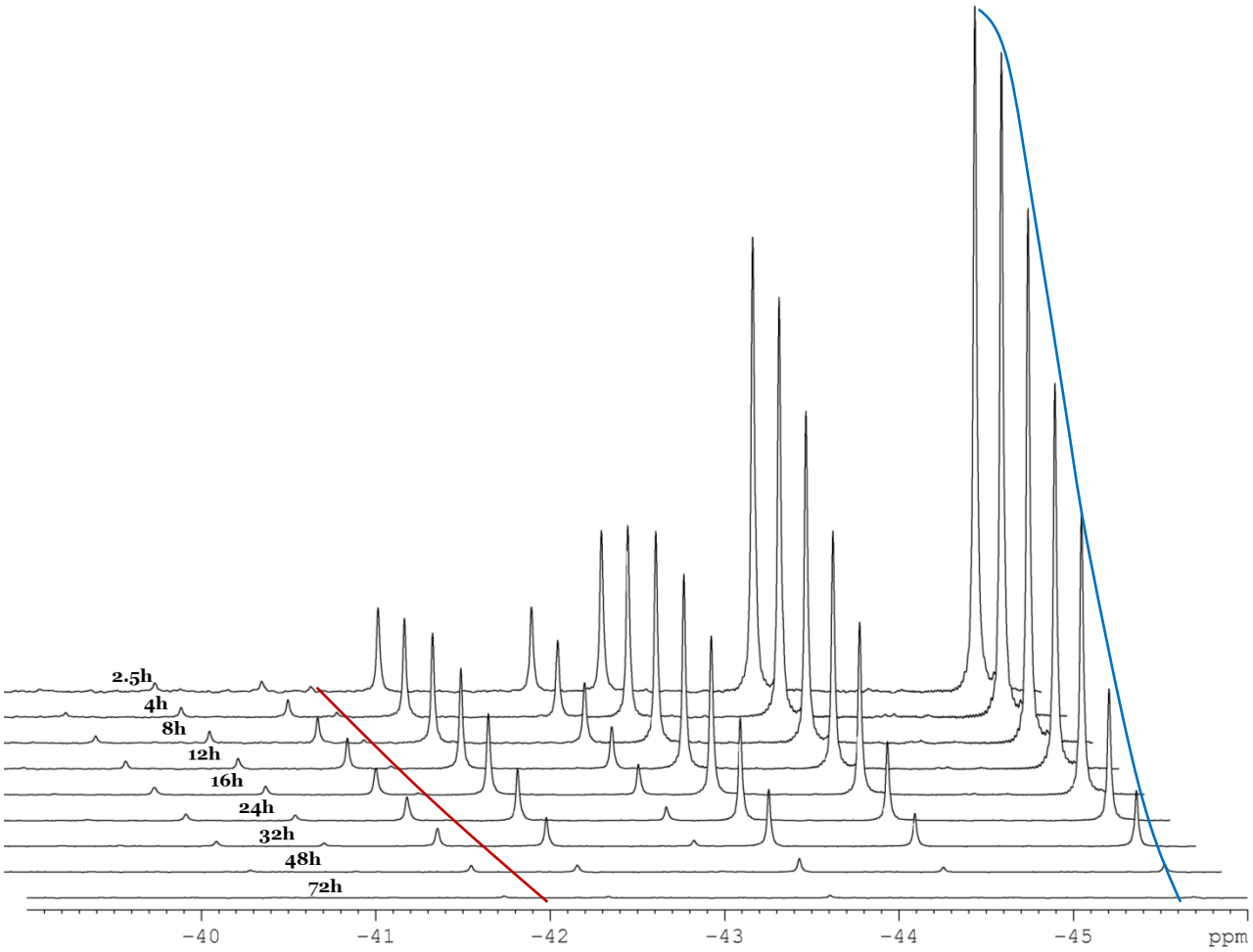

Figure 97. T^0 region of ^{29}Si NMR DEPT spectra versus reaction time at RT

The monomers formed at RT by hydrolysis and transalcoholysis reactions were traced according to their chemical shifts in analogue to [229, 230]. The substitution of an alkoxy group by an -OH group induces a conventional downfield shift by value of 0.90ppm - 0.60ppm for the replacement of a methoxy group and 2.14ppm - 1.78ppm for a propoxy group. The decrease of downfield shift nominal value with increase in amount of –OH groups on Si atom can be caused by the steric effect, as described in [231]. On the contrary, the shifts observed towards high fields can be attributed to the substitution of methoxy groups by propoxy groups, supplied by 1-PrOH. The value of such highfield shift is of about

-1.25 ppm regardless to the amount of –OH groups in the monomers. The full assignment of the species in T^0 region is presented on the Figure 98, where the substitution of methoxy group by –OH group is marked by green arrow; replacement of methoxy by propoxy group is marked by red arrow; and substitution of propoxy group by –OH group is marked with blue arrow.

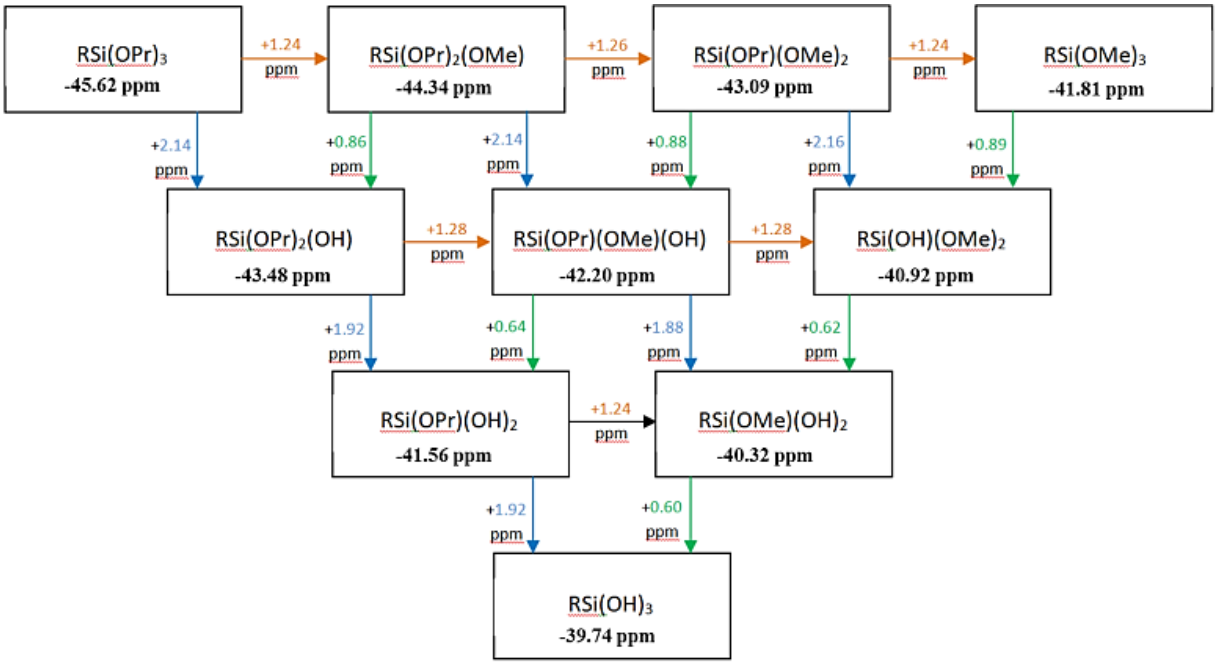

Figure 98. ^{29}Si NMR at RT, T^0 species assignments and substitution rules, R=$(CH_2)_3$-SH

It is very intriguing, but fact, that the transalcoholysis reaction took place immediately from the beginning of reaction. Propoxy groups of 1-PrOH almost fully substituted the methoxy groups of the pristine McPTMS, since the peak at -45.62 ppm, attributed to $RSi(OPr)_3$ (blue curve) is the most intense from the first stages of reaction, and the peak at -41.81 ppm, assigned to $RSi(OMe)_3$ (red curve) is very weak. The signal at -39,74 ppm is almost negligible, but it is not clear if the lifetime of $RSi(OH)_3$ species is very short due to high probability of further condensation or the polarization transfer function is not even for these species. Same concerns exist for other species bearing –OH group, but in a less extent.

3.4.3 ^{29}Si NMR Characterization of the NBBs growth at 100°C

As expected from the FTIR observations and the ^{1}H NMR results, the increase in temperature also affects the hydrolysis-condensation reaction rates. The Single Pulse experiments and DEPT pulse sequence were employed for the description and quantitative evaluation of structural units. The Single Pulse sequence allowed to obtain spectra after significantly longer acquisition (ten times more than DEPT spectra) and lower signal-to-noise ratio, but without any interference related to structural properties of NBBs. On the other hand, the DEPT sequence allowed the acquisition of high quality spectra in short time. Both spectra were compared by means of relative intensities of T^0-T^3 units at selected reaction times, and the integrated values are presented on the Figure 99.

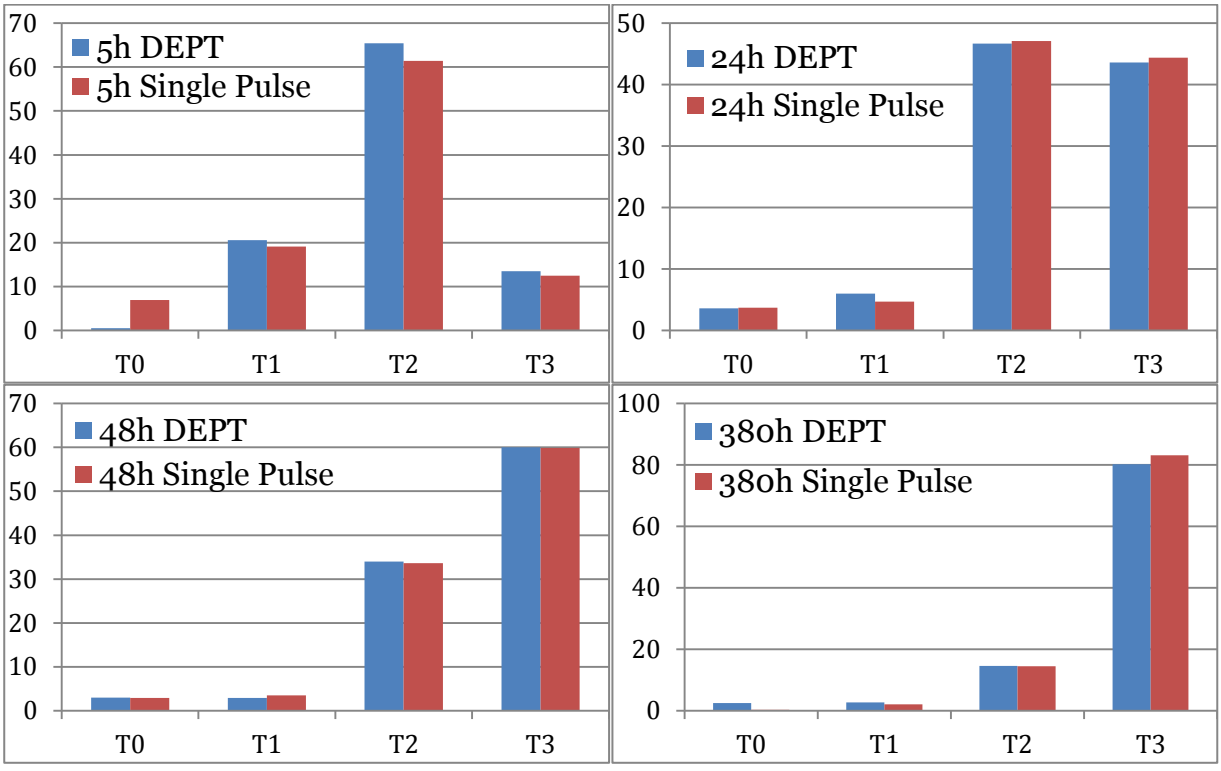

Figure 99. Comparison of the integrated areas of T^0-T^3 units of spectra acquired by DEPT and Single Pulse sequences for 5, 24 48 and 380 hours reactions.

As it can be seen, the integrated values from the two experiments are in agreement with good confidence, with exception of T^0 units after 5 hours reaction, allowing to quantitatively analyze DEPT spectra acquired from early reaction stages to 380 hours with no restrictions.

Figure 100 represents ^{29}Si spectra, acquired with DEPT sequence and highlights the changes that species undergo from 0,5 to 48 hours of reaction at 100°C.

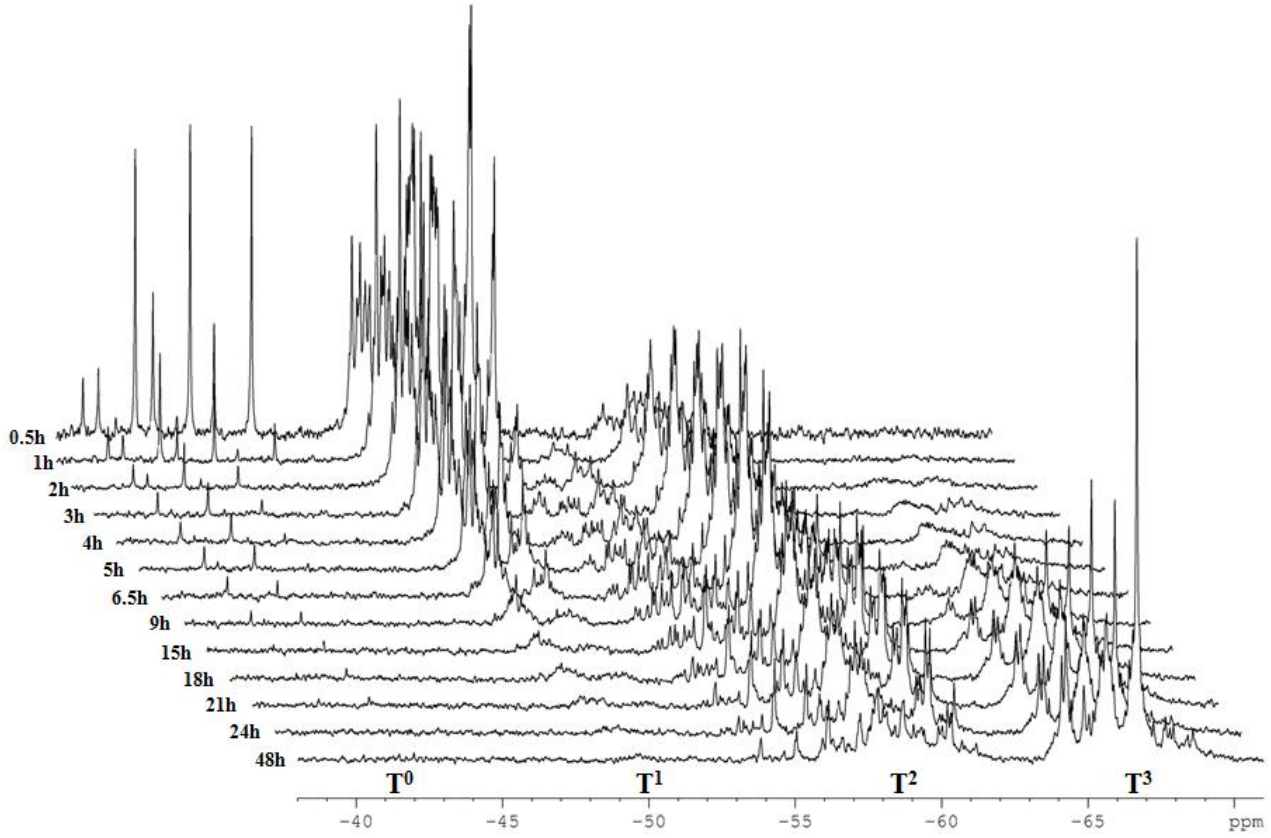

Figure 100. ^{29}Si DEPT spectra of thiol functionalized NBBs versus reaction time at 100°C.

The structural evolution is characterized by gradual decrease of T^0 and T^1 units in time, recombination of T^2 species and formation of T^3 oligomers, which are represented by three main groups of peaks (Figure 100). Fast decrease in amount of T^0 units within the early stages of reaction at 100°C suggests that fast hydrolysis of McPTMS leads to rapid partial condensation of monomers into various dimers (T^1 region).

Since the acquired spectra represent quantitative distribution of all detected species, the T units development in time can be followed in comparison to calculated amount of water produced in situ. The integrated amounts of T^n units are presented versus reaction time at 100°C together with in situ water contents at both RT and 100°C temperature conditions in the Figure 101.

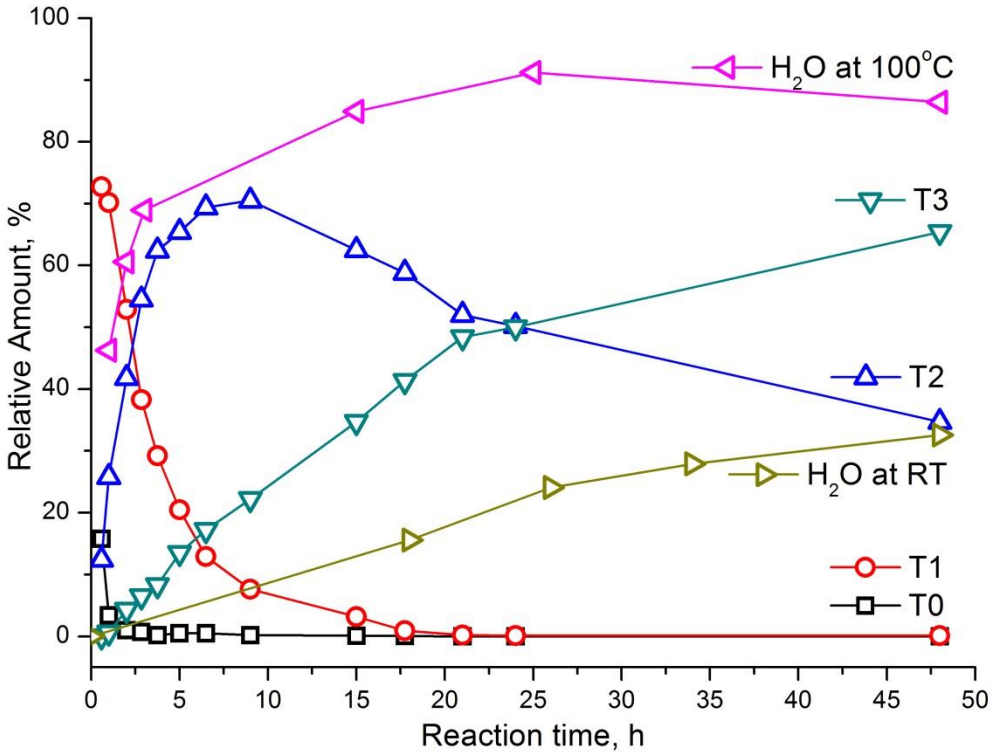

Figure 101. Evolution in time of T-species and In Situ produced water at 100°C and RT, respectively.

The esterification reaction at 100 °C after 1 h leads to the availability of an amount of water that is about the same provided after 48 hours at room temperature. T^3 units start to appear already after 2 hours, when the water content reaches more than 60% of theoretical amount, and increase almost linearly in quantity till 24 hours, when the maximal amount of available water (91%) is reached. If compared to room temperature reaction, where T^3 units were not detected after 84 hours with 45% of water produced by that time, it appears that the development of T^3 units is possible only with a threshold

amount of available water. At 100 °C, T^3 units become the main species after 24h, reaching a value of 65 % after 48h reaction. These facts, the appearance of T^3 units after 2 hours and their evolution to become the main species after 24 hours of reaction are in a good agreement with time dependent trend of cage-like species detected by the FTIR analysis of the reaction run at 100 °C.

The degree of condensation (DOC), represented by the following equation:

$$DOC = \frac{T^1 + 2T^2 + 3T^3}{3\left(T^0 + T^1 + T^2 + T^3\right)} \times 100$$

was calculated for each analyzed step of 100 °C reaction and is graphically represented on the Figure 102. The DOC of the sample reacted at RT is also shown, but can only be considered as a semi-quantitative result due to the previous discussion of the effective polarization transfer of exploited DEPT pulse sequence.

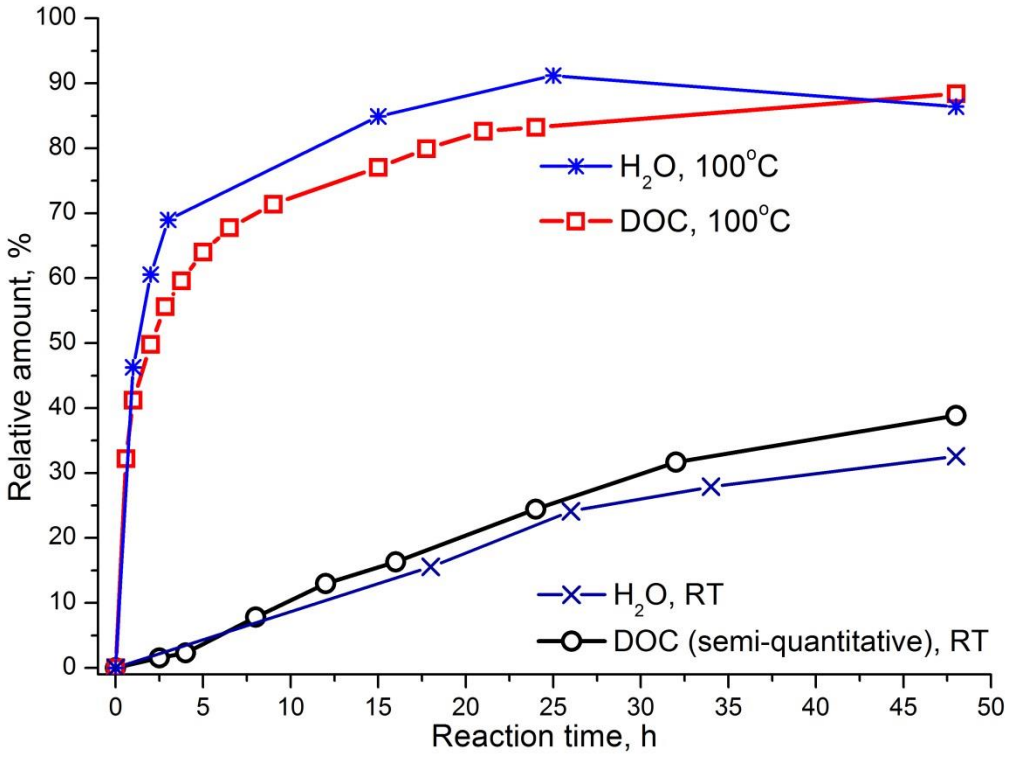

Figure 102. DOC versus reaction time with In Situ produced water for 100°C and RT.

DOC follows the same trends as amount of water, produced in situ with increasing reaction time for both RT and 100°C reactions, highlighting strong relation of H_2O availability to condensation extent. Nevertheless, the detailed analysis of NBBs evolution in time can demonstrate particular features of dependence of structural development on the water availability.

The behavior of T^0 units (-39 ppm – 45,5 ppm) at 100°C (Figure 103) differs from the room temperature conditions, such as the $RSi(OPr)_3$ (blue line in Figure 103) monomers are rapidly consumed by 1 hour of reaction; however, $RSi(OPr)_2(OMe)$ (green line) and $RSi(OPr)(OMe)_2$ (red line) monomers survive till 5 and 21 hours respectively.

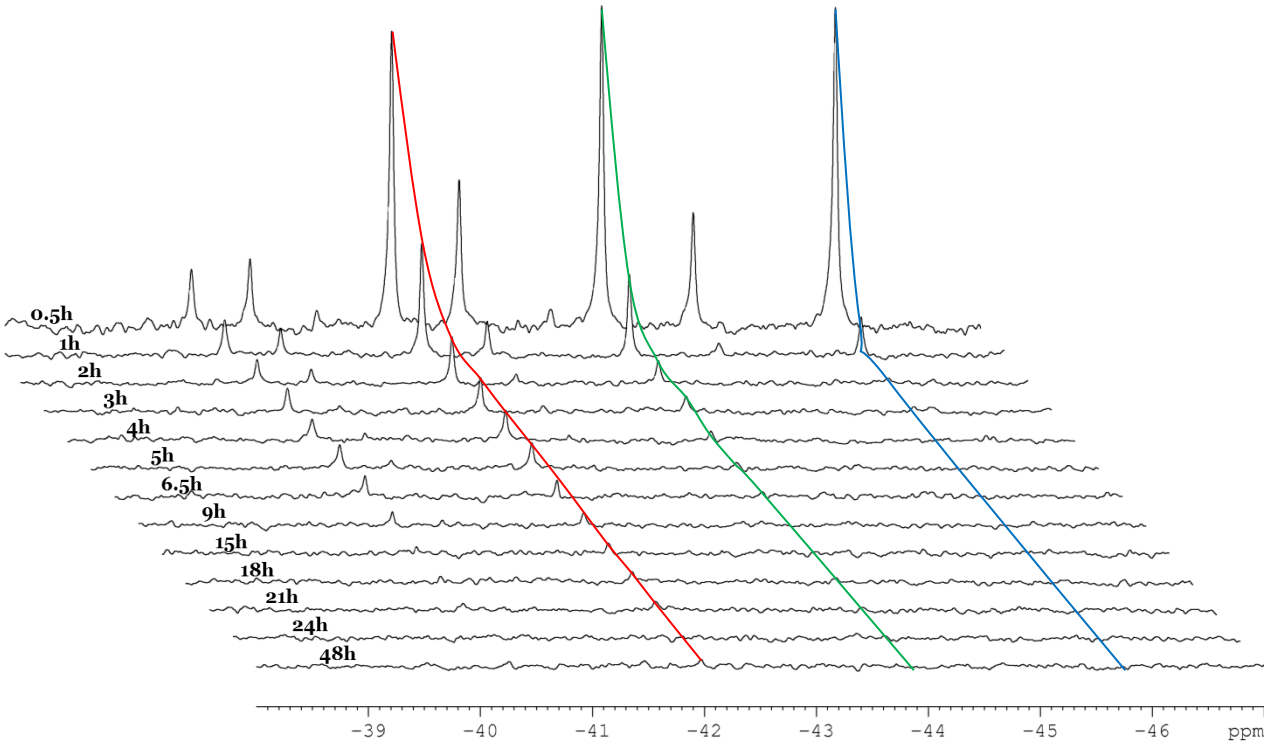

Figure 103. T^0 range of ^{29}Si DEPT spectra of NBBs versus reaction time at 100°C (0.5-48h).

Resonances attributed to partially condensed species from -47 to -63 ppm (T^1 and T^2) represent superposition of a vast number of individual components, which differ by alkoxy/-OH functions and structural features. The regions are enlarged on the Figures 104 and 105 for T^1 and T^2 regions respectfully.

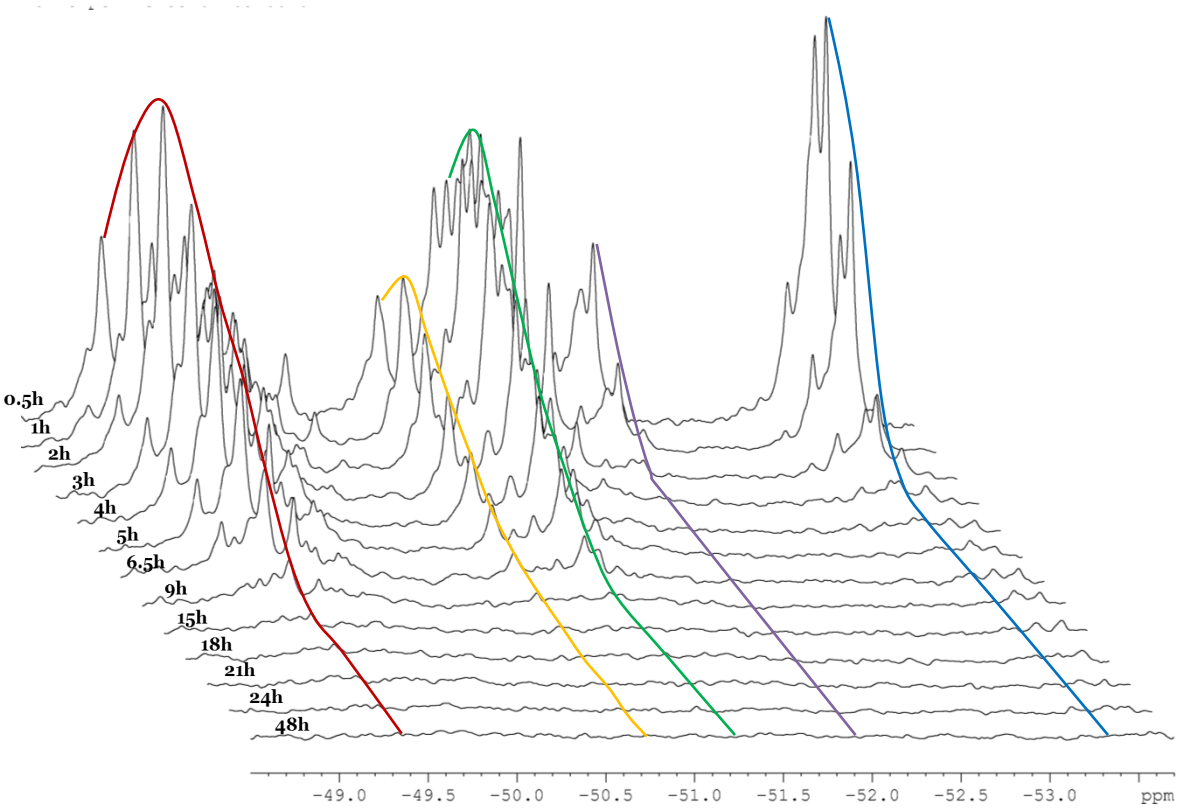

Figure 104. T^1 range of ^{29}Si DEPT spectra of NBBs versus reaction time at 100°C.

The T^1 region can be divided into 3 groups of signals centered at -49.4 ppm, -51,25 ppm and -53.5 ppm. The most high field shifted signal is due to $T_2(OPr)_4$ linear dimers (blue line in Figure 104). The two overlapped peaks at -52 ppm can be attributed to $T_2(OPr)_3(OH)$ and $T_2(OPr)_2(OMe)(OH)$ species (violet), which are quickly consumed by further condensation already by 2 hours of reaction. The green curve on the Figure 104 corresponds to the group of $T_2(OPr)(OMe)_3$, $T_2(OPr)_2(OH)_2$, $T_2(OPr)(OMe)_2(OH)$, whereas the yellow curve at -50,75 ppm is attributed to long lasting $T_2(OMe)_4$ dimers. The rapidly consumed $T_2(OMe)_3(OH)$ species showed their resonance during the first 2 hours at -50 ppm. The group of peaks, centered at -49.4 ppm can be assigned to $T_2(OMe)_2(OH)_2$ and $T_2(OPr)(OMe)(OH)_2$ species; however, they are expected to be consumed on the early stages of reaction in analogue to the other hydrolyzed dimers. Thus, the assignment of the group of resonances at -49.4 ppm can be argued in the favor of terminal T^1 units of linear species, or those participating in branching of T^3 units species, and possessing two –OH

groups. Same conclusions can explain the overcrowding of the sub-region form -50,5 to -52 ppm.

Figure 105 presents the T^2 region with the vast amount of signals, which undergo broadening with reaction time, suggesting the development of variety of species. Detailed analysis and species attribution are therefore complicated, but nevertheless the sub-groups assignment can be performed. Formation of the cyclic species and their further rearrangement to more complex architectures is a known feature of silsesquioxanes polymerization under acidic conditions [219, 220]. The signals of cyclic products show a low field shift in comparison to the linear T^2, because the cyclization reduces the valence angles, and so the density of positive charge on Si atom reduces [206].

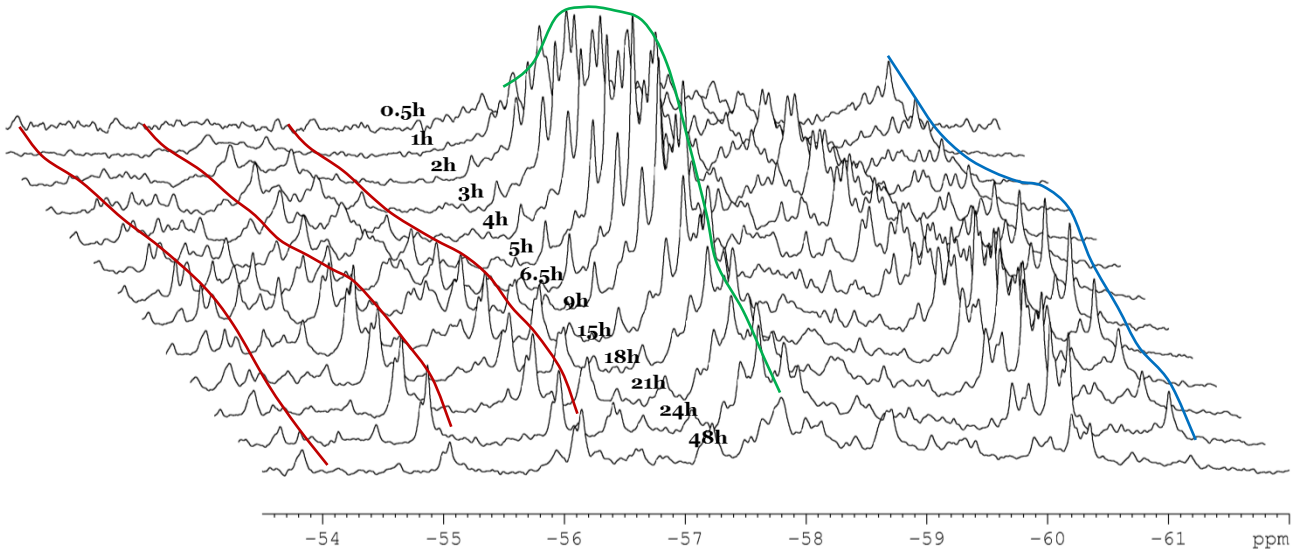

Figure 105. T^2 range of ^{29}Si DEPT spectra of NBBs versus reaction time at 100°C.

The smaller cycles demonstrate low field shift as a result of increasing internal tension, thus the sharp signal at -56.26 ppm (red) can be attributed to the most constrained T_3 cyclic units, which were also detected by FTIR in purified DBLT6 sample. Considering the MALDI TOF results, which detected $T_3(OPr)_5$ species in abundance after 24 hours of reaction, the signal at -56,26 ppm can be assigned to these cycles. Another two sharp peaks at -55,1 ppm and -54,15 ppm, taking into account the substitution rules from

the Figure 98, can be assigned to $T_3(OPr)_4(OMe)$ and $T_3(OPr)_4(OH)$ species respectfully, also in agreement with MALDI. The peak attributed to $T_3(OPr)_4(OMe)$, shows the same behavior with reaction time as $T_3(OPr)_5$, however the $T_3(OPr)_4(OH)$ is consumed faster.

The group of resonances centered at -58 ppm (green) is due to 4-membered rings, bearing different alkoxy or –OH groups. Their amount increases from the first hours of reaction, reaching the maximum by 6,5 hours. The signals in the range from -59 ppm to -61,1 ppm can be attributed to linear species , 5, 6 -membered rings, open chain structures and also to terminal Si atoms of ladder-like structures [232].

Since it is well known [232] that the half-peak width decreases with increase in regularity of the species skeleton, the extraordinarily sharp signal at -61,2 ppm (blue) can be attributed to the T^2 -silicon of incompletely condensed $T_6(OH)_2$ cages. The amount of these units start to grow at the same time, when the 4-membered rings start to fade (6,5 hours), which is also confirmed by FTIR. Since the main building blocks of cage-like structures are these rings, such simultaneous development indirectly suggests the 4-membered rings recombination into the cages [232].

The T^3 region, presented on the Figure 106 can be divided into 3 separated groups of peaks. The most high-field shifted, centered at -66,7 ppm (blue line in Figure 106) starts to rapidly develop after 6,5 hours of reaction. This signal sharpened dramatically around 15 hours of reaction, suggesting that amount of closed T_8 cages rapidly increased. At this reaction time, the water produced In-Situ reached the value of 86% of the theoretical amount, strengthening the idea that water availability plays a major role in the formation of structures with complex architecture.

The broad signal lying beneath is due to T^3 Si atoms of incomplete $T_6(OH)_2$ cages and those of branched incomplete $T_6(OH)T^2(OR)(OR')$ cages, which also may be connected with other T^2 and T^3 species via linear oligomers (R and R' stand for methyl, propyl, or H).

Another sharp signal at -64,9 ppm (red line in Figure 106) is attributed to T_6 cage-like structure, since the 3-membered rings, detected in T^2 region can build this type of cage in one step, by condensing Si atoms bearing the –OH function [232]. The broad signal (green), which appears centered at -65,65 ppm can be assigned to $T_4T^2(OR)T^2(OR')T^2(OR'')$ cages with one Si atom missing [232]. Vast amount of possible combinations in such species causes the large peak broadening.

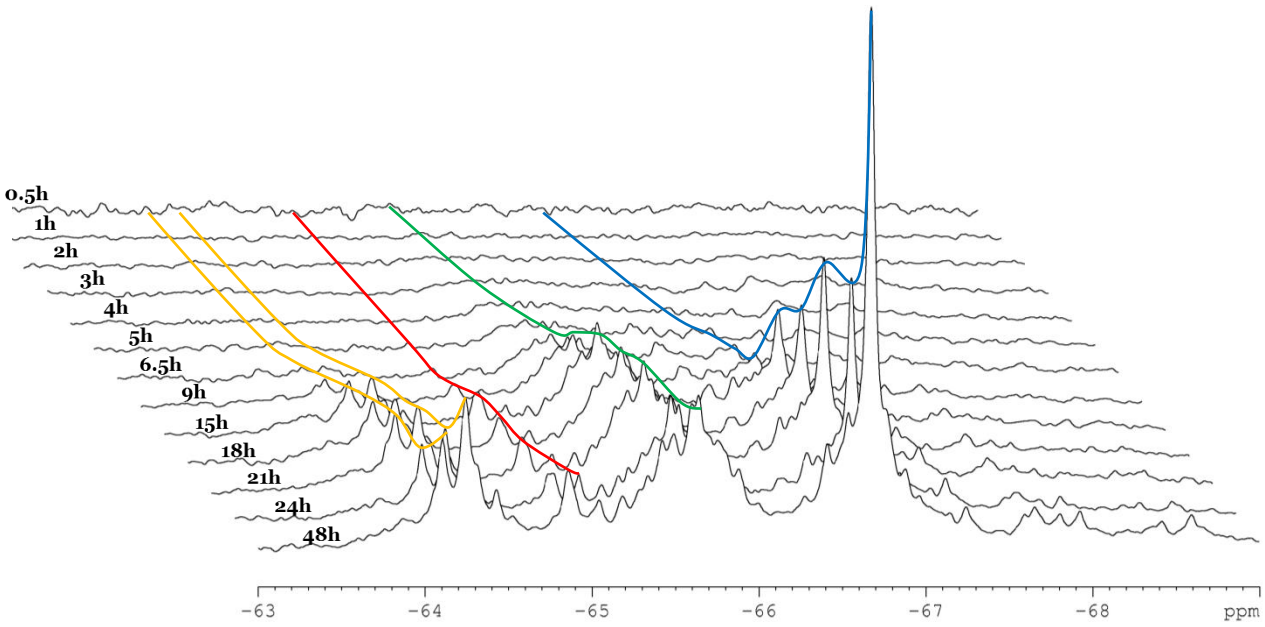

Figure 106. T^3 range of ^{29}Si DEPT spectra of NBBs versus reaction time at 100^{o}C.

The two sharp peaks at -64,1 ppm and -64,25 ppm (yellow) are attributed to the ladder-like species, made of different number of cycles. They begin to appear on the spectra at the same time with T_8 cages (15 hours), but do not demonstrated similar rapid growth.

The structural development of T^3 species after 24 hours reaction is noteworthy, and for the convenience, the magnification of the corresponding region with the samples reacted up to 380 hours at 100 °C is presented on the Figure 107.

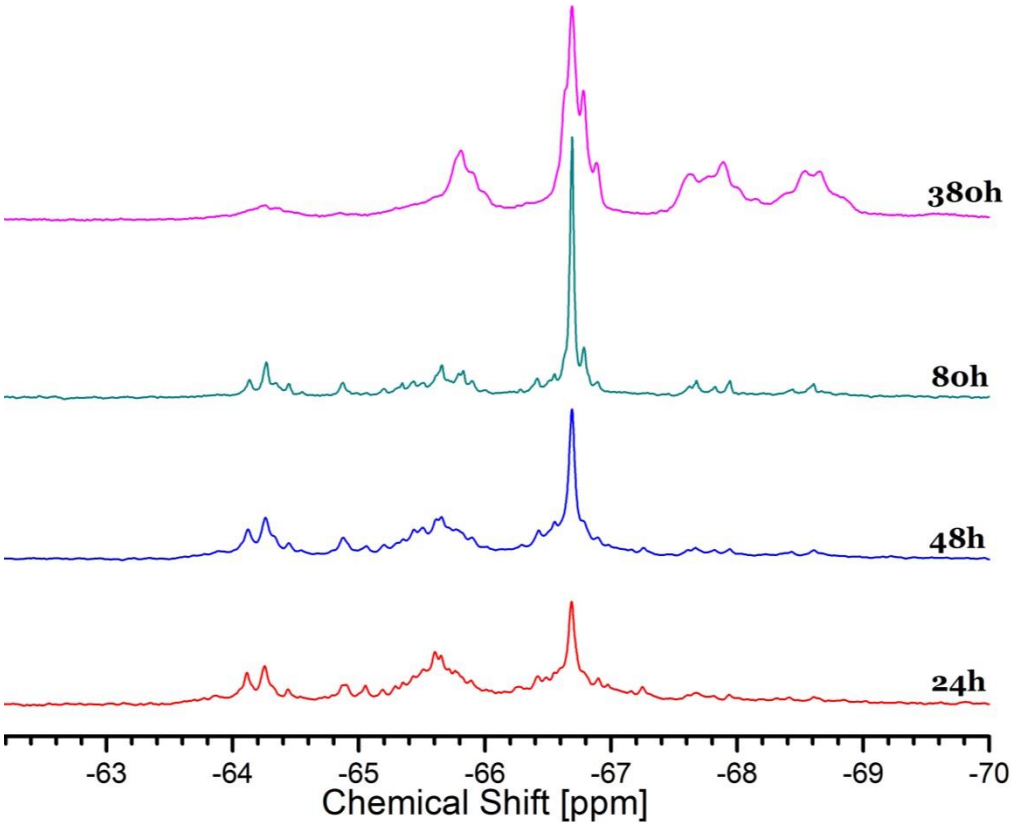

Figure 107. ^{29}Si DEPT spectra of thiol functionalized NBBs versus reaction time at 100°C.

Besides the species assigned above, new species appear in high field region of T^3 range after 48 hours of reaction. The signals at -67,8 ppm and -68,6 ppm are already well visible after 80 hours and very well developed by 380 hours. Since in cages with number of silicon atoms greater than eight the cycles would be larger and, as a result of decreasing internal tension, the signal would be high-field shifted [206], these two signals can correspond to the higher member cages as T_{10} and T_{12}. However, preferable formation of T_8 cage-like species over the T_{10} T_{12} and other fully condensed species is known due to stability of 4-membered rings [232], which were detected on the earlier stages of reaction in T^2 region. Indeed, it appears that the fade of 4-membered rings amount starting from 6,5 hours of reaction is caused by their further rearrangement into T_8 cages and ladder-like species. On the other hand, the assignment of 5- and 6-membered rings is complicated by the overcrowding of the corresponding spectral range, and consequently the pathway of formation of T_{10} and T_{12} cages is unclear.

After 380 hours of reaction, the broadening of all signals is observed. The branching or co-condensation of incompletely condensed cages may result in formation of poly-cage structures with higher molecular weights. As a result, restricted mobility of such species as well as the vast amount of possible structural combinations are the main causes of observed signals broadening. Apart from that, the signal attributed to the ladder-like species almost disappears by 380 hours of reaction, suggesting the ladders rearrangement into cage-like structures, which was also observed by FTIR. Since the chemical shift position of ladder-like species is independent of the number of rings [196, 233], it is difficult to attribute to a specific number of rings the ladders found at -64,1 ppm and -64,25 ppm, and estimate their contribution to formation of T_{10} and T_{12} cages.

As a final remark on T^3 units structural development, it's worth to say that the most intense and sharp signals (pointing out high extent of species organization), related to both cages and ladder-like species, are found after 80 hours of reaction, whereas increasing the reaction time leads to fade of ladder-like species and formation of poly-cages from not fully condensed cage-like species.

3.4.4 Gel Permeation Chromatography (GPC) Characterization of the NBBs Growth

GPC strengthen the results obtained by FTIR and ^{29}Si NMR and the discussion of observed structural evolution. The GPC traces, obtained after 2, 6, 24, 72, 96 and 380 hours of reaction at 100°C are presented on the Figure 108.

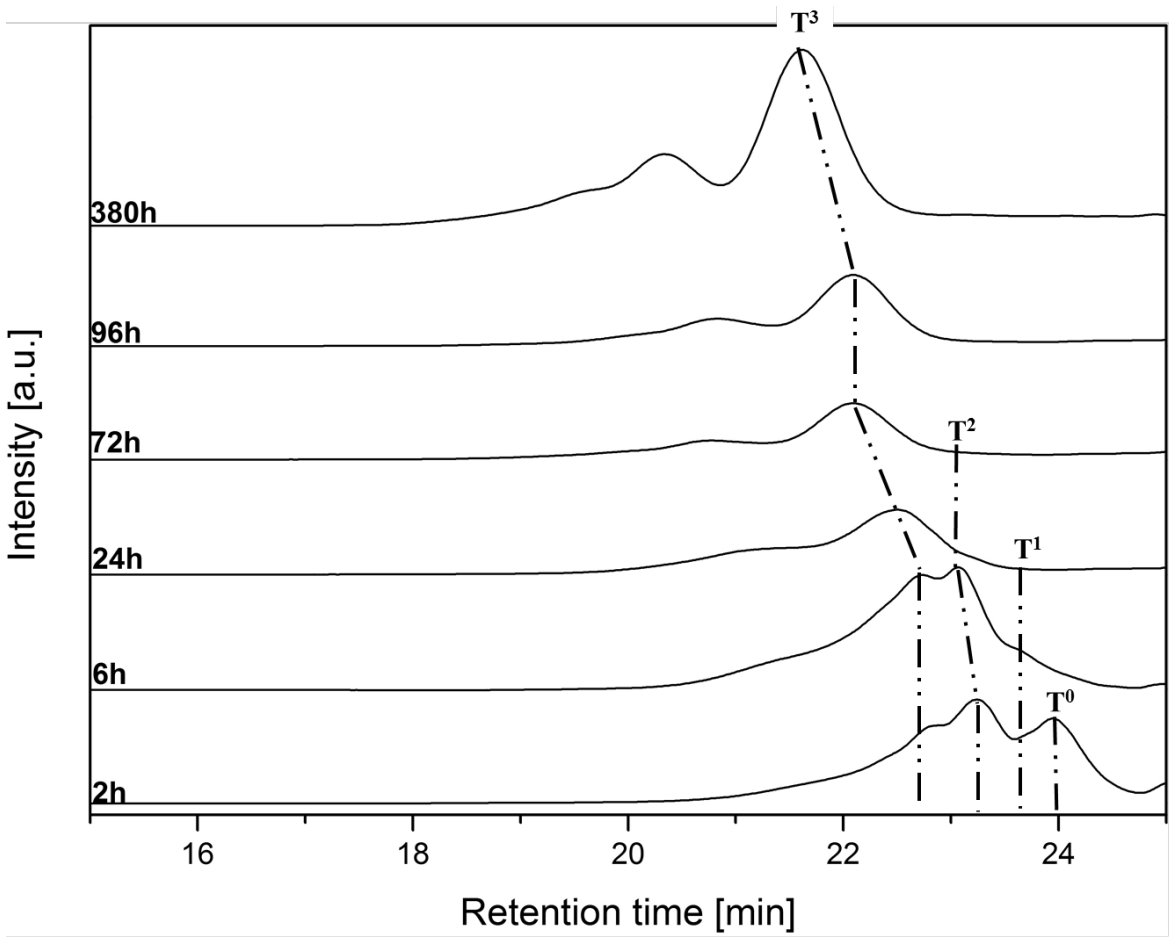

Figure 108. GPC traces of NBBs versus reaction time at 100°C, flow = 1ml*min^{-1}.

For the sake of clarity, the correlation between GPC signals and structural T-units is made. It is strictly true only for T^0 species, nevertheless the majority of species found in GPC traces, may consist of T^1, T^2 or T^3 units, observed with ^{29}Si NMR. Oligomers size distribution was evaluated by size exclusion and the quantification of oligomers molecular weight was performed by polystyrene standards calibration.

In agreement with NMR, a variety of small oligomers were detected at the initial stages of condensation, within 2 hours of reaction at 100 °C. Three peaks with retention volumes 23.95, 23.23 and 22.85 ml correspond to T^0+T^1, T^2 and small amount of T^3 units respectfully. After running the reaction for 6 hours, T^0 species disappear from the traces and T^1 units are represented by the shoulder at 21.37 ml of retention volume. Then, also T^1 species disappear after 24 hours of reaction, in agreement with the NMR study.

T^2 units show an increase in molecular weight from 2 to 6 hours of reaction, since the retention volume of detected peak decreases to 22.73 ml. T^2 species are detected also after 24 hours of reaction with the shoulder at 23,2 ml. The GPC trace analysis trend for T^2 units is in line with ^{29}Si NMR results, showing that they were the main species by 6,5 hours and heavily recombined by 24 hours of reaction.

T^3 species also increased in size from 2 to 24 hours, and were detected at 22.75 ml of retention volume by 6 hours and at 22.47 ml by 24 hours of reaction. It is notable, that already after 6 hours of reaction another broadly distributed population is observed at 21.22 ml. This peak may correspond to initial formation of ladder-like species and poly-cages, as their formation was detected by NMR after 6,5 hours of reaction. With further increasing reaction time, T^3 species expanded in molecular dimensions until 72 hours, reaching masses of 760 Da and 1427 Da, derived by calibration from the 22.1 and 20.77 ml retention volumes respectfully. Taking into account ^{29}Si NMR analysis, the detected peaks may be attributed to T^3 units in a form of cages and ladders, since mainly this type of species were found by 72 hours of reaction. The plateau in dimensional growth is observed from 72 hours till 96 hours of reacting with notable increase in amount of poly-species at 20,77 ml of retention volume. After 380 reacting hours NBBs still demonstrated 2 populations: at 21.62 ml, represented by cage-like species (950 Da) and at 20.32 ml represented by ladder–like silsesquioxanes and complex poly-cages (1770 Da).

3.4.5 The –SH Function in NBBs During Growth at 100°C: Results and Discussion

Apart from structural features of the NBBs, it is also important to control the organic functionality preservation throughout the synthesis procedures. FTIR confirmed the detection of the weak and broad S-H stretching band (2559 cm^{-1}) in all investigated samples, reacted at 100°C, but the quantitative analysis is restricted due to the very low signal intensity. Thus, the ^{1}H NMR was exploited, and the collected stack spectra are presented on the Figure 109 versus reaction time at 100°C . These spectra cover the time range from 0,5 hours of reaction till 48 hours. The assignment of the peaks was reported on the Figures 92 and 93.

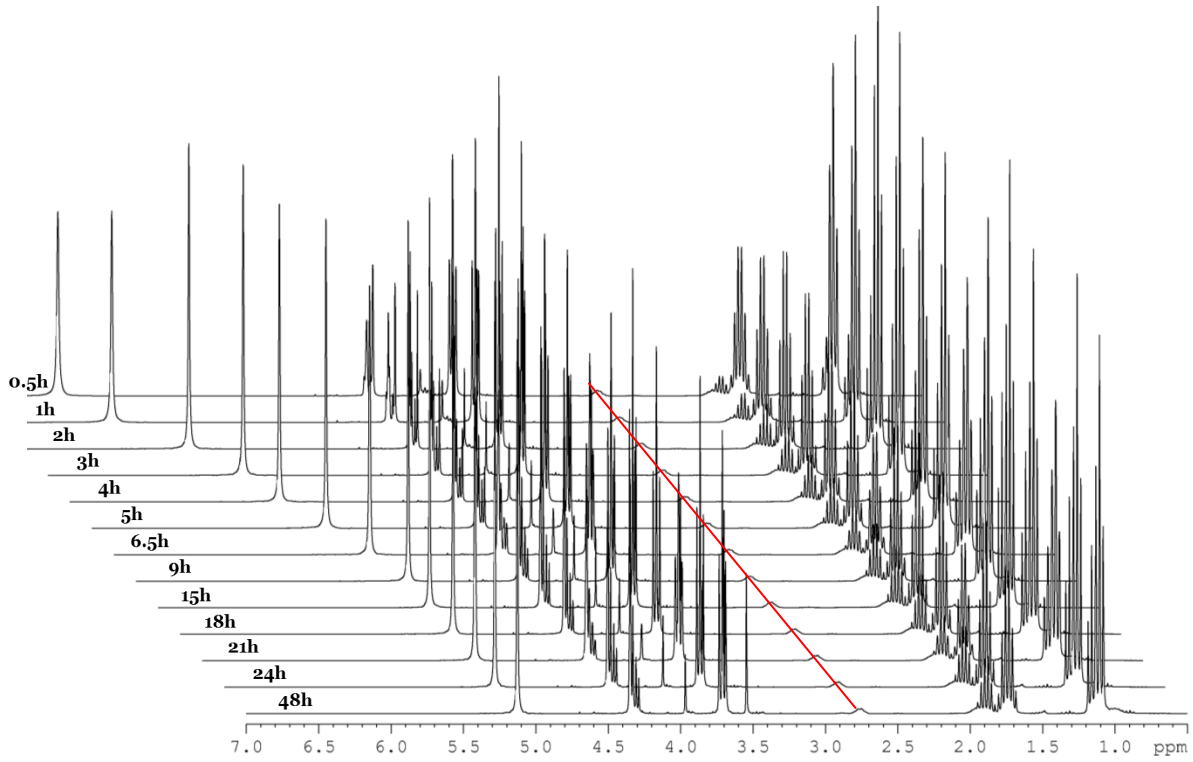

Figure 109 . ^{1}H NMR spectra of NBBs reacting at 100°C versus reaction time.

The weak broad signal at 2,73 ppm (red line in the Figure 109) corresponds to the HS-C**H**$_2$-CH_2-CH_2SiO_3 proton of mercaptopropyl chain and shows negligible variations till 24 hours of reaction. On the contrary, for longer reaction times, the investigated signal

loses its intensity in the favor of a newly appeared down-field shifted peak (2,84 ppm), as highlighted on the Figure 86.

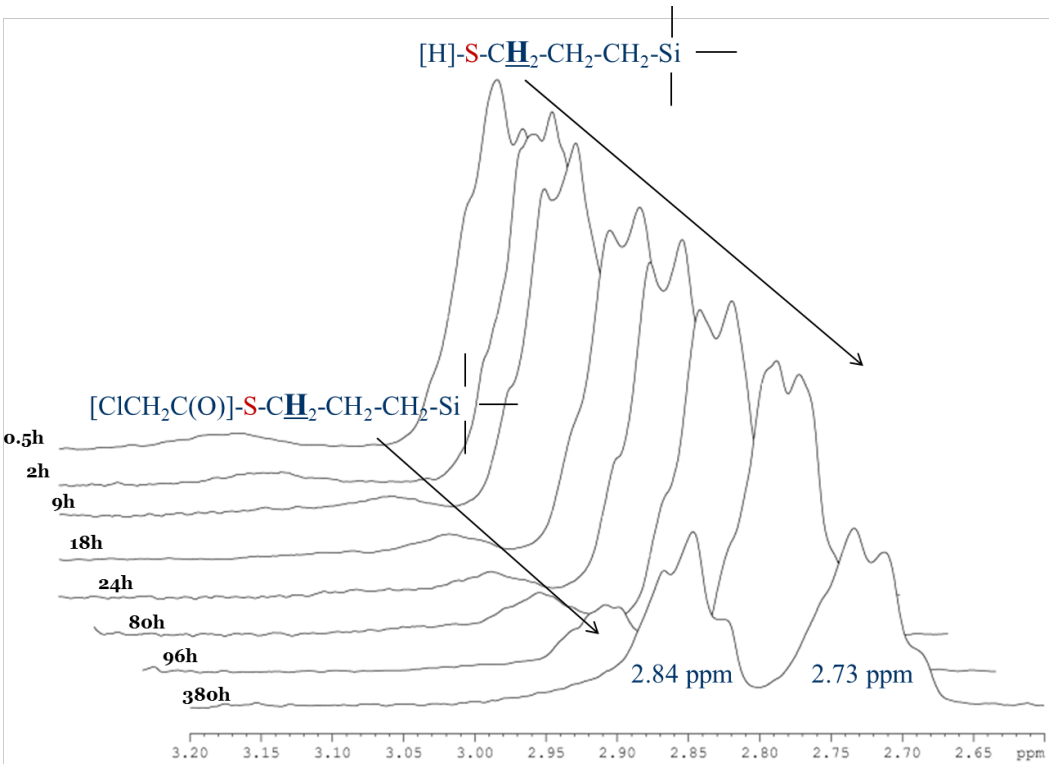

Figure 110 . ^{1}H NMR spectra of NBBs reacting at 100°C versus reaction time.

The decrease in intensity of the signal due to the HS-C**H**$_2$-CH$_2$-CH$_2$SiO$_3$ chain occurs as a result of the formation of a parasite compound, leading to the partial loss of the thiol functionality. Peaks integration revealed a 10% decrease of the 2. 73 ppm peak at 80 hours and 40% at 380 hours of reaction. In order to assign the new resonance at 2.84 ppm, the 2D ^{1}H-^{13}C HMBC and ^{1}H-^{13}C HSQC correlation experiments were recorded on samples reacted for 72 and 380 hours, as presented on the Figures 111 and 112.

The ^{1}H-^{13}C HSQC experiment run on the sample reacted for 380 hours allowed to detect in the ^{13}C spectrum a new signal due to the secondary carbon atom in the mercaptopropyl chain, which appeared to be low field shifted at 33,2 ppm. It is assigned to [ClCH$_2$C(O)]-S-CH$_2$-**C**H$_2$-CH$_2$-SiO$_3$, according to the de-shielding effect exerted on secondary carbon by the chloroacetic acid moiety in the adduct (Figure 111 top).

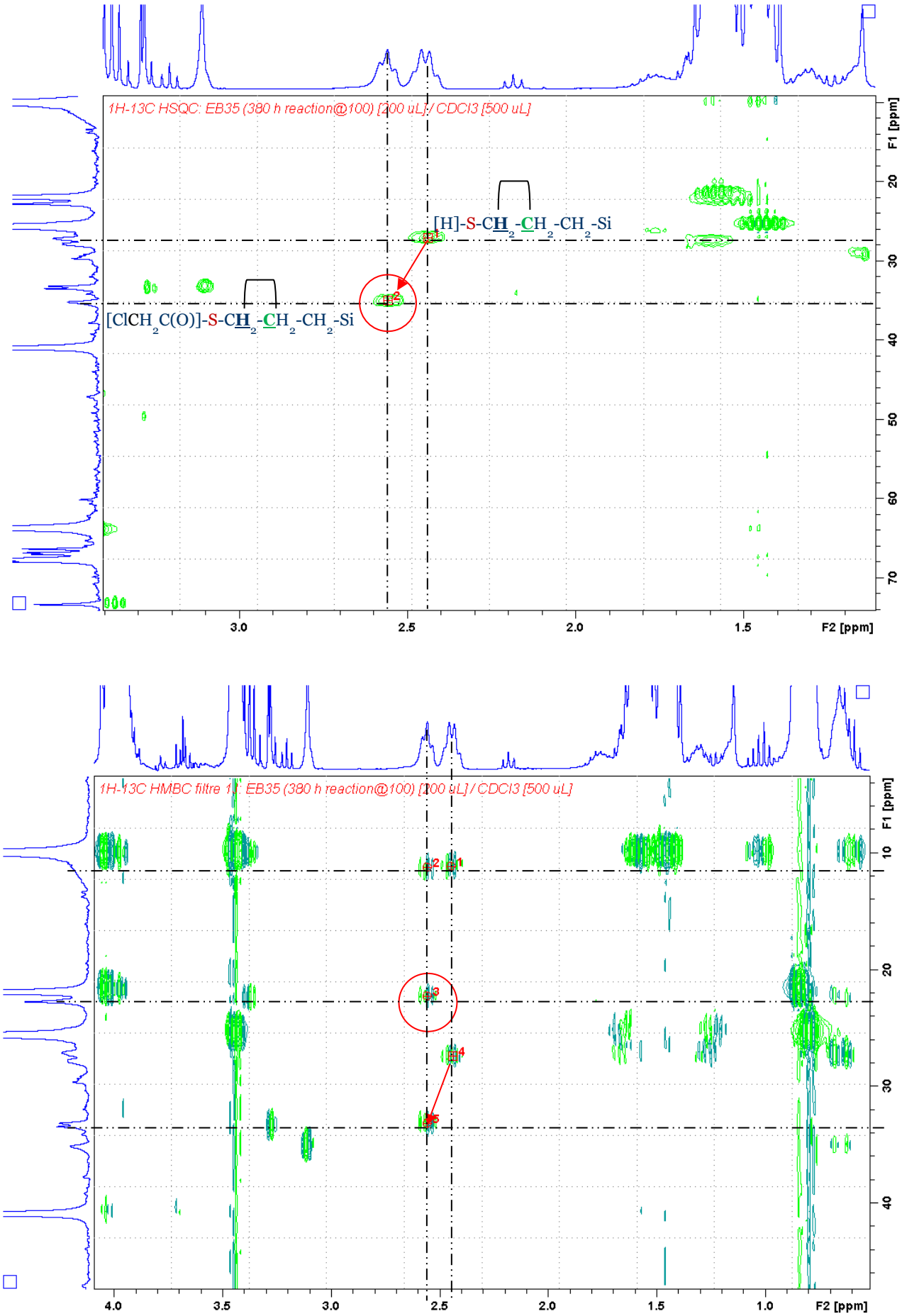

Figure 111 . ^{1}H-^{13}C HSQC (top) and ^{1}H-^{13}C HMBC NMR spectra of NBBs after 380 hours.

These results allowed to assign cross-peaks of ^{1}H-^{13}C HMBC spectrum and identify the new component (#3 in ^{1}H-^{13}C HMBC spectra). The 2D ^{1}H-^{13}C HMBC experiment was also performed on the 72 hours reaction sample, which presents the new species in less than 10% amount (Figure 112). For the sake of clarity, this new parasite [$ClCH_2C(O)$]-S-**$\underline{CH}_2$**-CH_2-CH_2-SiO_3 species will be labeled **g2** in the following discussion, whereas H-S-**$\underline{CH}_2$**-CH_2-CH_2-SiO_3 will be referred to as **g1.**

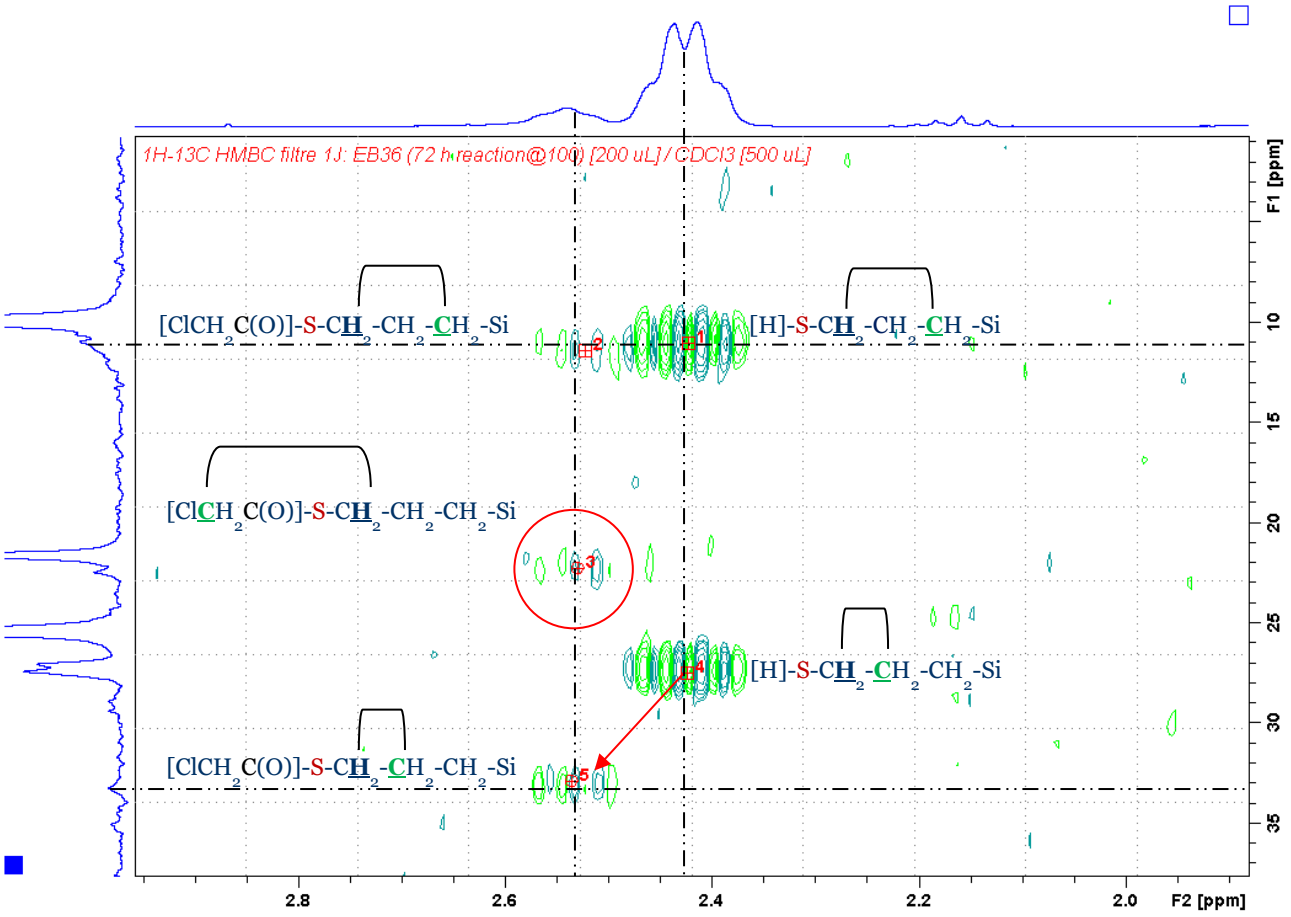

Figure 112 . ^{1}H-^{13}C HMBC NMR spectrum of NBBs after 380 hours of reaction (in $CDCl_3$).

It is noteworthy, that the loss of –SH functionality happens only after long reaction times (>24 hours), reaching a 10% lowering after 80 hours of reaction, when according to ^{29}Si NMR the yield in cage-like species reaches its maximum.

Finally, the stability of NBBs was checked on the samples reacted at 100 °C for 80 hours : after ageing at 23 °C for 90 days, they did not demonstrate significant changes in chemical and structural composition, keeping the 90% of –SH reactivity .

3.4.6 ^{1}H DOSY NMR characterization of NBBs

In order to clarify the structure populations pointed out by the GPC study in relation to architectural features, ^{1}H DOSY (Diffusion Ordered Spectroscopy) NMR experiments were applied to NBBs characterization, according to previously published technical reports [234,235]. ^{1}H DOSY was used to separate the different compounds in reaction mixture, based on their translational diffusion coefficient and calculate the NBBs species dimensions in dependence on the reaction time.

The NBBs were diluted in deuterated THF (THF-d8) for better spectral resolution and decrease of solution viscosity (10% v/v of NBBs). In order to “calibrate” the NBBs species size, 1% m/v of Octakis(trimethylsiloxy)silsesquioxane (Q_8M_8) was added to the final solution. The strength of the gradient field along the NMR tube was increasing in 32 steps, and ^{1}H NMR spectra were collected after each step.

The pulse parameters were adjusted after trial experiments to be suitable for all species of the reaction mixture. Particularly, the gradient pulse length δ and the diffusion time Δ were considered for the case of two molecules largely differing in size: propyl-chloroacetate (a smaller molecule which diffuses faster) and Q_8M_8 standard (bigger and slower diffusing). The result of experiment with adjusted parameters is presented on the Figure 113, where the field gradient strength increases from top to bottom of the stack spectra. Since propyl-chloroacetate (4,1 ppm, red curve on the Figure 113) diffuses faster, the resulting NMR signal with increase of the gradient strength attenuates faster in comparison to bigger Q8M8 molecule (0,22 ppm, green curve on the Figure 113). The pulse

parameters were adjusted in such way, that the signals of all the detected species attenuated evenly with gradient strength increase, which allowed to reduce the errors in further calculations.

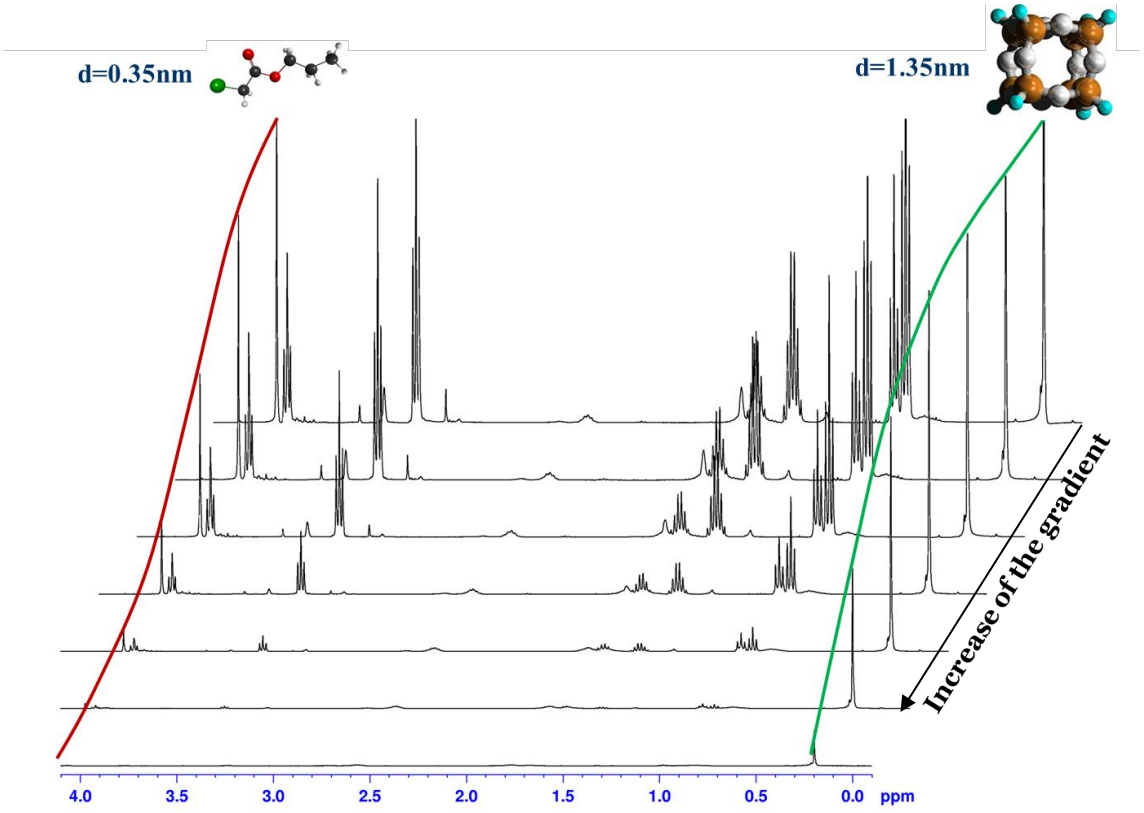

Figure 113 . ^{1}H DOSY NMR spectra of NBBs after 380 hours of reaction (in THF-d8), field gradient increases from top to bottom.

By plotting signal intensities of the detected species as a function of gradient field strength, the diffusion curves (examples of propyl-chloroacetate and Q_8M_8 are presented on the Figures 114 and 115) were acquired. Fitting of these curves by exponential function allowed to derive the diffusion coefficient **D** of analyzed species. It should be underlined, that it is important to analyze well-resolved signals of the ^{1}H spectra to reduce the errors in the fitting and acquire accurate results. It appeared that only **g1** (H-S-C**H**$_2$-CH$_2$-CH$_2$-SiO$_3$) and **g2** ([ClCH$_2$C(O)]-S-C**H**$_2$-CH$_2$-CH$_2$-SiO$_3$) signals among those related to the NBBs were

not overlapped with the ones related to by-products. Considering the low intensity of **g2**, only **g1** was selected for the further analysis.

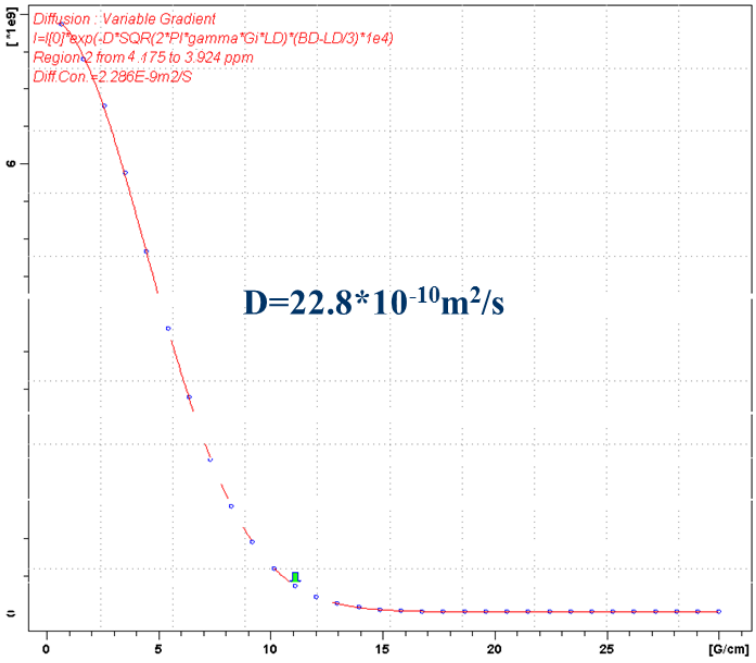

Figure 114. The fitting of propyl-chloroacetate peak intensity attenuation curve versus field gradient increase by ^{1}H DOSY NMR of NBBs after 380 hours of reaction (in THF-d8)

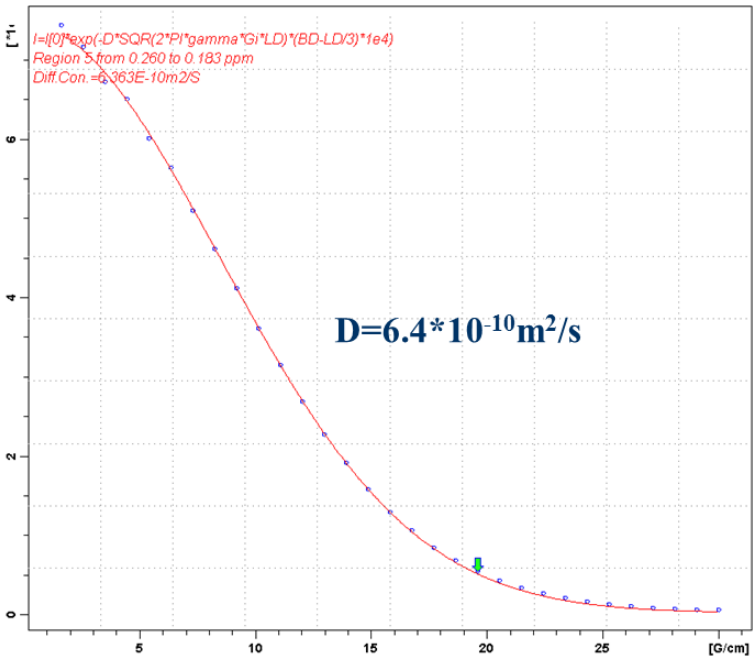

Figure 115. The fitting of Q_8M_8 peak intensity attenuation curve versus field gradient increase by ^{1}H DOSY NMR of NBBs after 380 hours of reaction (in THF-d8)

It is known that the change in viscosity can affect the value of diffusion coefficient, thus making difficult to directly relate the **D** values changes to the growth of molecular objects in the reacting solution. Addition of Q_8M_8 powder into the NMR tube containing the sample allowed calibration of **D** values of **g1** species in respect to "standard" $\mathbf{D}_{Q8M8}$. Such normalization indirectly considered possible solution viscosity changes with increase of reaction time and related the hydrodynamic diameter of the different species to standard Q_8M_8 ones. As a matter of fact, the hydrodynamic diameters $\mathbf{d}_H$ depend on diffusion coefficient **D** and known constants [236] by the equation:

$$d_H = \frac{k_b * T}{3 * \pi * \eta * D}$$

, T = 298K, kb = $1.38*10^{-23}JK^{-1}$, η(THF-d8) = 0,501cP

Figure 116 represents the $\mathbf{D_{g1}/\ D_{Q8M8}}$ values versus reaction time at 100°C. It is clear that increasing reaction time leads to the decrease in **D** values, thus assessing the NBBs size growth with the reaction time.

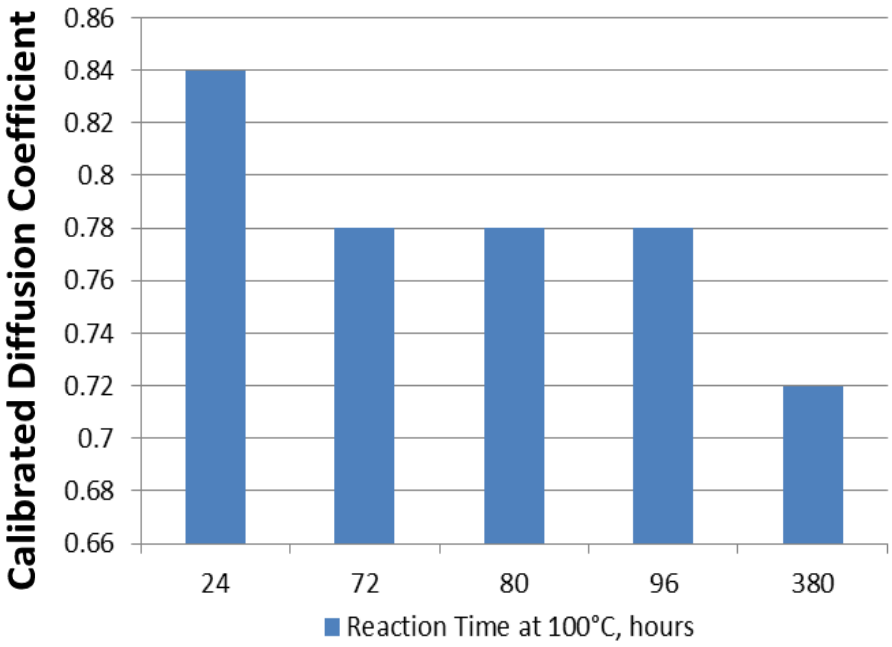

Figure 116. Calibrated diffusion coefficients $\mathbf{D_{g1}/\ D_{Q8M8}}$ versus reaction time at 100°C.

Since the $\mathbf{D_{g1}/\ D_{Q8M8}}$ ratio is proportional to the $\mathbf{d_H}$ (Q_8M_8)/ $\mathbf{d_H}$ (**g1**) ratio, and considering that hydrodynamic diameter $\mathbf{d_H}$ of Q_8M_8 species is 1,32 nm, the values of $\mathbf{d_H}$ (**g1**) can be calculated for the different reaction times (Table 11)

Reaction time (h)	**Normalized D**, $*10^{-10}$ m^2s^{-1}	**Hydrodynamic diameter d_H,** nm
24	0.84	1.57
72	0.78	1.69
80	0.78	1.69
96	0.78	1.69
380	0.72	1.83

Table 11. Normalized diffusion coefficients **D** and hydrodynamic diameters $\mathbf{d_H}$ of species corresponding to **g1**,(^{1}H 2.73ppm) resonance by ^{1}H DOSY NMR in THF-d8 at T=298K.

It is worth of noting that the GPC registered two well-separated populations in the experimental traces, whereas ^{1}H DOSY detected only one NBBs size after long reaction times (>70 hours). As ^{29}Si NMR detected cage-like, ladder-like (or poly-cycles) and poly-cage-like species after long reaction times, the reason of the lack in agreement between the two techniques may be hidden in the different sensitivity of the GPC and DOSY techniques to the architectural features of the NBBs.

Indeed, the DOSY technique is much more sensitive than GPC to the molecular weight and to the diffusion ability of each different fragment constituting the complex oligomers. This fact makes DOSY results more reliable in giving details on the total molecular weight of the NBBs. On the other hand, the porous media of the GPC columns is more sensitive than DOSY to the structural anisotropy of the NBBs oligomers.

For example, since the ladder structure made of four tetrasilsesquioxane cycles has the same molecular weight as T_8 cage, DOSY would detect only one diffusion coefficient if both species are present, whereas in GPC columns, the T_8 cage would fit to the pores easier than ladder, resulting in two different populations.

The powerful synergy of DOSY, GPC and ^{29}Si NMR techniques allows to describe, the samples, which reacted less than 48 hours as complex structures consisting of linear, cyclic, ladder-like and cage-like structures, as represented on the Figure 117. For longer reaction times the linear and cyclic units rearrange to ladder-like and cage-like structures, as schematically represented on the Figure 118.

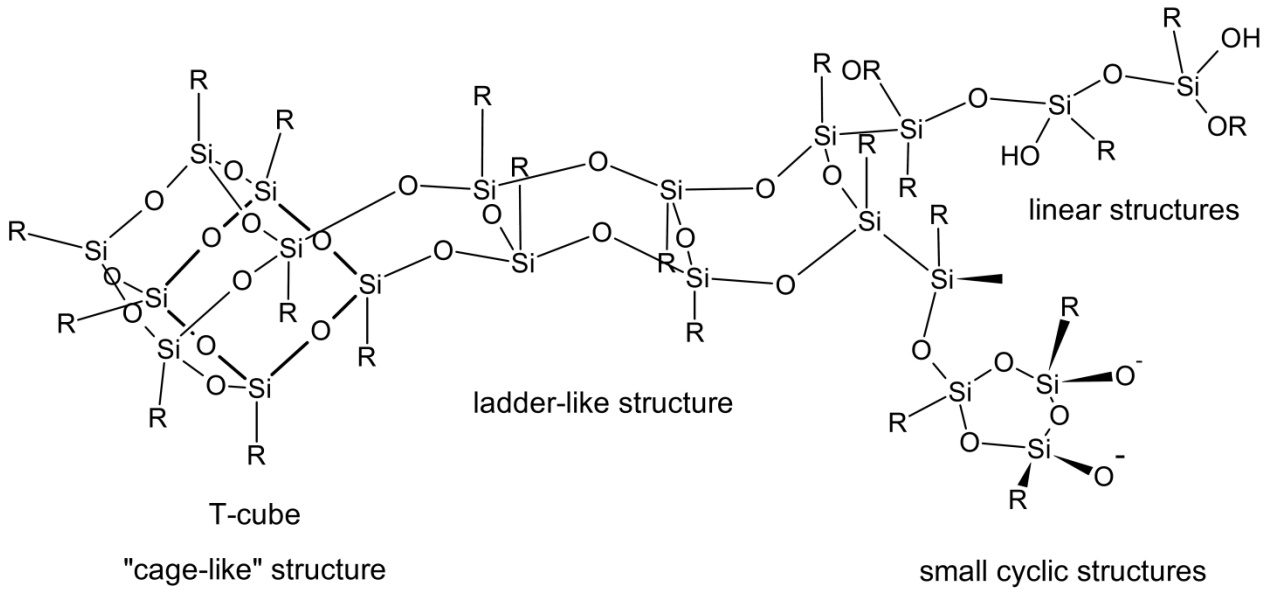

Figure 117. Possible architectures of the samples, reacted less than 48 hours, R=$(CH_2)_3SH$.

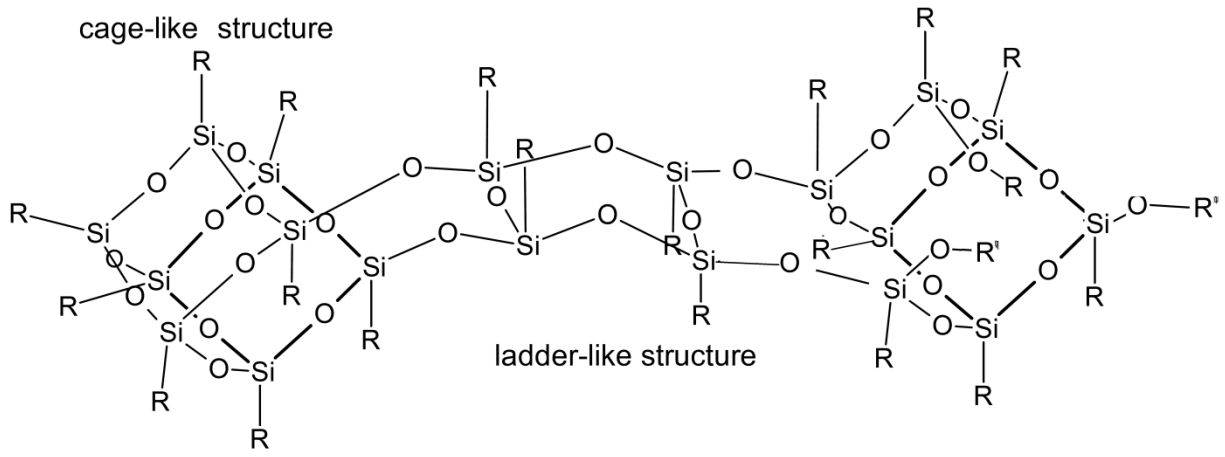

Figure 118. Possible architectures of the samples, reacted more than 72 hours, R=$(CH_2)_3SH$.

3.5 Conclusions

The ISWP route was exploited for the Sol-gel preparation of Si-based SH–functionalized NBBs, starting from 3-Mercaptopropyltrimethoxysilane (McPTMS). The water provided through the esterification reaction of chloro-acetic (ClAA) acid and 1-propanol enabled the hydrolysis-condensation of McPTMS. Since the structural features of NBBs and their shape anisotropy may play a major role in tuning the properties of NBBs – based nanocomposites, the NBBs were characterized by various techniques.

The assessed yield in cage-like and ladder-like structures was related to the esterification reaction parameters and the choice of employed catalyst. In particular, the FTIR analysis with the profile fitting of the siloxane bands allowed quantifying the different silsesquioxanes species in the NBBs. The hydrolysis ratio defined by the ratio r between ClAA and 1-PrOH, and the addition of TFA or DBTL clearly ruled out the NBBs structural units growth.

The amount of cage-like structures was demonstrated to be enhanced using TFA and increasing the value r. However, in over-stoichiometric conditions, the structural development appeared unaffected by the used catalyst, since the products obtained using DBTL and TFA presented the same cage-to- ladder ratio and distribution of molecular species, according to the GPC results. As a general trend, the GPC traces show a clear shift to lower retention time with increasing the water availability corresponding to the formation of larger structures. However, with under-stoichiometric (r= 1 and 1.5) and stoichiometric (r=3) amounts of water, the use of TFA rather than DBTL leads to a more efficient control on the obtained structures. For r = 6 the development of silsesquioxane structures appears only slightly dependent on the employed catalyst, in agreement with the results of the ^{29}Si NMR and FTIR spectra

The presence of TFA makes difficult to assess the dependence of silsesquioxane growth on the theoretical amount of water provided by ISWP, since TFA also interfere in the esterification process. Consequently, DBTL creates the most favorable conditions for relating the oligomers growth to the parameter r. Moreover, in the chemistry of silicones the reactivity of TFA towards siloxane cycles may lead to cleavage of siloxane bonds and structural rearrangement in the ring-opening polymerization process.

The MALDI-TOF spectra strengthen the results of FTIR and GPC techniques, pointing out the limited crosslinking process in the case of under-stoichiometry conditions (DBTL1) leading mainly to the formation of small linear T_3 species and minor amount of T_4 and T_5 cyclic species. On the contrary, the sol-gel reactions run in water over-stoichiometry conditions (DBTL6) drive the network to develop T_3-T_8 oligomers organized as multimeric open cages and ladder-like species.

Further optimization of the hydrolysis-condensation extent with preferential cage-like and ladder-like small oligomers formation can be reached by time-dependent analysis. The introduction of additional processing variables such as the different reaction's temperature (room temperature (RT) in contrast to 100^{o}C) allows to follow the kinetics of NBBs structural development at the early stages of Sol-Gel reaction and unravels the competition features of hydrolysis vs. transalcoholysis reactions. In order to achieve these objectives, several multinuclear solution NMR experiments have been exploited.

From the ^{29}Si NMR results obtained by following the reaction at RT, it appeared, that the transalcoholysis reaction took place immediately from the beginning of reaction, potentially slowing down hydrolysis – condensation processes by inducing the steric hindrance of pristine McPTMS. Indeed, the T^3 units did not form during 84 hours of reaction and only the T^2 units appeared after 10 hours and weakly developed in time, demonstrating low extent of condensation in NBBs at RT.

The ^{1}H NMR observations allowed to follow the kinetics of esterification reaction and relate the water production rate to the kinetics of NBBs growth. The content of water produced In-Situ was derived by spectral deconvolution, showing the yield of only 45% of theoretical amount by 84 hours of reaction at RT.

The increase of reaction temperature to 100°C resulted in fast hydrolysis of pristine McPTMS and full recombination of partially condensed T^1 units already after 9 hours of reaction. It is noteworthy to say, that the esterification reaction produced 45% of water already by 1 hour and reached the maximal possible amount by 24 hours of reaction at 100°C.

It is very intriguing, that the development of T^3 units into cage-like structures by rearranging of cyclic T^2 units appeared possible only with a threshold amount of available in situ water (more than 60% of theoretical value).

The Degree of Condensation, calculated for both temperature conditions followed the same trends as amount of water produced in situ with increasing reaction time in respect to employed temperature, highlighting strong relation of H_2O availability to condensation extent.

FTIR analysis confirmed, that already from the early stages of reaction (9 hours at 100°C) open chains, linear $T_2(OH)_4$ and cyclic species tend to rapidly recombine into cage-like structures, reaching maximum yield of T_8 cages by 72 hours of reaction.

Detection and quantification of the ladder-like structures apart from cage-like species by ^{29}Si NMR, fulfilled the FTIR weak points, confirming that the maximal yield of both types of structures was reached by 80 hours of reaction at 100°C, whereas increasing the reaction time leaded to recombination of ladder-like species and formation of poly-cages.

Apart from structural features of the NBBs, the organic counterpart preservation control showed that the loss of –SH functionality happens only after long reaction times (>24 hours), reaching a 10% lowering after 80 hours of reaction. The stability of NBBs was checked by ageing at 23 °C for 90 days, and did not evidence any changes in chemical and structural composition, keeping the 90% of –SH reactivity.

^{1}H DOSY experiments allowed to calculate the NBBs species dimensions in dependence on reaction time, since the acquired diffusion coefficients of NBBs were proportionally related to the well-known hydrodynamic diameter of Q_8M_8, added to analyzed liquids as reference.

The extraordinary synergy of ^{1}H DOSY (sensitive to molecular weight and to the diffusion ability of each different fragment constituting the complex oligomers), GPC (sensitive to the structural anisotropy of the NBBs oligomers) and ^{29}Si NMR (quantitatively sensitive for identification of structural units of NBBs) techniques allowed to describe in full complexity the NBBs structural features development with increasing reaction time.

Such structural elucidation allowed to relate the kinetics of water production (^{1}H NMR) by the ISWP process to the kinetics of NBBs growth.

Chapter 4 Perspectives

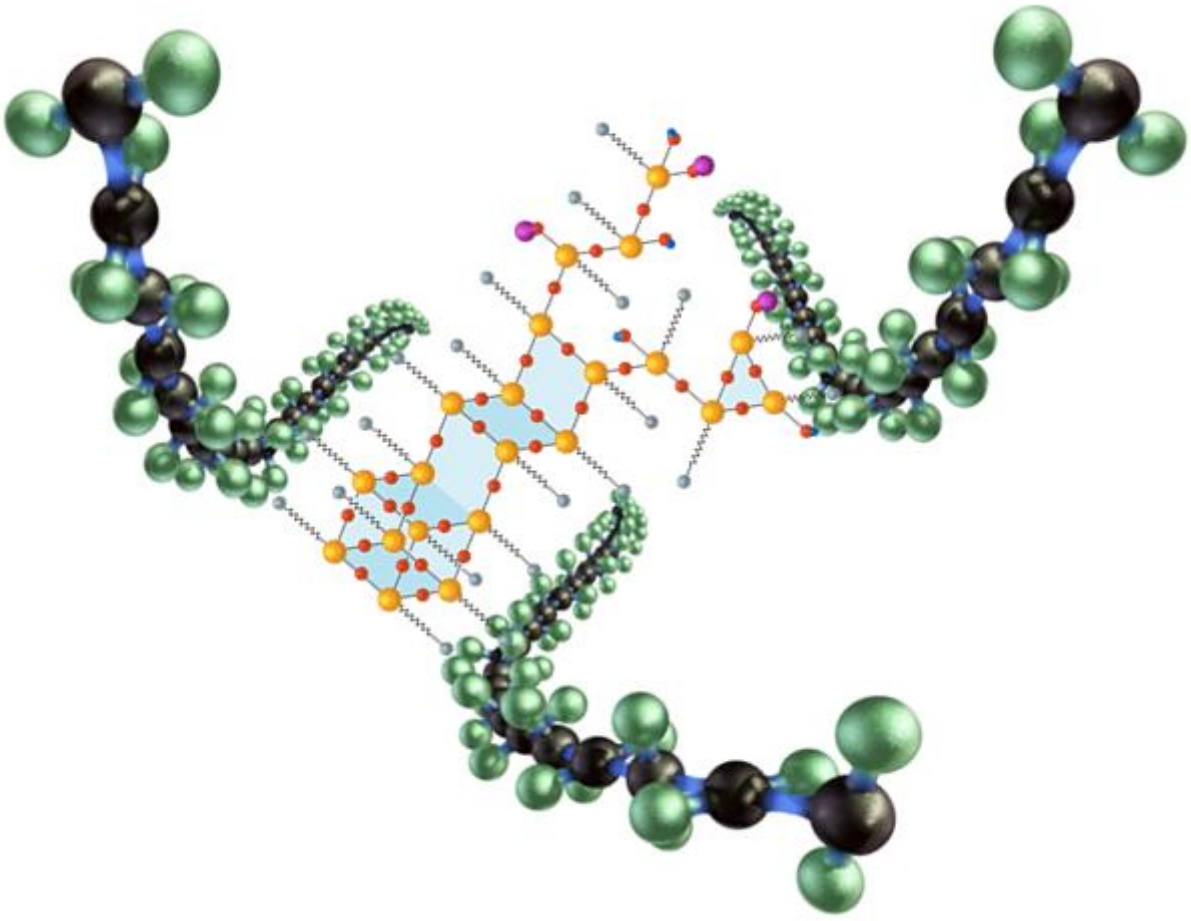

4.1 [Elastomers – NBBs] Nanocomposites: Approach

Nanofillers are playing an increasingly important role in the field of elastomers due to reinforcement effect in the polymer-matrix nanocomposites, with enhancement of desired properties, reduction in material costs and possible decrease in environmental impact. In the last decades a lot of research [237] was carried out on polymers and elastomers filled with different nano-scaled materials such as inorganic oxide particles (TiO_2, SiO_2), metal particles, nano-graphite, carbon nanotubes particularly to tuning the filler particles size, shape and superficial properties with the aim to provide effective nanocomposite reinforcement. Generally, a large amount of conventional fillers (e.g. 40%) are required to attain the desired mechanical properties in nanocomposites. However, a large amount of filler may reduce the processability of the materials, increase product weight as well as induce brittleness and affect the transparency of the finished goods. This leads to a continuous demand for new, low cost, low weight, environmentally friendly elastomer nanocomposites with improved mechanical properties. SiO_2 is commonly used in the rubber industry to improve the static and dynamic mechanical properties. The reinforcement effect of silica in rubber composites depends on the filler-rubber and filler-filler interactions, which determine the formation of a percolative filler network in the rubber matrix, essential for providing effective reinforcement [183,184]. The interactions between nanocomposite components depend on the filler particles size and shape, surface characteristics of the filler, chemical nature of the polymer and on the extent of the Organic -Inorganic interface. Recently, it was demonstrated that particle anisotropy and alignment can provide, beside an increase of the filler-filler interactions, a relevant percentage of immobilized elastomer chains leading to a higher reinforcement [184].

In the last years it was also reported that even small loading of POSS (polyhedral oligomeric silsesquioxanes) [185, 186] and ladder-like [187] nano-units with tailored morphology, when incorporated into different polymers, strongly improves their mechanical properties. These results prompt to utilize as filler in elastomer-based nanocomposites anisotropic hybrid Organic - Inorganic nano-units with highly reactive surface groups, allowing to simultaneously tuning both filler-filler and filler-elastomer interactions by varying nano-units structural parameters.

Promising candidates for this objective are the SH-functionalized Nano Building Blocks (NBBs), synthesized and characterized in the frame of this work. Thanks to the collaboration with Prof. R. Scotti at the Department of Materials Science of University of Milano-Bicocca, we approached to new-age elastomer nanocomposites, which are expected to demonstrate highly improved mechanical properties with low loadings of NBBs (0,5% - 5% w/w), thus presenting both economic and environmental advantages. Such promising expectations are based on the results of preliminary dynamic-mechanical (DMA) experiments that were carried out on elastomer-NBBs nanocomposites samples, prepared by addition of SH-functionalized NBBs (1% w/w) to the Styrene Butadiene Rubber (SBR) .

SH-functionalized NBBs were synthesized by Sol-Gel chemistry via the in-situ water production (ISWP) approach, as reported in Chapter 3 of this work. The reaction was kept for 80 hours to yield in cage- and ladder-like species, as well as to keep the availability of –SH functionality at high extent (90% of initial active –SH groups).

The nanocomposites were prepared by the swelling technique. Pre-dried SBR was swollen for 1 night in toluene. The resulting solutions were split into different flasks for addition of different amounts of as-made NBBs solutions. The loads were 0; 0,5; 1; 3; 10; 30 % weight of solid NBBs in addition to 100% of solid elastomer. The mixtures were left under vigorous stirring for 1 hour and later were cast in Petri dishes under aspiration hood

overnight for obtaining the solvent evaporation. The complete elimination of the volatiles was reached by heating to 70°C under vacuum (12mbar) for 1 hour. Resulting solid [SBR+NBBs] nanocomposites were processed to form 2mm thick sheets for characterization.

Thanks to the contribution of Matteo Redaelli, a PhD fellow from the group of Prof. R. Scotti at the Department of Materials Science of University of Milano-Bicocca, the nanocomposites were characterized by a multi-technique approach, including Electron Spin Resonance (ESR); Thermo Gravimetric Analysis (TGA) and Differential Scanning Calorimetry (DSC); and Time Domain Magic Sandwich Echo NMR (MSE NMR). Brief summary of the characterization techniques and results of analysis are presented as follows.

The electron spin resonance (ESR) with the use of nitroxide radical, introduced as a spin probe, allowed checking the rigidity of the rubber chains. ESR measurements were performed on uncured composites with different NBBs loads after introduction of the spin probe (nitroxide radical) in the rubber matrix. The ESR measurements are sensitive to the dynamics of the spin probe molecules, determined by the rotational correlation time, i.e. the time required for a complete rotation of the nitroxide radical around its axis. Thus, free, limited or hindered motion can be evidenced depending on the physical or chemical interaction with the surrounding NBBs-SBR network. The measurements on the [SBR+NBBs] nanocomposites showed, that the increase in NBBs load hinders the mobility of the nitroxide radical, suggesting the decrease in polymeric chains mobility, and thus the increase in the polymer matrix crosslinking degree.

TGA analyses, which were run at constant air flow (50 cm^3 min^{-1}) up to 1000 °C at a heating rate of 10 °C min^{-1}, confirmed the decrease of sample's mass loss with increasing NBBs load, demonstrating the increase of thermal stability of nanocomposites. Moreover,

DCS analyses displayed the changes of T_g (glass transition temperature) values with increasing the load of NBBs. The T_g value for pure SBR (-25,07 ^oC) increases to -24,80 ^oC for nanocomposite with 10% of NBBs load and to -22,04 ^oC for the nanocomposite with 30% of NBBs load. Thus, the results of thermal analyses suggested the incorporation of the NBBs into the polymer matrix via the formation of crosslinks.

The incorporation of NBBs inside the polymer matrix was also studied by FTIR analyses, which displayed the growing in intensity of the Si-O-Si (1220-940cm^{-1}) asymmetric stretching vibration band with the increase of NBBs load in the nanocomposites. The structural units of NBBs kept their integrity in the nanocomposites, showing vibrational bands at 1065 cm^{-1} (ladder-like structures), 1126 cm^{-1}(T_8 cages), and 1184 cm^{-1}(poly-cages structures), according to the previous assignments in this work. The band at 2559 cm^{-1}, attributed to S-H stretching in the nanocomposites was not detected in the nanocomposites spectra. However, the weakness and broadness of this band in NBBs spectra did not allow to interpret its disappearance in nanocomposites as the result of formation of new S-based links among NBBs and SBR.

Detection of the polymer mobility and determination of the immobilized polymer fraction was assessed by the Magic Sandwich Echo NMR (MSE), that was run at the university of Milano Bicocca. The purpose of this pulse sequence experiment is to refocusing magnetization in dipolar coupled systems when it has lost coherence due to multiple dipolar interactions between spins. In particular, the aim is to refocusing magnetization even after times much longer than the apparent T_2 relaxation time, therefore avoiding the loss of the earlier parts of the FID signal due to ringing or other instrumental effects. At the core of the MSE sequence is the fact that applying a RF pulse to a dipolar coupled system leads, in the so called Double Tilted Rotating (DTR) frame, to the effective interaction Hamiltonian:

$$H_{eff} = \frac{3\cos^2 \xi - 1}{2} H_d$$

where H_{eff} is the standard dipolar Hamiltonian and $\xi = \arctan(\omega_1/(\omega_o - \omega))$. Here ω_1 is the Larmor frequency associated to the intensity of the RF pulse, ω its frequency, and ω_o the Larmor frequency related to the static magnetic field. By tuning these parameter to choose a proper value of ξ, the effective interaction Hamiltonian can become negative, therefore leading to a reversal of the time evolution of the system [245].

The MSE experiment employs resonant pulses, the last $\xi = \pi/2$ pulse having an opposite phase than in the original form of the echo; this allows the sequence to refocus not only dipolar interacting spins, but also defocusing due to chemical shift or field inhomogeneities (linear spin interactions) Analyses were performed starting from reasonably high temperature (39°C) in order to avoid effects from the glass transition (associated to Time Domain-NMR detected rigid fractions up to 50°C over the thermal and mechanical Tg).

Acquired signal intensities (I – for nanocomposites, I_o – for pure SBR) in the time (t) region between 0 and 0.2 ms were separated then into two contributions: the rigid part, which generates a Gaussian function (A) with a decay coefficient D^2_{res} and the mobile part, which produces an exponential decay much slower (sometimes flat) characterized by the relaxation time T_{2B}, as represented by the equation:

$$\frac{I}{I_0} = A\ exp\left\{-\frac{9}{40} D_{res}^2 t^2\right\} + B\ exp\left\{-\frac{t}{T_{2B}}\right\}$$

This fitting of acquired signal intensities versus acquisition time derived the values of immobilized fractions in nanocomposites, showing 4% of immobilization for 10% NBBs-loaded sample and 14% for the 30% one in comparison to pure SBR.

The dynamic mechanical characterization of uncured samples was performed by a Rubber Process Analyzer on the low-loaded (0,5% and 1% of NBBs content) composite samples. The strain sweep tests were carried out at T = 70 °C and 1 Hz from 2.0% to 100% of elongation, and the results are presented on the Figure 119, which shows that 1% NBBs loading improves the mechanical properties of obtained nanocomposite in comparison to the pure SBR. However, higher loadings (i.e 10% and 30%) were demonstrated to negatively affect the mechanical performance.

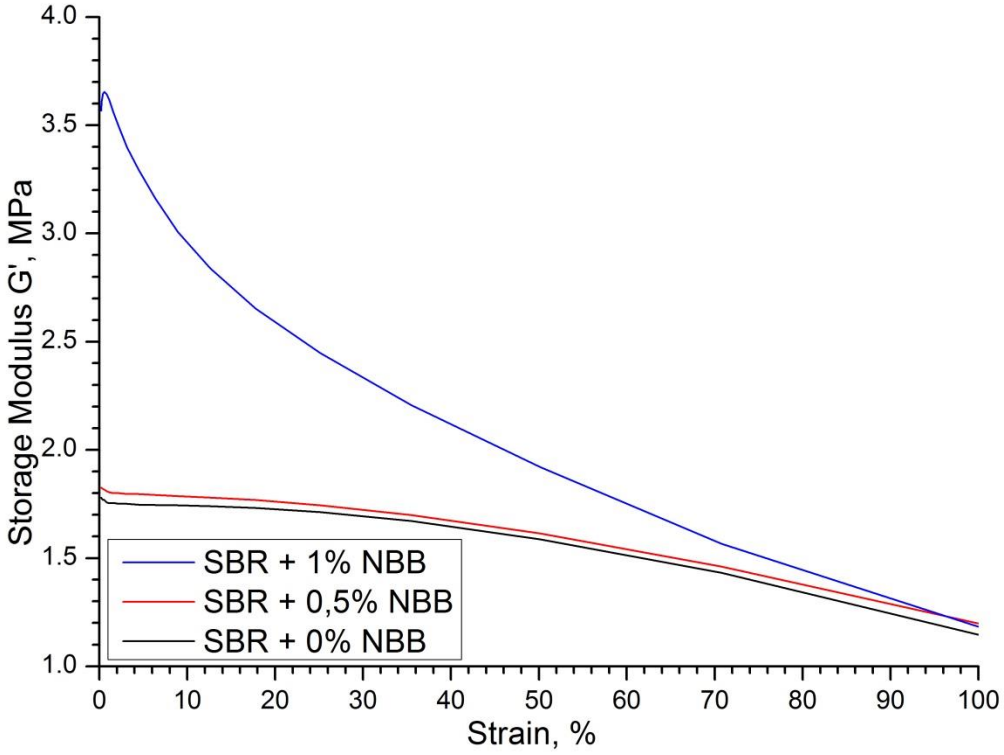

Figure 119. Storage Modulus G' versus strain for pure SBR, 0,5% and 1% - loaded nanocomposites.

The performed analyses directly and indirectly suggest the incorporation of the NBBs into the SBR matrix, with the modification of the mechanical behavior of the nanocomposites. Nevertheless, they are not able to elucidate the nature and extent of nanocomposites' components interaction.

4.2 [Elastomers – NBBs] Nanocomposites: NMR analysis

High Resolution Solid State NMR is known as a powerful technique in structural characterization, but it also finds large application in the study of interfaces in nanocomposites. Moreover, currently its application in the study of the structure and dynamics of elastomer nanocomposites widens, since it can provide clear information on the changes in elastomer structure, filler structural features, and conformation of polymer chains in such materials, unraveling interfacial interaction between elastomer blocks and filler nano-units in final solid materials [238, 239].

In the past, the researchers of the Solid State NMR laboratory "Klaus Müller" at the University of Trento contributed to the understanding of the mechanical and protective properties behavior of different metal oxide-based polymer nanocomposites, by highlighting the nature of filler-matrix interactions [238, 239, 241-243]. Since the final elastomer-NBBs composites are solids, the contribution of Solid State NMR is paramount to observing and analyzing the structural development of elastomers incorporated with NBBs on their way from wet chemistry to solid materials.

The promising [SBR-NNBs] systems appeared to be very complex for NMR investigation, since the commercially available Styrene Butadiene Rubber (SBR SLR 4630 - Schkopau, purchased from Styron) contains numerous additives, apart from medium styrene/high vinyl components. These additives contribute to the spectra and complicate the analysis of low-loaded (1-10% NBBs content) nanocomposites, making practically impossible to study the interactions on the SBR-NBBs interfaces in dependence on the filling load.

In order to get insight in the nature of polymer-filler interaction and clarify the importance of –SH function of NBBs, the model system was employed, based on the commercially available polybutadiene (PBD). The nanocomposites were prepared in the same way as [SRB+NBBs] ones, with the same NBBs loadings, but using the polybutadiene matrix. These PBD-based nanocomposites are currently being investigated by means of multi-nuclear Solid State NMR, in the laboratory "Klaus Müller" in the University of Trento in collaboration with Dr. Emanuela Callone

4.2.1 ^{13}C MAS NMR: Proton Decoupled Single Pulse

The preliminary results of ^{13}C NMR study are presented on the Figure 91.

The spectra were acquired with proton decoupled single pulse (SP) Magic Angle Spinning Nuclear Magnetic Resonance (MAS NMR) sequences under the following conditions: ^{13}C frequency: 100.07 MHz, π/2 pulse length: 3.5 μs, ^{1}H decoupling pulse power: 47 kHz, recycle delay: 4 s, 2k scans, spinning 5,5 kHz,

The spectra (Figure 120) show two typical resonances of a poly-1,4-butadiene at 28.3 and 130.2 ppm in 1:1 ratio, referred to the –CH2- and the =CH, respectively in the sequence proposed in Figure 121. The resonances appear quite narrow because the elastomer functional groups undergo rapid motion, which averages nearly all the dipolar and chemical shift interactions.

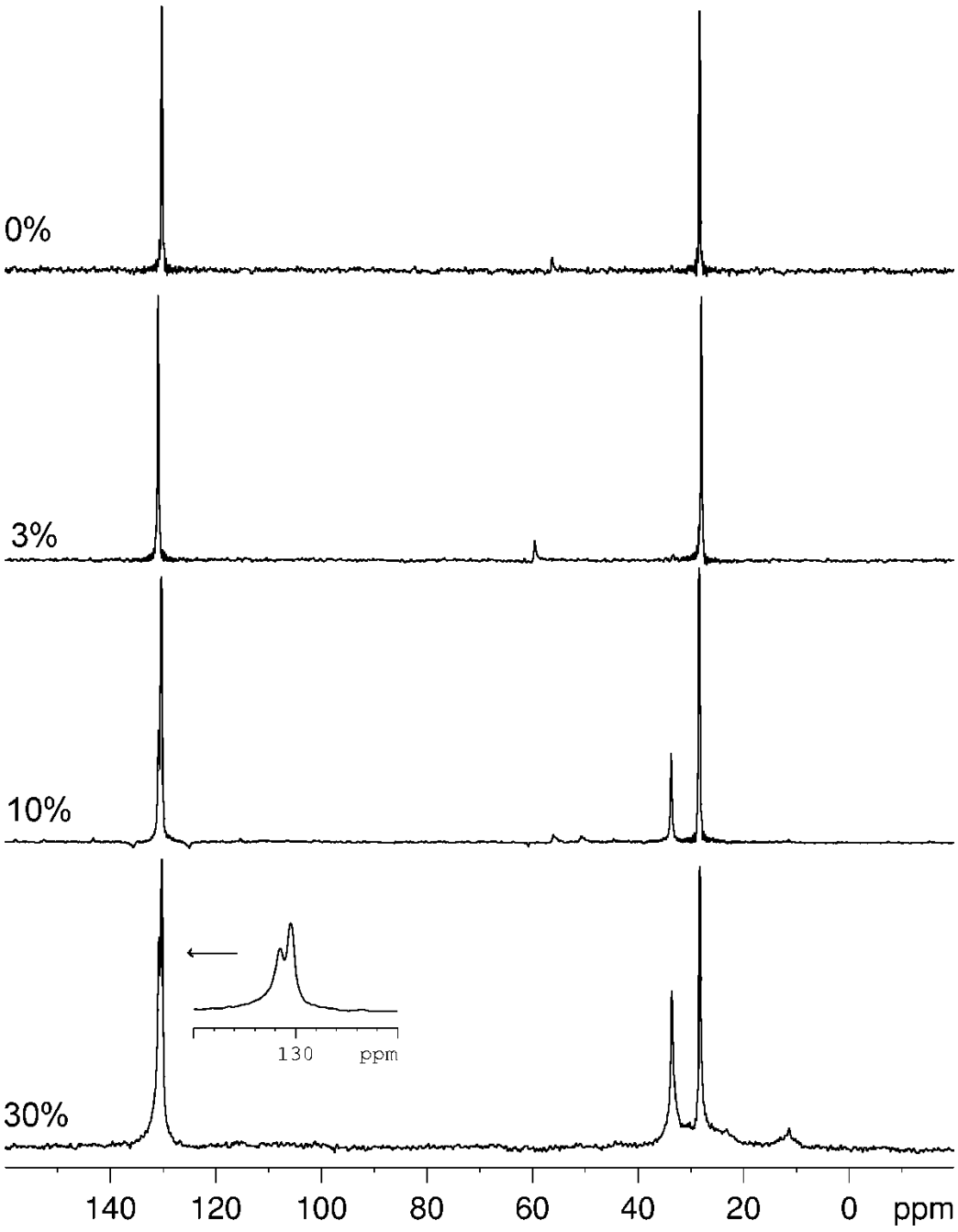

Figure 120. ^{13}C proton decoupled MAS NMR spectra of PBD with different loads of NBB as indicated directly on the spectra. Peaks at 60 ppm are spinning sidebands.

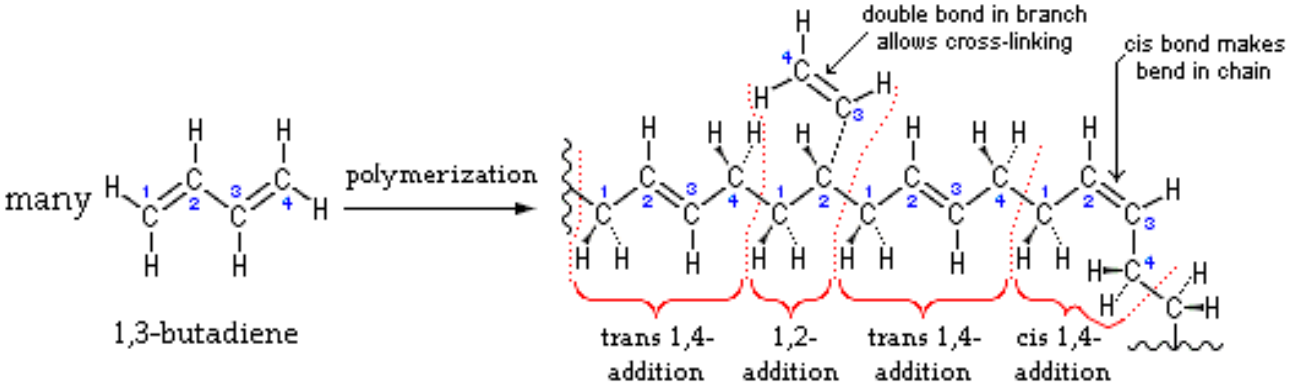

Figure 121. Structural units of polybutadiene (PBD) and possible configurations.

The spectrum remains unchanged with the addition of NBBs up to 3%wt. Instead, the samples with 10% and 30%wt of NBBs present two additional peaks at 33, 6 and 130.8 ppm, respectively. Moreover, the 30% shows a broad band in the -CH2- region and small broad peaks at 23.2 and 11.4 ppm, due to the NBB resonances. The two new resonances increase with NBB amount clearly indicating that NBBs interact with the elastomer inducing a structural change. On the basis of previous works on low weight model polymers, Zinan et al. assessed that the transformation from cis to trans of the 1,4-units induces a downfield shift of 5.3-5.4ppm [246]. Accordingly, the downfield shift of 5.3 ppm of the new aliphatic peak, which appears in the spectra of PBD with high loads of NBBs at 33.6 ppm, suggests a progressive conversion modulated by the NBB amount. With 3% NBB load the cis/trans ratio is 97:3, that increases to 70:30 for 10% load and finally to 65:55 for the 30% load. Contemporarily, the double bond resonance is progressively split in two peaks with a distance of 0.6 ppm.

The observed reduction of the FID length of acquired spectra, with increase of NBBs load, suggested the reduction of mobility in evaluated PBD-NBBs nanocomposites. In the frequency domains, only the cis polymer peaks show sinc type lateral lobes due to FID truncation, which then disappear in the spectrum with high NBB load.

4.2.2 ^{13}C MAS NMR: Cross Polarization Variable Contact Time

Through solid state NMR analysis it is possible to detect molecular motion at different levels by analyses of spin-lattice relaxation times, both in the laboratory (T_1) and in the rotating frame ($T_{1\rho}$). Proton $T_{1\rho(H)}$ are in a low range of frequency (kHz), which allows to observe molecular motion in small domains (2 nm). In spite of this, the Cross Polarization Magic Angle Spinning Nuclear Magnetic Resonance (CP MAS NMR) experiments technique allows to evaluate the changes in the mobility and conformation, since these parameters affect both homonuclear and heteronuclear interactions. It is well known, that the peak intensity depends on the rate of cross-polarization from the protons to near-neighbor carbon-13 nuclei, described by the time constant T_{CH}, and the relaxation time of the $T_{1\rho(H)}$ [240]. Thus, measuring spectrum intensity (M) as a function of CP contact time (t), it is possible to extract cross-relaxation parameters T_{CH} (cross-polarization rate constant) and $T_{1\rho(H)}$ (spin–lattice relaxation time).

The high mobility of the polymeric chains can be changed by filler addition. In the solid state NMR the variable contact time (VCT) experiments are able to highlight possible differences among samples, since the CP spectrum intensity depends on two competing factors: the magnetization transfer by dipolar coupling and the spin-lattice relaxation times in the rotating frame. The fast molecular motion of flexible polymers, such as PBD, reduces the interaction among the ^{1}H-^{13}C dipole moments, and consequently the cross-polarization is a slow process. [240] Thus, it is expected that intense signals can be obtained with long contact times, which is in agreement with rubbery materials. The array of variable contact spectra, for contact times from 0.2 to 9 ms, was acquired, and the VCT curves are shown in the Figure 122, where the maximum intensity is reached at around 10ms contact time.

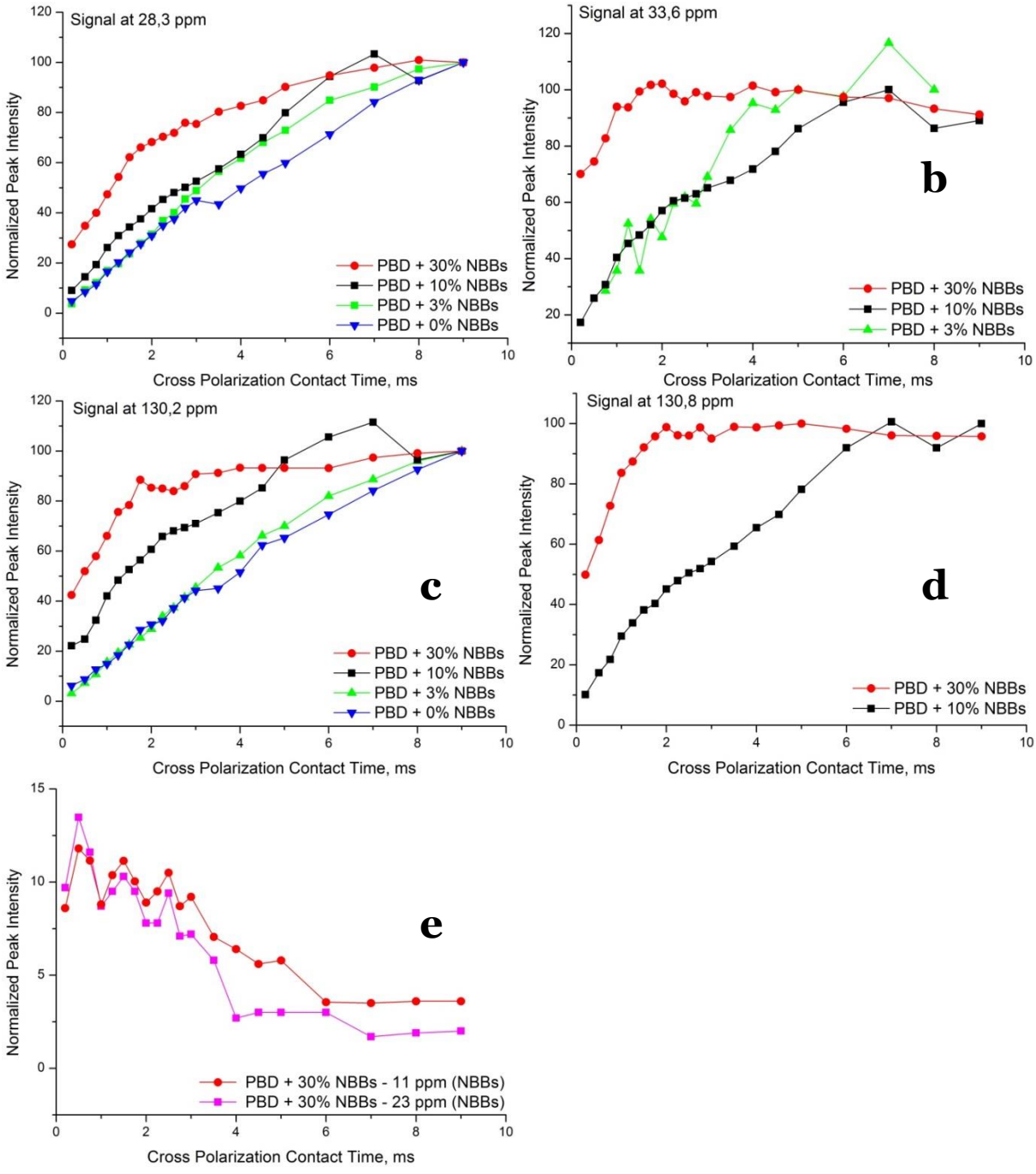

Figure 122. Magnetization curves extracted from ^{13}C VCT MAS NMR experiments for the samples with different NBBs loads.

From a qualitative point of view, it is possible to see that the effect of NBBs load is a decrease of the slope of the magnetization curve for both 28,3 ppm and 130,2 ppm peaks (Figures 122 a and c), indicating a reduced mobility of the polymer. This effect is more dramatic for the new peaks detectable at 33, 6 ppm and 130,8 ppm for high NBBs loads

(Figures 122 b and d). As a matter of facts, the magnetization curve of the peaks attributed to NBBs, measurable only for the sample with the 30% load(11 ppm, 23 ppm), shows a fast decay (Figure 122 e).

The stronger effect of slope decrease for magnetization curves of new peaks (33, 6 ppm and 130,8 ppm) indicates that this part of the polymer is closer to the NBBs filler

Numerical estimation of T_{CH} and $T_{1\rho(H)}$ values can be derived by fitting of the obtained experimental curve with single or multiple exponential laws according to homogeneity, segregation and/or domain size:

$$M(t) = M_0 \cdot e^{\frac{-t}{T_{1\rho(H)}}} \cdot (1 - e^{\frac{-t}{T_{CH}}})$$

where; M(t) is the peak intensity as a function of contact time t, M_o is the normalization constant, $T_{1\rho(H)}$ is the proton spin-lattice relaxation time in the rotating frame, and T_{CH} is the cross-polarization time constant [244].

The calculated values of $T_{1\rho(H)}$ are presented in the Table 12. The very long $T_{1\rho(H)}$ values of pure PBD are in agreement with typical values of rubbery materials. This indicates that the chains are well separated, promoting elasticity. The NBBs addition induces a certain extent of rigidity that increases with the NBBs load shortening the cross-polarization process. This is particularly true for the chains in the trans configuration that is promoted by the presence of the filler, as shown by the low values reported in Table 12. It seems that the stronger interaction is between methylene groups of the PBD chain and NBBs. The data obtained for pure PBD or with low amount of filler are probably under-estimated due to the short contact time range selected.

NBB load	$T_{1\rho(H)}$ (ms)			
	130,2 ppm	130,8 ppm	28,3 ppm	33,6 ppm
0%	12,6	-	16,94	-
3%	8,16	-	6,82	3,52
10%	3,07	5,52	5,93	2,87
30%	0,68	1,22	2,46	0,55

Table 12. Proton $T_{1\rho(H)}$ relaxation times extracted from ^{13}C VCT MAS NMR experiments for the samples with different NBBs loads

4.2.3 Outlook

Complementary to ^{13}C NMR characterization, the ^{29}Si NMR study in polymer matrix can "open the shutter from the other side", allowing to deepen the interaction understanding. Moreover, ^{1}H DOSY NMR that only recently has become an in-situ pertinent tool for interfaces investigation [244], can point out the relationships between NBBs and polymers. With DOSY, both the interaction can be quantified and dynamics of possible chemical exchange analyzed. Varying the PBD molecule length and changing the structural features of NBBs may allow to following the incorporation process and developing complex characterization methods for the systems with desired elastomer and NBBs. These perspectives will be examined with further analyses that are in progress.

Final Remarks

The research activity in the frame of my PhD experience was focused on the synthesis and structural characterization of hybrid Organic-Inorganic materials with different application fields (materials for VOC sensing and for polymer–based nanocomposites), exploiting the conventional sol-gel method or the Nano Building Block (NBBs) approach with the in situ water production route.

In the first part of the work the co-condensation of TEOS and organofunctional alkoxysilanes allowed preparation of Hybrid Sol-Gel Networks The synergic use of XRD with NMR allowed to study in deep the phase interaction. The hybrid coatings, prepared by dip-coating technique demonstrated similarity in structural features with the bulk xerogels. Two different approaches were combined to study the coatings sorption ability towards selected Volatile Organic Compounds (VOC). The coatings appeared promising in the field of detection and removal of VOCs at low temperatures, possessing the ability to quickly desorb entrapped volatiles. Fine adjustments of such hybrids can allow to discriminate between similar compounds and decrease the water sorption phenomenon, since not only the microstructure, but the polarity of the effective hybrid coatings surface plays decisive role in sorption process.

In the second part of the work the synthesis parameters were fine tuned in order to obtain Si-based SH–functionalized NBBs. The water provided in-situ through the esterification reaction of chloro-acetic acid and 1-propanol enabled the hydrolysis-

condensation of –SH functionalized alkoxysilane. The choice of exploited catalyst (TFA or DBTL) and esterification reaction parameters variations clearly ruled out the preferences in NBBs structural units formation. Varying the reaction temperature conditions allowed to follow the kinetics of esterification reaction and relate the water production rate to the kinetics of NBBs growth, highlighting strong correlation of H_2O availability to condensation extent. The complementary exploitation of multi-nuclear NMR, FTIR and GPC techniques elucidated in full complexity the NBBs structural features development during reaction.

As a highlight, NBBs demonstrated themselves as very promising candidates for polymer-based nanocomposites, since their shape anisotropy could play a major role in tuning of such hybrid materials properties. For this application, the NBBs synthesis parameters were tuned to yield in cage-like and ladder-like species as their main structural units. It appeared, that low loadings of NBBs (1%w/w) into polymer matrix highly improved the mechanical properties of nanocomposites. However, the interactions on the NBBs-polymer interfaces should be studied in more details.

References

[1] Merhari L. Hybrid Nanocomposites for Nanotechnology. Springer, LLC; 2009. doi:10.1007/978-0-387-30428-1.

[2] Corriu, R. & Anh, N. T. Molecular Chemistry of Sol-Gel Derived Nanomaterials. Angew. Chemie (John Wiley & Sons, Ltd, 2009). doi:10.1002/ange.200904371

[3] Kickelbick G. Hybrid Materials. Synthesis, Characterization and Applications. WILEY-VCH Verlag GmbH & Co. KGaA, Weinheim; 2007.

[4] Guglaylmi M, Kickelbick G, Martucci A. Sol-Gel Nanocomposites. Springer New York Heidelberg Dordrecht London; 2014. doi:10.1007/978-1-4939-1209-4.

[5] Gómez-Romero P, Sanchez C. Functional Hybrid Materials edited. WILEY-VCH Verlag GmbH & Co. KGaA, Weinheim; 2004

[6] Lofgreen JE, Ozin GA. Controlling morphology and porosity to improve performance of molecularly imprinted Sol-Gel silica. Chem Soc Rev. 2014;43(3):911–933. doi:10.1039/C3CS60276A.

[7] Tagliazucca V. Nanostructured hybrid organic / inorganic materials by the nano-building blocks (NBB) approach. 2010; ISBN 978-88-8443-339-8

[8] Schmidt HK, Geiter E, Mennig M, Krug H, Becker C, Winkler R. The Sol-Gel Process for Nano-Technologies : New Nanocomposites with Interesting Optical and Mechanical Properties. J Sol-Gel Sci Technol. 1998; 13:397–404. doi:10.1023/a:1008660909108.

[9] Butler T., MacCraith B., McDonagh C. Leaching in sol–gel-derived silica films for optical pH sensing. J Non Cryst Solids. 1998;224(3):249–258. doi:10.1016/S0022-3093(97)00481-X.

[10] Bernards I. N. M., van Bommel M. J., Boonstra A. H. Hydrolysis-condensation processes of the tetra-alkoxysilanes TPOS, TEOS and TMOS in some alcoholic solvents // J. Non. Cryst. Solids. 1991. V. 134. P. 1–13.

[11] Bredereck K., Effenberger F., Tretter M. Preparation and characterization of silica aquasols // J. Colloid Interface Sci. 2011. V. 360.12. P. 408–414.

[12] C. J. Brinker; G. W. Scherer. Sol–Gel Science: The Physics and Chemistry of Sol–Gel Processing.; 1990. ISBN-10: 0-12134970-5

[13] Mackenzie JD. Sol-Gel research - Achievements since 1981 and prospects for the future. J Sol-Gel Sci Technol. 2003;26(1-3):23–27. doi:10.1023/A:1020720831098.

[14] Sanchez C, Ribot F, et al. “Chimie douce”: A land of opportunities for the designed construction of functional inorganic and hybrid Organic-Inorganic nanomaterials. Comptes Rendus Chim. 2010;13(1-2):3–39. doi:10.1016/j.crci.2009.06.001.

[15] Schubert U. Silica-based and transition metal-based inorganic-organic hybrid materials - A comparison. J Sol-Gel Sci Technol. 2003;26(1-3):47–55. doi:10.1023/A:1020729100148.

[16] Haas K, Rose K. Hybrid Inorganic / Organic Polymers With Nanoscale Building Blocks : Precursors , Processing , Properties and Applications. Rev Andvanced Mater Sci. 2003;5:47–52.

[17] Beari F, Brand M, Jenkner P, et al. Organofunctional alkoxysilanes in dilute aqueous solution: new accounts on the dynamic structural mutability. J Organomet Chem. 2001;625:208–216. doi:10.1016/S0022-328X(01)00650-7.

[18] Sanchez C, Galo GJ, Ribot F, Grosso D. Design of functional nano-structured materials through the use of controlled hybrid Organic-Inorganic interfaces. Comptes Rendus Chim. 2003; 6(8-10):1131–1151. doi:10.1016/j.crci.2003.06.001.

[19] C. Sanchez, F. Ribot, T. Lalot, C. R. Mayer, Designed Hybrid Organic–Inorganic Nanocomposites from Functional Nanobuilding Blocks, Chemistry of Materials 2001 13 (10), 3061-3083, DOI: 10.1021/cm011061e

[20] Rozes L, Steunou N, Fornasieri G, Sanchez C. Titanium-oxo clusters, versatile nanobuilding blocks for the design of advanced hybrid materials. Monatshefte fur Chemie. 2006;137(5):501–528. doi:10.1007/s00706-006-0464-6.

[21] Soler-Illia GJD, Sanchez C, Lebeau B, Patarin J. Chemical strategies to design textured materials: From microporous and mesoporous oxides to hierarchical structures. Chem Rev. 2002;102(11):4093–4138. doi:10.1021/cr0200062.

[22] Liu Y, Huang Y, Liu L, Thermal stability of POSS/methylsilicone nanocomposites, Comp. Sci. and Tech., 2007, 67 – 2864-2876 .

[23] Ayandele E, Sarkar B, Alexandridis P. Polyhedral Oligomeric Silsesquioxane (POSS)-nanoparticle localization in ordered structures formed by solvated block copolymers, Macromol. Chem. Phys., 2013; 214.

[24] Ayandele E, Sarkar B, Alexandridis P. Block copolymer – nanoparticle nanocomposite: structure, functional properties. Prog. in Pol. Sci, 2015, 40, 33-62

[25] Yu B, Wang X, Xing W, et al. Enhanced thermal and mechanical properties of functionalized graphene/thiol-ene systems by photopolymerization technology. Chem Eng J. 2013;228:318–326. doi:10.1016/j.cej.2013.04.093.

[26] Boissiere C, Grosso D, Chaumonnot A, Nicole L, Sanchez C. Aerosol route to functional nanostructured inorganic and hybrid porous materials. Adv Mater. 2011;23(5):599–623. doi:10.1002/adma.201001410.

[27] Dirè S, Tagliazucca V, Brusatin G, et al. Hybrid organic/inorganic materials for photonic applications via assembling of nanostructured molecular units. J Sol-Gel Sci Technol. 2008;48(1-2):217–223. doi:10.1007/s10971-008-1752-x.

[28] Litchfield DW, Baird DG. The rheology of high aspect ratio nano-particle filled liquids. Rheol Rev. 2006;2006:1–60.

[29] Lee K-S, Kobayashi S. Polymer Materials: Block-Copolymers, Nanocomposites, Organic/Inorganic Hybrids, Polymethylenes. Springer Heidelberg Dordrecht London New York Library; 2010. doi:10.1007/978-3-642-13627-6.

[30] Suib SL. New and Future Developments in Catalysis: hybrid materials, composites and organocatalysts. Elsevier B.V; 2013.

[31] Thomas S, Maria HJ, Joy J, Chan CH, Pothen LA. Natural Rubber Materials, Volume 2: Composites and Nanocomposites. RSC Polymer Chemistry; 2014.

[32] Seeck OH, Murphy BM. X-RAY DIFFRACTION: Modern Experimental Techniques. CRC Press; 2014.

[33] Kazmiruk V, SCANNING ELECTRON MICROSCOPY, INTECH; 2012, ISBN 978-953-51-0092-8

[34] Leng Y. MATERIALS CHARACTERIZATION: Microscopic and Spectroscopic Methods. John Wiley & Sons (Asia); 2008.

[35] Keller JU, Staudt R. GAS ADSORPTION EQUILIBRIA: Experimental Methods and Adsorptive Isotherms. Springer Science; 2005.

[36] Dunne LJ, Manos G. Adsorption and Phase Behaviour in Nanochannels and Nanotubes.; 2010. doi:10.1007/978-90-481-2481-7.

[37] Gallagher PK, Brown M. Handbook of Thermal Analysis. Elsevier; 2003.

[38] Gunther H. NMR spectroscopy: An Introduction. John Wiley & Sons, Inc; 1980.

[39] Macomber R. A Complete Introduction to Modern NMR Spectroscopy. John Wiley & Sons, Ltd; 1998.

[40] Blümich B., Essential NMR; 2004. doi:10.1007/b95236.

[41] Balci M. Basic 1H- and 13C-NMR Spectroscopy. Elsevier; 2005. doi:10.1016/B978-044451811-8.50011-5.

[42] Bonhomme C. Solid State Nuclear Magnetic Resonance : Applications to Materials, lectures course at UPMC, Paris, France

[43] Keeler J. Understanding NMR Spectroscopy 2nd Edition. 2010:526. Available at: http://eu.wiley.com/WileyCDA/WileyTitle/productCd-0470746084.html.

[44] Grant DM, Harris RK. Encyclopedia of Nuclear Magnetic Resonance. 2002. doi:10.1002/9780470034590.emrstm0095.

[45] Baldwin, J. E., Williams, R. M. & Edition, S. High-Resolution NMR Techniques in Organic Chemistry. (2009).

[46] Brown, S. P. Applications of high-resolution 1 H solid-state NMR. Solid State Nucl. Magn. Reson. **41,** 1–27 (2012).

[47] Vega, A. & Scherer, G. Study of structural evolution of silica gel using 1H and 29Si NMR. J. Non. Cryst. Solids **111,** 153–166 (1989).

[48] Ogasawara, T., Yoshino, A., Okabayashi, H. & Connor, C. J. O. Polymerization process of the silane coupling agent 3-aminopropyltriethoxy silane – 1 H NMR spectra and kinetics of ethanol release. **180,** 317–322 (2001).

[49] Mendez-Vivar, J. & Mendoza-Bandala, A. Spectroscopic study on the early stages of the polymerization of hybrid TEOS-RSi(OR')3 sols. J. Non. Cryst. Solids **261,** 127–136 (2000).

[50] R.A. Assink, B.D. Kay, J. Colloids Surfaces A 74 (1993) 1.

[51] S. Prabakar, R.A. Assink, N.K. Raman, S.A. Myers, C.J. Brinker, J. Non-Cryst. Solids 202 (1996)

[52] S. Prabakar, R.A. Assink, J. Non-Cryst. Solids 211 (1997) 39.

[53] Alam, T. M. DEPT polarization transfer in 29Si-NMR investigations of organically modified alkoxysilanes. *Spectrochim. Acta Part A Mol. Biomol. Spectrosc.* **53,** 545–552 (1997).

[54] Brunet, F. Polymerization reactions in methyltriethoxysilane studied through 29

Si NMR with polarization transfer. *J. Non. Cryst. Solids* **231,** 58–77 (1998).

[55] Olejniczak, Z. *et al.* 29Si MAS NMR and FTIR study of inorganic-organic hybrid gels. *J. Mol. Struct.* **744-747,** 465–471 (2005).

[56] Kao, H., Lee, L. & Palani, A. C CPMAS NMR Spectroscopy as a Versatile and Quantitative Tool for Determination of Mercury Adsorption Capacity in Thiol-Functionalized Mesoporous Silica SBA-1. **80,** 3016–3019 (2008).

[57] Zhao, H., Shu, J., Chen, Q. & Zhang, S. Quantitative structural characterization of POSS and octavinyl-POSS nanocomposites by solid state NMR. *Solid State Nucl. Magn. Reson.* **43-44,** 56–61 (2012).

[58] Gaillet, C., Lequart, C., Debeire, P. & Nuzillard, J. M. Band-selective HSQC and HMBC experiments using excitation sculpting and PFGSE. *J. Magn. Reson.* **139,** 454–459 (1999).

[59] Reynolds, W. F. & Enriquez, R. G. Gradient-selected versus phase-cycled HMBC and HSQC: Pros and cons. *Magn. Reson. Chem.* **39,** 531–538 (2001).

[60] Website of Hebrew University NMR lab, http://chem.ch.huji.ac.il/nmr/index.html

[61] W. Claridge, High-Resolution NMR Techniques in Organic Chemistry, Elsevier 2009, ISBN-13: 978-0-08-054818-0

[62] G. Schottner, K. Rose and U. Posset, Scratch and Abrasion Resistant Coatings on Plastic Lenses—State of the Art, Current Developments and Perspectives, J. Sol-Gel Sci. Technol., 2003, 27, 71-79

[63] K.H Haas, S. Amberg-Schwab, K. Rose, G. Schottner, Functionalized coatings based on inorganic–organic polymers (ORMOCER®s) and their combination with vapor deposited inorganic thin film, Surface Coat. Tech., 1999, 111, 72- 79

[64] J. Wen, K. Jordens, G.L. Wilkes, Hybrid organic/inorganic coatings fir abrasion resistance on plastic and metal substrates, Better Ceramics Through Chemistry VII: Organic /Inorganic Hybrid Materials, ed. Mater. Res. Soc. Symp. Proc,, 1996, 435, 207-213

[65] B., Silva, C. J. R. & Pereira, E. V. Organic–inorganic hybrid sol–gel coatings for metal corrosion protection: a review. J. Coatings Technol. Res. **12,** 1–35 (2014)

[66] W. Geffchen, E. Berger, Deutsches Reichspatent, DE736421 asigned to Jenär Glaswerk Schott&Gen, 1939, Jena (Germany)

[67] K. Izumi, H. Tanaka, Y. Uchida, N. Tohge, T. Minami, Hydrolysis of trifunctional

alkoxysilanes and corrosion resistance of steel sheets coated with alkoxysilane-derived-films, J. Mater. Sci. Lett., 1993, 12, 724-727

[68] M. Menning, C. Schelle, A. Duran, J.J. Damborena, M. Guglielmi and G. Brusatin, Investigation of Glass-Like Sol-Gel Coatings for Corrosion Protection of Stainless Steel Against Liquid and Gaseous Attack, J. Sol-Gel Sci. Technol., 1998, 13, 717-722

[69] P. Galliano, J.J. Damborenea, M.J. Pascual and A. Durán, Sol-Gel Coatings on 316L Steel for Clinical Applications, J. Sol-Gel Sci. Technol., 1998, 13, 723-727

[70] J. Gallardo, A. Durán, J.J Damborenea, Electrochemical and in vitro behaviour of sol–gel coated 316L stainless steel, Corrosion Sci., 2004, 46, 795-806

[71] J. Gallardo, A. Duran, I. Garcia, J.P. Celis, M.A. Arenas and A. Conde, Effect of Sintering Temperature on the Corrosion and Wear Behavior of Protective SiO2-Based Sol-Gel Coatings, J. Sol-Gel Sci.Technol., 2003, 27, 175-183

[72] Kumar, N., Jyothirmayi, a., Soma Raju, K. R. C. & Subasri, R. Effect of functional groups (methyl, phenyl) on organic-inorganic hybrid sol-gel silica coatings on surface modified SS 316. Ceram. Int. **38,** 6565–6572 (2012)

[73] Chawada, G. & Dholakiya, B. Organic–inorganic hybrid sol–gel pretreatments for corrosion protection of mild steel in neutral and acidic solutions. Res. Chem. Intermed. 1–16 (2013). doi:10.1007/s11164-013-1479-3

[74] Zheludkevich, ML, et al., "Active Protection Coatings with Layered Double Hydroxide Nanocontainers of Corrosion Inhibitor." Corros. Sci., 52 602–611 (2010)

[75] S.P. Pappas, Radiation curing, science and technology, ed. Plenum Press, New York, 1992

[76] F. Bauer, H.-J. Gläsel, U. Decker, H. Ernst, A. Freyer, E. Hartmann, V. Sauerland, R. Mehnert, Prog. Org. Coat. 47 (2003) 147.

[77] F. Bauer, R. Flyunt, K. Czihal, M.R. Buchmeiser, H. Langguth, R. Mehnert, Macromol. Mater. Eng. 291 (2006) 493.

[78] M. Fedel, F. Deflorian, S. Dirè, V. Tagliazucca, R. Bongiovanni, L. Vescovo, Characterization of Nano-structured UV cured Acrylic Coatings, ECS Transaction, 2009

[79] Esposito Corcione, C., Striani, R. & Frigione, M. Novel hydrophobic free-solvent UV-cured hybrid organic-inorganic methacrylic-based coatings for porous stones. Prog. Org. Coatings **77,** 803–812 (2014).

[80] Esposito Corcione, C., Striani, R. & Frigione, M. Organic-inorganic UV-cured methacrylic-based hybrids as protective coatings for different substrates. Prog. Org. Coatings **77,** 1117–1125 (2014).

[81] Mohseni, M., Bastani, S. & Jannesari, A. Influence of silane structure on curing behavior and surface properties of sol–gel based UV-curable organic–inorganic hybrid coatings. Prog. Org. Coatings **77,** 1191–1199 (2014).

[82] Figueira, R. B., Silva, C. J. R. & Pereira, E. V. Hybrid sol–gel coatings for corrosion protection of hot-dip galvanized steel in alkaline medium. Surf. Coatings Technol. **265,** 191–204 (2015).

[83] G.W. Sherrer, R. Flatt, G. Wheeler, Materials science esearc for the conconservation of sculpture and monuments, MRS Bull., 2001, 26, 24-50

[84] P. Laurie, Preservation of Stone, U.S. Patent 1.607.762, 1926

[85] J.D. Mackenzie and E. Bescher, Factors Governing the Coating of Organic Polymers by Sol-Gel Derived Hybrid Materials, J.Sol-Gel Sci. Technol., 2003, 27, 7-14

[86] E. Carretti, L. Dei and R.G. Weiss, Soft matter and art conservation. Rheoreversible gels and beyond, Soft Matter, 2005, 1, 17-22

[87] E. Smy, Sol-Gel; Potential Creative Applications for the Artist, Focusing on the Colloidal Alkali Silicate Route, J. Sol-Gel Sci. Technol., 1998, 13, 233- 236

[88] C.J. Brinker, Sol-Gel preservation of mankind's cultural heritage in objects constructured of stone, Sandia Lab. Geochemical Dep, Technical report, 1998, 1-36

[89] E.K. Kim, J. Won, J-Y. Do, S.D. Kim, Y.S. Kang, Effects of silica nanoparticle and GPTMS addition on TEOS-based stone consolidants, J. Cult. Heritage, 2009, 10, 214–221

[90] F. Tanno, S. Saka, K. Takabe, Antimicrobial TMSAC-added wood-inorganic composites prepared by the sol-gel process, Mater. Sci. Res. Int., 1997, 3, 137-142

[91] B. Dal Bianco, R. Bertoncello, Sol–gel silica coatings for the protection of cultural heritage glass, Nucl. Instrum. Methods Phys. Res B, 2006, 266, 2358–2362

[92] M. Berger, Nanotechnology materials to the rescue of stone monuments, 2008, http://www.nanowerk.com/spotlight/spotid=4587.php

[93] C. Domingo et al., Possibilities of monitoring the polymerization process of silicon-based water repellents and consolidants in stones through infrared and Ra-

man spectroscopy, Progress in Organic Coatings, 2008, 63, 5–12

[94] Kiele, E. Methyl-modified hybrid organic-inorganic coatings for the conservation of copper. J. Cult. Herit. **15,** 242–249 (2014).

[95] Peng, S. et al. Surface & Coatings Technology Performance evaluation of mercapto functional hybrid silica sol – gel coating on copper surface. Surf. Coat. Technol. **251,** 135–142 (2014).

[96] C.C. Chen, D.J. Lin, T.M. Don, F.H. Huang, L.P. Cheng, Preparation of organic–inorganic nano-composites for antireflection coatings, J. Non-Cryst. Solids, 2008, 354, 3828–3835

[97] D. Chen, Y. Yan, E. Westenberg, D. Niebauer, N. Sakaitani, S.R. Chaudhuri, Y. Sato and M. Takamatsu, Development of Anti-Reflection (AR) Coating on Plastic Panels for Display Applications, J.Sol-Gel Sci. Tech., 2000, 19, 77-82

[98] O. Takahashi et al., Japanese Patent 298545, 1994, 29854 H-J.

[99] Jeong, D-K. Kim, S-B. Lee, S-H. Kwon, K. Kadono, Preparation of Water-Repellent Glass by Sol–Gel Process Using Perfluoroalkylsilane and tetraethoxysilane, J. Colloid Interface Sci., 2001, 235, 130-134

[100] Y. Furukawa, T. Yoneda, Synthesis and properties of fluorosilicone wih perfluorooctylundecyl side chain, J. Polym. Sci. Part A: Polym. Chem., 2003, 41, 2704-2714

[101] Si, F. et al. A superhydrophobic surface with high performance derived from STA-APTES organic-inorganic molecular hybrid. J. Colloid Interface Sci. **407,** 482–487 (2013).

[102] Soliveri, G. et al. Engineered organic/inorganic hybrids for superhydrophobic coatings by wet and vapour procedures. J. Mater. Sci. **49,** 2734–2744 (2014).

[103] Kumar, D. et al. Development of durable self-cleaning coatings using organic–inorganic hybrid sol–gel method. Appl. Surf. Sci. **344,** 205–212 (2015).

[104] D. Avnir, S. Braun, O. Lev, M. Ottolenghi, Enzymes and other proteins entrapped in sol-gel materials, Chem. Mater., 1994, 6, 1605-1614

[105] E. Angeletti, C. Canepa, G. Martinetti, P. Venturello, Tetrahedron Lett., 1988, 29, 2261

[106] A.C. Blanc, The preparation and use of novel immobilised guanidine catalysts in base-catalysed epoxidation and condensation reactions, Green Chem., 2000, 2,

283.

[107] M.A. Harmer, Q. Sun, M.J. Michalczyk, Z. Yang, Unique silane modified perfluorosulfonic acids as versatile reagents for new solid acid catalysts, Chem. Commun., 1997, 1803.

[108] Suzuki, el al. Synthesis and catalytic properties of sulfonic acid-functionalized monodispersed mesoporous silica spheres. **111,** 350–358 (2008).

[109] Suzuki, T. M. et al. Direct synthesis of amino-functionalized monodispersed mesoporous silica spheres and their catalytic activity for nitroaldol condensation. **280,** 224–232 (2008).

[110] 97 C.T. Kresge, M.E. Leonowicz, W.J. Roth, J.C. Vartuli, J.S. Beck, Nature 1992, 359, 710.

[111] D.J. Macquarrie, R. Sartorio, Understanding the influence of the immobilization procedure on the catalytic activity of aminopropylsilicas in C-C forming reactions, Appl. Catal. A, 2003, 246, 183 – 188

[112] H.H.P. Yiu, P.A. Wright and N.P. Botting, Enzyme immobilisation using siliceous mesoporous molecular sieves, Micro. Meso. Mater., 2001, 44- 45, 763-768

[113] J.M. Gómez, J. Deere, D. Goradia, J. Cooney, E. Magner and B.K. Hodnett, Transesterification Catalyzed by Trypsin Supported on MCM-41, Catal. Lett., 2003,

[114] J. Yang , G.W. Stevens and A.J. O'Connor, Adsorption of lysozyme and trypsin by modified MCM-41 with postsynthesis hydrothermal treatment and hydrophobic functionalisation, J. Aust. Ceram. Soc., 2008, 44, 1-6

[115] Y. Li, G. Zhou, W. Qiao and Y. Wang, Immobilization of Porcine pancreas lipase on fiber-like SBA-15 mesoporous material, Mater. Sci. Eng: B, 2009, 162, 120-126

[116] Peralta-Perez, M. R., Saucedo-Castaneda, G., Gutierrez-Rojas, M., and Campero, A. Journal of Sol-Gel Science and Technology 20 (1), 105 (2001)

[117] T.K. Jain, I. Roy, T.K. De and A. Maitra, Nanometer Silica Particles Encapsulating Active Compounds: A Novel Ceramic Drug Carrier, J. Am. Chem. Soc., 1998, 120, 11092-11095

[118] B. Thierry, L. Zimmer, S. McNiven, K. Finnie, C. Barbé, H.J. Griesser, Langmuir, 2008, 24, 8143

[119] M.M. van Schooneveld et al., Nano Lett., 2008, 8, 2517

[120] Moritz, M. & Geszke-Moritz, M. Mesoporous materials as multifunctional tools in

biosciences : Principles and applications. Mater. Sci. Eng. C **49,** 114–151 (2015).

[121] Wang, G. et al. Functionalized mesoporous materials for adsorption and release of different drug molecules : A comparative study. J. Solid State Chem. **182,** 1649–1660 (2009).

[122] Nakamura, M. et al. Colloids and Surfaces B : Biointerfaces Size-controlled synthesis, surface functionalization, and biological applications of thiol-organosilica particles. Colloids Surfaces B Biointerfaces **79,** 19–26 (2010).

[123] Nakamura M, Near-Infrared Fluorescent Silica / Porphyrin Hybrid Nanorings for In Vivo Cancer Imaging. 3539–3546 (2012). doi:10.1002/adfm.201200219

[124] Nakamura, M., Time-lapse fluorescence imaging and quantitative single cell and endosomal analysis of peritoneal macrophages using fluorescent organosilica nanoparticles. Nanomedicine Nanotechnology, Biol. Med. **9,** 274–283 (2013).

[125] Tiwari, P. M., Vig, K., Dennis, V. & Singh, S. R. Functionalized Gold Nanoparticles and Their Biomedical Applications. Nanomaterials 31–63 (2011). doi:10.3390/nano1010031

[126] Ming, M., Chen, Y. & Katz, A. Synthesis and Characterization of Gold - Silica Nanoparticles Incorporating a Mercaptosilane Core-Shell Interface. 8566–8572 (2002).

[127] Suk, M. & Jik, Y. Stimuli-responsive polymers and nanomaterials for gene delivery and imaging applications ☆. Adv. Drug Deliv. Rev. **64,** 1046–1059 (2012).

[128] M. Barboiu, C. Guizard, N. Hovnanian, L. Cot, New molecular receptors for organico of biological interest for the facilitated transport in liquid and solid membranes, Separ. Purif. Technol., 2001, 25, 211-218

[129] G. Tishchenko and M. Bleha, Diffusion permeability of hybrid chitosan/polyhedral oligomeric silsesquioxanes (POSS^{TM}) membranes to amino acids, J. Membr. Sci., 2005, 248, 45-51

[130] O.S. Wolfbeis, Materials for fluorescence-based optical chemical sensors, J. Mater. Chem., 2005, 15, 2657-2669

[131] Etienne, M. *et al.* Molecular Transport into Mesostructured Silica Thin Films : Electrochemical Monitoring and Comparison between p 6 m , P6 / mmc , and Pm 3 n Structures. (2007). doi:10.1021/cm0625068,

[132] Etienne, M., Grosso, D. & Sanchez, C. Electrochemical evidences of morphological transformation in ordered mesoporous titanium oxide thin films. *ChemComm*

4566–4568 (2005). doi:10.1039/b508093b

[133] C. Rottman, G.S. Grader, D. Avnir, Chem Mater., 2001, 13, 3631

[134] Ou, J. *et al.* Recent advances in preparation and application of hybrid organic-silica. 126–140 (2013). doi:10.1002/elps.201200344

[135] Nicole, L., Curie, M. & Organometallique, L. D. C. Advanced selective optical sensors based on periodically organized mesoporous hybrid silica thin films. 2312–2313 (2004).

[136] Tatikonda, A. K., Tkachev, M. & Naaman, R. A highly sensitive hybrid organic-inorganic sensor for continuous monitoring of hemoglobin. *Biosens. Bioelectron.* **45,** 201–205 (2013)

[137] C. Malins, B.D. MacCraith, Dye-doped organically modified silica glass for fluorescence based carbon dioxide gas detection, Analyst ,1998, 123, 2373- 2376

[138] C. Von Bulzingslöwen, A.K. McEvoy, C.McDonagh, B.D. MacCraith, I. Klimant, C. Kraus et al., Sol-gel based otpical carbon dioxide sensor employing dual luminophore referencing for application in food packaging technology, Analyst, 2002, 127, 1478-1483

[139] Liang, Y., Huang, J., Zang, P., Kim, J. & Hu, W. Molecular layer deposition of APTES on silicon nanowire biosensors : Surface characterization, stability and **pH response**. *Appl. Surf. Sci.* **322,** 202–208 (2014).

[140] Choung, J.-H., Lee, Y.-W., Choi, D.-K. & Kim, S.-H. Adsorption Equilibria of Toluene on Polymeric Adsorbents. *J. Chem. Eng. Data* **46,** 954–958 (2001).

[141] Jaubert JN, Barth D, Perrin L, Determining volatile organic compounds' adsorption isotherms on dealuminated Y zeolite and correlation with different model, J. OF CHEM. AND ENG. DATA, 47, 2002 **DOI:** 10.1021/je025590q

[142] Canet, X. *et al.* Adsorption of Alkanes and Aromatic Compounds on Various Faujasites in the Henry Domain. 2. Composition Effect in X and Y Zeolites. *J. Chem. Eng. Data* **52,** 2127–2137 (2007).

[143] Kosuge, K., Kubo, S., Kikukawa, N. & Takemori, M. Effect of Pore Structure in Mesoporous Silicas on VOC Dynamic Adsorption/Desorption Performance. *Langmuir* **23,** 3095–3102 (2007).

[144] Borovin, E., Callone, E., Ceccato, R., Quaranta, A. & Dirè, S. Adsorptive properties of sol–gel derived hybrid organic/inorganic coatings. *Mater. Chem. Phys.* **147,** 954–962 (2014).

[145] Wolfbeis, O., Reisfeld, R. & Oehme, I. in *Optical and Electronic Phenomena in Sol-Gel Glasses and Modern Application SE - 2* **85,** 51–98 (Springer Berlin Heidelberg, 1996).

[146] Calvo-Muñoz, M.-L. *et al.* Chemical sensors of monocyclic aromatic hydrocarbons based on sol–gel materials: synthesis, structural characterization and molecular interactions. *J. Mater. Chem.* **12,** 461–467 (2002).

[147] Calvo-Muñoz, M. L., Chemical sensors of monocyclic aromatic hydrocarbons based on sol-gel materials: Kinetics of trapping of the pollutants and sensitivity of the sensor. *Sensors Actuators, B Chem.* **87,** 173–183 (2002).

[148] Wang, S. *et al.* Organic/inorganic hybrid sensors: A review. *Sensors Actuators, B Chem.* **182,** 467–481 (2013).

[149] Melde, B. J., Johnson, B. J. & Charles, P. T. Mesoporous Silicate Materials in Sensing. 5202–5228 (2008). doi:10.3390/s8085202

[150] Salon, M. B., Abdelmouleh, M. & Boufi, S. Silane adsorption onto cellulose fibers : Hydrolysis and condensation reactions. **289,** 249–261 (2005).

[151] Vasiljević, J. *et al.* Study of flame-retardant finishing of cellulose fibres: Organic-inorganic hybrid versus conventional organophosphonate. *Polym. Degrad. Stab.* **98,** 2602–2608 (2013).

[152] Schramm, C., Rinderer, B. & Tessadri, R. Non-formaldehyde, crease resistant agent for cotton fabrics based on an organic-inorganic hybrid material. *Carbohydr. Polym.* **105,** 81–89 (2014).

[153] Girardi, F. *et al.* Hybrid organic-inorganic materials as coatings for protecting wood. *Prog. Org. Coatings* **77,** 449–457 (2014).

[154] Barletta, M., Puopolo, M., Tagliaferri, V. & Vesco, S. Retrofitting of solar glasses by protective anti-soiling and -graffiti coatings. *Renew. Energy* **66,** 443–453 (2014).

[155] R.H. Glaser, G.L. Wilkes, C.E. Bronnimann, J. Non-Cryst. Solids 113 (1989) 73

[156] CRC Handbook of Chemistry and Physics - R.C. Weast ed. CRC Press Inc., Boca Raton, FL (USA), 1986

[157] M. Carraro, S. Gross, Hybrid Materials Based on the Embedding of Organically Modified Transition Metal Oxoclusters: A Review, *Materials* **2014**, *7*, 3956-3989; doi:10.3390/ma7053956

[158] P. Gouzerh and M. Che, Polyoxometalates (POMs) revisited and the “missing link”

between the bottom up and top down approaches, l'actualite chimique, 2006, 298, 9-22

[159] Gross, S. Oxocluster-reinforced organic-inorganic hybrid materials: effect of transition metal oxoclusters on structural and functional properties. *J. Mater. Chem.* **2011**, *21*, 15853–15861

[160] Rozes, L.; Cochet, S.; Frot, T.; Fornasieri, G.; Sassoye, C.; Popall, M.; Sanchez, C. Titanium oxoclusters: Vesatile nano-objects for the design of hybrid compounds. *Mater. Res. Soc. Symp. Proc.* **2007**, *1007*, doi:10.1557/PROC-1007-S15-02

[161] F Ribot, E. Martinez-Ferrero,. Functionalized alkoxy tin clusters as nanobuilding blocks for hybrid materials, Progress in Solid State Chemistry 33 (2005) 89e97

[162] F Ribot, A. Strachota et al. Tin-based "super-POSS" building blocks in epoxy nanocomposites with highly improved oxidation resistance/ Polymer 55 (2014)

[163] M. Bahrami, R. Laine, Why do cages self-brominate, Phys Chem Chem Phys, 2014

[164] Maki Itoh, et al, Characterization and Some Insights into the Reaction Chemistry of Polymethylsilsesquioxane or Methyl Silicone Resins, International Journal of Polymer Science, 2012, doi:10.1155/2012/526795

[165] a) M.M. Sprung, F.O. Guenther, J. Am. Chem. Soc. 77 (1955) 3996..

b) Kaneko, Preparation of cage-like octa(3-aminopropyl)silsesquioxane trifluoromethanesulfonate in higher yield with a shorter reaction time. *J. Mater. Chem.* **22,** 14475–14478 (2012).

[166] Coughlin, E. B., Gunji, T., Itoh, M., Matsukawa, K. & Naka, K. Silsesquioxanes : Recent Advancement and Novel Applications. (2012).

[167] S. Fabritz, Bioconjugation of Peptides on Cube-octameric Silsesquioxanes. Thesis, University of Darmstadt (2013)

[168] Nischang I., Brueggemann O., Svec F., Advances in the preparation of porous polymer monoliths in capillaries and microfluidic chips with focus on morphological aspects. Anal. Bioanal. Chem. 397, 953-960, 2010

[169] Choi, J. H., Lee, J. W., Yang, S. H. & Cheong, W. J. Ground organic monolith particles as chromatographic separation media. *Bull. Korean Chem. Soc.* 34, 291–294 (2013).

[170] Vieira, E. G. et al. Study on soluble heavy metals with preconcentration by using a new modified oligosilsesquioxane sorbent. J. Hazard. Mater. 237-238, 215–222 (2012).

[171] Baccile, N. & Babonneau, F. Organo-modified mesoporous silicas for organic pollutant removal in water : Solid-state NMR study of the organic / silica interactions. **110,** 534–542 (2008).

[172] Kao, H., Lee, L. & Palani, A. C CPMAS NMR Spectroscopy as a Versatile and Quantitative Tool for Determination of Mercury Adsorption Capacity in Thiol-Functionalized Mesoporous Silica SBA-1. **80,** 3016–3019 (2008).

[173] Zhu, P., Hu, L., Wang, D., Zhang, Q. & Song, S. Synthesis of (3-mercaptopropyl)trimethoxysilane-modified ZMS and study of the enhancement of ammonia-nitrogen removal from water. *Mater. Sci. Forum* **686,** 461–467 (2011).

[174] Wang, W., Chen, M., Chen, X. & Wang, J. Thiol-rich polyhedral oligomeric silsesquioxane as a novel adsorbent for mercury adsorption and speciation. *Chem. Eng. J.* **242,** 62–68 (2014).

[175] Cole, M. A. & Bowman, C. N. Evaluation of Thiol-Ene Click Chemistry in Functionalized Polysiloxanes. 1749–1757 (2013). doi:10.1002/pola.26551

[176] He, H. *et al.* Mesostructured Nanomagnetic Polyhedral Oligomeric Silsesquioxanes (POSS) Incorporated with Dithiol Organic Anchors for Multiple Pollutants Capturing in Wastewater. (2013).

[177] Cole, M. A., Jankousky, K. C. & Bowman, C. N. Thiol-ene functionalized siloxanes for use as elastomeric dental impression materials. Dent. Mater. 30, 449–455 (2014).

[178] Chen, M. *et al.* Facile preparation of organic-silica hybrid monolith for capillary hydrophilic liquid chromatography based on ‘ thiol-ene ’ click chemistry. *J. Chromatogr. A* **1284,** 118–125 (2013).

[179] Rozga-Wijas, K. Synthesis of New Polyfunctional Cage Oligosilsesquioxanes and Cyclic Siloxanes by Thiol-ene Addition. 588–594 (2012). doi:10.1007/s10904-012-9652-5

[180] Xue, L., Li, L., Feng, S. & Liu, H. A facile route to multifunctional cage silsesquioxanes via the photochemical thiol e ene reaction. *J. Organomet. Chem.* **783,** 49–54 (2015).

[181] Hall D.E., Moreland J.C., Fundamentals of Rolling Resistance. Rubber Chem Technol. 2001;74(3):525–539. doi:10.5254/1.3547650.

[182] Fröhlich J, Niedermeier W, Luginsland HD. The effect of filler-filler and filler-elastomer interaction on rubber reinforcement. Compos Part A Appl Sci Manuf.

2005;36(4):449–460. doi:10.1016/j.compositesa.2004.10.004.

[183] Litchfield DW, Baird DG. The rheology of high aspect ratio nano-particle filled liquids. Rheol Rev. 2006;2006:1–60

[184] R. Scotti, L. Conzatti, M. D'Arienzo, B. Di Credico, L. Giannini, T. Hanel, P. Stagnaro, A. Susanna, L. Tadiello, F. Morazzoni, "Shape controlled spherical (0D) and rod-like (1D) silica nanoparticles in silica/styrene butadiene rubber nanocomposites: Role of the particle morphology on the filler reinforcing effect", Polymer 55 (2014) 1497

[185] Liu Q, Ren W, Zhang Y, Zhang Y. Curing reactions and properties of organic-inorganic composites from hydrogenated carboxylated nitrile rubber and epoxycyclohexyl polyhedral oligomeric silsesquioxanes. Polym Int. 2011;60(3):422–429. doi:10.1002/pi.2964

[186] Chang FC. POSS related polymer nanocomposites. Prog Polym Sci. 2011;36(12):1649–1696. doi:10.1016/j.progpolymsci.2011.05.002.

[187] Li, S., Simon, G. P. & Matisons, J. G. The Effect of Incorporation of POSS Units on Polymer Blend Compatibility. (2009). doi:10.1002/app

[188] Ayandele, E., Sarkar, B. & Alexandridis, P. Polyhedral Oligomeric Silsesquioxane (POSS)-Containing Polymer Nanocomposites. 445–475 (2012). doi:10.3390/nano2040445

[189] Matejka, L. Electrical and thermomechanical properties of epoxy-POSS nanocomposites., European Polymer Journal, **47,** 861–872 (2011).

[190] Matejka, L. & Pleštil, J. Effect of POSS on thermomechanical properties of epoxy – POSS nanocomposites., European Polymer Journal, **48,** 260–274 (2012).

[191] Wang X, Wang X, Song L, et al. Preparation and thermal stability of UV-cured epoxy-based coatings modified with octamercaptopropyl POSS. Thermochim Acta. 2013;568:130–139. doi:10.1016/j.tca.2013.06.038

[192] Kuo, S. & Chang, F. Progress in Polymer Science POSS related polymer nanocomposites. *Prog. Polym. Sci.* **36,** 1649–1696 (2011).

[193] Raftopoulos, K. N. & Pielichowski, K. Segmental dynamics in hybrid polymer / POSS nanomaterials. *Prog. Polym. Sci.* (2015). doi:10.1016/j.progpolymsci.2015.01.003

[194] Chruściel, J. J. & Leśniak, E. Modification of epoxy resins with functional silanes, polysiloxanes, silsesquioxanes, silica and silicates. *Prog. Polym. Sci.* **41,** 67–121

(2015).

[195] Li GZ, Wang L, Toghiani H, Daulton TL, Koyama K, Pittman CU. Viscoelastic and Mechanical Properties of Epoxy/Multifunctional Polyhedral Oligomeric Silsesquioxane Nanocomposites and Epoxy/Ladderlike Polyphenylsilsesquioxane Blends. Macromolecules. 2001;34(25):8686–8693. doi:10.1021/ma011117q

[196] Chang, S., Matsumoto, T., Matsumoto, H. & Unno, M. Synthesis and characterization of heptacyclic laddersiloxanes and ladder polysilsesquioxane. *Appl.Organometal. Chem. 2010,* 241–246 (2010). doi:10.1002/aoc.1607

[197] Handke, M., Handke, B., Kowalewska, A. & Jastrze, W. New polysilsesquioxane materials of ladder-like structure. **926,** 254–263 (2009).

[198] Gao, Q., Qi, S., Wu, Z., Wu, D. & Yang, W. Synthesis and characterization of functional ladder-like polysilsesquioxane and their hybrid films with polyimide. *Thin Solid Films* **519,** 6499–6507 (2011).

[199] Ghosh, P., Han, G., De, M., Kim, C. K. & Rotello, V. M. Gold nanoparticles in delivery applications ☆. **60,** 1307–1315 (2008).

[200] Tokonami, S., Yamamoto, Y., Shiigi, H. & Nagaoka, T. Synthesis and bioanalytical applications of specific-shaped metallic nanostructures : A review. *Anal. Chim. Acta* **716,** 76–91 (2012).

[201] W.L.F. Armarego and C.L.L. Chai, *Purification of laboratory chemicals*, Butterworth-Heinemann, Amsterdam, Boston (2003).

[202] Tagliazucca, V. & Callone, E. Influence of synthesis conditions on the cross-link architecture of silsesquioxanes prepared by in situ water production route. *J Sol-Gel Sci Technol* 236–245 (2011). doi:10.1007/s10971-011-2599-0

[203] Li, D. *et al.* The effect of adding PDMS-OH and silica nanoparticles on sol – gel properties and effectiveness in stone protection. *Appl. Surf. Sci.* **266,** 368–374 (2013).

[204] Burkhalter, R. S. *et al.* Controlled tin catalyzed hydrolysis of 3-acryloxypropyltrimethoxysilane with mono- and multi-functional mercaptans. *J. Organomet. Chem.* **724,** 213–224 (2013).

[205] Orel, B., Hydrolysis and Solvolysis of Methyltriethoxysilane Catalyzed with HCl or Trifluoroacetic Acid : IR Spectroscopic and Surface Energy Studies. , J Sol-Gel Sci, 251–265 (2005).

[206] L. Matějka, O. Dukh, J. Brus, W.J. Simonsick Jr, and B. Meissner, J. Non-Cryst.

Solids, 270. 34 (2000).

[207] J. Cervantes, R. Zárraga, and C. Salazar-Hernández, Organotin catalysis in organosilicon chemistry, Appl. Organomet. Chem., 26, 157 (2012).

[208] Z. Sassi, J.C. Bureau, A. Bakkali, Spectroscopic study of TMOS-TMSM-MMA gels: previously identification of the networks inside the hybrid material, Vib. Spectrosc. 28 (2002) 299–318

[209] Handke, M., Kowalewska, A. & Mozgawa, W. Spectroscopic study of ceramic precursors obtained by hydrolytic condensation of ethoxycyclotetrasiloxane, *J. Mol. Struct.* **887,** 152–158 (2008).

[210] Handke, M. & Jastrzebski, W. Vibrational spectroscopy of the ring structures in silicates and siloxanes. J. Mol. Struct. 704, 63–69 (2004).

[211] H. Yoshino, K. Kamiya, and H. Nasu, IR study on the structural evolution of sol-gel derived SiO2 gels in the early stage of conversion to glasses, J. Non-Cryst. Solids 126, 68 (1990)

[212] E. S. Park, H. W. Ro, C. V. Nguyen, R. L. Jaffe and D. Y. Yoon, Infrared Spectroscopy Study of Microstructures of Poly(silsesquioxane)s, Chem. Mater, 2008, 20, 1548–1554

[213] Seki, H., Kajiwara, T., Abe, Y. & Gunji, T. Synthesis and structure of ladder polymethylsilsesquioxanes from sila-functionalized cyclotetrasiloxanes. *J. Organomet. Chem.* **695,** 1363–1369 (2010).

[214] Handke, M. & Jastrze, W. Vibrational spectroscopy of the double 4- , 6-membered rings in silicates and siloxanes, *J. Mol. Struct.* **747,** 671–675 (2005).

[215] a) W Noll, in Chemistry and Technology of Silicones, Academic Press, New York (1968); b) L. Wilczek and J. Chojnowski, Macromolecules, 14, 9 (1981).

[216] Z. Xu, C.Ni, B. Yao, L. Tao, C. Zhu, Q. Han, and J. Mi, Colloid Polym. Sci. 289, 1777 (2011)

[217] F.J. Feher D. Soulivong, and A. G. Eklund, Chem. Commun. 68, 399 (1998)

[218] F.J. Feher, D.A. Newman, and J.F. Walzer, J. Am. Chem. Soc., 111, 1741(1989).

[219] Brunet, F. Populations of Oligomers in sol-gel condensation, *J. Non. Cryst. Solids* **163,** 221-225, (1993).

[220] F. Devreux, Boilot, J. Sol-Gel polymerization in alkoxysilanes 29Si NMR study of kinetics. *Mater. Sci. Eng. B* **37,** 197–200 (1996).

[221] H. Marsmann, W. Martienssen, and O. Madelung, Chemical Shifts and Coupling Constants for Silicon-29, Springer, Berlin, Heidelberg, New York, 2008, p. IX.

[222] Cordes, D. B., Lickiss, P. D. & Rataboul, F. Recent Developments in the Chemistry of Cubic Polyhedral Oligosilsesquioxanes. *Chem. Rev.* **110,** 2081–2173 (2010).

[223] B.J. Hendan and H.C. Marsmann, "Silsesquioxanes as models of silica supported catalyst -, APPL ORGAN, 13(4), 1999, pp. 287-294

[224] J. Fu, L. Shi, Y. Chen, S. Yuan, J. Wu, X. Liang, and Q. Zhong, J. Appl. Polym. Sci. 109, 340 (2008)

[225] W.E. Wallace, C. M. Guttman, J. M. Antonucci, J.Am.Soc. Mass. Spectrom. 10, 224 (1999)

[226] R.J.J. Williams, R. Erra-Balsels, Y. Ishikawa.H. Nonami, A N. Mauri, C. C. Riccardi, Macromol. Chem. Phys. 202, 2425 (2001)

[227] H. Mori, M.G. Lanzendörfer, A.H.E. Müller, and J.E. Klee, Macromolecules 37, 5228 (2004).

[228] Zhang, X. Study of three-dimensional configurations of organic / inorganic hybrid nanostructural blocks : A quantum chemical investigation for cage structure of (c -glycidoxypropyl) silsesquioxanes. *J. Mol. Struct.* **872,** 197–204 (2008).

[229] Pouxviel, J. c. & Boilot, J. p. Nmr study of the sol/gel polymerization. J. Non. Cryst. Solids 89, 345–360 (1987).

[230] H. Marsmann. Oxygen-17 and Silicon-29 NMR Spectroscopy, Springer, Berlin, 1981.

[231] Hook, R. J. A 29Si NMR study of the sol-gel polymerisation rates of substituted ethoxysilanes. J. Non. Cryst. Solids 195, 1–15 (1996).

[232] Kaneko, Y. *et al.* Silsesquioxanes : Recent Advancement and Novel Applications. *Int. J. Polym. Sci.* 1–130 (2012). doi:doi:10.1155/2012/453821

[233] Unno M, Nonacyclic Ladder Silsesquioxanes and Spectral Features of Ladder Silsesquioxanes, Int. Jour. of Pol. Sci., ID 723892, (2012)

[234] Ribot, F. *et al.* In situ evaluation of interfacial affinity in CeO2 based hybrid nanoparticles by pulsed field gradient NMR. *Chem. Commun. (Camb).* **3,** (2005)

[235] Van Lokeren, L., Ben Sassi, H., Van Assche, G. & Ribot, F. Quantitative analysis of polymer mixtures in solution by pulsed field-gradient spin echo NMR spectrosco-

py. *J. Magn. Reson.* **231,** 46–53 (2013).

[236] Holz, M., Mao, X., Seiferling, D. & Sacco, A. Experimental study of dynamic isotope effects in molecular liquids: Detection of translation-rotation coupling. *J. Chem. Phys.* **104,** 669 (1996).

[237] Thomas, S., Maria, H. J., Chan, C. H. & Pothen, L. A. Natural Rubber Materials, volumes 1-2, (2014).

[238] L.Wahba, M. D'Arienzo, S. Dirè, R. Donetti, T. Hanel, F. Morazzoni, M. Niederberger, N. Santo, L. Tadiello and R. Scotti, "Novel non-aqueous sol-gel route for the in-situ synthesis of high loaded silica-rubber nanocomposites", *Soft Matter*, (2014), **10**, 2234-2244.

[239] A. Susanna, L. Armelao, E. Callone, S. Dirè, M. D'Arienzo, B. Di Credico, L. Giannini, T. Hanel, F. Morazzoni, R. Scotti, "ZnO nanoparticles anchored to silica filler. A curing accelerator for isoprene rubber composites", *Chem. Eng. J.* , 00, (2015), 000.

[240] M.R.G. Coelho," R.A.S. San Gil" & M.I.B. Tavaresbv" Carbon-13 High-Resolution Solid State NMR Study of Polybutadiene", Polymer Testing 15 (1996) 485-490

[241] R. Di Maggio, S. Dirè, E. Callone, F. Girardi, G. Kickelbick, Polymer , **51** (2010), 832-841.

[242] F. Deflorian, M. Fedel, S. Dirè, V. Tagliazucca, R. Bongiovanni, L. Vescovo, M. Minelli, M.G. De Angelis, "Study of the effect of organically functionalized silica nanoparticles on the properties of UV curable acrylic coatings", *Progress in Organic Coatings*, 72 (2011) 44-51.

[243] R. Di Maggio, E. Callone, F. Girardi, S. Dirè, "Structure-related behaviour of hybrid organic-inorganic materials prepared by different synthesis conditions from Zr-based NBBs and 3-methacryloxy propyl trimethoxysilane", *J. Appl.Polym.Sci* , (2012) **125**, 1713-1723

[244] Bonhomme, C., Gervais, C. & Laurencin, D. "Progress in Nuclear Magnetic Resonance Spectroscopy Recent NMR developments applied to organic – inorganic materials", *Prog. Nucl. Magn. Reson. Spectrosc.* 77**,** 1–48 (2014).

[245] Kay Saalwachter, Breakdown in the efficiency factor of the mixed Magic Sandwich Echo: A novel NMR probe for slow motions, Chemical Physics Letters 516 (2011) 106–110

[246] Z. Zinan, X. Demin, Z. Jianguo, W. Qinyi, F. Zhiliu, 2 a new peak T4 in the 13C-NMr spectrum of polybutadiene". Pol. Commun. 1983, 1, 1-3

Appendix A

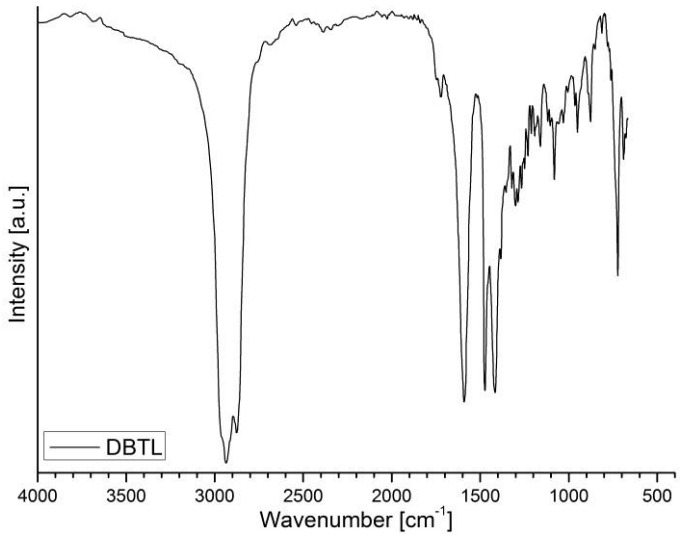

Figure A1. FTIR transmission mode spectrum and typical characteristics of DBTL

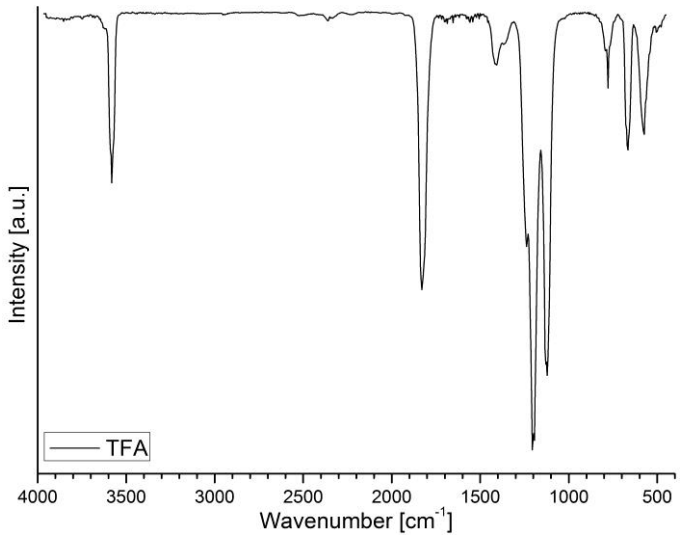

Figure A2. FTIR transmission mode spectrum and typical characteristics of TFA

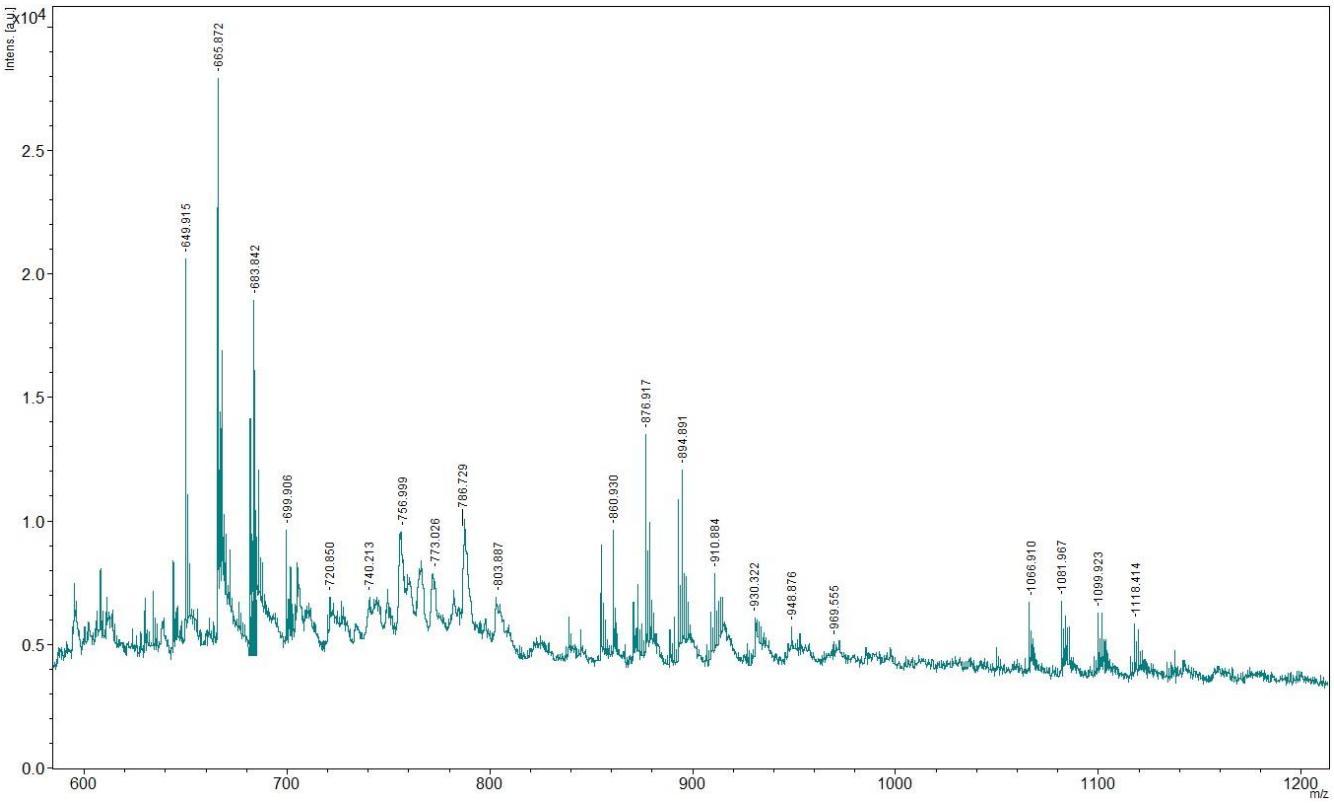

Figure A3. MALDI TOF spectrum of DBTL6 sample.

Acknowledgements

This piece of work, apart from my personal efforts, is built by contributions of many, and all the participated persons are greatly acknowledged.

Particularly I would like to say enormous thanks to Prof. Sandra Dirè for her diligence in tutoring. She became the very special person in my life, by sharing the scientific knowledge and building up my analytical world view. Thank you, Sandra, for looking deep inside important things, still noticing the fun and joyful ones. It made my stay in Trento exciting, valuable in research, and transformed obtained analytical approach to the way of living.

Special thanks are going to the rest of my Trentino family: Prof. Riccardo Ceccato for his valuable advices and sharing of the expertise; Dr. Emanuela Callone for her patience to my requests, continuous coaching in NMR, and always shining smile; Dr. Marco Ischia for his help in taming of capricious instruments; Prof. Gian Domenico Soraru for the discussions of the most important aspects; Prof. Alberto Quaranta for introducing me to the field of UV-Vis; Prof. Graziano Guella for the help with MALDI TOF measurements and their discussion; lab technicians Livio Zottele and Alexia Conci for their rapid solution for any of my requests; and all the PhD fellows of department of Industrial Engineering of University of Trento for their critical advices and discussions.

Many thanks are going overseas to UPMC - Collège de France (Paris, France): Dr. F. Babonneau for giving me a chance to work 4 month in in such a strong team; Dr. Francois Ribot for his patience in sharing with expertise and brilliant suggestions; Dr. Christel Gervais for suggestions in deconvolution techniques, and all other team members of LCMCP lab for their help and advices.

Particular thanks are addressed to Prof. R. Scotti from the University of Milano-Bicocca for his interesting inspirational ideas and proposal for collaboration. PhD fellow Matteo Redaelli from the group of R. Scotti is highly acknowledged for his efforts in materials characterization in the frame of our collaboration.

I am deeply grateful to my family and friends for their constant encouragement.

Certainly, it would not be possible to achieve reported results without financial support. I am pleased to gratefully thank the INSTM and UNITN for providing co-funding of my PhD scholarship in the memory of Klaus Müller.

COST Action MP1202 (“Rational design of hybrid organic/inorganic interfaces: the next step towards advanced functional materials” 2012-2016); Bilateral agreement between University of Trento and Collège de France and Foundation Hugot (Collège de France) are greatly acknowledged as well.